A STUDY OF STRUCTURE, ELECTRICAL PROPERTIES

AND ELECTRICAL DEGRADATION OF UNDOPED

AND NICKEL DOPED BARIUM TITANATE

Sudhir R. Kulkarni
B.E., M. S. University of Baroda, Baroda, India, 1974
M.Tech., Indian Institute of Technology Kanpore, India, 1976

The dissertation "A Study of Structure, Electrical Properties and Electrical Degradation of Undoped and Nickel Doped Barium Titanate" by sudhir R. Kulkarni has been examined and approved by the following Examination Committee:

Nicholas G. Eror, Thesis Advisor
Professor

Thomas M. Loehr
Professor

Jack H. Devletian
Associate Professor

Paul Clayton
Associate Professor

ACKNOWLEDGEMENTS

TABLE OF CONTENTS

LIST OF TABLES

LIST OF FIGURES

ABSTRACT

Barium titanate has a wide variety of applications, due to its ferroelectric, dielectric and piezoelectric properties. Some of these applications are as transducers, memory, delay line and capacitors. Due to its high dielectric constant barium titanate is by far the most widely used material for multi layer ceramic capacitors. Degradation is still a common malady in this material even after the many reported studies. A majority of the previous studies were not carried out on thermodynamically defined samples.

In this investigation thermodynamically well defined and high purity $BaTiO_3$ with various Ba/Ti ratios and $BaNi_xTi_{1-x}O_3$ with x = 0.005 to x = 20 at. % were prepared by the liquid mix technique. The observed X-ray diffraction pattern for $BaTiO_3$ showed very little change in lattice parameter with Ba/Ti ratio whereas Raman spectroscopy was very sensitive to these small changes from the stoichiometry. Nickel solubility was estimated to be 1.5 at. % Ni in $BaTiO_3$ at 1275^0 C. The solubility of nickel was also found to be a function of sintering temperature where higher temperatures led to lower solubility. By X-ray diffraction and Raman methods it was shown that the second phase formed at 1.5 at. % Ni doping is a hexagonal $BaTiO_3$. The Raman method has shown that this hexagonal phase has a different lattice dynamics than the hexagonal phase which is formed in pure $BaTiO_3$, though X-ray patterns are the same for both these phases. Temperature dependent Raman spectra showed that the room temperature Raman spectrum of barium titanate is a combination of first order and second order scattering proceses.

Electrical conductivity measurements between 200 and 550^0 C have shown that in this temperature range, the conduction was by a band process and it was

predominantly electronic in nature. The band gap for undoped stoichiometric barium titanate was found to be 2.74 ± 0.05 eV.

The electrical conductivity with the different Ba/Ti ratios and various amounts of Ni doping was measured between 850 and 1100^0 C and between 10^0 to 10^{-22} atm. of oxygen. The effect of nickel doping on the conductivity was observed for small doping (0.0005 at.%). For the 0.01 at % nickel doped sample the conductivity was proportional to $Po_2^{-1/4}$ between Po_2, 10^{-8} and 10^{-22} atm. indicating the dominance of the acceptor dopants. As the nickel increased the minimum in the conductivity and thus the n to p transition was shifted to a lower partial pressure of oxygen and the p-type conductivity increased. For the 1 at. % nickel doped sample electronic compensation was observed. At 900^0 C and 10^{-13} atm. of Po_2, nickel changes valency from +3 to +2. Nickel substituted on the titanium site in the barium titanate lattice with +3 valence.

For $BaTiO_3$, the data were found to be proportional to -1/6 power of oxygen partial pressure for the pressure range 10^{-8} to 10^{-22} atm., and proportional to $Po_2^{+1/4}$ for the oxygen pressure range $> 10^{-4}$ atm. The deviation from the ideal Ba/Ti ratio was found to be accommodated by neutral vacancy pairs.

Pure $BaTiO_3$ with various Ba/Ti ratios showed little degradation at 10 kv/cm. stress at 250^0 C, but as the Ni increased the resistance to degradation decreased. Resistance to degradation was found to be sensitive to the Ba/(Ti + Ni) ratio. When this ratio was greater than unity the samples have high degradation resistance. This study did not show any correlation between the degradation and the migration of oxygen vacancies towards the cathode.

Microscopic observation did not yield information about the second phase, (10 to 20 at.% nickel doped samples) mainly due to the poor contrast between the two phases, although two different methods of etching were employed. The Raman

technique however showed promise that it can make in situ structure and phase determination nondestructively.

In the Raman spectra of reduced barium titanate an extra band at 820 cm^{-1} has been observed. This band was correlated to the presence of oxygen vacancies.

1. INTRODUCTION

Discovery of an extremely high dielectric constant and of ferroelectricity in barium titanate (1) aroused great industrial interest in this material. With this, miniaturization of existing components and development of circuit elements with unique properties and high durability was made possible. A dielectric constant/volume ratio hundreds of times greater than many other known capacitor materials, coupled with high dielectric strength, allowed substitution of $BaTiO_3$ as a capacitor material where previously paper and other materials were used. Piezoelectric and ferroelectric properties encouraged use in transducer, memory and delay line applications.

A problem which is persisting even today in the use of barium titanate as a capacitor material is dielectric degradation. In the case of barium titanate degradation means an increase in the electrical conductivity with time under the application of an electric stress.

Extensive work was carried out at Linden labs. (State College Pa) during 1955 to 1966 to address degradation and aging problems. This is summarized in a review article by Gruver et. al. (2). Thereafter, various investigations have been carried out on degradation of single crystals (3, 4) polycrystalline $BaTiO_3$ (4 - 8) and multi - layer capacitors. (9)

Gruver et. al. (2) proposed that, degradation is caused by the migration of oxygen vacancies towards the cathode under the applied electrical stress and corresponding reduction of Ti^{+4} to Ti^{+3} thus creating 3d band electrons, which contribute to the increased conductivity. They also empirically determined methods to improve resistance to degradation by introducing small amount of second phase at the grain boundaries to impede the motion of oxygen vacancies

and by the use of dopants. Dopants going on the Ti site should have a valency greater than +4 e.g. U^{+6}, W^{+6}, Nb^{+5} etc. or by dopants on the Ba site with a valency greater than +3 e.g. La^{+3} and by dopants going on the oxygen site should have a valency less than -2 e.g. F^{-1} etc.. The materials used by them were thermodynamically not well defined. Also they assumed that at a firing temperature of 1300^0 C, $BaTiO_3$ is reduced and cooling back to room temperature reoxidizes the surface with the bulk remaining reduced with oxygen vacancies and Ti^{+3}.

The phenomenon observed during degradation by Lehovec and Shirn (4) and various other investigators, is colour region development. It is observed that under electrical stress first a blue region develops at the cathode and a brown region at the anode. However, after a few minutes under the applied electrical stress a clear area develops within the brown area near the anode and a white halo surrounds the blue region near the cathode. With time the blue and brown areas increase and eventually the blue region penetrates the brown region and the sample fails. Based on this colour region development and measurement of potential distribution at various points between anode and cathode, it was suggested that, a high conductivity zone originates from the cathode and a low conductivity zone originates from the anode. The area near the anode is rich in oxygen vacancies.

From various studies (1-9,84,85) it appears that, a very clear understanding of the degradation mechanism is still lacking. Never-the-less, oxygen vacancies, ratio of Ba/Ti and point defect structure play a very important role in the degradation. Most of the past investigations were carried out with poorly defined materials. Thus, it was thought that a new study with well defined samples would help resolve some of the above mentioned oddities.

In this study high purity $BaTiO_3$ samples with various Ba/Ti ratios were prepared by the Liquid Mix Technique first described by Pechini (10). Also samples with various amounts of Ni with fixed Ba/Ti+Ni ratio were made. Powders and pellets were characterized by X-Ray powder diffraction and Raman spectroscopy. Defect structure, electrical conductivity and current versus voltage behavior of these samples were investigated to determine the resistance to degradation. This included the testing for Schottky emission, or space-charge limited current or ohmic behavior. The dielectric constant at two frequencies was also measured. In addition an attempt was made to identify the valency state of Ni by the ESR method.

2. LITERATURE REVIEW

2.1 Defects in Ternary Compounds

Review of the disorder in binary compounds was first published by Kroger and Vink (11). Thereafter Schmalzried and Wagner (12) rigorously derived the relationships between various disorders for ternary compounds such as spinel, AB_2O_4, and perovskites, ABO_3.

In deriving the relationships between various defects, a thermodynamically defined system is assumed. Various point defects which are possible, ionic and electronic, are considered and equilibrium defect concentrations as a function of thermodynamic variables are derived. The thermodynamic variable generally used is the partial pressure of the anion, and all other variables are held constant.

For the system $BaTiO_3$ which is equivalent to ABO_3 the various defects and notations are shown in Table 2.1. Depending on the concentration of an individual defect, various intermediate conditions can exist giving different relationship between defects.

The calculated P_{O2} dependence of fully ionized defect concentrations for $BaTiO_3$ is shown in Table 2.2. Figure 2.1 is the isothermal pressure dependence of various defect concentration for the neutrality condition in the intermediate region $[V_O^{\cdot\cdot}] = [V_A''] + 2\ [V_B'''']$ (Shottky disorder) and Figure 2.2 for the intermediate neutrality condition $[\ n\ ] = [\ p\ ]$.

2.1.1 Effect of foreign atoms

As is well known from elemental semiconductors, a small amount of aliovalent impurity, whether intentionally or accidentally added has a pro-

Table 2.1

DEFECT NOTATIONS

A_A	Cation A on its normal lattice site	Ba_{Ba}
B_B	Cation B on its normal lattice site	Ti_{Ti}
O_O	Anion O on its normal site	O_O
$A_i^{..}$	Divalent cation A on an interstitial site	$Ba_i^{..}$
$B_i^{....}$	Tetravalent cation B on an interstitial site	$Ti_i^{....}$
$O_i^{''}$	Divalent anion O on an interstitial site	$O_i^{''}$
V_A	Cation vacancy on site A	$V_{Ba}^{''}$
V_B	Cation vacancy on site B	$V_{Ti}^{''''}$
$V_O^{..}$	Anion vacancy in normal O site	V_O
$A_B^{''}$	Cation A on normal B site	$Ba_{Ti}^{''}$
$B_A^{..}$	Cation B on normal A site	$Ti_{Ba}^{..}$
$V_O^{..}$	Doubly ionized oxygen vacancy on O site	
n	Electron	n
p	Electron hole	p
$\cdot$	indicates single + charge with respect to neutral site	
$'$	indicates single - charge with respect to neutral site	

Table 2.2

P_{O_2} DEPENDENCE OF COMPLETELY IONIZED DEFECT CONCENTRATIONS
IN THE TERNARY OXIDE ABO_3

Defect	$[n]=2[V_O^{\cdot\cdot}]$	$[V_O^{\cdot\cdot}]=[V_A^{''}]+2[V_B^{''''}]$	$[n]=[p]$	$[p]=2[V_A^{''}]+4[V_B^{''''}]$
$[n]$	-1/6	-1/4	0	-3/16
$[p]$	1/6	1/4	0	3/16
$[V_O^{\cdot\cdot}]$	-1/6	0	-1/2	-1/8
$[V_A^{''}]=[V_B^{''''}]$	1/4	0	3/4	3/16
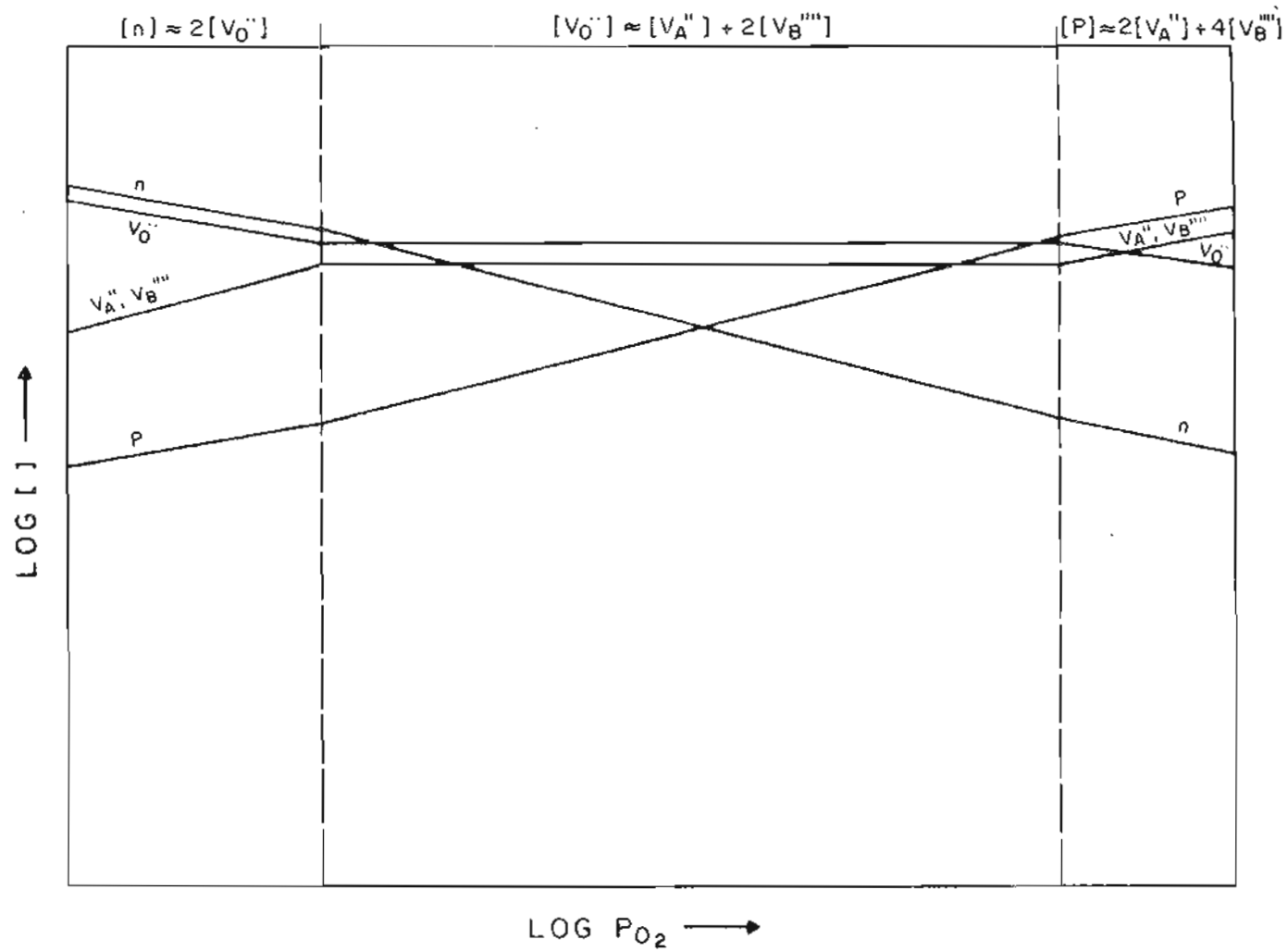
Figure 2.1   CALCULATED DEFECT CONCENTRATION VS. OXYGEN PRESSURE IN ABO$_3$ INTERMEDIATE NEUTRALITY CONDITION IS $[V_O^{\cdot\cdot}] = [V_A''] + 2[V_B'''']$
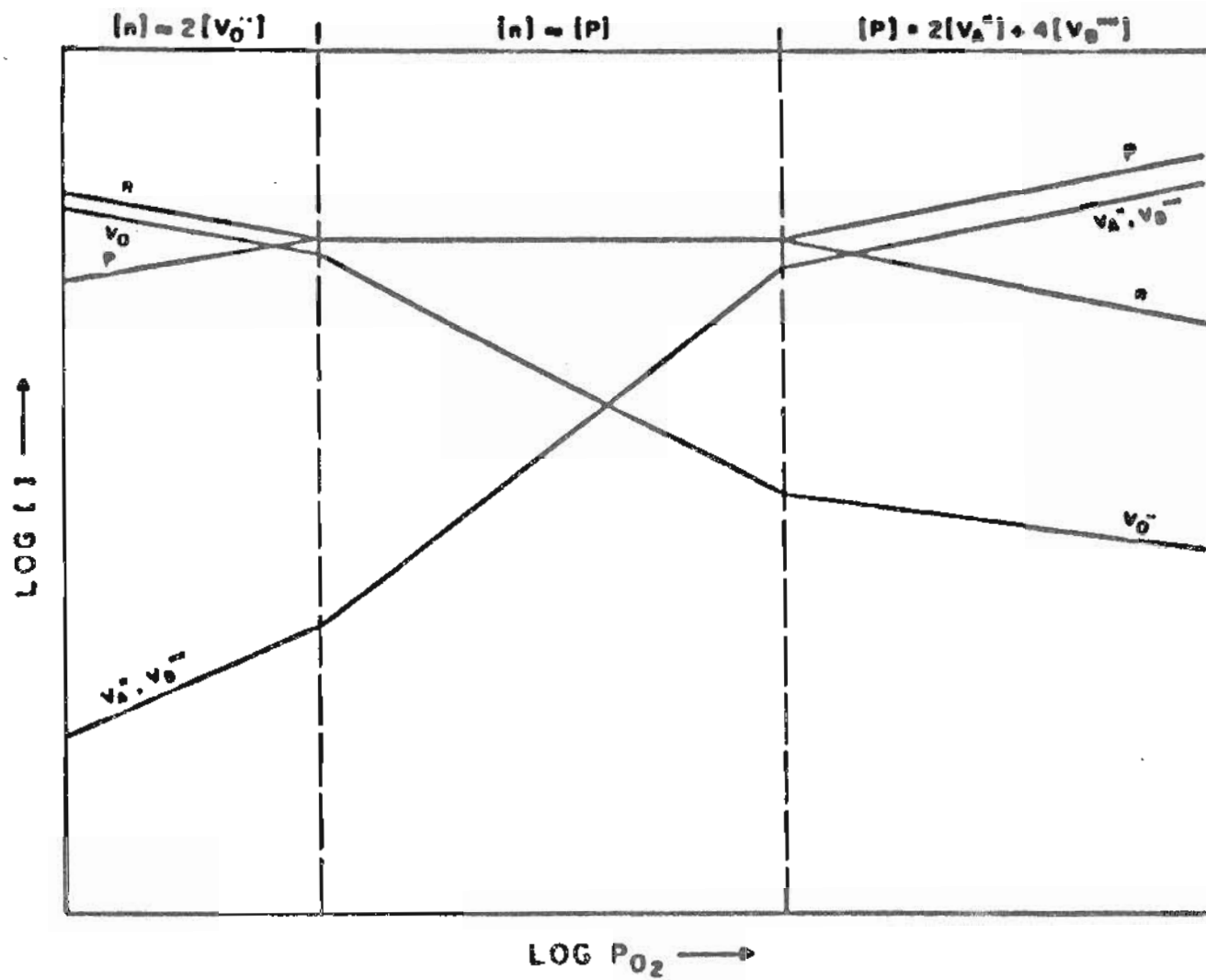
Figure 2.2   CALCULATED DEFECT CONCENTRATIONS VS. OXYGEN PRESSURE IN ABO_3
INTERMEDIATE NEUTRALITY CONDITION IS $[n] = [p]$

nounced effect on the electrical conductivity.

Foreign atoms may be incorporated on any site in the crystal. Normally the size of the foreign atom determines the site which it will occupy in a crystal lattice and to a lesser extent it also depends upon the valency of the foreign atom.

We are concerned with the incorporation of foreign atoms on cation sites. Depending upon the valency of the foreign atom and the atom it replaces, it may yield or trap single or multiple electrons. The extent to which it does so, depends upon the band gap of the host crystal, ionization energy of the impurity in the band gap, and temperature.

Obviously the amount of impurity will have a pronounced effect. This effect depends upon the impurity concentration. Specific relationships between the various defects will be obtained, depending upon the impurity concentration. Tables 2.3 and 2.4 give the calculated P_{O2} dependence of defect concentration for the case of donor-doped and acceptor-doped behavior, respectively. While deriving these relationships it is assumed that, at the lowest P_{O2} all the impurity is completely ionized and the dominant defects are intrinsic electrons and $V_O^{..}$. Also the impurity is singly ionized.

Figure 2.3 and Figure 2.4 give the plot of log defect concentration vs log P_{O2} for the donor-doped and the acceptor-doped cases, respectively.

An interesting case will be one where the foreign atom changes its valency state at a particular temperature and P_{O2}.

2.1.2 Defect structure via equilibrium electrical conductivity

There have been several studies of the defect structure of undoped $BaTiO_3$

Table 2.3

P_{O_2} DEPENDENCE OF DEFECT CONCENTRATIONS IN THE

DONOR-DOPED ABO_3

Defect	$[n]=2[V_O^{..}]$	$[n]=[I_m^.]$	$[I_m^.]=2[V_A''+4[V_B'''']$	$[p]=2[V_A'']+4[V_B'''']$
$[n]$	-1/6	0	-1/4	-3/16
$[p]$	1/6	0	1/4	3/16
$[V_O^{..}]$	-1/6	-1/2	0	-1/8
$[I_m^.]$	0	0	0	0
$[V_A'']=[V_B'''']$	1/4	3/4	0	3/16

Table 2.4

P_{O_2} DEPENDENCE OF DEFECT CONCENTRATIONS IN THE

ACCEPTOR-DOPED ABO_3

Defect	$[n]=2[V_O^{\cdot\cdot}]$	$[I_m']=2[V_O^{\cdot\cdot}]$	$[I_m']=[p]$	$[p]=2[V_A'']+4[V_B'''']$
$[n]$	-1/6	-1/4	0	-3/16
$[p]$	1/6	1/4	0	3/16
$[V_O^{\cdot\cdot}]$	-1/6	0	-1/2	0
$[I_m']$	0	0	0	0
$[V_A'']=[V_B'''']$	1/4	0	3/4	3/16
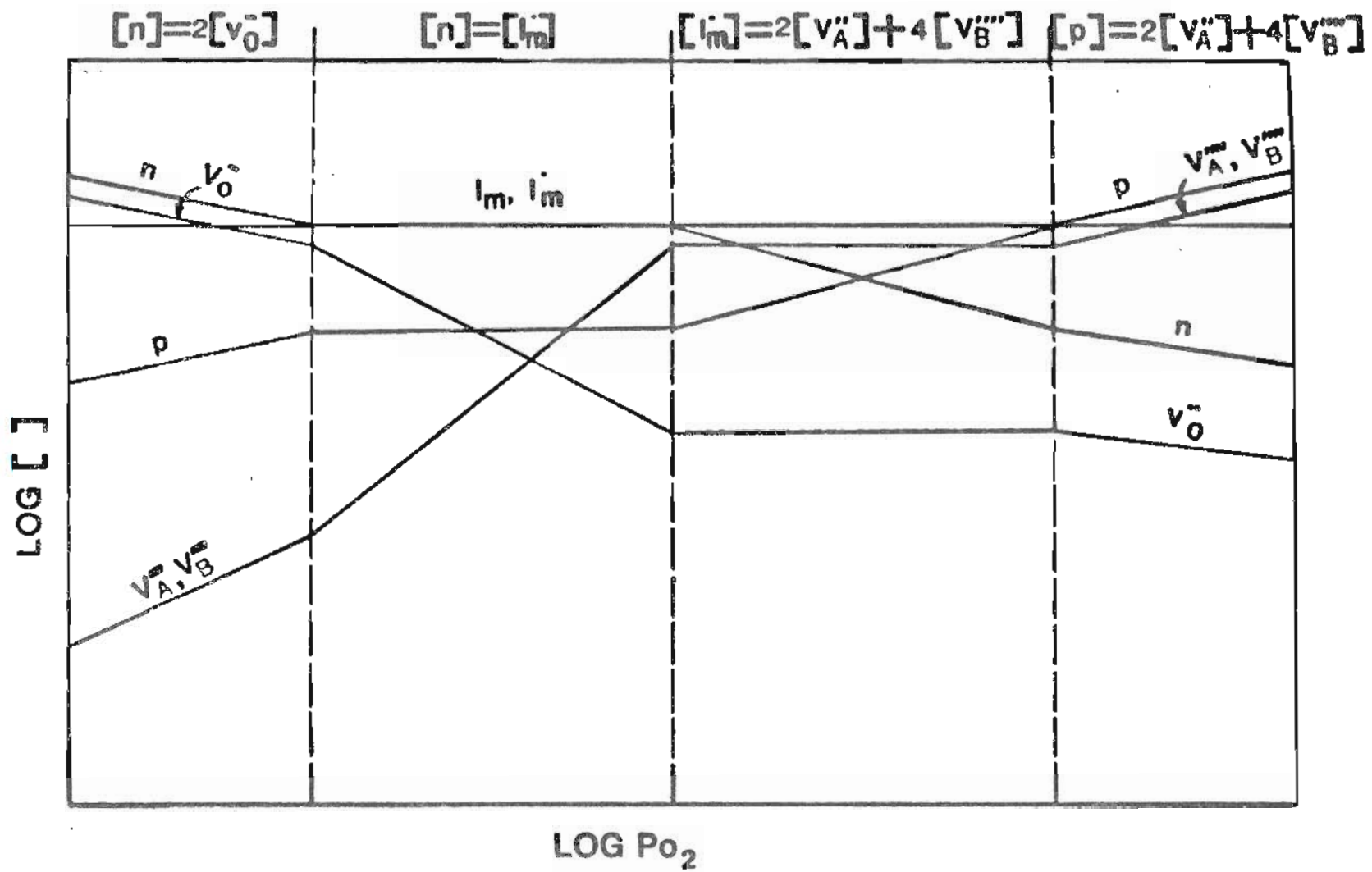
Figure 2.3 CALCULATED DEFECT CONCENTRATIONS VS. OXYGEN PRESSURE FOR DONOR-DOPED ABO_3

$[n]=2[V_O^{\cdot\cdot}]$ $[l_m']=2[V_O^{\cdot\cdot}]$ $[l_m']=[p]$ $[p]=2[V_A'']+4[V_B''''']$
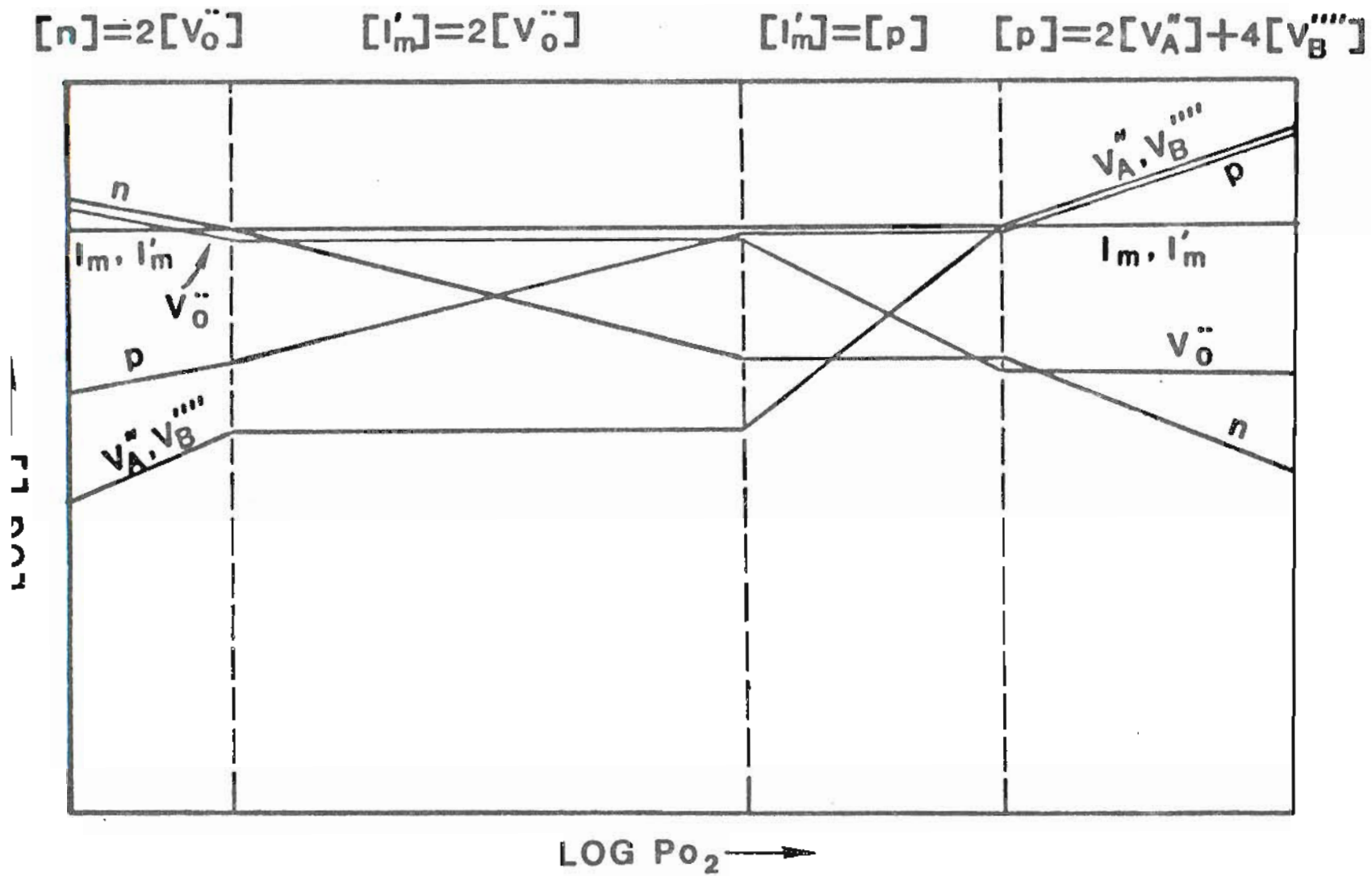
Figure 2.4 CALCULATED DEFECT CONCENTRATION VS. OXYGEN PRESSURE FOR ACCEPTOR-DOPED ABO_3

via equilibrium electrical conductivity measurements, of polycrystalline as well as single crystal samples (13 - 19).

Long and Blumenthal (15,16) observed the effect of stoichiometry on equilibrium electrical conductivity for temperatures between 800 and 1200^0 C. These samples were polycrystalline. All samples were Ti rich, with the Ba/Ti ratio varying between 0.940 and 0.970. In the low oxygen pressures they found samples to be n-type and the slope of $\log \sigma$ vs $\log P_{O2}$ varied between -1/4.1 and -1/5.1. An intrinsic band gap energy of 3.1 eV was reported. They also reported that the conductivity of samples with different Ba/Ti ratio was different, but it was not a function of that ratio. Based on the above facts they proposed a complex defect structure, involving singly and doubly ionized oxygen vacancies and various acceptor levels arising from V_{Ba}. This proposition is based on the fact that, at all time in any region one must consider both electrons and holes and their respective mobilities. If the mobilities of electrons and holes are considered in this material, then there is no necessity of considering both types of conductivity, in the extreme n-type or p-type conductivity region.

Kosek and Arend (14) investigated single crystal as well as polycrystalline samples. Their work was in the p-type region and they reported that the slope of $\log \sigma$ vs $\log P_{O2}$ varied between 1/4 and 1/5.

Eror and Smyth (19) investigated the electrical conductivity of single crystal $BaTiO_3$ between 800 and 1200^0 C and oxygen pressures from 10^0 to 10^{-19} atm. Their crystals were also on the Ti rich side. They reported a band gap of 75.3 ± 0.4 kcal/mole (3.25 eV) and at the low oxygen partial pressures, log conductivity varying as $P_{O2}^{-1/6}$. Based on these results, they proposed a defect model consisting of the formation of a neutral vacancy complex of $(V_{Ba}'', V_{\ddot{O}})$ and

in the low P_{O2} region, doubly ionized oxygen vacancies. At high P_{O2}, i.e. p-type region, the defect structure is dominated by filling of the oxygen vacancies created by the excess titanium.

Chan, Sharma and Smyth (20) reported the results of the electrical conductivity of polycrystalline samples with $Ba/Ti = 0.995$ and temperatures 750 to 1000^0 C and oxygen pressure between 10^{-20} and 10^{-1} atm.. These samples were prepared by the liquid mix technique. The impurity was predominantly acceptor in nature. Their results were the same as Eror and Smyth (19). They proposed that at the lowest P_{O2} and highest temperatures the predominant defects are doubly ionized oxygen vacancies. The intermediate region is controlled by the acceptor impurities, which are inherently present.

Seuter (17) studied the electrical conductivity of polycrystalline, as well as single crystal samples. He reported a shift in the conductivity minima to high P_{O2} as the Ba/Ti ratio was increased from unity. However he did not find a similar shift when the ratio was decreased from unity.

Various studies have been reported pertaining to the effects of donor and acceptor dopants (21-28). Donor dopants have been extensively studied due to the positive temperature coefficient of resistivity effect found in these compositions near the curie temperature.

Chan et. al. (21) investigated the effect of Al doping. The results are consistent with their previous results (20). The defect model also remains the same as proposed by them for the undoped barium titanate with the titanium rich composition.

Daniels and Hardtl (22) observed the conductivity of undoped and La-doped samples between 700 and 1200^0 C and P_{O2} between 10^0-10^{-18} atm. They

reported the slope of log σ vs log P_{O_2} to be -1/4 between 700 and 900^0 and falls to -1/5 at 1200^0 C for the undoped material. For La doping of 0.1 % the sample becomes n-type at room temperature and they found various slopes in three regions, depending upon the amount of La addition. Based on their observations they proposed a defect structure consisting of singly ionized barium vacancies (V'_{Ba}) for the high P_{O_2} region, where the material is p-type. For the n-type region, in the intermediate oxygen activity range, doubly ionized oxygen vacancies predominate, and for the lowest P_{O_2} singly ionized oxygen vacancies predominate. For the doped material the dominant defects proposed are $[V''_{Ba}]$, $[L_a^{\cdot}]$ and $[V_o^{\cdot}]$ with an individual defect predominant in a certain oxygen activity range. They reported the band gap to be 2.9 eV. Daniels (23) reported the effect of Ga as a acceptor dopant and confirmed the model proposed by Daniels and Hardtl (22).

The latest study on this system was reported by Piotrowski et. al. (29). They investigated single crystal $BaTiO_3$ over the temperature range of 800 - 1025^0 C. They reported the slope of log σ vs log p_{O2} varying as -1/4 in the n-type, and 1/5.3 in the p-type region. Based on these observations, they proposed a defect model consisting of singly ionized oxygen vacancies to be the predominant defect in the n-type region, and $[V''_{Ba}]$ and $[V''''_{Ti}]$ in the p-type region. They also proposed that, doubly ionized oxygen vacancies are favored when a Ti excess is present to account for the differences in their slope of log σ vs log P_{O_2} and the work of Eror and Smyth (19). They also measured the transient conductivity with time, while equilibrium with the new partial pressure of oxygen was being achieved.

2.1.3 Defect Structure via Thermogravimetric Method

Eror and Smyth (30) reported gravimetric measurements on undoped and donor doped $BaTiO_3$ and TiO_2. They observed the reversible weight change of oxygen content, between specified states of oxidation and reduction, proportional to the dopant concentration. They also reported that the each added oxygen atom compensates for $2La^{+3}$ or $2Nb^{+5}$ and each oxygen ion compensates for one Tb^{+4} and for Mn^{+6}. Based on these observations they proposed at high donor concentrations, BaO is structurally accommodated in an ordered fashion, similar to the accommodation of SrO in $Sr_3Ti_2O_7$ and $Sr_4Ti_3O_{10}$ (n $SrTiO_3 \cdot$ SrO).

Hennings (31) investigated undoped $BaTiO_3$ and La doped $BaTiO_3$. He reported a slope of -1/4 for the log [V_O total] versus log P_{O2} plots for the temperature range of 1100 to 1250^0 C, for undoped materials. From the value of the slopes he concluded that the predominant defects are singly ionized oxygen vacancies. The activation energy of singly ionized oxygen vacancies was found to be 4.7 eV. He also reported the reduced La-doped $BaTiO_3$, in contrast to the undoped $BaTiO_3$, contains only negligible oxygen vacancies. From these measurements he confirmed the defect structure previously reported by Daniels and Hardtl (22,23).

Hagemann and Hennings (33) observed the oxygen vacancy concentration, of acceptor (Cr, Mn, Fe, Co, Ni) doped $BaTiO_3$, thermogravimetrically. The range of the dopant level observed was 0.1 to 1.0 mole% and the range of oxygen partial pressure was 1.5 atm. to 1.5×10^{-11} atm.. They found the increase in the vacancy concentration was approximately one-half of the dopant concentration for Cr and Co doped samples. In the case of the Mn doped samples, it was nearly equal to the acceptor concentration and was much less than the acceptor

concentration for the Fe and Ni doped samples. From this they concluded that the defect structure in the intermediate range is controlled by the added acceptor impurities and their charge, and in the very low oxygen partial pressure, doubly ionized oxygen vacancies are the dominant defects. This model differs from the model suggested by Hennings (31). Since in both cases experimental results have been provided to support the model, the only conclusion which can be drawn is that the materials used by Hennings (31) contained significant concentrations of acceptor impurities.

Novak and Arend (32) were the first to report the maximum oxygen non-stoichiometry in pure $BaTiO_3$ to be only 0.07 at % at 1000^0 C, by using a chemical technique. This chemical technique involved the decomposition of $BaTiO_3$ in hydrochloric acid in the presence of a surplus of Fe^{+3} ions with a subsequent colorimetric determination of the reduced Fe^{+2} ions.

Arend and Kilborg (34) measured the weight loss in polycrystalline $BaTiO_3$ reduced in hydrogen at different temperatures. The loss at different temperatures can be expressed as $BaTiO_{3-x}$, where x = 0.0036 at 1275^0 C, x = 0.0124 at 1375^0 C and x = 0.0233 at 1500^0 C. The loss was reversible by annealing in oxygen at 850^0 C for 5 hrs. They also reported a change in phase due to the reduction at temperatures above 1350^0 C. The phase changes from cubic to hexagonal.

2.1.4 Defect Structure of Other Materials with Perovskite Structure e.g. $SrTiO_3$, $CaTiO_3$, $PbTiO_3$ etc.

George and Grace (35,36) measured the equilibrium electrical conductivity as a function of temperature (1100 - 1300^0 C) and partial pressure of oxygen, and under the same conditions measured the Seeback coefficient, of a $CaTiO_3$ single crystal. They reported that at low P_{O2}, doubly ionized oxygen vacancies

are the predominant defects. The enthalpy of formation of oxygen vacances was found to be 93 ± 4 Kcal/mole. They also observed the transient electrical conductivity between two states of equilibrium P_{O2}, for single crystal $CaTiO_3$. They observed the diffusion coefficient for oxygen to be 5.2×10^{-6} cm^2 sec^{-1} at 1200^0 C. The enthalpy of motion of oxygen vacancies was found to be 13 Kcal/mole.

Walter and Grace (37,38) performed similar measurements for single crystal $SrTiO_3$ and reported doubly ionized oxygen vacancies to be the dominant defect. The enthalpy of formation of oxygen vacancies was found to be 86.5 ± 3 Kcal/mole.

Balachandran and Eror (39,40) investigated the electrical conductivity, of polycrystalline $SrTiO_3$, with various Sr/Ti ratios, between 10^0 and 10^{-22} atm. of Po_2. The temperature range observed was 850 to 1050^0 C. They reported the log σ proportional to the -1/6 power of P_{O2} for $P_{O2} < 10^{-15}$, log σ varied as -1/4 power of P_{O2} for the oxygen partial pressure range of 10^{-15} to 10^{-8} atm., and log σ varied as +1/4 for the Po_2 higher than 10^{-8} atm.. From these data they concluded that, at the lowest P_{O2} doubly ionized oxygen vacancies are the dominant defects. At the intermediate range, the acceptor impurities, which are abundant naturally, and their related oxygen vacancies are the dominant defects. At the highest P_{O2} the oxygen vacancies are filled. They observed no effect of the Sr/Ti ratio on the conductivity. From these facts, they concluded the formation of a neutral vacancy pair $(V_{Sr}^{''}, V_{O}^{..})$.

Chan, Sharma and Smyth (41) also investigated the electrical conductivity of $SrTiO_3$, under the similar conditions of Balachandran and Eror. They also observed similar results. They also suggested that in the low Po_2 region doubly

ionized oxygen vacancies are the dominant defects, but they do not propose neutral vacancy complex formation.

Balachandran and Eror (42,43) investigated the electrical conductivity of polycrystalline $CaTiO_3$. Experimental conditions were the same as for their study of $SrTiO_3$ (39,40). They observed behavior similar to that of $SrTiO_3$. They proposed the same defect structure; e.g. doubly ionized oxygen vacancies in the very low P_{O2}, acceptor impurities and their related $(V_O^{\cdot\cdot})$ as the dominating defect, for the intermediate range of P_{O2}, and at the highest P_{O2} filling of oxygen vacancies and the formation of a neutral vacancy complex $(V_{Ca}^{''},V_O^{\cdot\cdot})$ for the TiO_2 rich side.

2.2 Electrical Conductivity and Transport Properties of $BaTiO_3$ and Other Perovskites

Measurement of d.c. conductivity, gives the total conductivity, ionic as well as electronic. One has to be cautious while analyzing the data from conductivity measurements with respect to temperature.

The most accepted theory of semiconductor and insulators is due to A. H. Wilson (44), who proposed a band theory. According to Mott and Gurney (45), the conductivity for a semiconductor or insulator is given by

$$\sigma = 2e\mu(NV)^{1/2}\left[\frac{2\pi mKT}{h^2}\right]^{3/4} \exp\left[\frac{-E}{2kT}\right] \qquad \text{for } n \ll N \qquad (2.1)$$

where μ = mobility of electrons

$\qquad$ N $\quad$ = Concentration of Impurity centers

$\qquad$ V $\quad$ = Volume of crystal

$\qquad$ n $\quad$ = No. of electrons in conduction band

$\qquad$ E $\quad$ = thermal ionization energy

Equation (2.1) can be written as

$$\sigma = \sigma_0 \, e^{\left(\frac{-A}{kT}\right)} \tag{2.2}$$

where $A = 1/2 \, E$ and $\sigma_0 = 2e\mu(NV)^{1/2}\left[\frac{2\pi mkT}{h^2}\right]^{3/4}$ Equation (2.2) applies when

negligible donors are ionized. When $n \gg N$ the conductivity becomes

$$\sigma = \sigma_0 \, e^{\left(\frac{-A}{kT}\right)} \tag{2.3}$$

where $A = E$

All of the above formulae assume the electronic conduction and the mobility of electrons and holes does not change in the temperature range of interest.

When the conductivity is dominated in different temperature ranges by the electrons from donors, and from the intrinsic process we get the expression.

$$\sigma = A\sigma_{01} \, e^{\left(-\frac{A_1}{kT}\right)} + \sigma_{02} \, e^{\left(\frac{-A_2}{kT}\right)} \tag{2.4}$$

In a log σ vs $1/T$ plot we observe a change in the slopes. There are regions of intrinsic and extrinsic dominance, respectively. One can then find the respective activation energies. Here A_1 corresponds to the impurity activation energy and A_2 corresponds to the intrinsic activation energy.

Simmons (46) has derived quantitative expressions for the free carrier density (n,p), the trapped-carrier density (n_t, n_p), the free carrier conductivity σ, and the trapped-carrier conductivity (σ_t), for insulators and semiconductors. From the ln σ vs T^{-1} plots one can obtain the above quantities. In a situation like this, one gets a change in the slope of ln σ vs T^{-1} plots, depending upon the various processes. By measuring the slopes then one can derive the various activation energies and the above quantities.

Branwood and Tredgold (47) measured the electrical conductivity of a $BaTiO_3$ single crystal as a function of temperature, applied field, electrode material and thickness. The crystals, used in the study, were grown by Remeika method. The temperature range was 15 to 480^0 C. The electrode materials used were Ag, Au, Cu, Cr, Al and Zn. The copper electrodes deteriorated rapidly with time, whereas Cr, Al and Zn remained stable and the conductivity also did not change with time. The specific conductivity for Ag and Au electrodes was almost the same as the specific conductivity with other electrodes, but after 5 days at 160^0 C and a 4kV/cm bias it increased. They explained this based on the migration of electrode material from the anode into the bulk of the crystal. Above the curie temperature (120^0 C) to 270^0 C, the slope of ln σ vs 1/T corresponds to an activation energy of 0.84 ± 0.2 eV. Above 270^0 C there is a sharp transition in the conductivity vs. temperature curve and the slope corresponds to an activation energy of $1.22 \pm .22$ eV. From this they concluded that above 270^0 C the conductivity is intrinsic with a band gap of 2.44 eV and below 270^0 C, the conductivity is impurity dominant with the activation energy of 1.7 eV and the donors are likely to be oxygen vacancies.

Matsonashvili (48) investigated the electrical conductivity of single crystal $BaTiO_3$, undoped and doped with Fe and Co, with respect to temperature. The temperature range was 20 to 300^0 C. He used silver and/or In-Ga electrodes. He reported no variation of the conductivity with the electrode materials. The conductivity was measured with a 1-15 KV/cm field. The samples were ohmic up to 5 kV/cm field. The slopes of log σ vs 1/T plot were the same up to the curie temperature (120^0 C), for undoped as well as the doped samples. From the slopes for the undoped samples he found the activation energy to be 0.78 eV. For the Fe and Co doped samples the activation energy was reported to be $\approx$ 1.6 and $\approx$

1.5 eV, respectively. He also reported that as the amount of Co increased the activation energy decreased.

Longo and Ricciardiello (49) observed the electrical conductivity of ABO_3 where (A = Ca, Sr, Ba and B = Ti, Zr, Ce) and their solid solutions between 800 and 1200^0 C. They measured both a.c. (1000 Hz) and d.c. conductivity for $BaTiO_3$ at 1000^0 C in air. They reported the sample to be n-type with the thermal ionization energy of 1.9 eV. and σ ac $= 2.610 \times 10^{-3} \Omega^{-1} cm^{-1}$ and σ dc $= 2.580 \times 10^{-3} \Omega^{-1} cm^{-1}$. Thus no ionic conductivity was found.

Weise and Lesk (50) investigated the electrical conductivity of the oxidized and reduced (reduced to various degrees) perovskites. Special interest here is in polycrystalline $BaTiO_3$, for which in the oxidized state they could measure the electrical conductivity from 400 to 1500^0 C in air. They reported the log ρ vs 1/T as a straight line for the entire range of temperature. From this they reported the band gap to be 2.47 eV and as the reduction increased, the activation energy decreased.

Ikushima and Hayakawa (51) reported that the Hall mobility for reduced $BaTiO_3$ single crystals between the temperature range of -195 to 165^0 C to be independent of temperature, and is ≈ 0.1 to 1 $cm^2V^{-1}s^{-1}$. Whereas Ryan and Subbarao (52) reported the value to be between 0.1 and 0.01 $cm^2V^{-1}s^{-1}$ for lanthanum doped $BaTiO_3$, and between 0.1 and 1.0 $cm^2V^{-1}s^{-1}$ for yttrium doped $BaTiO_3$ samples for the temperature range of 20 to 120^0 C.

Ikegami and Ueda (53) reported the electron mobility to be 0.1 $cm^2V^{-1}sec^{-1}$ for a $BaTiO_3$ single crystal. Berglund and Bear (54) investigated the Hall effect and the Seeback coefficient on reduced single domain crystals. They reported the electron mobility to be 0.5 $cm^2V^{-1}sec^{-1}$ from 126^0 C, which was the curie point of

their crystal, to 160^0 C. Below 126^0 C the mobility increased and became 1.2 $cm^2V^{-1}sec^{-1}$ at 26^0 C. From the Seeback coefficient they reported, the density of states effective mass for cubic $BaTiO_3$ to be (6.5 ± 2) m_O. Cox and Tredgold (55) reported the hole mobility in $BaTiO_3$ to be $\approx 10^{-4} cm^2 s^{-1} V^{-1}$, whereas Seuter (17) reported it to be 0.02 cm^2/ Vs.

Horie (55) et. al. reported the intrinsic energy gap as measured by optical absorption to be approximately equal to 3 eV. Whereas DiDomenico and Wemple (56) reported the band gap to be ≈ 3.3 eV, from the optical absorption data on a single crystal. For polycrystalline samples Seuter (17) and Eror and Smyth (19) reported the band gap to be 3.15 and 3.27 eV respectively from the high temperature equilibrium electrical conductivity measurements.

Berglund and Braun (58) investigated, the optical absorption coefficients, of polarized light on a reduced single domain $BaTiO_3$ crystal between 26 and 130^0 C. From these measurements, they reported that the impurity states to be approximately 0.2 to 0.3 eV. below the conductivity band minimum, superimposed on a free carrier and lattice absorption background. The deep impurity states are probably associated with the oxygen vacancies.

So far only two attempts have been made to identify the type of conductivity in $BaTiO_3$ between room temperature and 500^0 C. The most frequently, but many times erroneously quoted investigation is by Glower and Heckman (59). They investigated the conduction in a single crystal as well as polycrystalline $BaTiO_3$ between 100 - 600^0 C by means of a concentration cell. The single crystals were flux grown and the polycrystalline samples were made from the solid state reaction of $BaCO_3$ and TiO_2 powders. They concluded that the pure single crystals were electronic conductors between 100 - 600^0 C. The single crystals

containing 0.1 % iron were electronic conductors at 600^0 C, but had significant ionic conduction at 100^0 C ($\approx$ 54 %). Polycrystalline samples were electronic conductors at 500^0 C but were 100 % ionic conductors at 250^0 C. They also concluded that the mobile species in a single crystal were iron ions and not the titanium ions.

Recently Maier (60) et. al. investigated, the conductance by a concentration cell. The conductivity of single crystal and polycrystalline, $SrTiO_3$ and $BaTiO_3$, undoped as well as donor (La) and acceptor (Mn, Fe, Cr) doped samples were measured with respect to temperature. Except for undoped polycrystalline $BaTiO_3$ they did not find ionic conductivity in any other sample including single crystal $BaTiO_3$. They reported that at the 400^0 C the ionic conductivity was $\approx$ 7 to 10 % for polycrystalline $BaTiO_3$.

Gerthsen (64) et. al. measured the optical reflectivity and the electrical conductivity of hydrogen reduced $BaTiO_3$. They proposed that the conductivity is due to small polarons. Subsequently Reik and Heese (65) also explained the conductivity based on polaron hopping, but they could not apply this model to the high conductivities observed in the reduced materials.

Kahn and Leyendecker (61) first proposed an LCAO (Linear Combination of Atomic Orbitals) band model for perovskites and made the calculations for $SrTiO_3$. Calendini and Mesnard (62) made the band calculations based on LCAO for $BaTiO_3$. They came up with a similar energy band to that of $SrTiO_3$, in which the filled valency bands formed from oxygen 2p orbitals and the empty conduction bands derived from the titanium 3d orbitals. In cubic $BaTiO_3$, they indicated that the six lowest conduction band ellipsoids lie along the [100] direction of k space with the conduction band minima near the Brillouin zone boun-

dary. The longitudinal effective mass was found to be 260 m_O, unlike $SrTiO_3$ for which it was 20 - 50 m_O, and the transverse effective mass was about 0.4 m_O.

Calendini and Mesnard (63) also determined the electronic band structure of $BaTiO_3$ in the tetragonal phase according to the Slater and Koster interpolation scheme with nonorthogonal orbitals. They observed that the bands remain essentially the same as for cubic barium titanate except minor changes and the maximum of the conduction band is displaced from R : (1, 1, 1) π/a to Δ (1, 0, 0) Π/a and the transverse effective mass is reduced to 50 m_0.

2.3 Electron Spin Resonance

An electron with unpaired spin has a net magnetic moment which will align itself either with or against an applied magnetic field, resulting in two energy levels. These two energy levels are degenerate prior to the application of an external magnetic field. The two energy levels represent the spin quantum numbers, $m_s = -1/2$ and $m_s = 1/2$, the former being a low energy state aligned with the field. The energy separation of the two states is given by

$$E = gBH_o \qquad (2.5)$$

where

B = Bohr magneton

H_o = Field Strength

g = Spectroscopic splitting factor

The value of 'g' is not constant. For free electrons, g has a value of 2.0023 while for other chemical environments, the value of g varies.

Once the spin state degeneracy has been removed by the magnetic field,

energy in the microwave region is applied to the sample. Normally the magnetic field is then varied, until the energy separation between spin states is equal to the energy in the microwaves. At this point the electron will absorb energy and jump to the energy state of $m_s = 1/2$. A spectrometer will then show an absorption of energy, $E = h\nu = gBH_o$. The peaks are reported in terms of 'g' value.

Ikushima and Hayakawa (66) reported the ESR measurement on oxidized and reduced single crystal barium titanate. They observed three peaks, at g = 1.946, 1.922 and 1.932, and assigned these peaks to the presence of Mn^{+2} as an impurity in the sample. The same investigators (66 - 69) reported the study of ESR spectra of Mn doped barium titanate. The conclusions from which are: 1) Mn^{+3} resonance can be observed at temperatures below 10 K. 2) Mn^{+2} has a g = 2.0024 and A = 85 G (where A is a hyperfine splitting constant arising from a nucleus with $I > 0$) and usually exhibits some forbidden bands corresponding to $\Delta m = \pm 1$, at 77 K. and 3) Mn^{+4} has a g = 1.994 and A = 75G.

Recently Desu and Subbarao (70) investigated the ESR spectra of Mn doped barium titanate. They observed a peak at room temperature and 77 K. at g = 1.954 for 0.2 % Mn doping. The peak at g = 1.954 was assigned to Mn^{+4}. At 77 K they also observed an additional peak and multiplates, which were assigned to the presence of Mn^{+2}. These observations were made on polycrystalline samples.

There are various investigations (71-75), concerning the ESR spectra of Fe and Ni doped strontium titanate but not much work is reported on Ni doped barium titanate. Faughnan (71) reported the ESR spectra of Ni, Co and Fe doped strontium titanate single crystals. He observed a peak at 77 K in the reduced Ni doped sample and assigned it to the presence of Ni^{+2} at a cubic site, and in the oxidized (900^0 C, air) sample they observed an additional peak which was assigned to the Ni^{+3} in an axial site, [100] symmetry.

Koidl et. al. (72) reported ESR and optical absorption measurements on Ni doped strontium titanate. The ESR spectra was recorded at 77 K and at K band wavelength. The peaks due to the presence of Ni^{+2} and Ni^{+3} were observed.

Serway et. al. (73) investigated the ESR spectra of Mn doped strontium titanate single crystals. They observed three peaks at 300 K, in the reduced crystals. The first center was assigned to the Mn^{+2} ion having cubic symmetry. The g value for this center is $g = 2.0036 \pm 0.0005$. and $A = (82.6 \pm 0.1) \times 10^{-4} cm^{-1}$. The second center was characterized by an axially symmetric ESR spectrum with effective g values of $g^e = 2.00$ and $g^e = 5.9$. This center was assigned to $Mn^{+2}-V_O$. The third center has g values of $g^e = 7.945 \pm 0.001$ and $g^e < 0.4$ and was assigned to $Mn^{+3}-V_O$.

Kirkpatrick et. al. (74) reported the ESR spectra of Fe doped strontium titanate. The effective g values reported were $g^e = 5.993 \pm 0.001$, and $g^e = 5.961 \pm 0.001$ and $g^e = g^e = 2.0054 \pm 0.0007$. which were assigned to the presence of Fe^{+3}.

Nakabara and Murakami (75) reported the ESR spectra of Mn and Gd doped $Ba_{.97}Sr_{.03}TiO_3$ single crystals. They reported that Mn substituted for Ti and exist as Mn^{+2} in a reduced crystals and as Mn^{+3} in the fully oxidized crystals. The room temperature g value was reported to be 2.002 for Mn^{+2}.

Hagemann and Ihrig (76) investigated the valency of Fe, Mn, Cr, Co, Ni, and Zn dopants in barium titanate, in the oxidized and reduced, state and the effects of oxygen vacancies on it. The charge of the dopants was measured by the magnetic susceptibility method. They reported, no solubility limit was reached for any dopant except Fe for up to 2.0 mole % doping, and sintering in

air at 1400^0 C. For Fe, solubility was reached at 1.25 mole %. Fe. Ni and Zn do not change their valency states under the oxidized as well as the reduced (10^{-22} bar, 700^0 C.) conditions, their valency being +3, +2 and +2 respectively. Whereas Mn, Co and Cr changed their valency states. In the oxidized condition these dopants have a valency of +4, +3 and +4 respectively, and in the reduced condition, +2, +2 and +3 respectively. Change in the weight loss was observed corresponding to the change in valency of the dopants, indicating the creation of doubly ionized oxygen vacancies.

Faughnan and Kiss (77) investigated the ESR spectra of strontium titanate doped with either Mo/Fe or Mo/Ni. They reported that the transition ion substitutes for Ti^{+4} with a peak at 77^0 K at 9.1 GHz. due to Ni^{+2}. After irradiating the sample with ultraviolet rays a peak was observed due to Ni^{+3}.

2.4 Degradation Studies

As mentioned previously, Gruver et. al. (2) have summarized the work carried out on degradation of barium titanate and titanium dioxide at Linden labs during 1955-65.

According to them, as far as degradation is concerned, there is no difference between a compound in its ferroelectric and paraelectric state. Degradation of titanium dioxide (rutile) has great similarities to the degradation of barium titanate. They proposed the following mechanism for the degradation process.

A titanate is appreciably reduced at the firing temperatures, which is normally above 1200^0 C, the reoxidation upon cooling in air is rather fast above 1100^0 C but practically stops at some temperature between 600 and 900^0 C. As a consequence, the outside of a sample and to some extent each grain is oxidized,

but the interior still has an oxygen deficiency. This missing oxygen ion carries an effective charge of +2, which is neutralized by two electrons in the localized 3d levels of the Ti^{+4} ions, forming Ti^{+3} ions. At low temperatures, these Ti^{+3} ions are bound by a small energy of 0.1 - 0.2 eV to an individual anion vacancy, only a small part is separated from the anion vacancies. These electrons from the 3d band are responsible for the conduction. Under an applied field, anion vacancies move toward the cathode and oxygen will move toward the anode thus leading to the degradation of the material. They proposed stabilization by various methods. Substitution of the dopants on the Ti^{+4} site with elements having a valency more than +4, e.g. U^{+6}, Nb^{+5}, or by substitution on the Ba^{+2} site, with the elements having a valency more than +2, e.g. La^{+3}, or by substitution of the O^{-2} by F^{-1} etc.. The other method involved the presence of a small amount of second phase at the grain boundaries.

During these investigations it was also observed that protons play an important role in the degradation process. Hot pressed barium titanate made from very pure raw materials and pressed to near theoretical density was very stable, almost as stable as those materials which were stabilized by the dopants.

Electrical conductivity in an insulator or a dielectric can be separated into three regions. 1) Carrier injection at the electrode, 2) Motion in the bulk material and 3) Extraction of carriers at the other electrode. The controlling region determines the specific behavior of an insulator, depending on which, various mechanisms can exist. These mechanisms are: 1) Ohmic behavior 2) Schottky emission 3) Space-charge limited current 4) Tunnel emission.

In ohmic behavior, which most of the materials follow, a plot of log current versus log field has always a slope of unity. This law can be expressed as,

$$J = en\mu E \tag{2.6}$$

where

$J = $ Current density

$e = $ electron charge

$n = $ number of carriers

$\mu = $ mobility of carriers

$E = $ applied field

When there is a deviation from the ohm's law other types of behavior comes in to play. Schottky emission is expressed as follow

$$J = A\,T^2 exp\ \frac{|-(B - b\,E^{1/2})|}{kT} \tag{2.7}$$

where

$A = $ Richardson constant

$B = $ work function

$b = (\frac{e}{4\pi\epsilon})^{1/2}$

$T = $ absolute temperature

$k = $ Boltzmann constant

$\epsilon = $ permitivity

Thus we find here that log J should be proportional to $E^{1/2}$ at a constant temperature and log $\frac{J}{T^2}$ should be proportional to $\frac{1}{T}$ at a constant voltage, if Schottky emission is the charge transfer mechanism.

Tunnel emission from a metal to an insulator is essentially the same as field emission from a metal surface in to a vacuum as discussed by Azzaroff and Brophy (78). Current density in tunnel emission is described by Chynoweth (79) as

$$J = \frac{(e^2E^2\alpha)}{8\pi h\,\Delta\epsilon}\ exp\ -\left[\frac{8\pi\sqrt{2m^*}}{3he}\cdot\frac{\Delta\epsilon^{3/2}}{E}\beta\right] \tag{2.8}$$

where

$$m^* = \text{effective mass of electron}$$

$$\alpha, \beta = \text{correction factor}$$

$$\Delta\epsilon = \text{difference in vacuum work function of metal}$$

$$\text{and insulator}$$

The electric field must be greater than 10^7 volts/cm before the current density from this process becomes significant.

Space-charge limited current can exist in solids, similar to a space-charge limited current in a vacuum diode. Rose (80) described this and also stipulated the necessary condition for this is that the contacts to insulators should be ohmic. According to him, in this case the ohmic contacts mean that the electrode, which is capable of supplying free carriers to an insulator whenever needed. Also the insulator should be defect free, i.e. no trapping center for the free carriers. For this case he gave the following equation.

$$J \approx 10^{-13} \left[\frac{V^2 \mu \epsilon}{d^3} \right] \tag{2.9}$$

where

$$\mu = \text{drift mobility of carrier}$$

$$d = \text{distance bet. two electrodes}$$

$$\epsilon = \text{dielectric constant}$$

For an insulator with shallow traps of single level energy the equation becomes

$$J \approx 10^{-13} \left[\frac{V^2 (\mu \theta) \epsilon}{d^3} \right] \tag{2.10}$$

where

$$\theta = \left(\frac{N_c}{N_t} \right) \exp \frac{-E}{kT}$$

N_c = density of states in conduction band

N_t = trap density

E = ionization energy of traps

Branwood et. al. (81) investigated the current voltage characteristics of barium titanate at various fields up to 4 kV/cm. They found that initially up to a certain field strength that the system behaves ohmicly and at higher fields the behavior is not ohmic. They attributed this to a space-charge limited conduction and derived the formula

$$J = a \times \frac{v}{d} + b \left(\frac{v}{d} \right)^2 \qquad (2.11)$$

where

a = constant depending upon material

b = constant depending upon electrode

d = thickness

Mallick and Emtage (82) investigated the current voltage characteristics of polycrystalline barium titanate for fields up to 10^4 volts/cm. They used In - Ga amalgam for the electrodes and also observed ohmic behavior up to a certain applied voltage. They proposed the conduction mechanism to be the same as Heywang's model wherein small barriers at the grain boundaries act as traps, which control the current.

Benguigui (83) also reported on the current voltage characteristics of polycrystalline barium titanate. He observed that up to 110^0 C, after the ohmic region, $I \propto V^m$ where $m \approx 3$. From 110 to 350^0 C, after the ohmic region, initially $I \propto V^2$, followed by $I \propto V^m$, where $3 > m > 2$. Observation of negative resistance in this range was also reported.

An important paper by Lehovec and Shirn (4) will be discussed in some detail. They used polycrystalline barium titanate containing a substantial amount of calcium zirconate with a curie point at approximately 35^0 C, and a dielectric constant of 500 at 250^0 C. The samples were provided with aquadag electrodes. Applied fields were 2, 4 and 6 kv/cm. The current was measured with time and potential distribution at various points.

The principal result was the see - saw effect in most of their current versus time curves as shown in Figure 2.5 and 2.6. In this case the current first rises with time and then falls sharply and again goes up, whereas for a single crystal it was essentially steady. The potential distribution was observed as shown in Figure 2.7. Initially a straight line corresponding to a space independent behavior was observed, which became concave upward for up to 324 minutes, and finally concave downward with a inflection point in between. The inflection point shifts from the anode to the cathode with time. Conductivity was measured at 1000 volts from room temperature to 400^0 C. In the log σ versus log $1/T$ plots, from 127 to 400^0 C, straight line behavior with an activation energy of ≈ 1 eV was found. Colouration of the samples was also observed. The area adjacent to the cathode became blue and the area adjacent to the anode became dark brown. More complex colouration was observed, when point contacts were used. In that case a white halo surrounded the blue area adjacent to the cathode and a clear zone forms around the anode within the brown area. These colour regions move toward each other, with time and eventually the blue region penetrates the dark brown area and the sample fails. These colourations are not surface effects since they were observed throughout the sample. From these observations they concluded that the high conductivity zone originates from the cathode. The origin of the high conductivity area was not given but it was speculated that it might
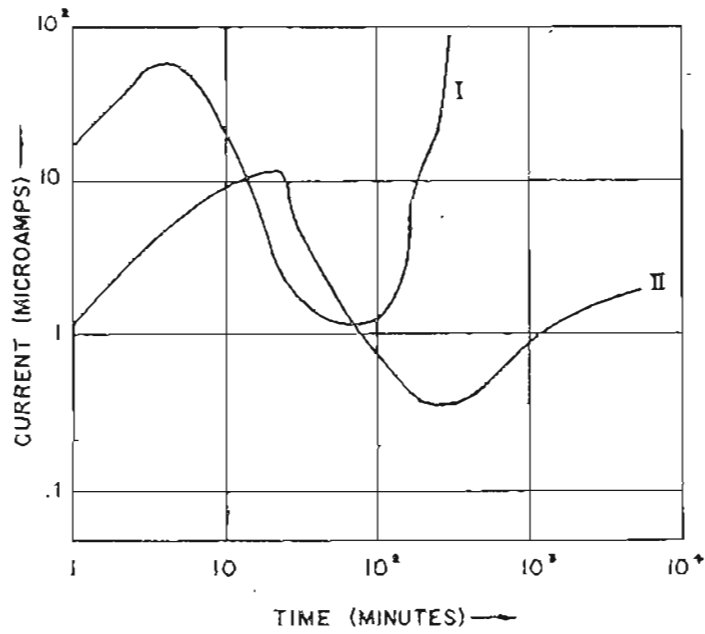
Figure 2.5   CURRENT IN BARIUM TITANATE AT 300⁰ C
FROM LEHOVEC & SHIRN (4)
I, 6000 V/cm II, 4000 V/cm
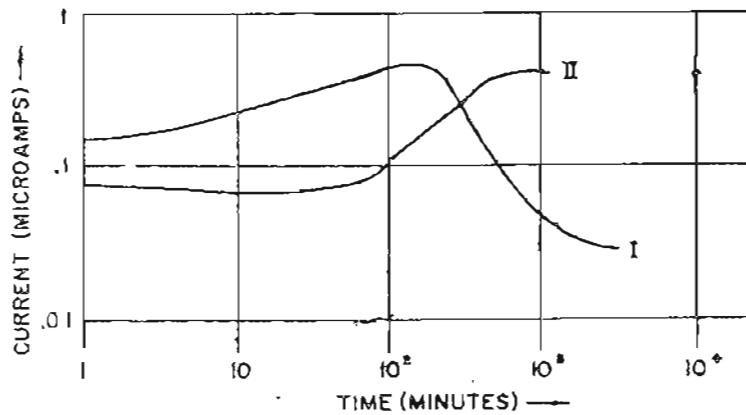
Figure 2.6   CURRENT IN BARIUM TITANATE AT 250⁰ C
FROM LEHOVEC & SHIRN (4)
I, 4000 V/cm II, 2000 V/cm
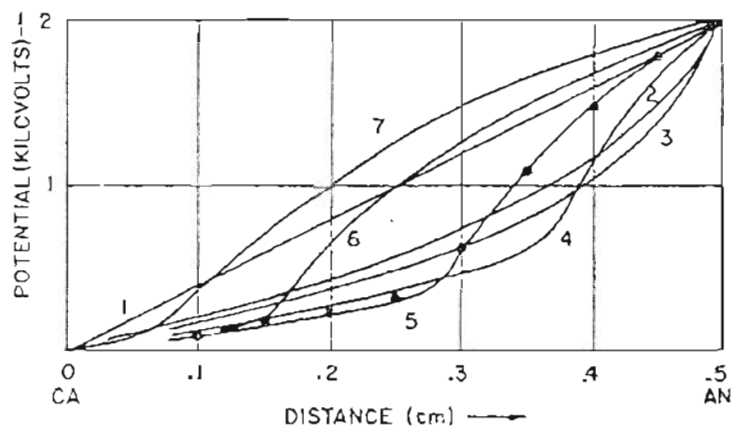
Figure 2.7 POTENTIAL DISTRIBUTION IN BARIUM TITANATE AT VARIOUS TIMES AND AT 250^0 C FROM LEHOVEC & SHIRN (4)
(1) 0, (2) 230, (3) 324, (4) 754, (5) 1470, (6) 2200 and (7) 3790 min.

be due to the injection and trapping of an electron by the oxygen vacancies.

Payne (5) investigated the current voltage characteristics with time and the conductivity mechanism by an oxygen concentration cell, for various commercial formulations. The conclusions were that the current decreases with time and then becomes steady for a given voltage. As the applied voltage increased the tendency for decreasing current stopped. The steady or lowest current was taken as an equilibrium current and plotted against the applied field. Two distinct types of behavior were observed. The first was ohmic behavior up to 10^3 volts at 150^0 C, and the second was $I \alpha$ const $\times V^{1/2}$ at a constant temperature. The data for the second type of behavior can be fitted to a straight line when plotted as $\log J$ versus $\sqrt{v/d}$, where $d \approx$ electrode spacing, a characteristic of Schottky emission. From further accelerated life tests at 150^0 C and 30 kV/cm, the materials showing ohmic behavior were reliable and took a long time to fail, whereas the materials showing Schottky emission were unreliable and failed early. He coupled these findings with the results of concentration cell measurements and showed that unreliable materials have ionic conduction ranging from 59 to 60% of the total conductivity between 150 and 250^0 C.

Schulze et. al. (8) investigated degradation under a high a.c. field at 150^0 C. They reported that Schottky emission during a.c. degradation is a sign of an unreliable dielectric. The Schottky emission begins after degradation under high fields. Initially the current necessary for space-charge and Schottky emission did not exist in a sample, but degradation made it possible to produce sufficient current at the high fields. How the degradation produced large current was not explained. A mechanism similar to Bussem (2) was proposed, based on the reduced grains and oxidized grain boundaries. Thus, grains provided the reservoir of oxygen vacancies, whose migration caused the degradation. The

activation energy for the degradation was found to be ≈ 1 eV. No colouration was observed in the degraded samples.

Keck (84) observed the effect of A/B ratio, as well as acceptor and donor dopants on degradation. Poor resistance to degradation was observed when the ratio was less than unity. La and Al were used as the donor and acceptor, respectively. With the addition of donor, resistance to degradation improved for samples whose A/B ratio was less than unity, but when the ratio was higher than unity the resistance to degradation decreased. The effect of acceptors was ambiguous. The activation energy for the conduction was in the range of 0.68 to 1.3 eV. The compositions, which were least resistant to degradation, showed the lower activation energy. No evidence for Schottky emission was observed. A couple of samples did exhibit a space-charge limited current behavior, and generaly showed poor resistance to degradation. No colouration was observed in the degraded samples.

Recently Rodell and Tomandal (85) reported the degradation of Mn doped barium titanate under a high d.c. field. Degradation was observed at 160^0 C and field strength of 3 kV μcm^{-1} for 250 hrs. A steady decrease in the resistance with time was observed for most of the samples. A couple of samples showed a sudden order of magnitude decrease in resistance, after 100 hrs. More scatter in the data was observed for the barium rich samples. The activation energy was found to be $1.13 \pm .1$ eV. The current versus applied field characteristics for the oxidized samples before degradation were ohmic and after degradation the relationship was found to be $I \propto V^s$ where $s \approx 2.4$. For the reduced samples, behavior was ohmic before and after degradation. The activation energy for conduction was 1.03 eV before degradation and 0.88 eV after degradation. The degradation mechanism proposed was based on the reduction of Mn from Mn^{+4} or Mn^{+3} to

Mn^{+2} and the movement of oxygen ions to form the $(Mn^{+2}-V_O^{..})$ complex.

2.5 Raman Spectra of Barium Titanate

It is well known, that barium titanate exists in five different polymorphs, over the temperature range of 70 to 1650 K. Table 5.1 gives the various crystal structure, space group, and the temperature of stability for barium titanate, taken from Jona and Shirane (86).

Due to the ferroelectric properties of a perovskite structure, its lattice dynamics have received considerable attention in the past (87, 88). The use of the Raman effect to study the lattice dynamics was suggested by Loudon (89), and carried out by various investigators. Although ample literature is available about the Raman spectra of barium titanate, controversy still exists whether room temperature Raman spectrum is first order or second order. Lattice dynamics of barium titanate was also investigated by IR and neutron diffraction methods (109, 110).

The symmetry of a molecule in the crystalline state is generaly lower than that of the liquid or gas phase, due to a strong intermolecular forces in the solid. Thus in the liquid or gas phase one has to consider the point group of the molecule of interest to deduce the allowed vibrations, whereas in the solids one has to also consider the effect of intermolecular forces on the point group.

In liquids the Raman effect shows no phonon propagation i.e. effectively the wave vector, $|k| = 0$ and only energy has to be conserved. Whereas for solids energy and momentum both have to be conserved. In liquids, molecules are randomly oriented, unlike solids where all the unit cells are oriented in the same direction in a single crystal.

If two phonons are simultaneously involved in a scattering process, we get second order Raman scattering. For first order scattering normally $|k| = 0$, but for second order $|k|$ can take any value. Due to this, first order bands are normally sharp whereas second order bands are broad. There are two ways of recognizing second order spectra from first order. First, group theoretical analysis will predict the first or second order spectra and will indicate the symmetry of the phonons involved. The second way is the observation of temperature dependence of the spectra. If the spectra are second order then it diminishes quickly with decreasing temperature as the two phonon process fades away quickly with decreasing temperature. The one phonon Stokes intensity decreases with decreasing temperature as $(n + 1)$, while the intensity of the two phonon spectra occurring at the same frequency, varies with the temperature as $(n+1)^2$.

Where $n = \left[\exp \left(\frac{h\omega}{kT-1} \right)^{-1} \right]$ as reported by Porto (90).

When a vacancy is introduced on a normally occupied lattice site, translational symmetry is decreased. Similarly when a foreign atom is substituted on a normal lattice site, the translational symmetry is lowered. Due to this disturbance in the translational symmetry properties, wave vector conservation loses its meaning, and the $|k|$ of a phonon can in essence, assume any value within the Brillouin zone. This means, similar to the two phonon process, scattering results from phonons of all values of $|k|$ and the resulting spectrum is broad. Colour centers or commonly known F centers in alkali halides are created when an anion vacancy is generated and a electron is trapped at it. A pronounced band can be obtained, (91-93) from F centers, by adjusting the frequency of the exiting laser, to coincide with the electronic transition in the band gap.

Experiments on mixed crystals $A_c B_{1-c}$ have generally yielded two types of characteristic spectra (94). In the first type a given spectral line changes as c is changed from 0 to 1. The spectral line shifts in frequency and this shift is linear with increasing c. Also as c increases, the line width increases and at $c = 1/2$ the line width is maximized. In the second type of behavior, as c increases, additional lines are seen, and the original lines shift very little in frequency. As c increases, the intensity of the new lines increases while that of old lines decreases.

Burns and Scott (95,96) observed the Raman spectra for $Pb_{1-x}Ba_x TiO_3$ and $PbTi_1-xZr_x O_3$ powders, where $0 \leq x \leq 1$. They observed the second type of behavior, i.e. as x increases the spectra changes and new lines emerge from the old lines. From consideration of the shifts in frequency for both cases band assignments were made.

Due to the ferroelectric properties of barium titanate its Raman spectra have received considerable attention (97 - 106). Room temperature Raman spectra of barium titanate were first investigated by Bobovich and Bursian (107) and by Ikegami (108), but there was considerable disagreement between these two investigators, regarding the band assignments. Subsequently Perry and Hall (97) observed the spectra of single crystal barium titanate between 5 and 473 K. At 393 K barium titanate transforms to a cubic form and by group theoretical analysis, no Raman mode is active in this phase. They did observe unchanged Raman spectra until 423 K, however.

In the Raman spectra of barium titanate at room temperature a peculiar band is observed at 175 $^-$ 180 cm^{-1}. Rousseau and Porto (99) assigned this band to a fano type interaction from one phonon and two phonon process. The

interaction arises from a broad band, close to the exiting line to 300 cm^{-1}, due to a two acoustical phonon process (2LA, 2TA, LA + TA), and a sharp band at 175 cm^{-1} from a single phonon Raman and IR allowed process.

DiDomencio et.al. (100) investigated the Raman spectra of single domain barium titanate and made band assignments. Although their results were similar to the previous workers in many respects, their interpretation was different.

From various band assignments the following conclusions can be drawn. 1) The sharp band at 307 - 309 cm^{-1} has been assigned to E_1 symmetry by all investigators. 2) Bands at 270 and 520 cm^{-1} are very asymmetric, especially the 520 cm^{-1} band. Both the bands have been assigned A_1 symmetry by most of the investigators. 3) Controversy still persists about the 185 and 720 cm^{-1} band assignments. 4) Existence of the soft phonon mode is in doubt.

An important contribution came from Eror and Loehr (111), in the use Raman spectroscopy as a analytical tool to precisely determine the stoichiometry of multicomponent compounds in general and barium titanate in particular. They determined 520 peak width as a function of the Ba/Ti ratio and shown for the first time that the Raman spectroscopy can precisely determine the cationic ratio in the multicomponent systems.

Godefroy et.al. (112) investigated the Raman spectra of reduced single crystal barium titanate and reported an extra peak at 760 cm^{-1}, which they assigned to the presence of oxygen vacancies.

3. OBJECTIVES

Is is clear from the literature survey that there are many publications regarding the degradation of barium titanate. Several investigators have discussed the possibility of oxygen ion removal at the anode and the migration of oxygen vacancies with the corresponding reduction of Ti^{+4} to Ti^{+3}. The migration of oxygen vacancies toward the cathode may facilitate Schottky emission. Also during degradation colour center development was observed.

There are only two oxygen concentration cell experiments. These experiments clearly indicate that pure barium titanate does not have an appreciable ionic conductivity at 300^0 C, but the doped materials does. The point defect structure of a barium titanate is reasonab! well understood, although there are various explanations.

Most of the investigations performed in the past on barium titanate were on samples, made from ceramic preparation methods. These samples were thermodynamically poorly defined. There is no direct experimental evidence of the migration of oxygen vacancies that has been suggested during degradation. It is felt that the degradation is not well understood, hence this contribution.

It is proposed that thermodynamically defined (30) samples made by the liquid mix technique (10) be prepared. Undoped as well as Ni doped samples, with the various Ba/Ti ratio will be prepared. The powders will be characterized by X-ray, Raman spectroscopy and SEM techniques. The sintered pellets will be made from these powders. The solubility of Ni will be determined by X-ray, Raman, SEM and by optical microscopy techniques.

We propose to measure the electrical conductivity from 200 to 550^0 C by the four point van der Pauw technique. From these data the band gap, type of

conductivity, the ionization energy of nickel and the carrier concentration will be calculated.

Electrical conductivity will be measured between 850 and 1100^0 C, with respect to various partial pressures of oxygen. Information about the defect structure and ionic and electronic compensation can be derived from these data.

Finally these samples will be subjected to a degradation study. In this, it is proposed to measure the current with respect to time for 60 - 80 hrs at field levels from 0.08 to 17 kV/cm, at 150, 200 and 250^0 C. It is expected that the samples will degrade under these condition and these degraded samples will be characterized by Raman and SEM techniques. Thus, an insight in to the degradation mechanism can be obtained.

4. EXPERIMENTAL PROCEDURE

4.1 SAMPLE PREPARATION

Consider the Gibbs phase rule,

$$P + F = C + 2 \qquad (4.1)$$

where

P = number of phases present

F = degrees of freedom

C = number of constituents

For a single phase binary system we have three degrees of freedom. After fixing total pressure and temperature the remaining variable may be the activity of one of the components. The partial pressure of the anion is usually chosen as the remaining variable. Under these conditions the binary compound is thermodynamically defined. In the ternary compound, ABO_3, the number of degrees of freedom is increased by one. Therefore, to define the system thermodynamically, in addition to the above mentioned three degrees of freedom one more has to be defined independently. This can be done by fixing the ratio of the two cations A/B, if A and B has a negligible volatility at high temperature.

When the compound is made by normal ceramic methods, it involves a mechanical communition, which is likely to introduce impurities. Also it involves elevated temperature sintering, and homogenization depends upon solid state diffusion, this promotes crystal growth and yields a poorly dispersed oxide. Due to all of this, the compositional homogeneity throughout the bulk is in question.

Another method of preparation of mixed oxides, which is an improvement over the ceramic method, is pyrolysis of the precipitations from precursers (112,

113). This method suffers from a restriction imposed by stoichiometric requirements of the complex salt, with several cations and lack of homogeneity during the precipitation process (114).

By using the liquid mix technique (10) ultra high purity mixed oxides can be prepared. The limitation on the purity comes from the purity of starting materials, and the weighing accuracy. This method yields homogeneity on the atomic scale, and very fine particle size (few hundred angstroms), as no high temperature processing for solid state diffusion is required. Thus the A/B ratio is very precisely defined.

In this method the desired cations are complexed in a weak organic acid separately, or taken as a salts, which are soluble in a weak organic acid solution. The only restrictions come from the requirements, that the particular cation solution be stable with respect to time, (absence of precipitation) and temperature. Also they should be stable when the cation solutions are mixed together and heated to the boiling point of the solvent.

In preparing samples the following solutions were used as a source of respective cations. Tetraisopropyl titanate (du Pont Co. Tyzor), henceforth called TPT was used as a source of titanium. Barium carbonate (Johnson - Matthey Corp. Spec. pure), was used as the source of barium. For nickel, nickel carbonate (Johnson-Matthey Corp. Puratronic grade 2) was used. Ethylene glycol (Fisher Scientific AR grade) was used as a solvent. The weak organic acid used was citric acid monohydrate (Fisher Scientific AR grade).

The amount of the respective cations was determined gravimetrically to better than 0.001% precision. A very dilute titanium stock solution was used. First the TPT solution was weighed, and the titanium gram atomic weight was

calculated accurately. Then depending upon the Ba/Ti ratio, or Ba/Ti + Ni ratio desired, the required amount of barium carbonate or barium carbonate + nickel carbonate was added to the weighed TPT solution. To this solution a mixture of ethylene glycol + citric acid (200 ml of ethylene glycol + 60 g of citric acid) was added, and the resulting mixture was stirred at room temperature. The stirring was continued until a clear solution was obtained. The clear solution is an indication that the desired cations are filly dissolved and that the system is homogeneous. The clear solution was then slowly heated to drive off organic solvent and isopropanol so as to obtain a transparent polymeric glass. This was then fired at 750^0 C in air for 24 hrs, to obtain the barium titanate powder. The samples were prepared with various Ba/Ti ratios as shown in Table 4.1 and of general formula $BaTi_{1-x}Ni_xO_3$ as shown in Table 4.2.

For various measurements, samples were made in disc shape from these powders. To make pellets, approximately 70 mg of powder was mixed with a drop of polyvinyl alcohol (4% soln. in water) and pressed in a die, of 12 mm diameter, under 40,000 psi of load. Pellets were sintered at 1275^0 C, 4 hrs in air, and then slowly withdrawn from the furnace. All of the sintered samples had a density equal to 96 to 97% of the theoretical density. Densities were determined pycnometrically in xylyne (m).

4.2 X - Ray Diffraction

X - ray diffraction analyses were carried out by the following equipment. Powders which were fired at 750^0 C, were used in a Debye - Scherrer technique, with a Siemens - Kristalloflex - 2, diffraction unit. Cu Kα radiation with a nickel filter was used. All the data were collected at 30 kV exitation voltage, 32 mA of current, for 2.5 hrs.. The second unit used was a Norelco diffractometer and a

TABLE 4.1

Sample Compositions in Undoped BaTiO$_3$.

Sample notation	Ba/Ti ratio
K - 1	1.00000
K - 2	0.9904
K - 3	0.99994
K - 4	0.99942
K - 5	1.00042
K - 6	0.99901
K - 7	0.99501
K - 8	0.99200
K - 9	0.99799
K - 10	1.00500
K - 11	1.00200
K - 12	1.00800
K - 13	1.00020
K - 14	1.00080
K - 32	1.01000
K - 64	0.98500

TABLE 4.2

Sample Compositions in Nickel Doped BaTiO₃.

Sample notation	Ba/Ti+Ni Ratio	At.% nickel
K - 15	0.995	10
K - 16	0.995	20
K - 17	0.995	15
K - 18	0.995	5
K - 31	0.995	0.01
K - 33	0.995	0.1
K - 34	0.995	1.0
K - 60	0.995	1.5
K - 19	1.000	5
K - 20	1.000	10
K - 21	1.000	1.0
K - 22	1.000	0.5
K - 23	1.000	0.3
K - 24	1.000	0.8
K - 25	1.000	0.1
K - 26	1.000	0.05
K - 27	1.000	3.0
K - 29	1.000	0.005
K - 30	1.000	0.01
K - 61	1.000	1.5
K - 35	1.005	1.0
K - 36	1.005	0.1
K - 37	1.005	0.01

Sample notation	Ba/Ti+Ni Ratio	At.% nickel
K - 38	1.005	0.05
K - 39	1.005	0.5
K - 40	1.005	5.0
K - 62	1.005	1.5

Geiger counter, which was coupled to a PDP - 11 computer. For each sample four scans were added, and the computer gave the output in the form of intensity versus Bragg angle and calculated 'd' spacings. The third unit used was a General Electric XRD - 5 D/F. Here the output was measured with a Geiger counter and plotted by a strip chart recorder. Output was measured for 0 - 180^0 Bragg angle. Samples used in the Norelco and GE units were fired at 1275^0 C, and these results were used to measure the Lattice parameter. Lines from the back reflections and $\theta=90^0$ were used to determine the lattice parameter and a least squares method was used to fit the data.

4.3 Raman Spectral Measurements

Raman spectra were recorded for both powders and sintered pellets (sintered at 1275^0 C). Powders were placed in capillary tubes and the pellets were used directly. A schematic digram of the experimental arrangement is shown in Figure 4.1. Low and high temperature spectra was recorded for the powder specimens. For 273 and 77 K the capillary tubes containing powders were immersed in a cold finger dewar, containing either ice or liquid nitrogen, respectively (115,116). For high temperature, the capillary tube was placed in the center cavity of a copper rod which was heated from the bottom. Opening were made from two sides and the whole copper finger was covered with a pyrex tube to minimize heat losses. The temperature was measured by a thermocouple, which was inserted in the capillary tube.

The laser source was a Spectra - Physics Model 164-05 argon - ion laser. Various wavelengths were used, the most predominant was 514.5 nm, a green line. Excitation and the scattered wavelength were analyzed by a Jarrell - Ash 25 - 300 Raman spectrometer, equipped with an RCA C 31034 (Ga - As) photomulti-
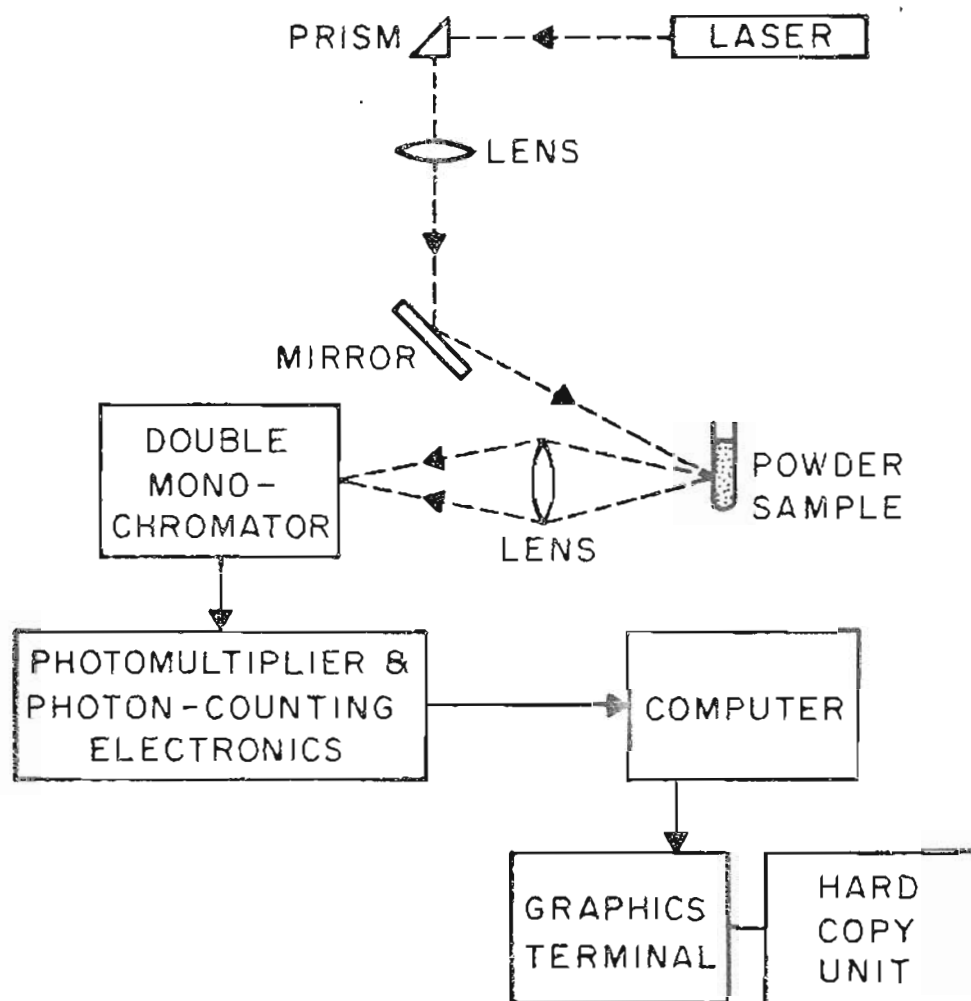
Figure 4.1 SCHEMATIC DIAGRAM OF THE COMPUTER - CONTROLLED LASER
RAMAN SPECTROPHOTOMETER

plier and Ortec amplifier/discriminator (model 9302). Photon counting was carried out by computer (Computer Automation LSI/2, 32 K memory). The laser beam was focused to a < 1 mm spot, and in a few cases $<.05$ mm spot, on the capillary or pellet as the case may be, by a lens system. The Raman scattered radiation was collected by a Nikkor f 1.2, 55 mm focal length, objective lens and focused onto the entrance slit of the double monochromator. An interactive graphics terminal (Tektronix, Inc. 4010-1) facilitated, rapid and accurate spectral analysis. For most of the samples at least three scans were summed and in many cases five to ten. This gave excellent signal to noise ratio and allowed the recording of weak signals. The laser power used was between 60 - 150 mW, slit width of 3 cm^{-1}, and scan rate of 2 cm^{-1}/sec.. Most of the spectra were recorded between 50 cm^{-1} and 1150 cm^{-1}, but on a few samples the spectra were recorded between 50 cm^{-1} and 2050 cm^{-1}.

4.4 Electrical Conductivity Measurements Between 200 - 550^0 C.

Samples were cut from the ceramic discs into a rectangular or square shape with edge lengths of about 5 mm, using either an airabrasive unit (S.S. White Industrial airabrasive unit, model F), or a low speed diamond saw (South Bay Technology, model 650). After cutting, the samples were polished on a 600 grit paper followed by rinsing in distilled water, ethanol and distilled water, in an ultrasonic bath.

Considering various methods of measuring electrical conductivity, it was felt that the most suitable method was the standard four point van der Pauw technique (117-122). In this method four contacts are made to the circumference of the sample, the only restrictions are that the sample be flat and it should not have isolated holes.

In the present case contacts were made at the four corners of the sample. Theoretical analysis (117,118) of the field and current lines thus produced leads to a following relationship between conductivity and measured quantities.

$$\sigma = 2 \ln 2 \frac{I}{\pi t f_{AB}(V_A + V_B)} \qquad (4.2)$$

where

$\sigma = $ conductivity

$t = $ sample thickness

$f_{AB} = $ Correction factor related to $\dfrac{V_A}{V_B}$.

$I = $ current

$V_A, V_B = $ voltage

Here voltages are measured by passing a known amount of current through two adjacent contacts and measuring V_A the voltage across the two opposite contacts, and then rotating the current flow by 90^0 and measuring V_B in the same manner.

Figure 4.2 illustrates the contact arrangement used. A switch box was used to direct current from a 1.5 Volt battery, through contact 1 and 7, and the current was measured across 3 and 5 (I_A). Then the voltage was applied to 1 and 3 and the current was measured across 7 and 5. Current was measured through the same contacts by reversing polarity of the voltage. Current was measured with a Keithley 616 digital electrometer with input impedance $> 10^{14}\Omega$. The factor f_{AB} depends upon the ratio of R_A/R_B. For an isotropic square sample and for $V_A/V_B = 1$, $f_{AB} = 1$. In the present case f_{AB} varied from 1 to 0.95.

To have meaningful conductivity measurements, electrical contacts to the sample should be ohmic, which is nontrivial (123,124). A number of techniques

AMPHENOL 57-40140 CONNECTOR
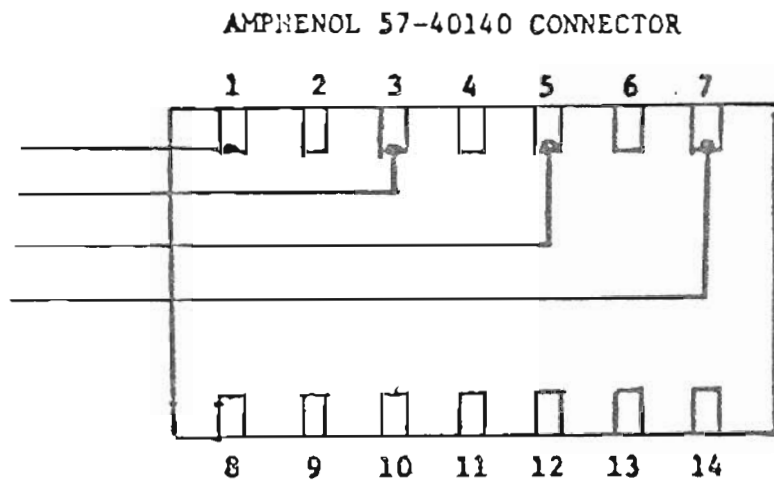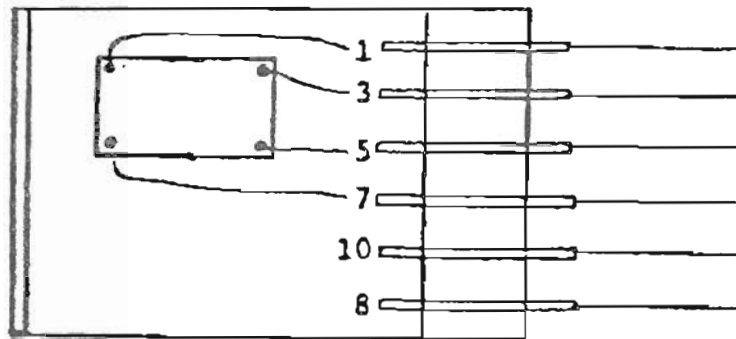
Figure 4.2   WIRING ARRANGEMENT FOR ELECTRICAL
CONDUCTIVITY MEASUREMENT

have been proposed for the case of ceramic oxides (125 - 130). Landis (127) observed that, indium amalgam rubbed on barium titanate produces ohmic contacts with low resistance. Fleming and O'Bryan (129) found that soldering In:Ga yielded ohmic contacts over a 10^4 range of applied field. The noble metals, Ag and Au do make ohmic contacts as indicated by Tredgold et al. (78).

In the present case contacts were made by rubbing $In_{.995}Ga_{.005}$ alloy on the sample, and then electrical connection was made by phosphor bronze pressure clips, which were covered in platinum foil. Platinum wire was connected from the foil to the outlet of the sample holder as shown in Figure 4.3. Each platinum wire was covered in a quartz capillary, in turn these capillaries were placed in a quartz tube which was connected to the sample holder made from quartz. This assembly was placed in a furnace, whose temperature was controlled within 0.5^0 C, with a proportional integrating differential type controller made by Lindberg. The actual sample temperature measurement was carried out by a second chromel alumel thermocouple, which was glued to the sample holder by GE 7031 varnish. Dry air (passed over silica gel) was blown through the furnace during the measurement. At each conductivity reading, current was measured for three orders of magnitude of voltage to ensure that the contacts behaved ohmically.

4.5 Electrical Conductivity Measurement at High Temperatures

The conductivity was measured by a four point technique. This four point method is slightly different from the van der Pauw technique. In this method samples were cut from sintered discs, (1275^0 C, 4 hrs, in air) in a rectangular form of about 5 mm by 10 mm size. Small notches were cut on the side as described, (131,132) to aid in holding the platinum wire of 0.25 mm diameter. Platinum wire was wrapped through these notches. Each sample was wrapped
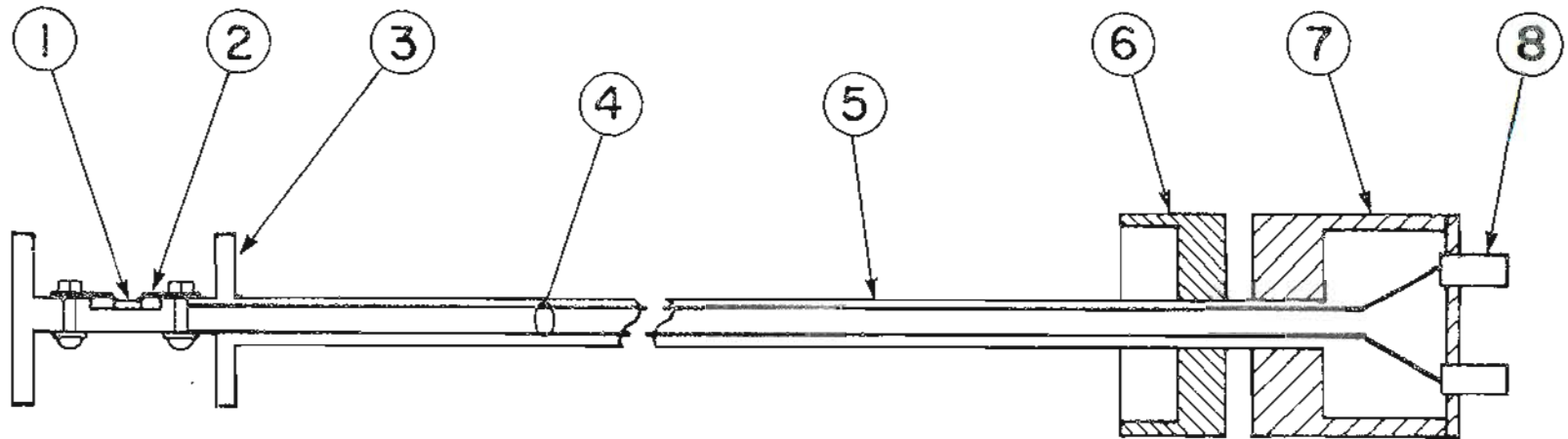
Figure 4.3   SAMPLE HOLDER ASSEMBLY FOR MODERATE TEMPERATURE
ELECTRICAL CONDUCTIVITY MEASUREMENT 1) SAMPLE, 2) PRESSURE
CONTACT CLIPS, 3) QUARTZ SAMPLE HOLDER 4) QUARTZ CAPILLARIES,
5) OUTER QUARTZ TUBE, 6) TUBE COVER AND 7) TEFLON COVER

with four wires. These wires served both the purposes of electrical contact leads and mechanical support to hold the sample in the hot zone of the furnace. Each platinum wire was insulated from the another by recrystallized high purity alumina insulators.

A standard pyrex joint to which six capillaries had been sealed vacuum tight was mounted on top of a mullite tube. The entire assembly, including sample is shown in Figure 4.4. Platinum wires from the sample and thermocouple leads were taken out from these capillaries and connections were made with various instruments.

The conductivity was measured between 850 and 1100^0 C as a function of oxygen partial pressure. To measure the conductivity a known amount of current was passed between the two outermost electrodes by a Keithley constant current source (model 225). The voltage was measured between the two innermost electrodes by a Keithley 191 digital electrometer having an input impedance $> 10^{10}\Omega$. The direction of the current was reversed and the voltage was measured again. The distance between the two innermost electrode was measured accurately, together with the width of the sample to determine the ratio (a/l). From this the conductivity was calculated as

$$\sigma = \left(\frac{a}{l}\right)\left(\frac{I}{V}\right) \tag{4.3}$$

All the conductivity measurements were carried out when the sample was in complete thermodynamic equilibrium with the oxygen partial pressure. This was checked by observing conductivity readings under the given conditions for eight hours, and by taking conductivity readings under the same conditions by approaching from higher and lower partial pressures of oxygen. The voltage reading was also measured for at least three orders of magnitude of current to ensure
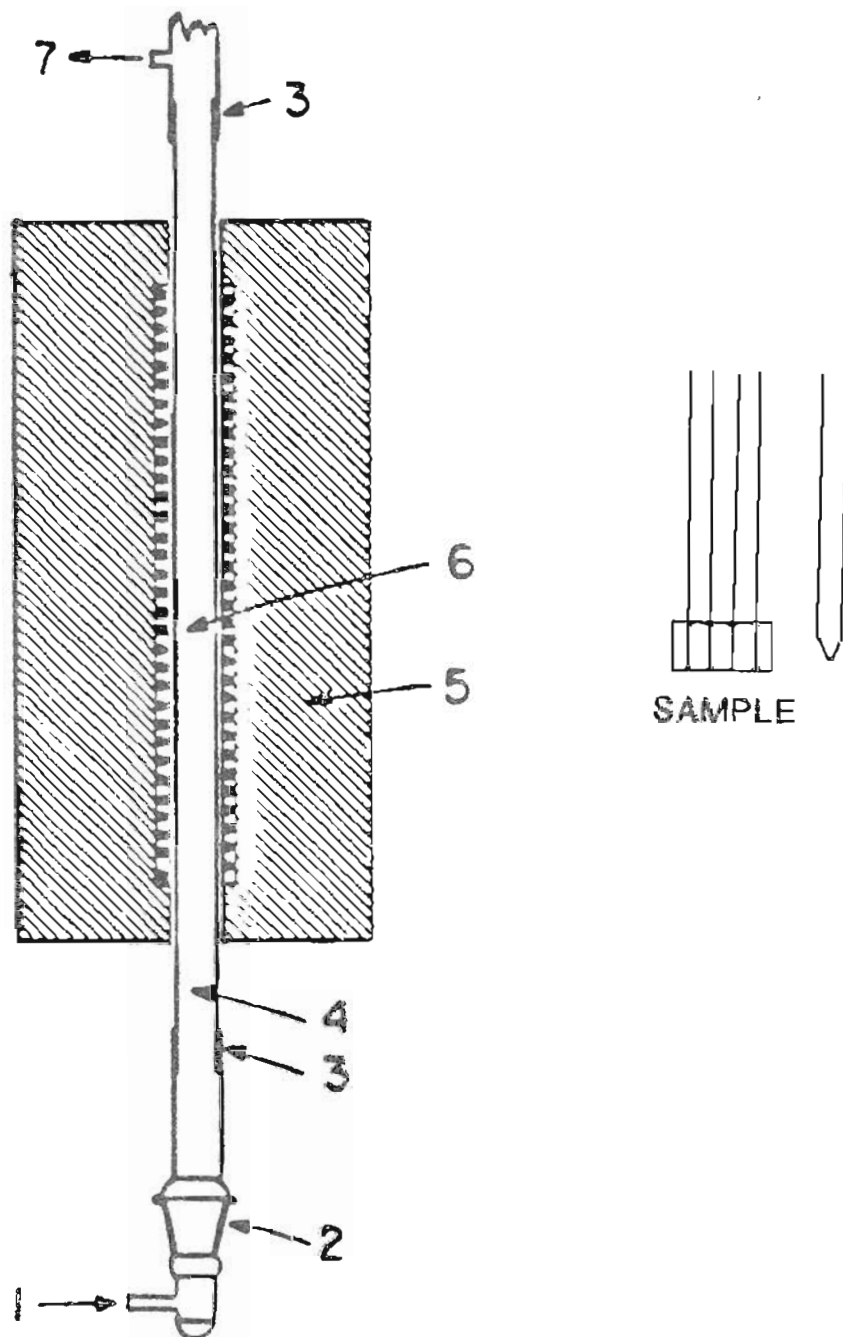
Figure 4.4 FURNACE REACTION TUBE ASSEMBLY 1) GAS INLET, 2) STANDARD
PYREX TAPER JOINT, 3) PYREX-MULLITE SEAL, 4) MULLITE TUBE,
5) FURNACE, 6) HOT ZONE AND 7) GAS OUTLET

the contacts behave ohmically.

Various partial pressures of oxygen were achieved by using gas mixtures. The theory and apparatus has been covered in detail by Eror (133) and Balachandran (134) and hence will not be elaborated here.

Oxygen partial pressures in the range of 10^0 - 10^{-4} atm. were achieved by pure oxygen and mixtures of oxygen and argon. The tanks of argon - oxygen were commercially available and each tank was individually analyzed for the oxygen content. Oxygen partial pressures between 10^{-4} to 10^{-6} atm. were achieved by controlling the flow rate of an argon - oxygen (50 ppm O_2) mixture, and pure argon. Oxygen partial pressures bellow 10^{-6} were achieved by using the desired amount of CO and CO_2 (supplied by Airco). Pressures less than 10^{-20} atm. were achieved by mixing H_2 and CO_2. The carbon monoxide used was grade 2.3, the carbon dioxide was 2.8 grade, and pure argon was grade 5.0. The schematic diagram of the gas cleaning and metering system is shown in Figure 4.5.

Oxygen, carbon monoxide and argon - oxygen mixtures, were passed through successive tubes containing magnesium perchlorate, ascarite and magnesium perchlorate. Argon was also passed through the above train but before entering the furnace, it was passed over copper turnings, which were heated to 450^0 C. The carbon dioxide was passed through tubes containing drierite, copper turnings at 450^0 C and drierite. Hydrogen was passed through drierite, copper turnings at 450^0 C and silica gel.

All gases were metered with conventional manometric flow meters using capillary construction, and di-butyl phthalate in two arms of the manometer and gas blow off column. Initially, calibration of gas flow rate, through the various
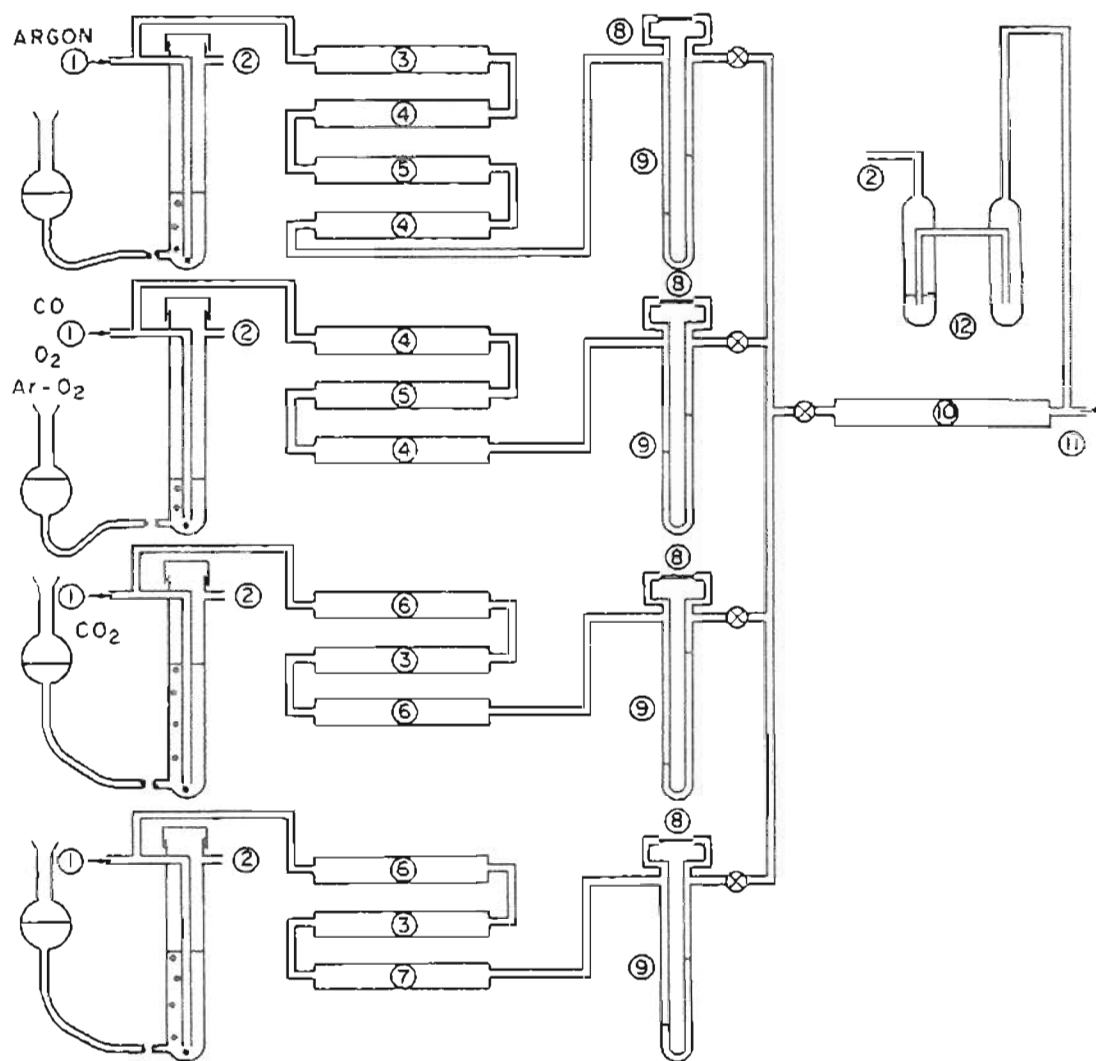
Figure 4.5 SCHEMATIC DIAGRAM OF THE GAS CLEANING AND
METERING TRAIN

capillaries was performed by the displacement of a bubble interface in a graduated burette using a soap solution. After metering, the gasses were passed through a mixing chamber containing glass beads and entered the furnace at the bottom of a vertical tube, exited through tube and exited at the top through a di-butyl phthalate bubbler.

4.6 Dielectric Constant Measurement

The dielectric constant was measured at two frequencies, 1 kHz and 1 MHz, between room temperature and 400^0 C. For this, ceramic disc samples were used. Discs of approximately 12 mm diameter were taken, and a center circular electrode of 4.5 mm diameter was applied. The electrode was $In_{.995}$ - $Ga_{.005}$ amalgam rubbed on to the surface, over which du-Pont conducting silver paste was applied. Before applying electrodes, the samples were polished on 600 grit paper and cleaned in distilled water and ethanol as described earlier. The samples used were approximately 1.2 to 1.4 mm thick.

The sample holder is shown in Figure 4.6. The sample was held between two brass rods, which also act as electrodes. The rods were 4.5 mm in diameter and were covered with a platinum foil for a short length to make good contacts with the sample. In turn these brass rods were supported by teflon bushings, which were fixed at the end of a steel tube of 3.5 cm diameter. Apart from mechanical support, the steel tube served the purpose of a guard electrode, for noise suppression. At the center of the steel tube a window was cut to facilitate sample changing. Samples were held under a small pressure by adjusting the length of the brass rods, as they were screwed in the teflon bushings. The complete assembly was placed in a quartz tube which was put in the furnace. The furnace temperature was controlled within $\pm.5^0$ C by a PID type controller.
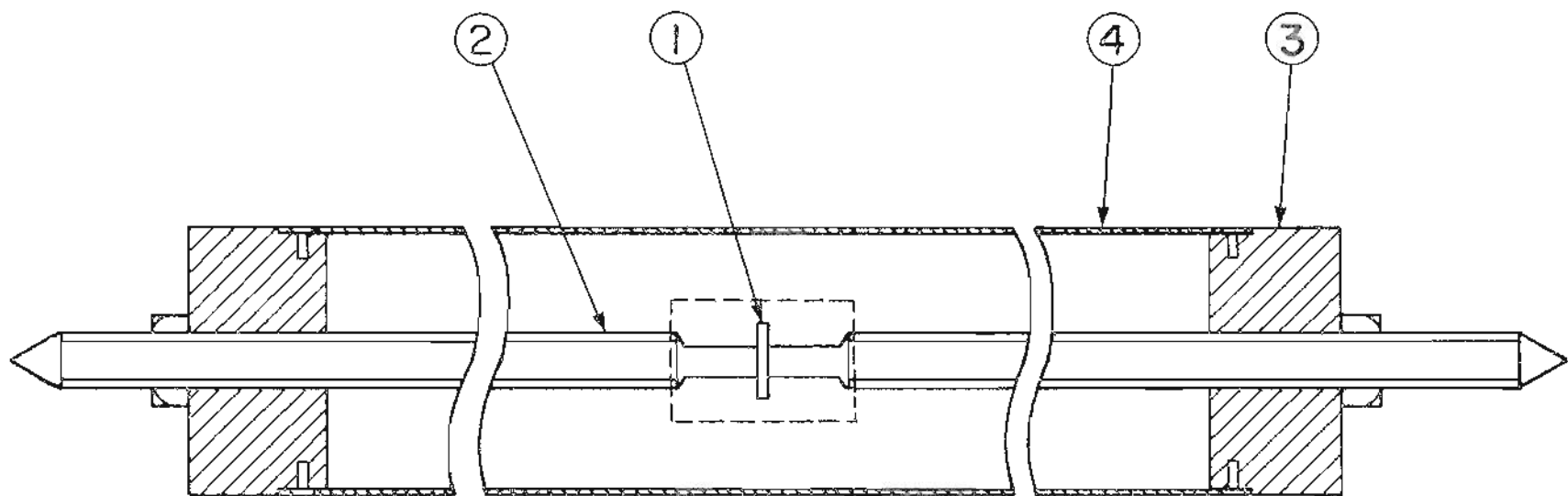
Figure 4.6   SAMPLE HOLDER FOR DEGRADATION MEASUREMENT   1) SAMPLE,
2) BRASS ELECTRODE, 3) OUTER STAINLESS STEEL TUBE,
4) TEFLON BUSHING

Actual sample temperature was monitored by a second thermocouple which was kept 2 mm away from the sample surface.

Capacitance was measured by a Boontan 72 BD capacitance bridge, which measured the capacitance at 1 MHz. At 1 KHz, the capacitance was measured by a HP 4260A universal bridge. The sample thickness and the electrode area was measured, and the dielectric constant was calculated from the capacitance.

4.7 Degradation Measurement

In this series of experiments current with respect to time at various field strengths at 150, 200 and 250^0 C was measured. Field strength varied from 0.83 to 17 kV/cm. Sample holder, sample size and electrodes were the same as in the dielectric constant measurement. Surface conduction was avoided since the electrodes did not extend to the edge of the disc and a guard electrode was used.

The schematic diagram of the current measuring apparatus is as shown in Figure 4.7. To accommodate a large range of applied voltage, two different power supplies were used. For the 0 to 60 volts range, a Heath Schlumberger model SP 2700 power supply was used. For higher voltages a Fluke model 410B power supply was used, this supply was capable of supplying 50 volts to 10 kV. Current was measured by a Keithley 610C electrometer in the ammeter mode. The electrometer had a output of 10 volts full scale deflection, which was used for a strip chart recorder. The recorder used was a HP Moseley 7100B strip chart recorder. These plots gave the variation of current with time. A varistor was used in parallel with the electrometer to protect it in case the sample failed. The temperature was controlled within $\pm.5^0$ C.

Each sample was placed in a furnace heated to 200^0 C, and 2 kV voltage was applied for 1 minute to check for any flaws. Once the specimen passed this

OVEN

SAMPLE

ELECTROMETER

RECORDER

+

DC POWER SUPPLY

−
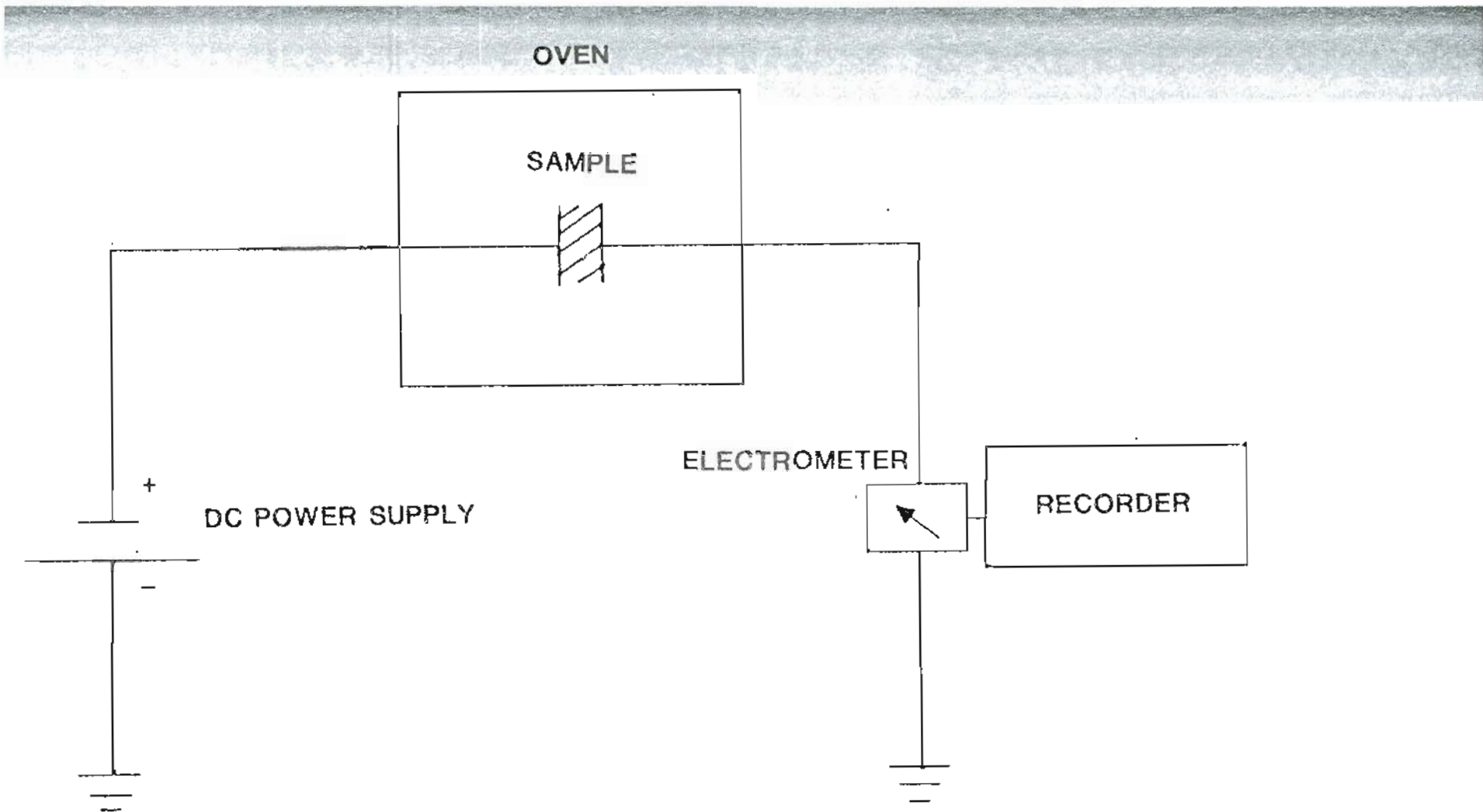
Figure 4.7   SCHEMATIC OF THE CURRENT MEASURING APPARATUS

test, the temperature was lowered to 150^0 C and the experimental voltage was applied and the current was recorded. The current was recorded for times between 24 and 80 hrs. Then the voltage was removed and the specimen was kept at that temperature for 2 hrs and then a higher voltage was applied. The sample thickness was 0.11 to 0.13 cm. The same procedure was followed at each temperature. This procedure was repeated on three samples to determine the repeatability of the results.

5. RESULTS AND DISCUSSION

5.1 SOLUBILITY OF END MEMBERS AND NICKEL

5.1.1 X-ray Diffractometry

The X - ray diffraction patterns of "as prepared" undoped powders, for the A/B ratios (A/B where A = Ba and B = Ti + Ni) of 1.0000, 1.01 and 0.985 are shown in Figure 5.1 a), b) and c) respectively. All three patterns are indexed as tetragonal and there are no additional lines present or significant lattice parameter changes. All of the lattice parameters are within ± 0.006 A of each other, which is within experimental error limits. Figures 5.2 a), b) and c) depict the X - ray diffraction pattern (intensity vs 2 θ) for undoped barium titanate with A/B ratios of 1.0000, 0.985 and 1.008, respectively. These samples were sintered at 1275^0 C for 6 hrs and then ground to make samples for the diffraction patterns.

The patterns can be indexed as tetragonal for the complete range of the A/B ratio studied. The lattice parameter was measured using the least square fit method. Figure 5.3 shows the variation of lattice parameter with the A/B ratio. For the A/B ratios between 0.995 and 1.0008 'a' remains essentially constant, and 'c' varies very little. Considering the accuracy of the process and the scatter in the data, 'c' and thus c/a can be considered as constant. On the titanium rich side, the extreme composition observed was with the ratio of 0.985, whose pattern is shown in Figure 5.2 c. It appears that for the ratio between 0.995 and 0.985 c/a remains constant. From Figure 5.3 it appears that the compositions between the A/B ratio of 0.995 to 1.0008 and above exist in a two phase region. From micrography and Raman spectra, it appears that compositions within the A/B ratio of 0.995 to 1.008 are in a single phase region, whereas any compositions below and above this region are in a two phase region. Thus
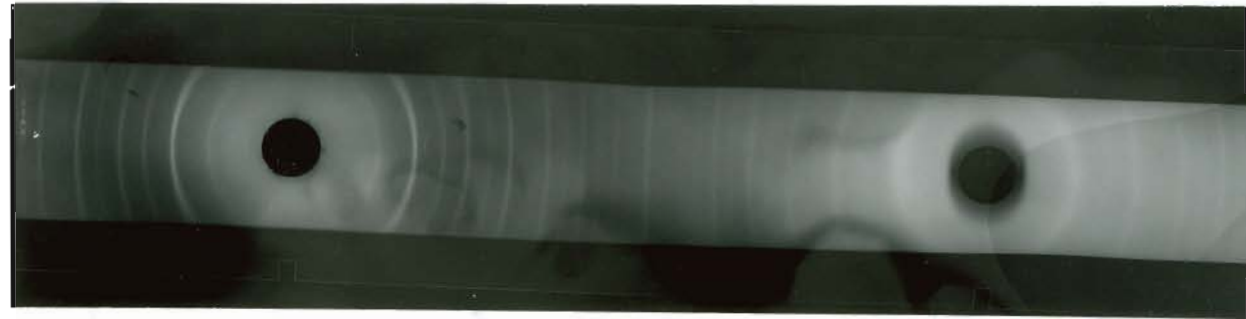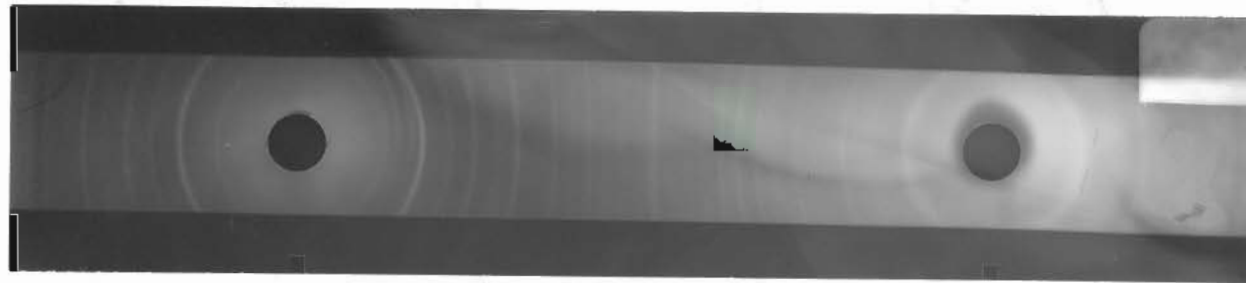
Figure 5.1   DIFFRACTION PATTERNS (PHOTOGRAPH) OF BaTiO$_3$

a) Ratio = 1.000 b) Ratio = 1.01 c) Ratio = 0.985
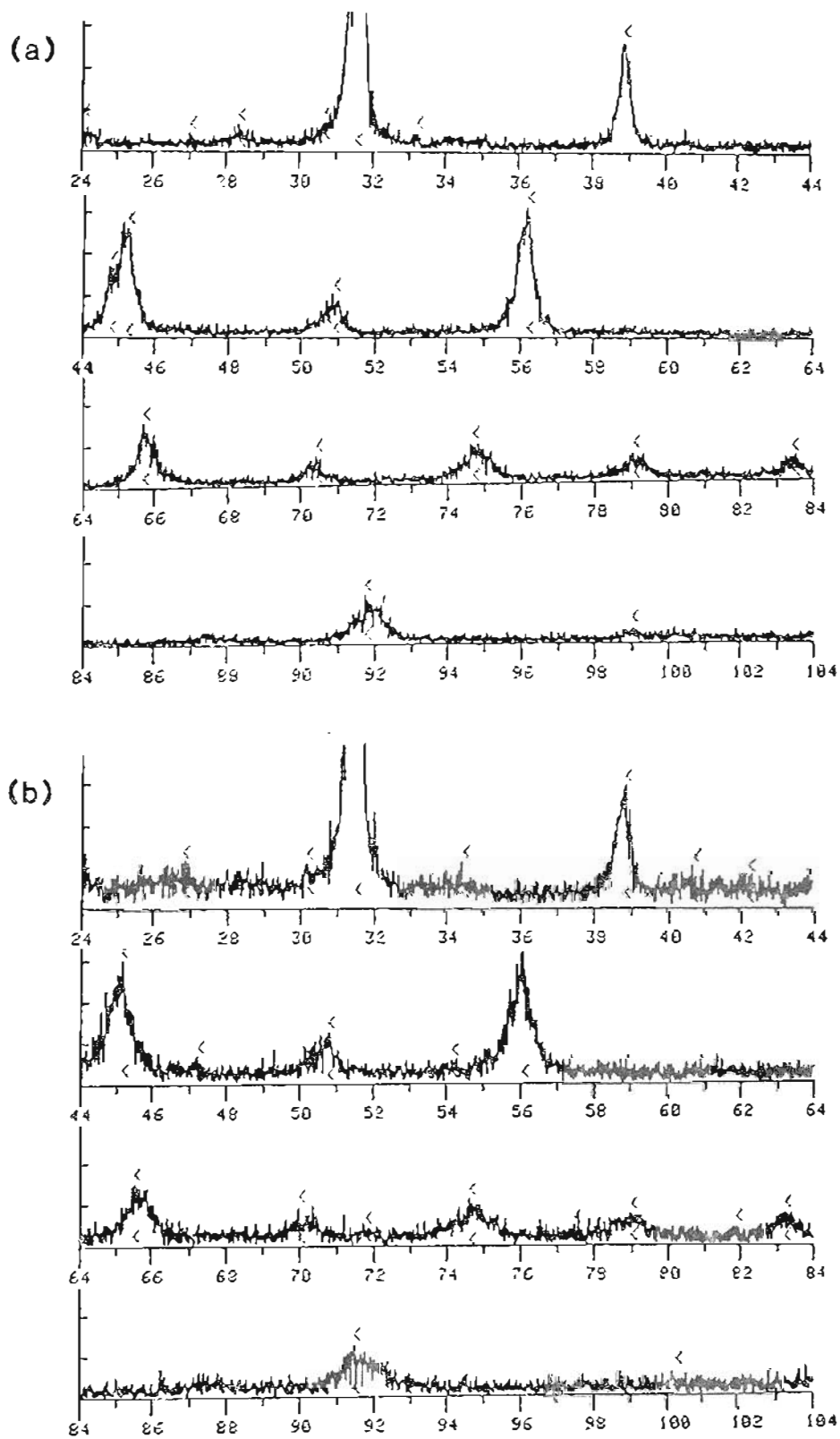
Figure 5.2   DIFFRACTION PATTERNS (INTENSITY VS 2 θ) OF BaTiO$_3$
AS A FUNCTION OF Ba/Ti RATIO
a) Ratio = 1.0000
b) Ratio = 0.985
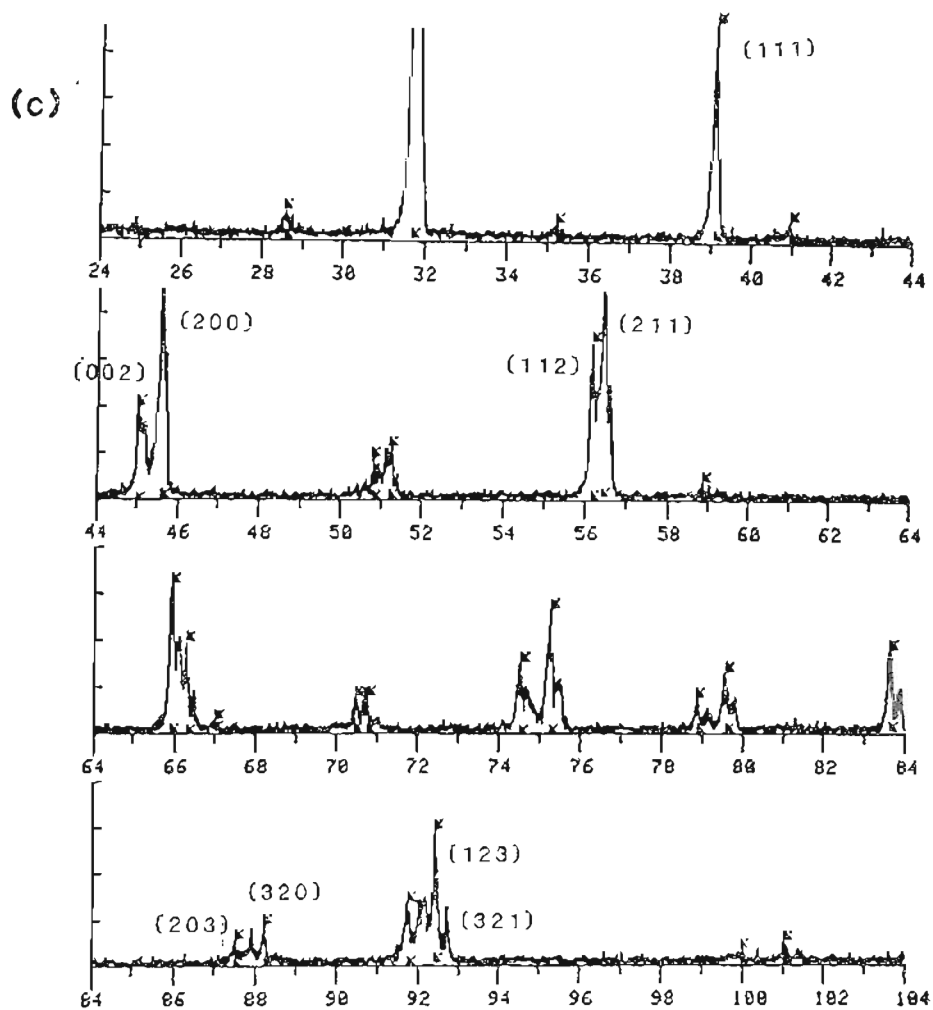
Figure 5.2   DIFFRACTION PATTERNS (INTENSITY VS 2 θ) OF $BaTiO_3$
(cont.)   AS A FUNCTION OF Ba/Ti RATIO
      c) Ratio = 1.008
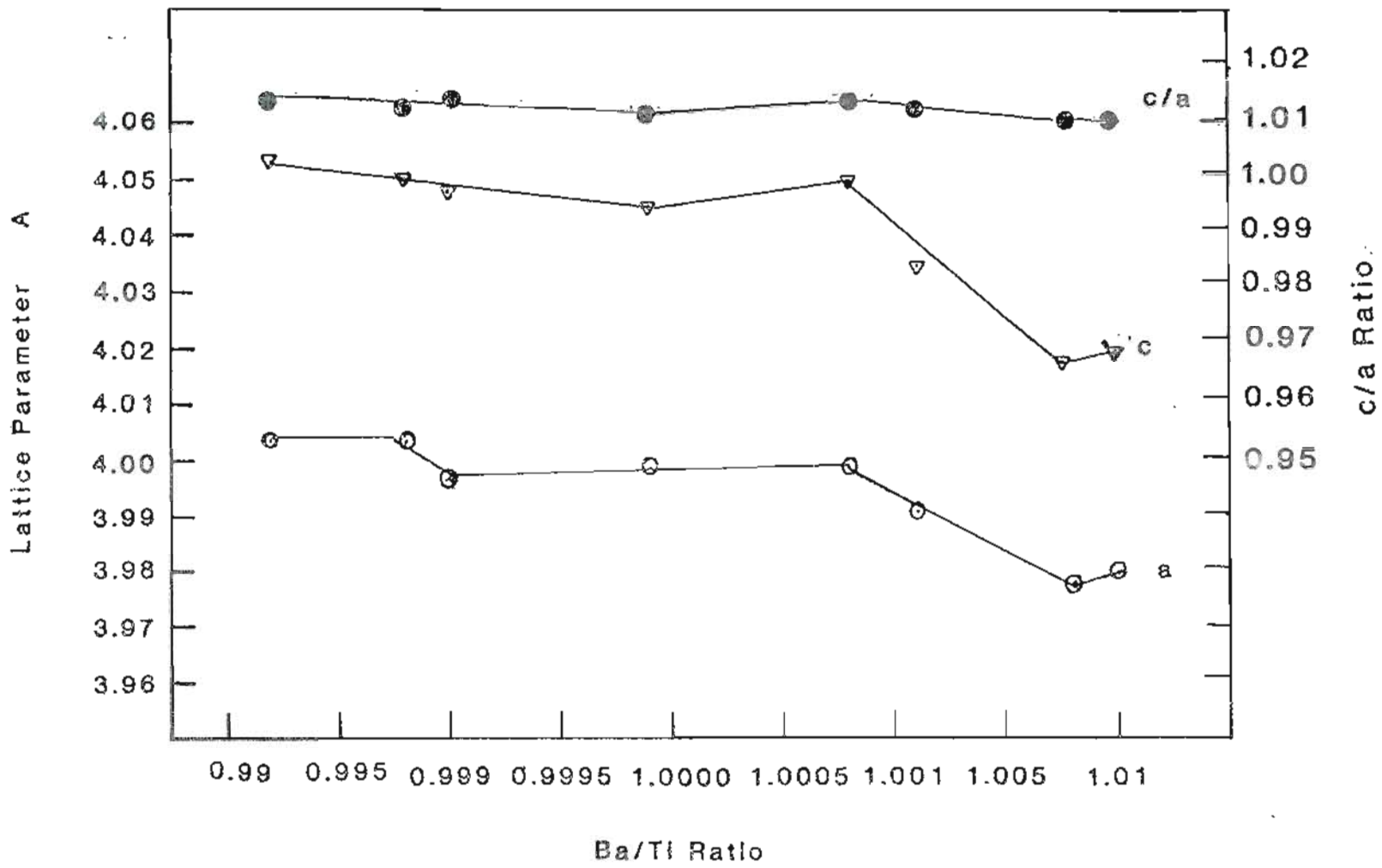
Figure 5.3 VARIATION OF LATTICE PARAMETER OF BaTiO$_3$ WITH THE Ba/Ti RATIO

the X - ray diffraction analysis seems to contradict the results of Raman spectroscopy and micrography analysis for the compositions having A/B ratios of 1.0008 to 0.995. In this range of composition, the lattice parameter changes very little, and taking accuracy of the process and scatter in the data into account, the X - ray results may not give reliable information, which appears to have happened in the present case. On the titanium rich side, it is expected that c/a should increase as the A/B ratio increases from unity. This is due the fact that in barium titanate it is the shift of Ti atoms, and O atoms which gives tetragonality to the structure. Thus the addition of Ti atoms will increase the lattice strain and tetragonality. This random increase in the lattice strain should give broad peaks, compared to the stoichiometric composition, which were indeed observed although an increase in the c/a was not observed. Comparing figures 5.2 (b) and (c) it is clear that on the Ba rich side, the diffraction peaks are sharper and a well defined tetragonal split is observed.

Figure 5.3 indicates that on the Ba rich side as the A/B ratio approaches 1.002 the lattice parameters starts decreasing. This decrease continues until the ratio is 1.008. For any A/B ratio higher than 1.008, 'c' and 'a' start increasing but c/a remains constant. Also, as the A/B ratio increases on the Ba rich side, the relative intensities of the (2 0 0), (1 1 1), (3 2 1), (2 1 1) and (1 1 2) peaks increase. The (2 0 3) and (3 0 2) peaks which were not visible in the Ti rich side also became visible. For compositions with the ratio of 1.008 and 1.01 the relative intensity of the (2 0 0) peak becomes roughly 3 times that of the (1 1 1) peak. Whereas for all other Ti rich compositions the (1 1 1) peak is stronger than the (2 0 0) peak. Also for these compositions the (2 0 2) and (0 0 2) peaks become visible.

The increase in the relative intensity of the peaks due to the addition of Ba is expected since the atomic scattering factor for Ba is nearly four times that of titanium and oxygen. The sharp peaks shifted to a lower 2θ as the ratio increased from 1.0008; suggesting uniform lattice compression due to the addition of barium. Uniform lattice compression coupled with the fact that the (2 0 0) peak intensity becomes three times that of (1 1 1), suggests that the barium is going on to the specific sites on the plane perpendicular to the c axis. It is proposed that a structural arrangement similar to the Ruddlesden-Popper phases in $SrTiO_3$ ($nSrTiO_3 \cdot SrO$) is taking place. For this structure a BaO layer is accommodated between unit cells of $BaTiO_3$, in the 'c' direction. A similar arrangement has been proposed by Eror and Smyth (30).

5.1.2 Micrography

Figure 5.4 (a) and (b) shows the photomicrograph of barium titanate with an A/B ratio of 1.01 at 4700 and 16000 magnification, respectively. Figure 5.4 (c) and (d) shows the micrograph of a sample with an A/B ratio of 1.005 at 5500 and 16000 magnification, respectively. Notice the small circular area in all these pictures, which is brighter than the matrix This we believe to be a second phase, although a microprobe analysis should be done to verify this. Although the X - ray diffraction pattern for these compositions, has not shown any extra lines, this does not discount the possibility of the presence of a second phase. These samples were thermally etched. Figure 5.5 shows the photomicrograph of the samples which were chemically etched, and in those samples most of the grain boundary area was etched away. This was especially so for the barium rich compositions. Whereas on the titanium rich side; the grain boundary area was not washed away. Figure 5.5 (a) and (b) shows the photomicrograph of samples with
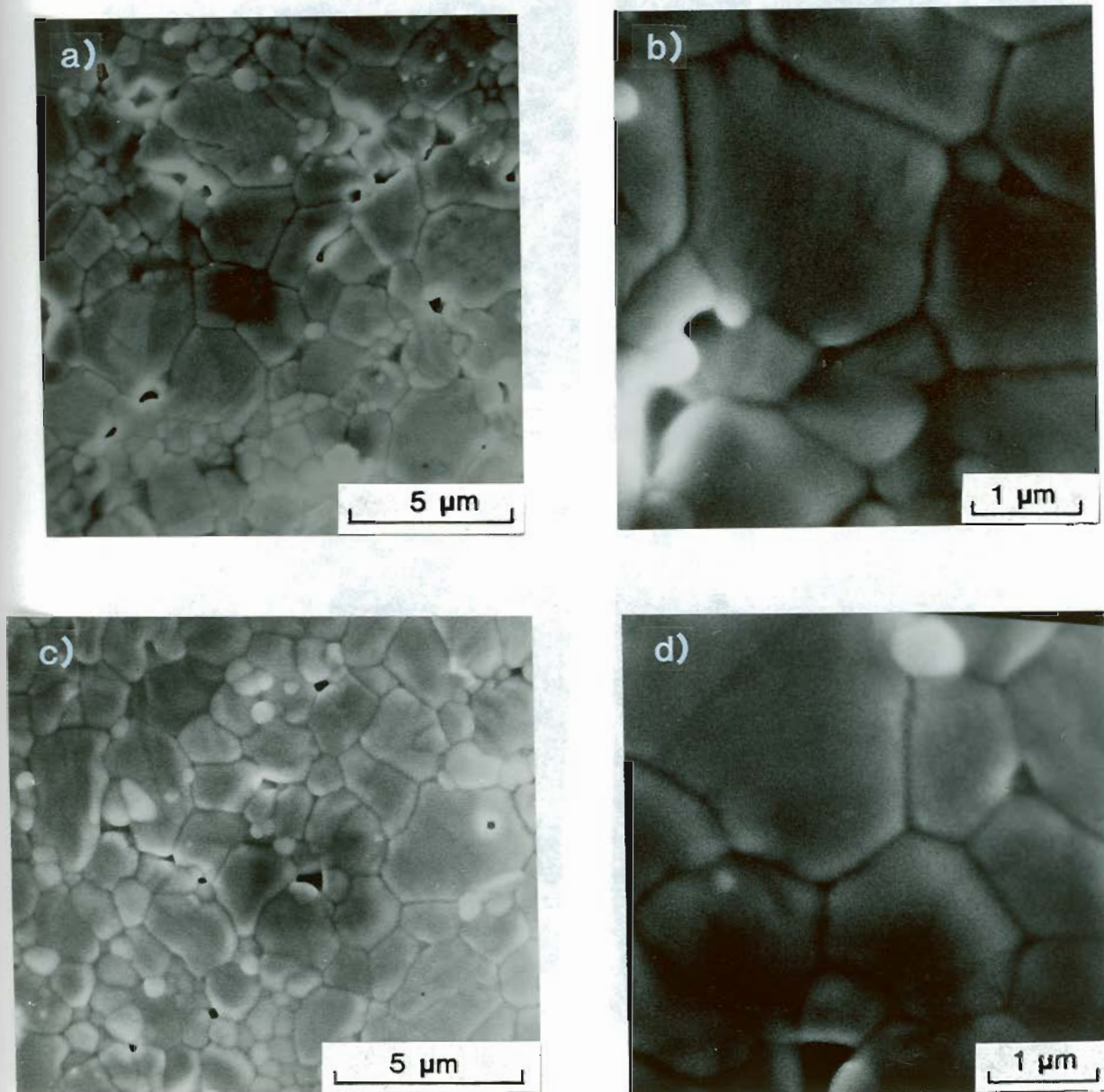
Figure 5.4 PHOTOMICROGRAPH OF THERMALLY ETCHED BaTiO$_3$ WITH THE A/B RATIO OF 1.005 AND 1.01. a) Ratio = 1.01 b) 1.01 c) 1.005 d) 1.005
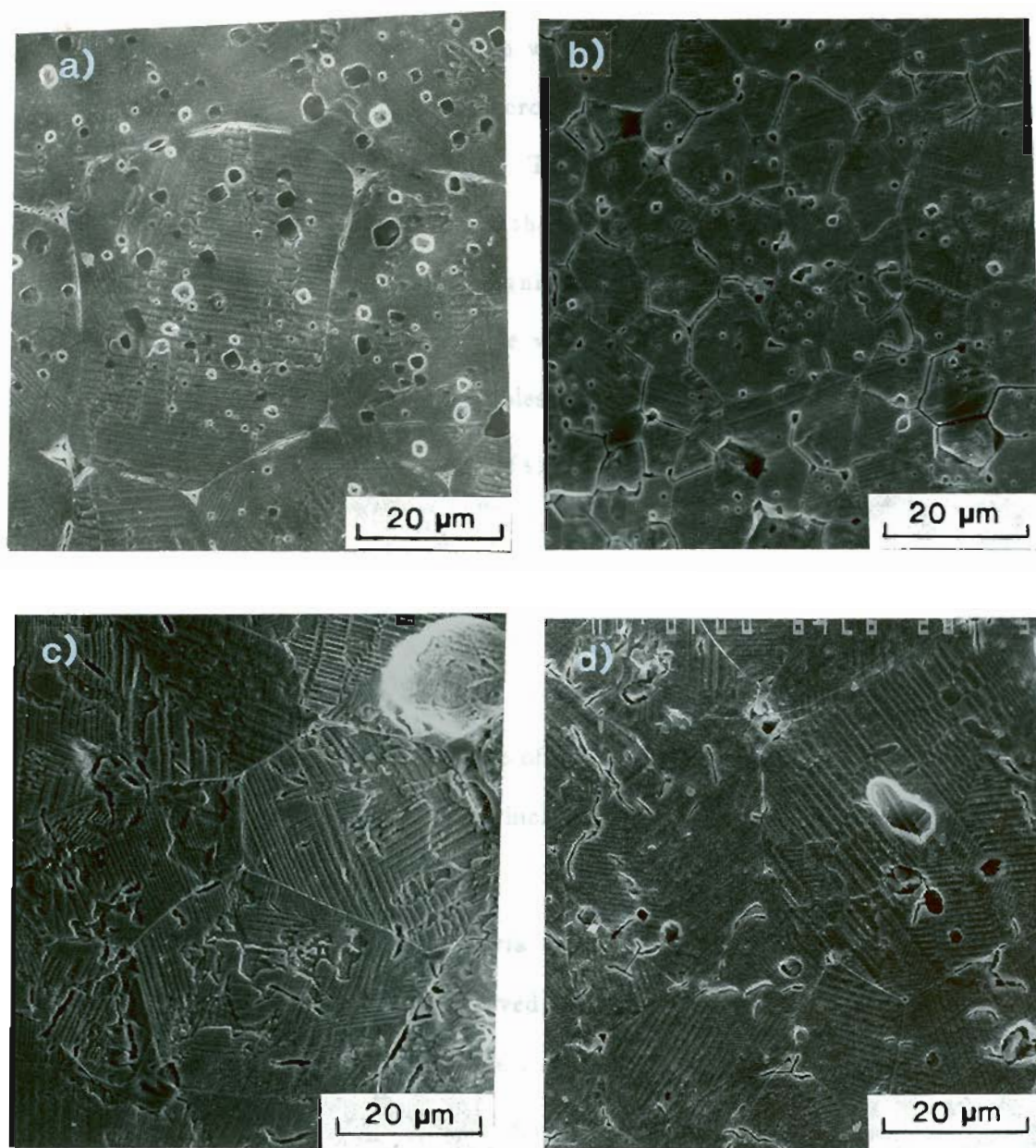
Figure 5.5   PHOTOMICROGRAPH OF CHEMICALLY ETCHED $BaTiO_3$ WITH VARIOUS
A/B RATIO. a) Ratio = 0.995 b) 1.005 c) 0.9999 d) 0.992

A/B ratios of 0.995 and 1.005, respectively, at 1000 magnification. These samples were chemically etched. In the chemically etched samples the ferroelectric domain structure is quite clear, which was not observed in the thermally etched samples. Figure 5.5 (c) shows the micrograph of a sample with an A/B ratio of 0.9999 which was chemically etched. There is no second phase apparent anywhere. Figure 5.6 (a) and (b) shows the micrographs of a sample with an A/B ratio of 0.995 at 4700 and 16000 magnification respectively. Figure 5.6 (c) and (d) shows the micrograph of a sample with an A/B ratio of 0.985 at 5500 and 3000 magnification respectively. Samples in Figure 5.6 were thermally etched.

From figures 5.6 (a), (b) and 5.5 (a) it is clear that the samples which were thermally etched do not show any second phase at the triple point whereas the samples which were chemically etched do show, at some triple points a darker area which may be a second phase. Also it is quite evident that as the barium concentration increases the grain size decreases. The smallest grain size (15 μm) was found for a sample with the ratio of 1.01. Also, as the barium concentration increased the grain boundary area which was etched away by chemical etching increased.

The first comprehensive equilibria in the BaO- TiO_2 system was published by Rase and Roy (135). They observed, a mixture of $BaTiO_3$ and Ba_2TiO_4, by X-ray diffractions in all compositions containing 33.5 to 50 mole % TiO_2, and which were solid phase reacted at temperatures between 1200^0 and 1600^0 C. They reported that a small amount of solid solution does exist toward the titanium rich side of $BaTiO_3$. They estimated the solid solubility of titanium dioxide to be approximately 3%, although they observed a mixture of 52 and 48 mole% titanium dioxide and barium oxide respectively, i.e. they did not examine the compositions between the A/B ratio of 1.000 to 0.923. To emphasize the
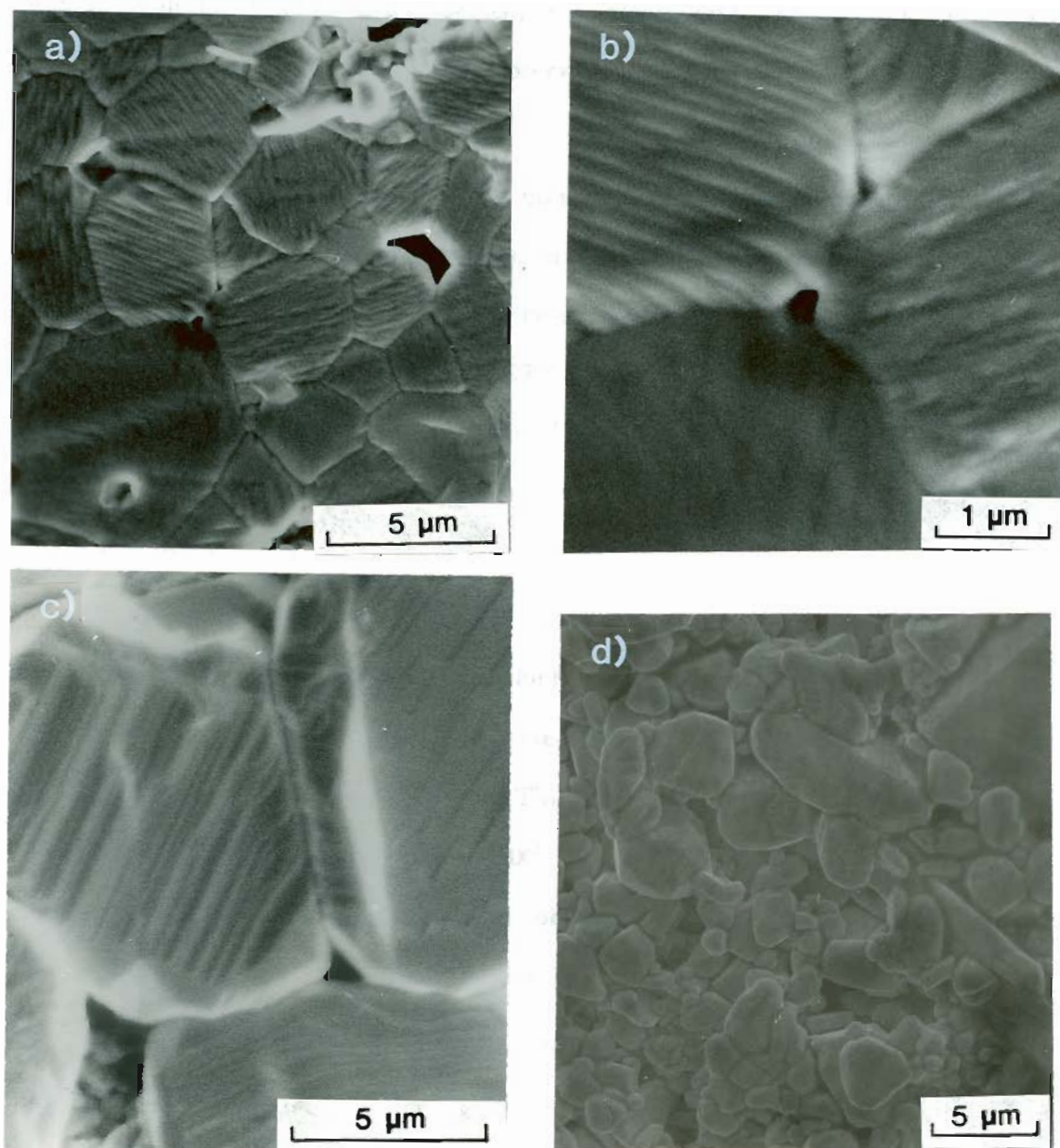
Figure 5.6 PHOTOMICROGRAPH OF THERMALLY ETCHED BaTiO$_3$ WITH THE A/B RATIO OF 0.995 and 0.985. a) Ratio = 0.995 b) 0.995 c) 0.985 d) 0.985

Negas et.al. (139) reported extensive work on the phase equilibria in the $BaTiO_3$ - TiO_2 system, (for the presence of excess TiO_2 from 60 to 90 mole%). They observed that the only stable phases in the $BaTiO_3$ - TiO_2 system were $Ba_6Ti_{17}O_{40}$, $Ba_4Ti_{13}O_{30}$, $BaTi_4O_9$ and $Ba_2Ti_9O_{20}$. The phases $BaTi_2O_5$ and $BaTi_5O_{11}$ were reported to be metastable. According to their study the equilibrium subsolidus phase assemblage for all compositions with less TiO_2 than the 6/17 A/B ratio are $BaTiO_3$ plus $Ba_6Ti_{17}O_{40}$. They concluded that the phase, $Ba_2Ti_5O_{12}$, observed by Jonker and Kwestroo was mistaken for the $Ba_6Ti_{17}O_{40}$ compound, and concurred with the finding of the $Ba_2Ti_9O_{20}$ phase, and that reheated $BaTi_2O_5$ converted to $BaTiO_3$ and $Ba_6Ti_{17}O_{40}$. They also suggested that the phase $BaTi_3O_7$ identified by Rase and Roy was actually $Ba_4Ti_{13}O_{30}$. Considering the data presented by the various investigators, we concur with the observations of Negas et.al. (139).

O'Bryan and Thomson (140) reported on the phase equilibria in the BaO - TiO_2 system. They found by reacting 66.7 mole% TiO_2, the lowest mole% in their study, at 1125^0 C, for 6hrs, the resulting phases were $BaTiO_3$, $BaTi_2O_5$ and $Ba_4Ti_{13}O_{30}$. When the reacting temperature was raised to 1300^0 C, the equilibrium phases were $BaTiO_3$ and $Ba_6Ti_{17}O_{40}$. They also reported difficulty in forming $Ba_2Ti_9O_{20}$ by low temperature reaction.

Recently Sharma et.al. (141) reported the observation of a second phase in $BaTiO_3$ with an A/B ratio of 0.995. The samples were sintered at 1420^0 C, for 2.5 hrs. In the second phase by electron microprobe analysis, they found the Ti/Ba ratio to be 3/1 and from this information they concluded that the second phase to be $Ba_6Ti_{17}O_{40}$.

In summary for the barium rich side there are not very many studies, and

the second phase formed is reported by Rase and Roy to be Ba_2TiO_4. In the present study on the barium rich side, a second phase is observed when the A/B ratio is 1.005. See figure 5.7 (a) which is the micrograph of a chemically etched sample with an A/B ratio of 1.005. In this sample an extensive amount of the grain boundary area is etched away. The micrograph also shows the possibility of a second phase at some triple points. For an A/B ratio of 1.002 the grain boundary area is not etched away (see Figure 5.7 b). Whereas for an X-ray diffraction pattern of a sample with the extreme A/B ratio of 1.01, there is an extra line at a 'd' spacing of $3.124°$ A, which is very close to the highest intensity line (3.079) of the Ba_2TiO_4 phase published by Rase and Roy. Our study shows that the solubility of BaO is negligible in $BaTiO_3$ and the second phase formed is Ba_2TiO_4. Also, excess barium acts as a grain refiner.

On the titanium rich side, a second phase is observed at triple points for the A/B ratio of 0.995, which is shown in figure 5.5 (a) and 5.6 (a) and (b). Figure 5.5 (d) shows the photomicrograph of a chemically etched sample with an A/B ratio of 0.992. In fig. 5.5 (a) and 5.6 (a) a second phase is quite clear at the triple point. Thus from these pictures it can be concluded that on the titanium rich side, a second phase occurs at the A/B ratio of 0.995. This result is in agreement with the findings of Sharma et.al. (141). The extreme titanium rich composition investigated in this study was with an A/B ratio of 0.985, whose photomicrograph is shown in figure 5.6 (c) and (d). This sample was sintered at $1275°$ C, for 6 hrs. Figure 5.7 (c) and (d) shows the same composition but sintered at $1350°$ C, for 4 hrs. The sample sintered at $1275°$ C does show a second phase, with various grain sizes, but no melted phase was observed. Whereas the sample sintered at $1350°$ C shows a uniform grain size which is finer than that of the $1275°$ C sintered sample. A careful look shows the grains which might have been grown
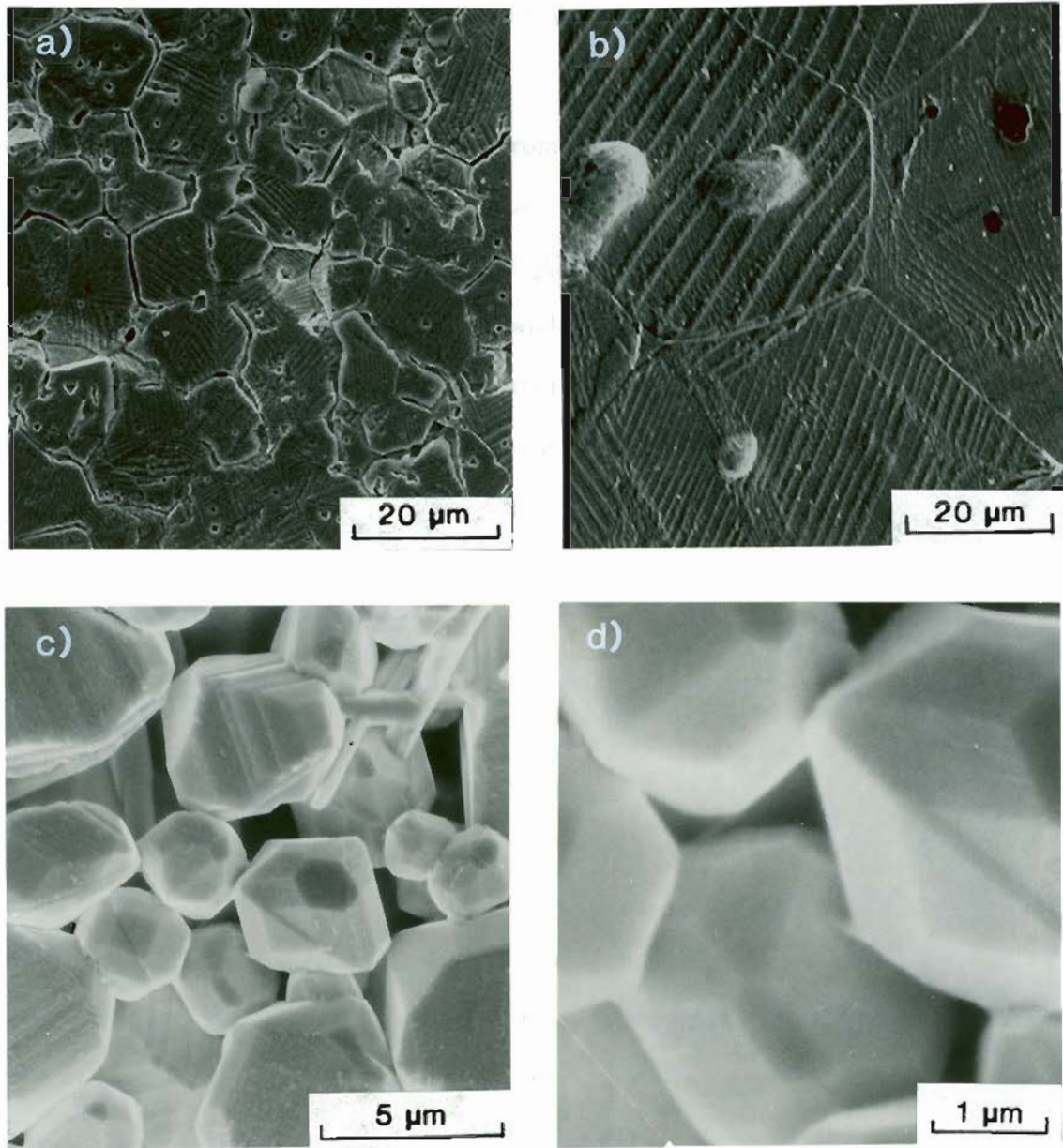
Figure 5.7   PHOTOMICROGRAPH OF 1330^0 C SINTERED $BaTiO_3$ WITH THE RATIO
OF 0.985, 1.005 AND 1.002. a) Ratio = 1.005, chemically etched
b) 1.002, chemically etched c) 0.985, thermally etched d) 0.985, thermally etched

from the melt, as it has got facets. Faceted grains can also be obtained due to the vapor phase effects. This sample was thermally etched providing a possibility for surface grains to grow freely from the melt or have vapor phase effect. To determine the second phase, an X-ray diffraction pattern was taken from the sintered pellet, after grinding.

Raman spectra were also taken from this pellet but neither the X-ray nor the Raman yielded any information about the second phase. Rase and Roy (135) have shown the second phase to be $BaTi_2O_5$. Subsequently Jonker and Kewstroo (137) proved this phase to be unstable and proposed formation of $BaTi_3O_7$ which was supported by Graham (138), but others (139, 141) found the second phase to be $Ba_6Ti_{17}O_{40}$. The present study substantiates the finding of the solubility limit of TiO_2 in $BaTiO_3$ by Sharma et.al. (141) but the X-ray and Raman data do not indicate the composition of the second phase. This may be due to the small amount of the second phase.

5.1.3 Solubility of Nickel in Barium Titanate

As in the case of undoped barium titanate, three different methods were used to determine the solubility of nickel in barium titanate. These are micrography, X-ray diffraction and Raman spectroscopy. Microscopy will be able to detect a small amount of second phase, whereas X-ray technique will probably require considerably more than 1% of the second phase. Thermal and chemical etching methods were tried but both had limited success, because the contrast between two phases is very poor.

In the present study powders were made by firing at 750^0 C. In the diffraction pattern of the as made powders no extra lines were observed until 15 at.% nickel doping. The powders were sintered at 1275^0 C. for 6 hrs and then

ground again to record the diffraction pattern. Figure 5.8 (a), (b), (c) and (d) shows the intensity versus 2θ patterns of 1, 3, 5 and 10 at.% nickel doped samples. Comparison of Figure 5.2 (a) with 5.8 (a), shows no change in the X-ray diffraction pattern, no extra lines are visible. The relative intensities of the various peaks also remain the same. Thus the 1 at.% nickel doped sample is tetragonal with the lattice parameters a = 3.9928 and c = 4.024 A, (c/a = 1.008). This is a decrease in lattice parameter from that of the undoped barium titanate with an A/B ratio of 1.0000, which has lattice parameters of a = 3.9989 A and c = 4.045 A (c/a = 1.0115). This decrease in lattice parameter was expected, since nickel has a smaller ionic radius than that of titanium. The fact that the c/a has decreased also suggests that nickel is going on the titanium site in the barium titanate lattice. It is the shift of titanium atom from the 1/2, 1/2, 1/2 position to 1/2, 1/2, 0.512 that gives the tetragonality to the otherwise cubic structure. Considering the ionic radius of nickel, which is 0.62, titanium which is 0.68, and barium 1.32, it is expected that nickel will replace titanium. Thus, when nickel with a smaller ionic radius than that of titanium replaces titanium, the lattice parameter and tetragonal distortion of the structure should decrease. This was indeed observed in the present case, thus indicating that the nickel is going on the titanium site in the lattice.

When comparing Figures 5.8 (b) and (a), we see that there are substantial (30) additional lines in 5.8 (b). The X-ray diffraction pattern for the 3 at.% nickel doped sintered sample is indexed as a two phase mixture. The additional phase present in large quantity is hexagonal barium titanate. The pattern for the hexagonal phase matched perfectly with the hexagonal pattern provided by Roth (142), in terms of peak positions and relative intensity. However it did not match with the hexagonal pattern as given by JCPD card # 8-372, though both
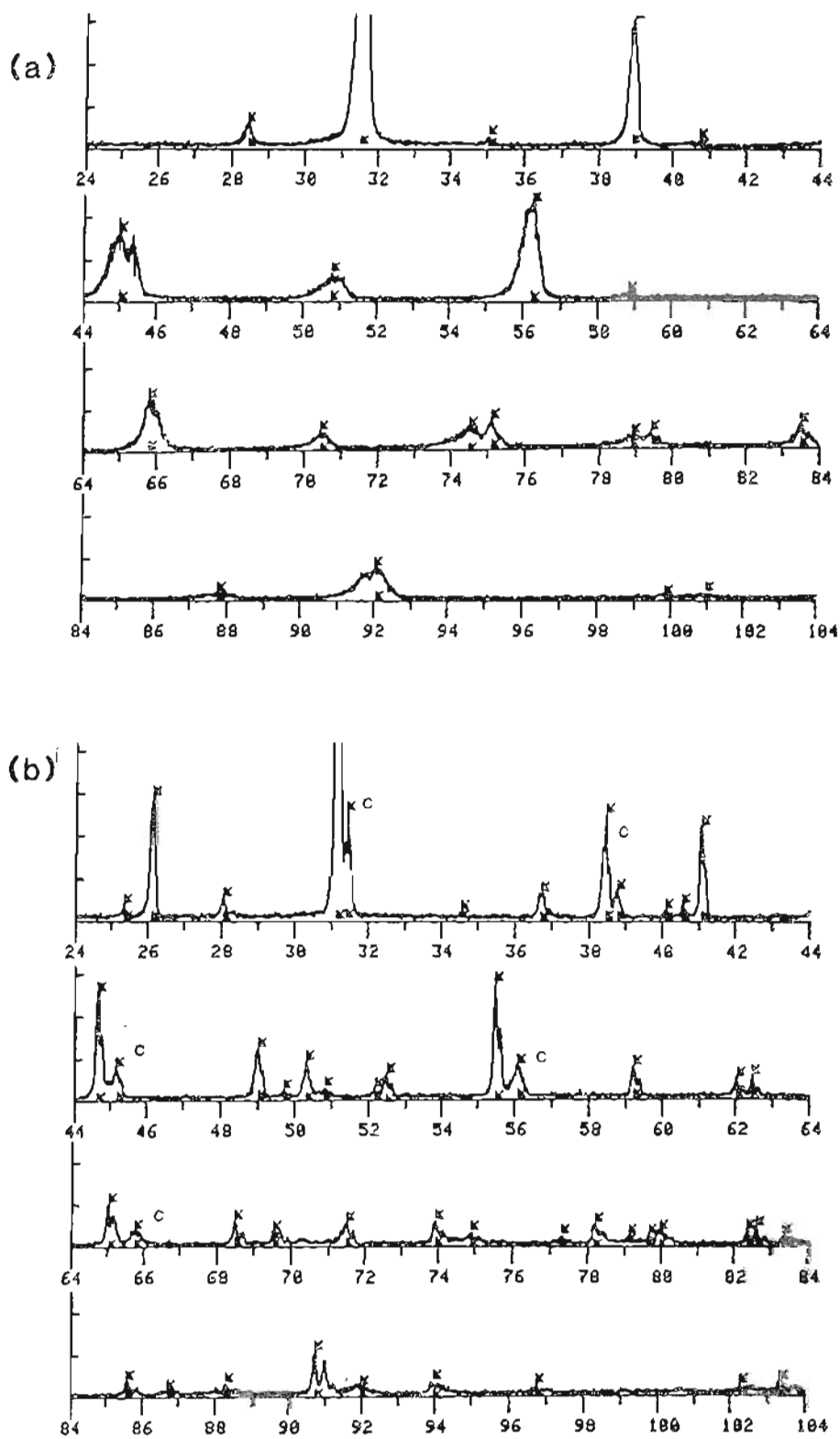
Figure 5.8   DIFFRACTION PATTERNS (INTENSITY VS 2θ) OF $BaNi_xTi_{1-x}O_3$
AS A FUNCTION OF NICKEL CONCENTRATION
a) 1 At.% Nickel
b) 3 At.% Nickel
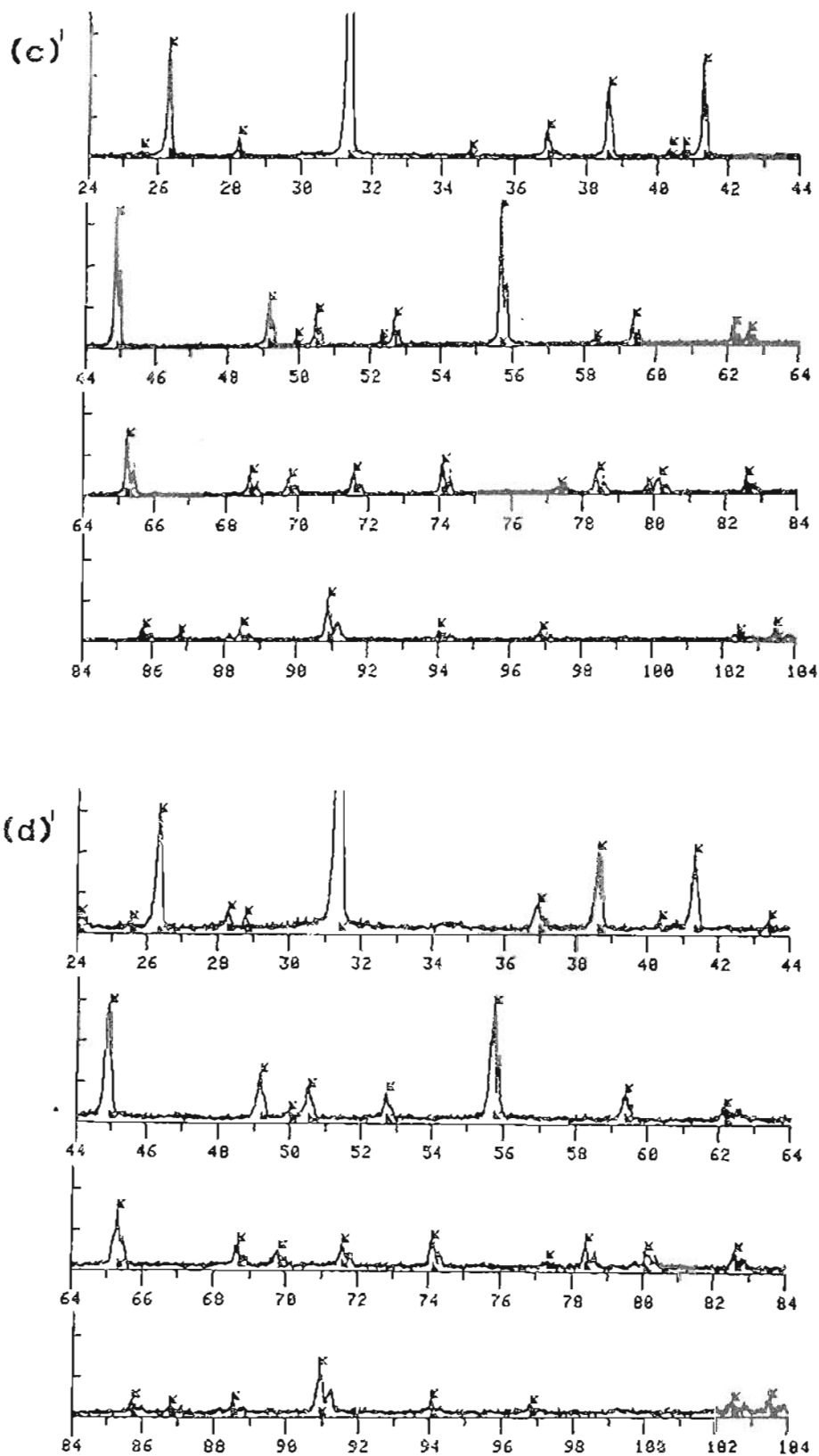
Figure 5.8   DIFFRACTION PATTERNS (INTENSITY VS 2θ) OF $BaNi_xTi_{1-x}O_3$
(cont.)   AS A FUNCTION OF NICKEL CONCENTRATION
c) 5 At.% Nickel
d) 10 At.% Nickel

patterns were similar. There are seven peaks present due to the original tetrago-nal phase, and these peaks could be indexed in terms of a cubic phase, with the lattice parameter a = 4.020 A. In figure 5.8 (b) peaks due to the cubic phase are marked with C. When comparing powder patterns of sintered samples of 5 at.% and 3 at.% nickel, the peaks due to the cubic phase have totally disappeared in figure 5.8 (c), which indicates a single phase with hexagonal structure. Similarly, the pattern for 10 at.% nickel doping is also a single phase with hexagonal struc-ture. Figure 5.9 shows the variation in the lattice parameter with nickel doping for the tetragonal phase. As the nickel increases both c and a decrease, as does c/a. At approximately 1.5 at.% the structure becomes cubic and the hexagonal second phase starts forming. In the hexagonal form the lattice parameter also decreases as the concentration of nickel increases. See Figure 5.10.

Photomicrographs for 0.5, 0.8, 1.0, 3, 5 and 10 at.% nickel doped sintered $(1275^0$ C, 6 hrs.) samples are shown in Figure 5.11 (a), (b), (c), (d), (e) and (f) respectively. It is clear from these photomicrographs that the phase contrast is very poor and two distinct phases can not be identified. Figure 5.11 (d) should definitely show a two phase mixture, as evident from the X-ray diffraction results but the photomicrograph does not reveal it. Only in the 5 and 10 at.% doped samples are bright circular areas are seen.

When the 1 at.% nickel doped sample was heated to 1350^0 C for 4 hrs, a peculiar microstructure developed which is shown in figure 5.11 (g). Criss - cross bands were seen on the surface. Figure 5.11 (h) shows one such band at higher magnification. It appears the bands were formed from a molten material.

Raman spectra for powders without any subsequent sintering were recorded. Figures 5.12 (a), (b) and (c) show the Raman spectra for 1, 3 and 5 at.% doped samples with an A/B ratio of 1.0000. For the 1 at.% nickel doped sample the
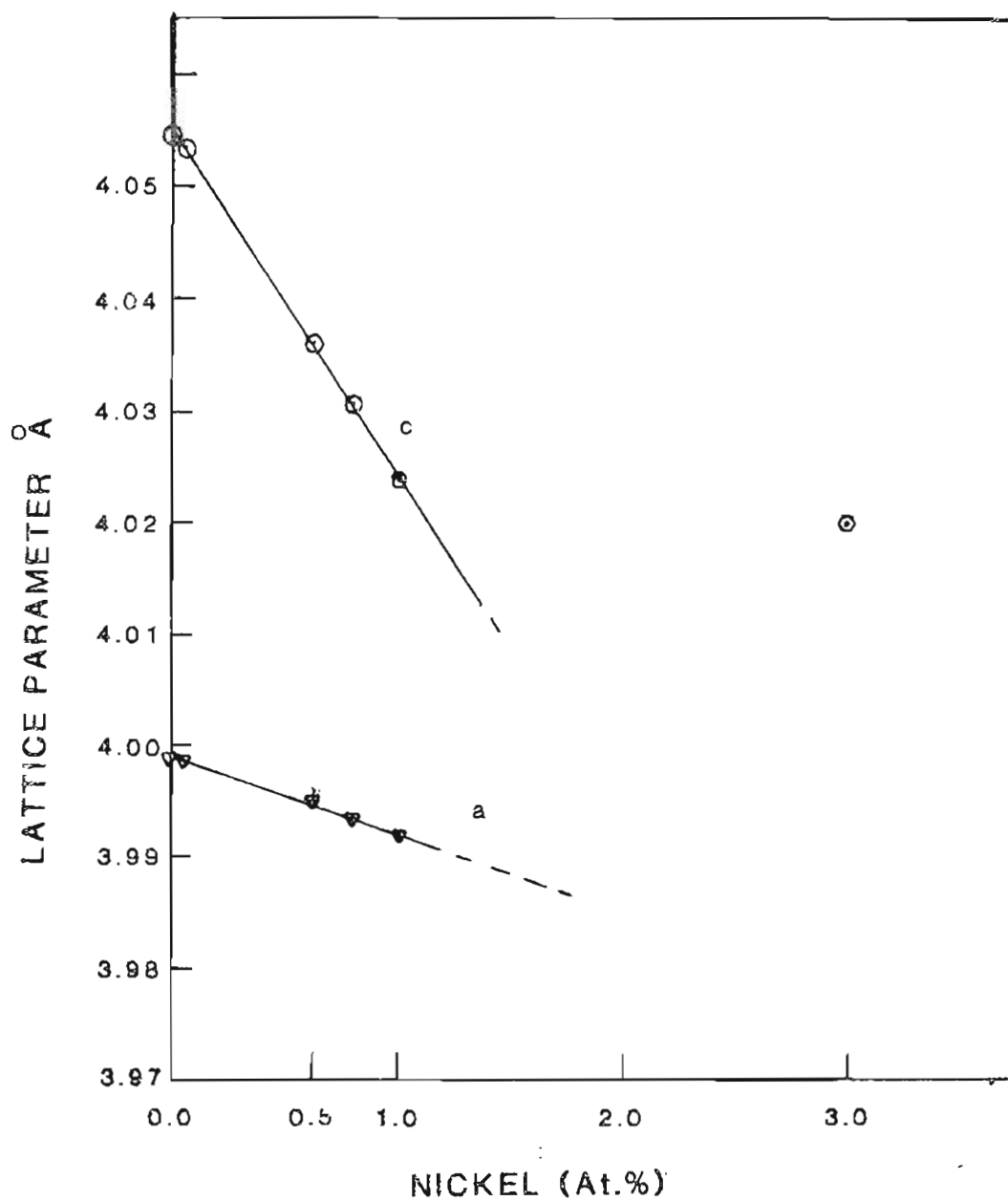
Figure 5.9 VARIATION OF LATTICE PARAMETER WITH NICKEL DOPING IN
THE TETRAGONAL PHASE
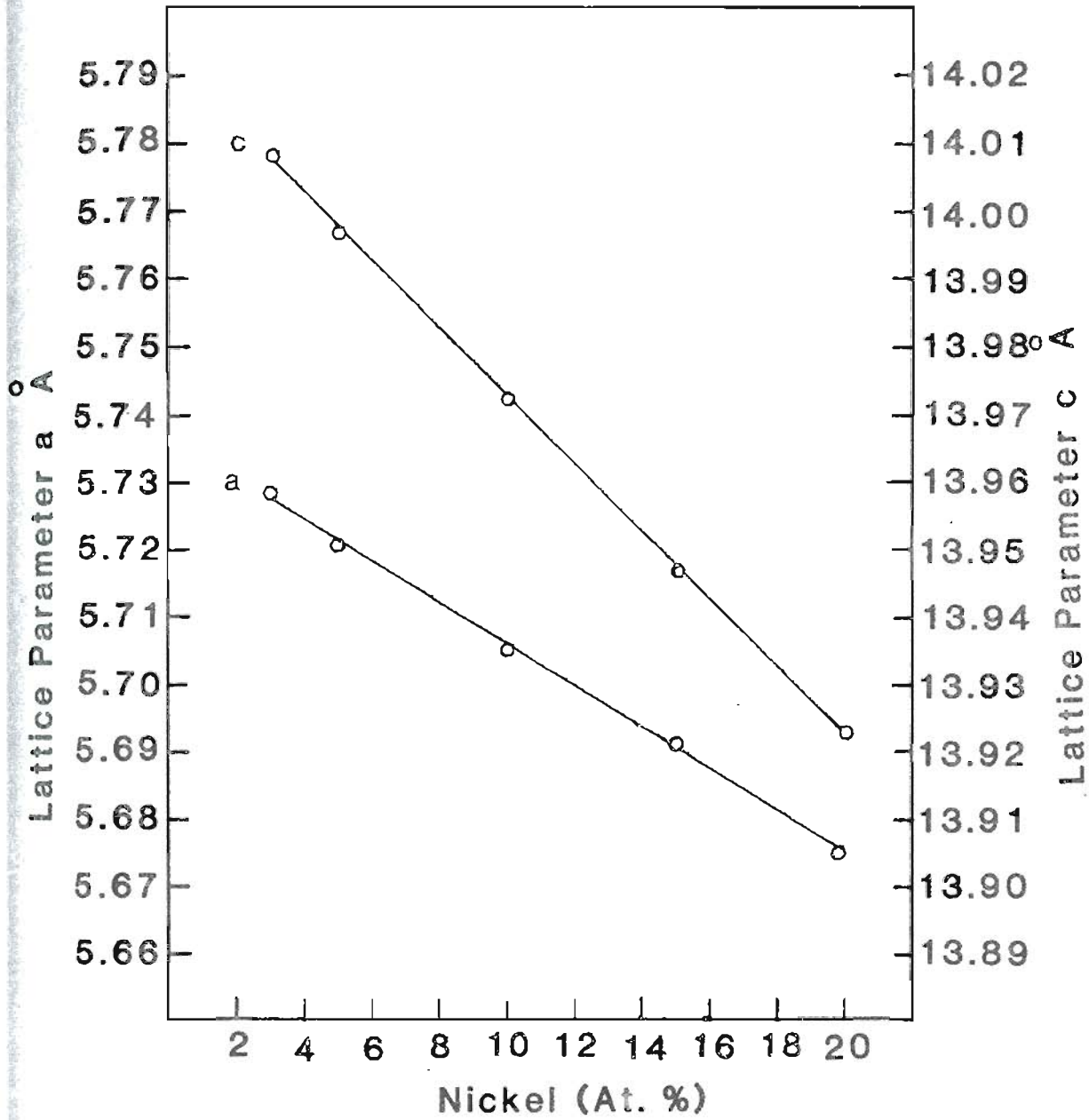
Figure 5.10 VARIATION OF LATTICE PARAMETER WITH NICKEL DOPING IN
THE HEXAGONAL PHASE
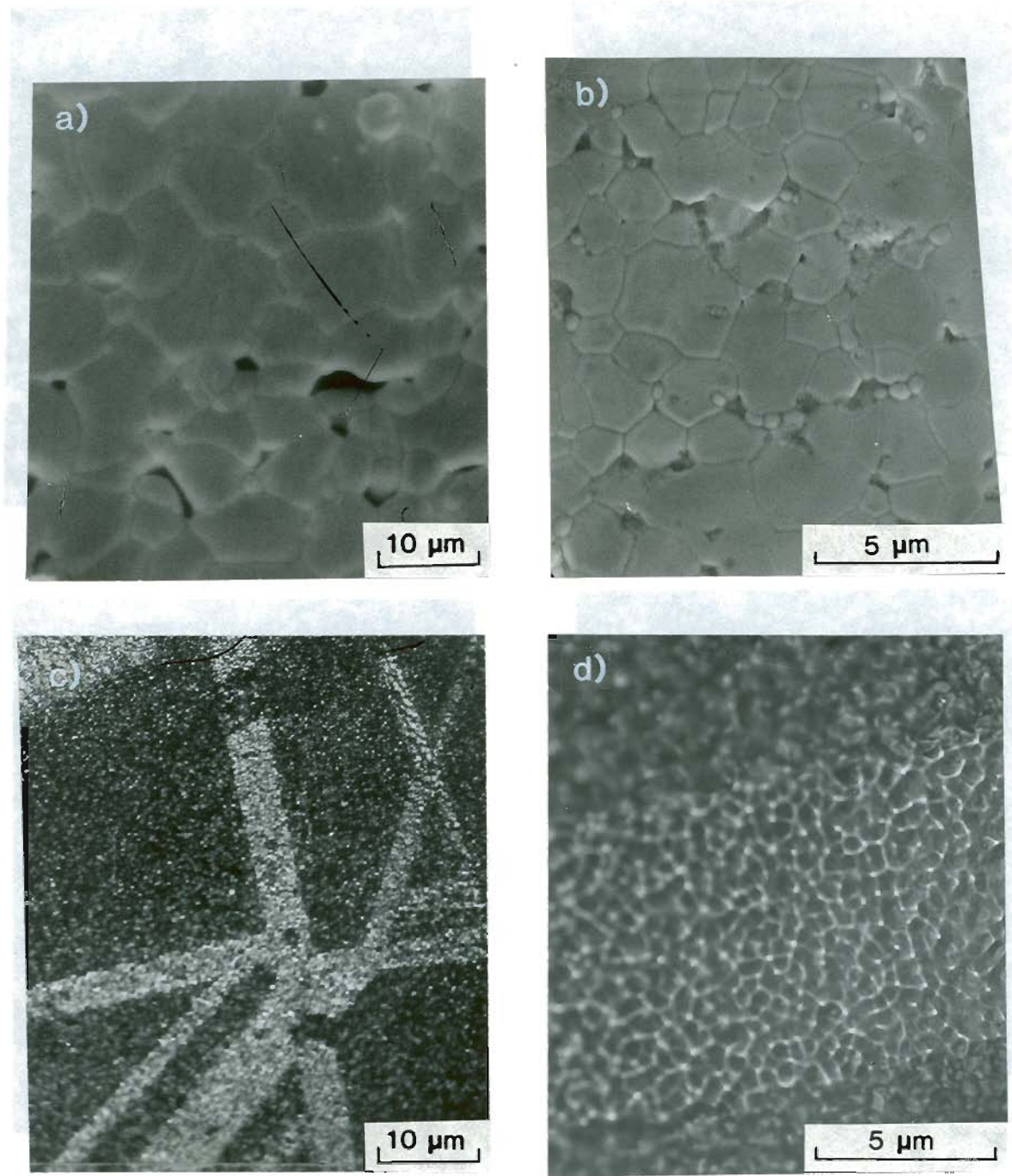
Figure 5.11   PHOTOMICROGRAPH OF NICKEL DOPED BaTiO$_3$, THERMALLY ETCHED.
a) 0.005 at.% Ni b) 0.008 at.% c) 0.01 d) 0.03
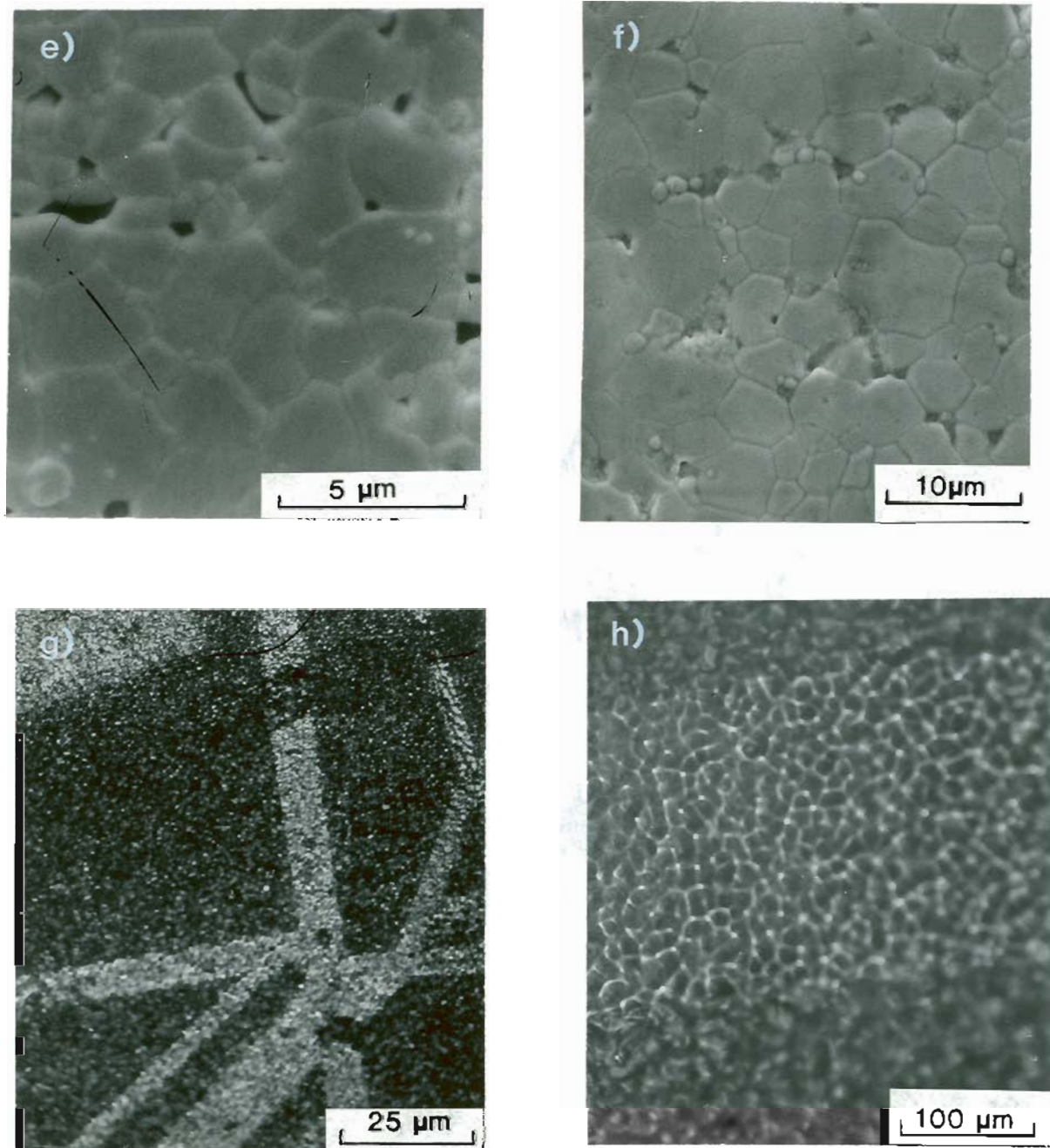
Figure 5.11   PHOTOMICROGRAPH OF NICKEL DOPED BaTiO$_3$, THERMALLY ETCHED.
(cont.)   e) 0.05 at.% Ni f) 0.1 at.% g) 0.01 at.% Sin. at 1350^0 C
         h) same as g but higher manification
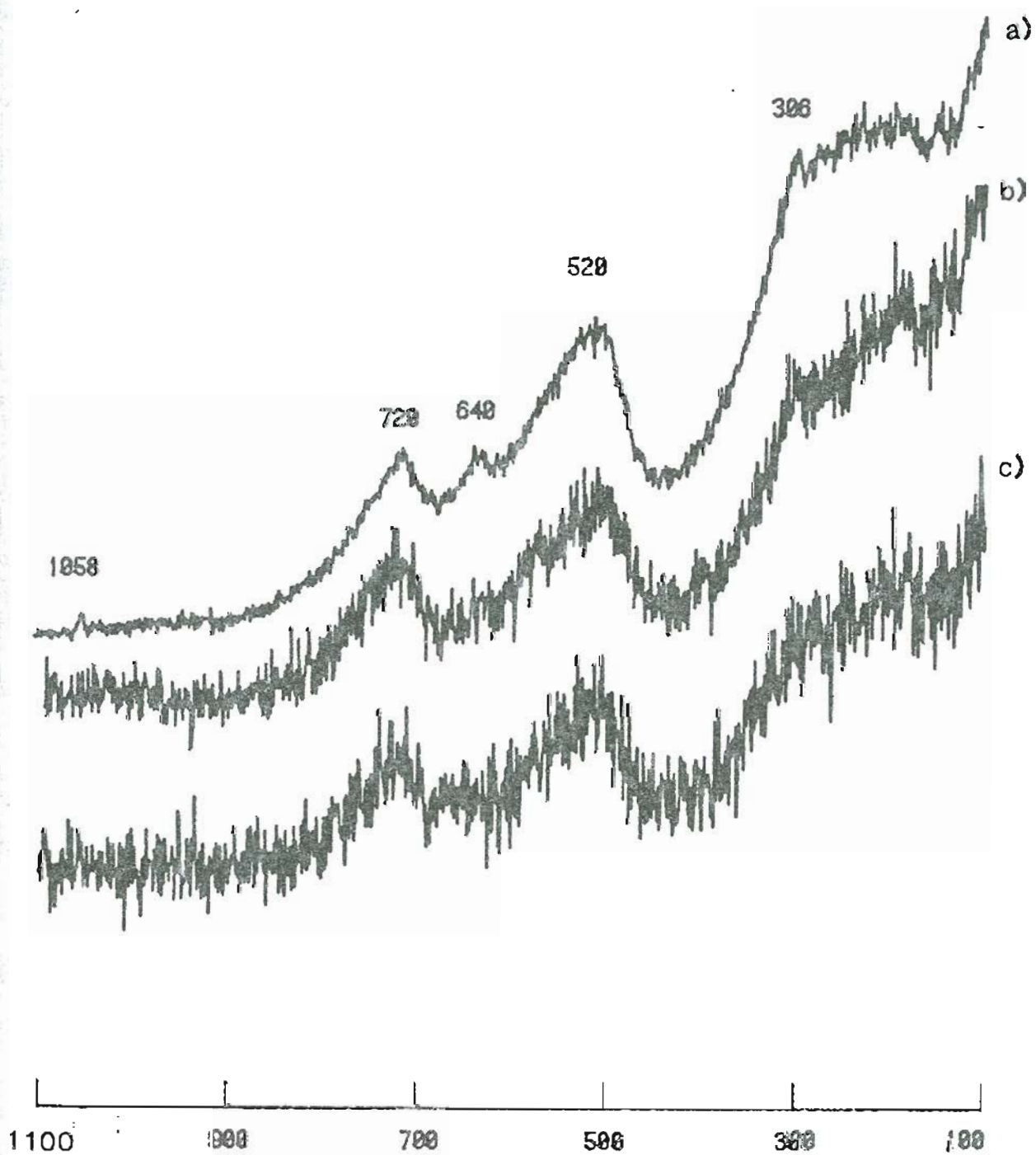
Figure 5.12   RAMAN SPECTRA OF Ni DOPED BaTiO$_3$ (AS MADE POWDERS)
a) 1 At.% Nickel, b) 3 At.% Nickel, c) 5 At.% Nickel

spectrum is that of the normal tetragonal structure, (Raman spectra will be covered in detail in the next section) with the most intense peak at 520 cm^{-1} and other peaks at 720, 640, 309 cm^{-1} etc. The spectrum for the 3 at.% nickel doped sample is not as intense but it shows all the features of the 1 at.% nickel doped sample plus an extra peak at 575 cm^{-1}. The spectrum for the 5 at.% nickel doped sample is the same as that of the 3 at.% nickel doped sample but it is not resolved as well.

Raman spectra for the sintered pellets with 1, 3, and 5 at.% nickel doping are shown in Figures 5.13 (a), (b) and (c) respectively. The 1 at.% nickel doped sample spectrum is the same as that of the respective powder spectrum, indicating a single phase tetragonal barium titanate. The spectrum for the 3 at.% nickel doped sample is different from that of the 1 at.% nickel doped sample. A strong extra band is observed at 585 cm^{-1}, a weak band at 632 cm^{-1}, and the 515 band is changed to 529 cm^{-1}, with an overall noisier spectrum. The spectrum for the 5 at.% nickel doped sample is similar to the 3 at.% doped sample spectrum, but it is more sharp. The most intense bands are at 585 and 527 cm^{-1}. This indicates the same phase is present in the 3 and 5 at.% nickel doped samples, and this phase is different from that of the 1 at.% nickel doped sample. From the X-ray studies the phase in the 3 and 5 at.% nickel doped samples is shown to be a hexagonal barium titanate.

Figure 5.14 (a) shows the Raman spectrum of the 1 at.% nickel doped sample whose microstructure is shown in figure 5.11 (g). The spectrum from the matrix region is typical of a tetragonal barium titanate, with a small extra peak at 635 cm^{-1}. The spectra from striped region is shown in Figure 5.14 (b), and which is quite different from the spectrum of tetragonal barium titanate. This spectrum has strong bands at 635, 221,154 in addition to weak bands at 520 and
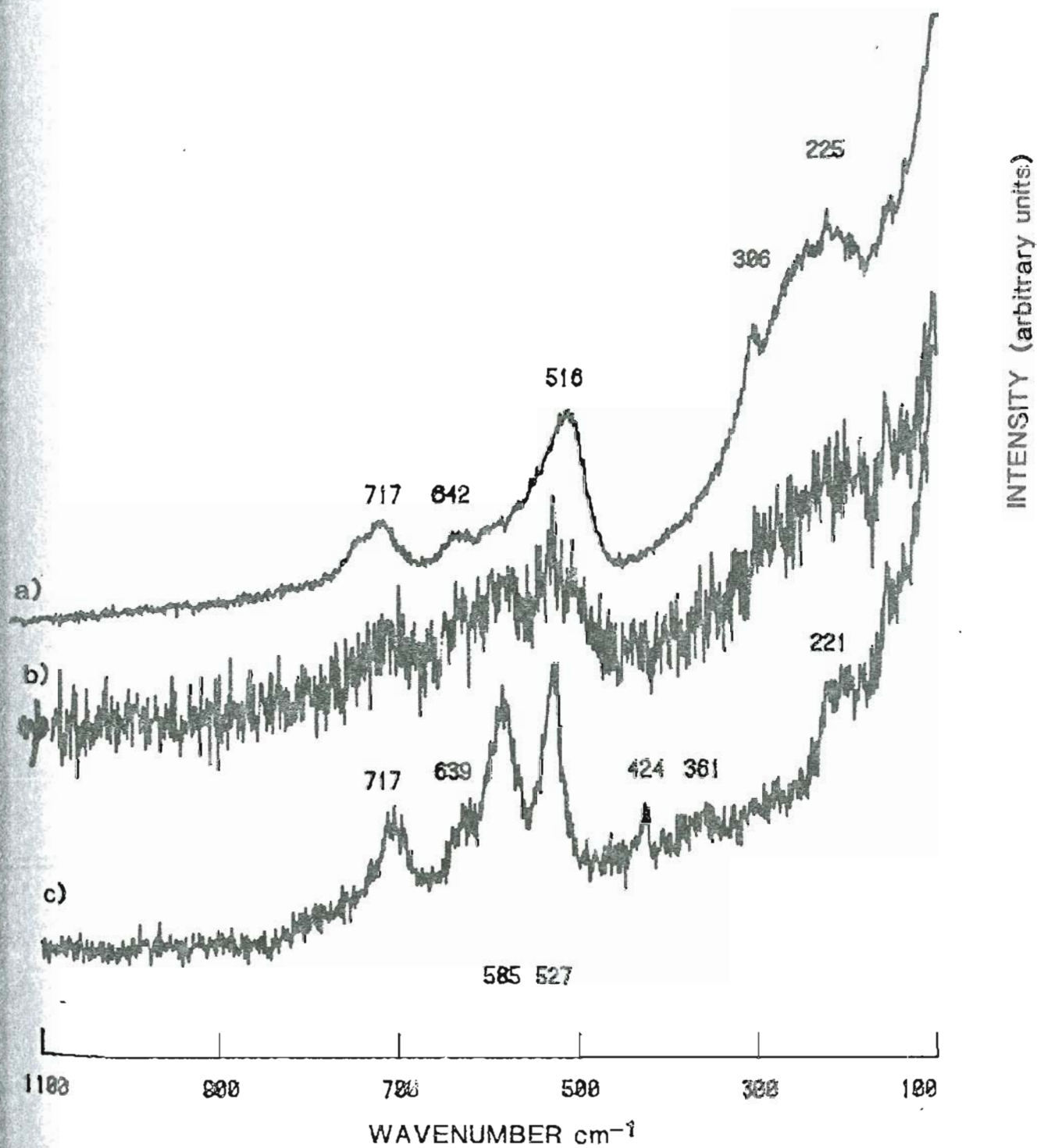
Figure 5.13   RAMAN SPECTRA OF Ni DOPED $BaTiO_3$ (PELLETS SIN 1275^0 C, 6 Hrs.)
a) 1 At.% Nickel, b) 3 At.% Nickel, c) 5 At.% Nickel
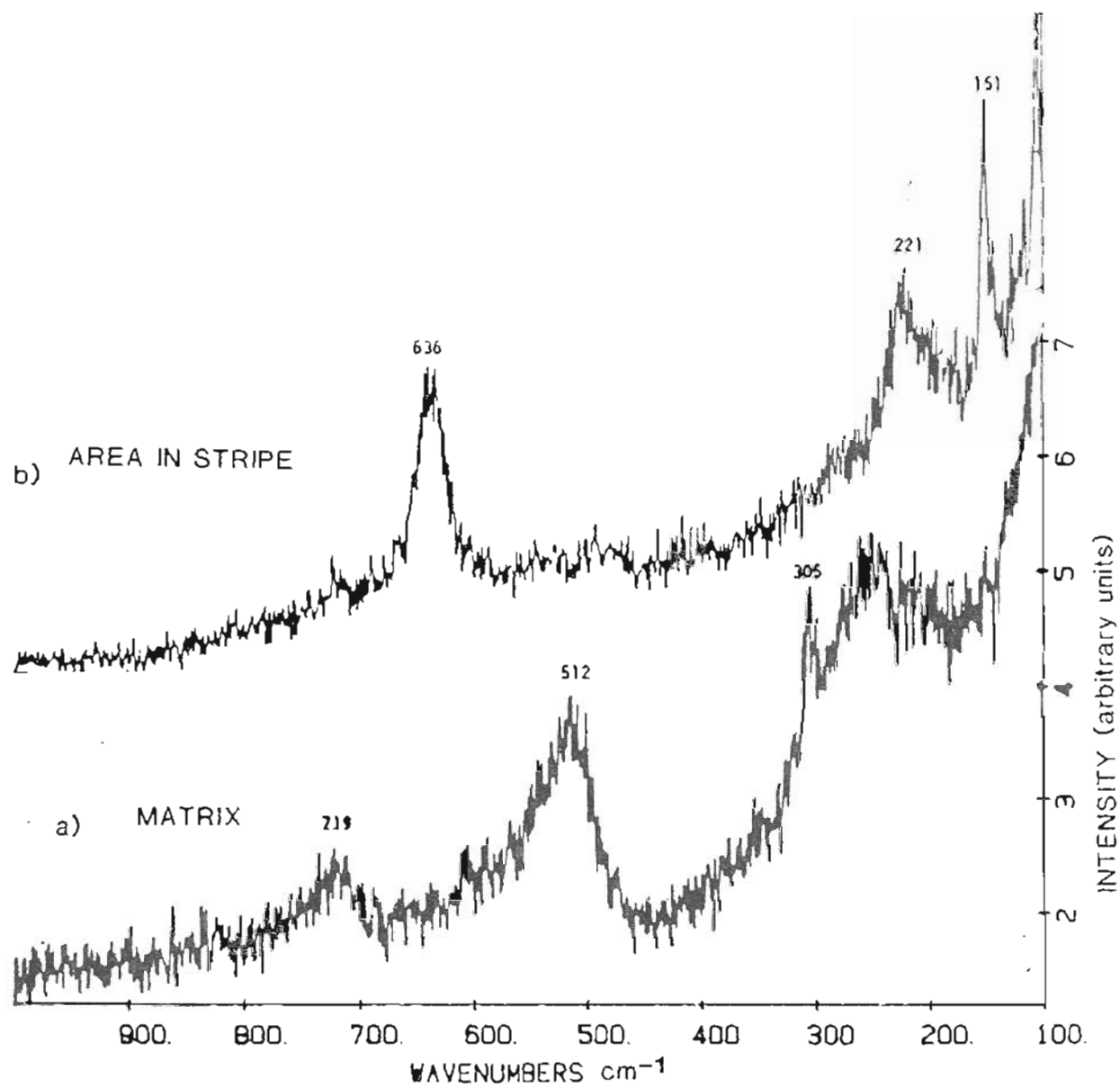
Figure 5.14 RAMAN SPECTRA OF $BaNi_1Ti_{99}O_3$ (IN TWO DIFFERENT REGIONS)
a) MATRIX REGION b) AREA IN STRIPE

715 cm^{-1}, which is indicative of the hexagonal phase.

The following conclusions can be drawn 1) The solubility of nickel appears to be around 2 at.% at 1275^0 C. 2) The solubility of nickel is a function of temperature - at higher temperature the solubility is lower. 3) At 1330^0 C the solubility is lower than 1 at.%. 4) Nickel stabilizes the hexagonal phase at lower temperatures than the 1468^0 C, reported for undoped barium titanate. 5) The second phase formed after the solubility limit reached is hexagonal barium titanate. 6) Nickel occupies the titanium site in the lattice.

5.2 Raman Spectroscopy of BaTiO$_3$ and Nickel Doped BaTiO$_3$.

5.2.1 Raman Spectra Of Stoichiometric BaTiO$_3$.

Interpretation and assignment of bands form the key to understanding the structure and the various bonds present in a vibrational spectra. With the appropriate selection rules, the number of Raman active, IR active and coincidences can be identified. As long as the structure of a compound remains the same the number of Raman active modes remains the same. Factor group analysis does not make a statement about the position (wave number or energy) and intensity of the bands, however.

Barium titanate has five different polymorphs. Table 5.1 shows the structure of the various polymorphs, the temperature range of their stability, their space group and site symmetries. Figure 5.15 shows the ideal cubic perovskite structure. Figure 5.16 shows the various distortions of a cubic structure to get the various other structures. In the ideal cubic perovskite structure, the smaller tetravalent cation is at the center of the cube, the large divalent cation is at the corners, of the cube and the divalent anions, usually oxygen are at the center of each face of cube.

TABLE 5.1

VARIOUS POLYMORPHS THEIR STRUCTURE, SPACE GROUP AND SITE SYMMETRIES OF $BaTiO_3$

Temperature Range ^0C	Structure of $BaTiO_3$	Space Group	Molecules per Unit Cell	# of Lattice Points per Unite Cell	Site Symmetries
-80 and bellow	Rhombohedral	$R_{3m} - C_{3v}^4$	1	1	$C_{3v}(1)$, $C_S(3)$, $C_1(6)$
-80 - 5	Orthorhombic	$A_{mm2} - C_{2v}^{14}$	2	2	$2\ C_{2v}(1)$, $3\ C_S(2)$, $C_1(4)$
5 - 130	Tetragonal	$P_{4mm} - C_{4v}^1$	1	1	$2\ C_{4v}(1)$, $C_{2v}(2)$, $3\ C_S(4)$, $C_1(8)$
130 - 1470	Cubic	$P_{m3m} - O_h^1$	1	1	$2\ O_h(1)$, $2\ D_{4h}(3)$, $2\ C_{4v}(6)$, $C_{3v}(8)$, $3\ C_{2v}(12)$, $3\ C_S(24)$
1470 - 1618	Hexagonal	$C_{63/mmc} - D_{6h}^4$	1	1	$D_{3d}(2)$, $3\ D_{3h}(2)$, $2\ C_{3v}(4)$, $C_{2h}(6)$, $C_{2v}(6)$, $C_2(12)$, $2\ C_s(12)$, $C_1(24)$
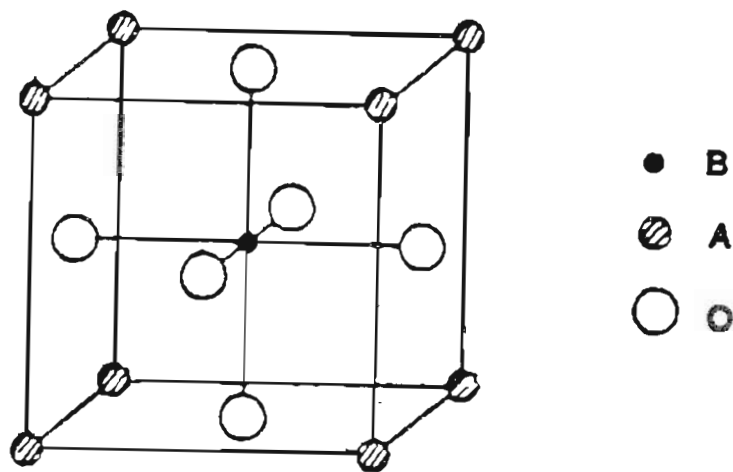
Figure 5.15   STRUCTURE OF CUBIC PEROVSKITE

A²⁺   B⁴⁺

CUBIC PEROVSKITE ABO_3

TETRAGONAL   ORHTORHOMBIC   RHOMBOHEDRAL
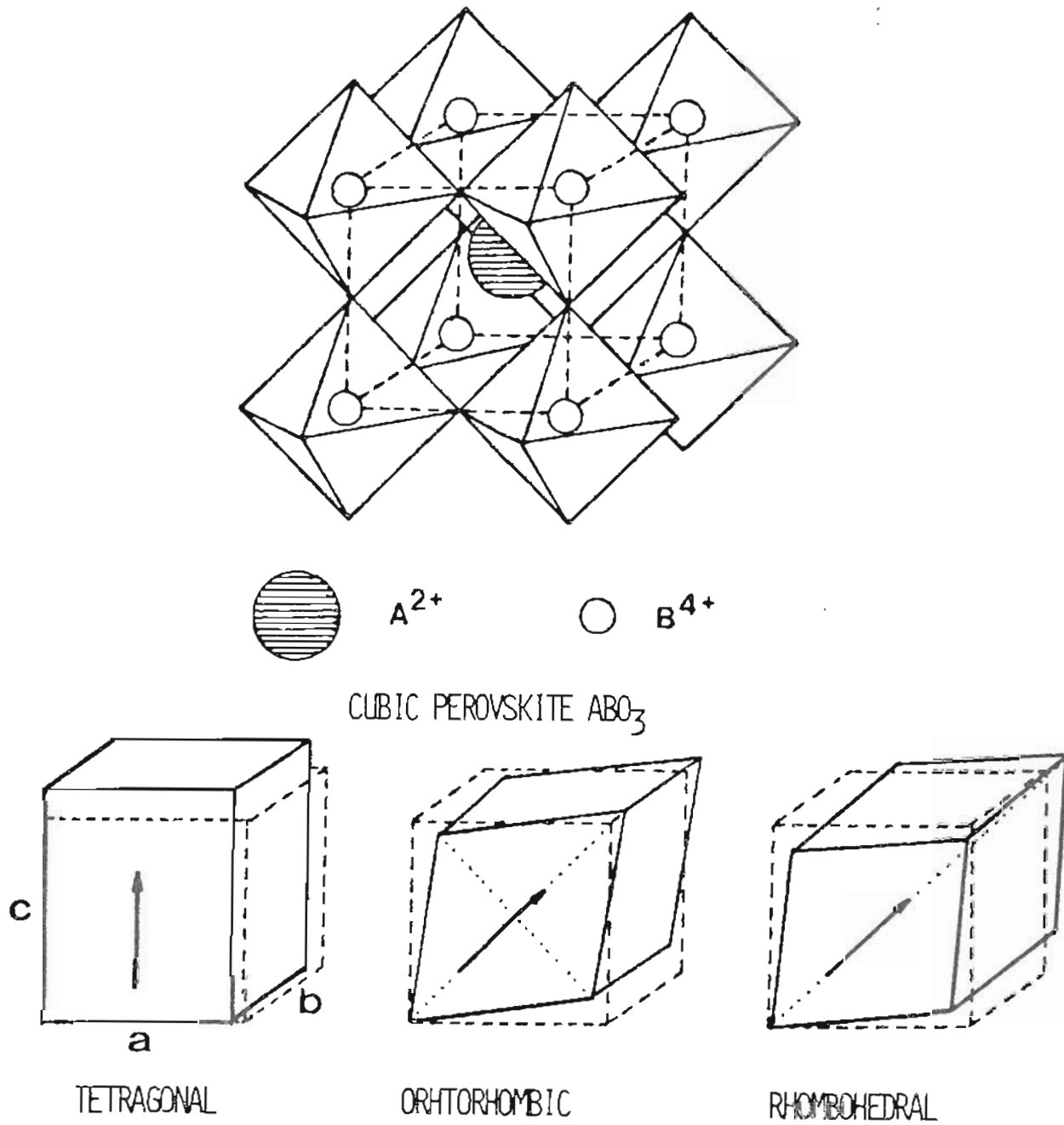
Figure 5.16   VARIOUS DISTORTIONS OF CUBIC PEROVSKITE STRUCTURE OF $BaTiO_3$

Basically two methods are available to do the factor group analysis. The first method developed by Bhagavantam and Venkatarayudu (143) is very laborious and with many points of uncertainity. Indecisiveness involved here is in the choice of primitive cell and the site symmetry of each atom. The other method is by Fateley et al. (144) which is a very simple, straightforward and fool proof correlation method. Factor group analyses for all phases of barium titanate were carried out by the correlation method, the results are shown in Table 5.2 and 5.3. Table 5.2 shows the total number of vibrational modes for a given structure of barium titanate for IR, Raman active modes and their coincidences. Table 5.3 shows the correlation between various Raman active modes in different structures.

The Raman spectra of undoped barium titanate for both the as made powder, and of the pellet made from the same material and sintered at 1275^0 C for 6 hrs. are shown in Figure 5.17. Figures 5.18 and 5.19 show the Raman spectra of barium carbonate and hexagonal barium titanate respectively. All the spectra were recorded under the same conditions.

From Figure 5.17 it is clear that in the powder samples extra peaks are observed at 1059 and 640 cm^{-1}, and spectrum in the region of 50 to 250 cm^{-1} is slightly different than that of the sintered sample. Whereas in the spectrum of a sintered sample, a shoulder is observed at 459 cm^{-1}. A strong band is observed at 1059 cm^{-1} in the spectrum of barium carbonate, and a strong band at 640 cm^{-1} in the spectrum of hexagonal barium titanate. Thus, in a mixture of hexagonal and tetragonal barium titanate and barium carbonate, one should see the strong bands due to the individual compounds. If a substance is present in a very small quantity then the first observed band will be the one which is strongest. Thus, here in the case of powder samples, the band at 1059 cm^{-1} is due to

TABLE 5.2

SYMMETRIES OF VIBRATIONAL MODES IN VARIOUS PHASES OF $BaTiO_3$

Structure of $BaTiO_3$	Types of Vibrational Mode	I.R. Active	Raman Active	Coincidences	Remarks
Hexagonal	$5 A_{1g} + 2 A_{2g} + 6 B_{1g} + B_{2g}$ $+ 6 E_{1g} + 8 E_{2g} + A_{1u} + 6 A_{2u}$ $+ 2 B_{1u} + 6 B_{2u} + 7 E_{1u} + 7 E_{2u}$ 57	$6A_{2u} + 7 E_{1u}$ 13	$5 A_{1g} + 6 E_{1g}$ $+ 8 E_{2g}$ 19	nil	-
Cubic	$3 F_{1u} + F_{2u}$ 4	F_{1u} 3	nil	nil	F_{2u} comming from Osub2
Tetragonal	$3 A_1 + B_1 + 4 E$ 8	$3 A_1 + 4 E$ 7	$3 A_1 + B_1 + 4 E$ 8	A_1 and E 7	B_1 comming from O_2
Orthorhombic	$4 A_1 + 4 B_1 + 3 B_2 + A_2$ 12	$4 A_1 + 4 B_1$ $+ 3 B_2$ 11	$4 A_1 + 4 B_1$ $+ 3 B_1 + A_2$ 12	$A_1, B_1,$ B_2 11	A_2 comming from O_2

TABLE 5.3

CORRELATION OF VARIOUS RAMAN ACTIVE SPECIES

Hexagonal D_{6h}^4	Cubic O_h^1	Tetragonal C_{4v}^1	Orthorhombic C_{2v}^{14}	Rhombohedral C_{3v}^4
A_{1g}	F_{1u}	A_1	A_1	A_1
-	-	-	A_2	-
E_{1g}	-	E	-	-
-	-	-	B_1	-
E_{2g}	F_{2u}	B_1	B_2	E
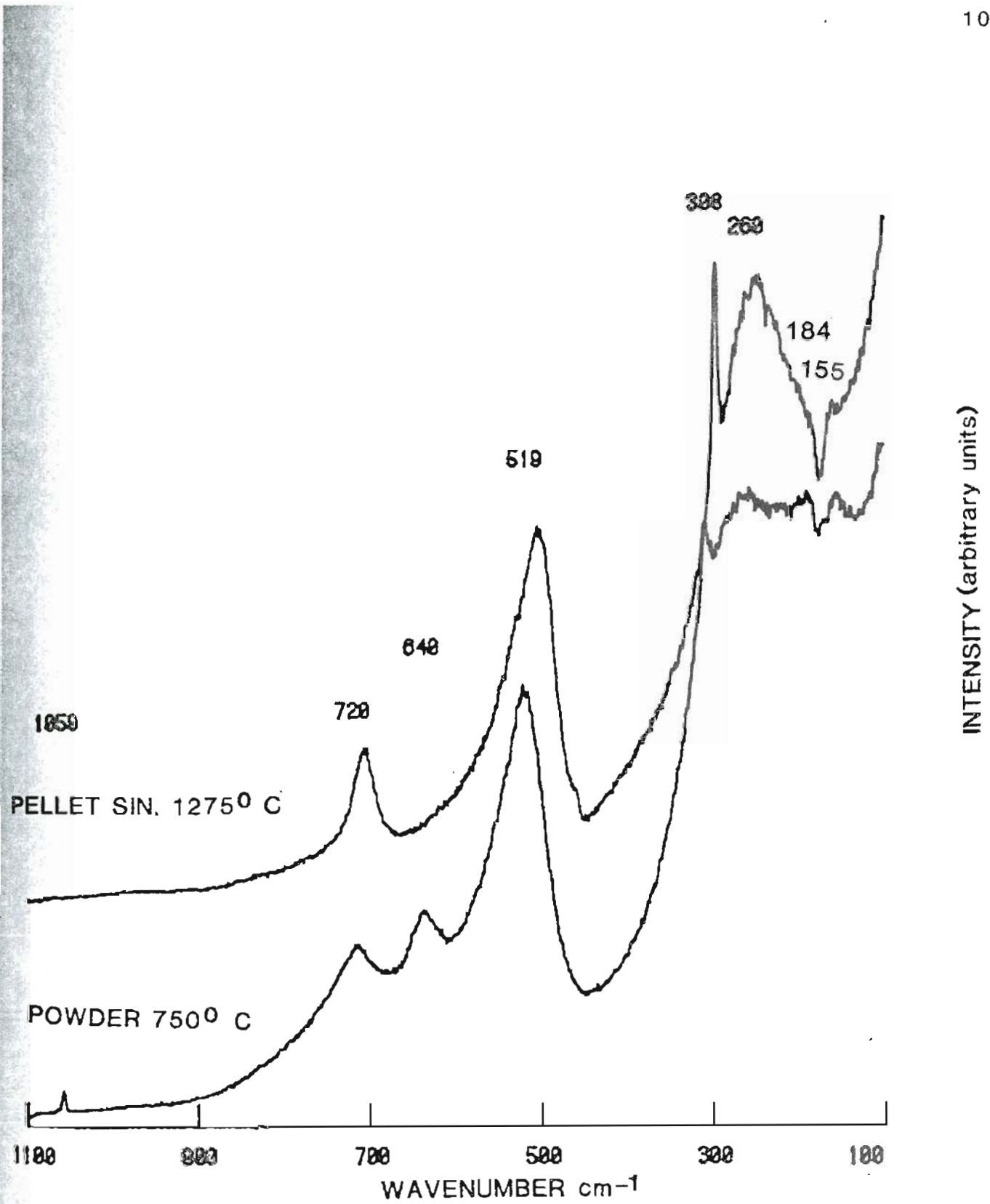
Figure 5.17   RAMAN SPECTRA OF $BaTiO_3$
(AS MADE POWDER AND PELLET SIN. 1275^0 C, 6 Hrs.)
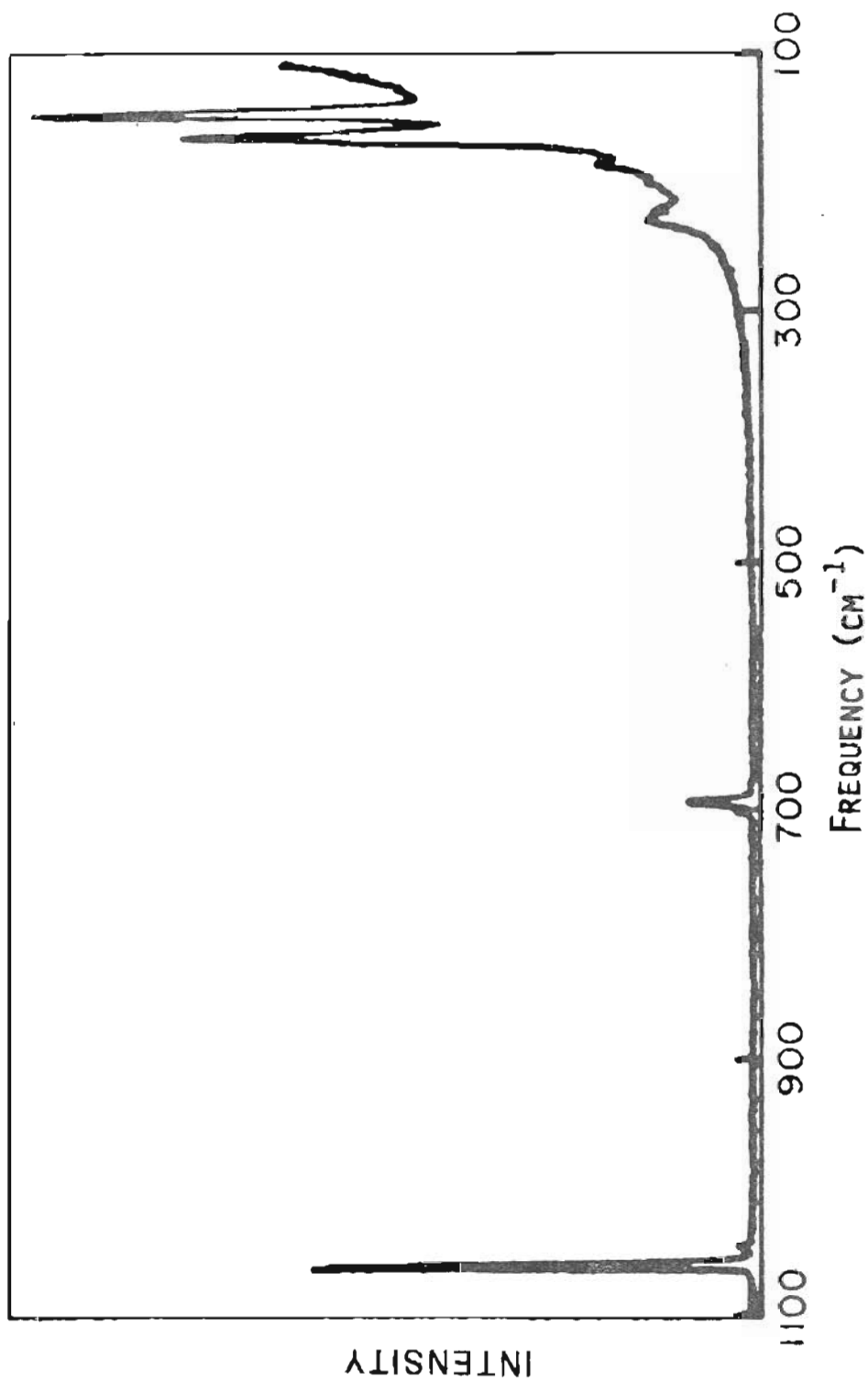
Figure 5.18   RAMAN SPECTRUM OF $BaCO_3$
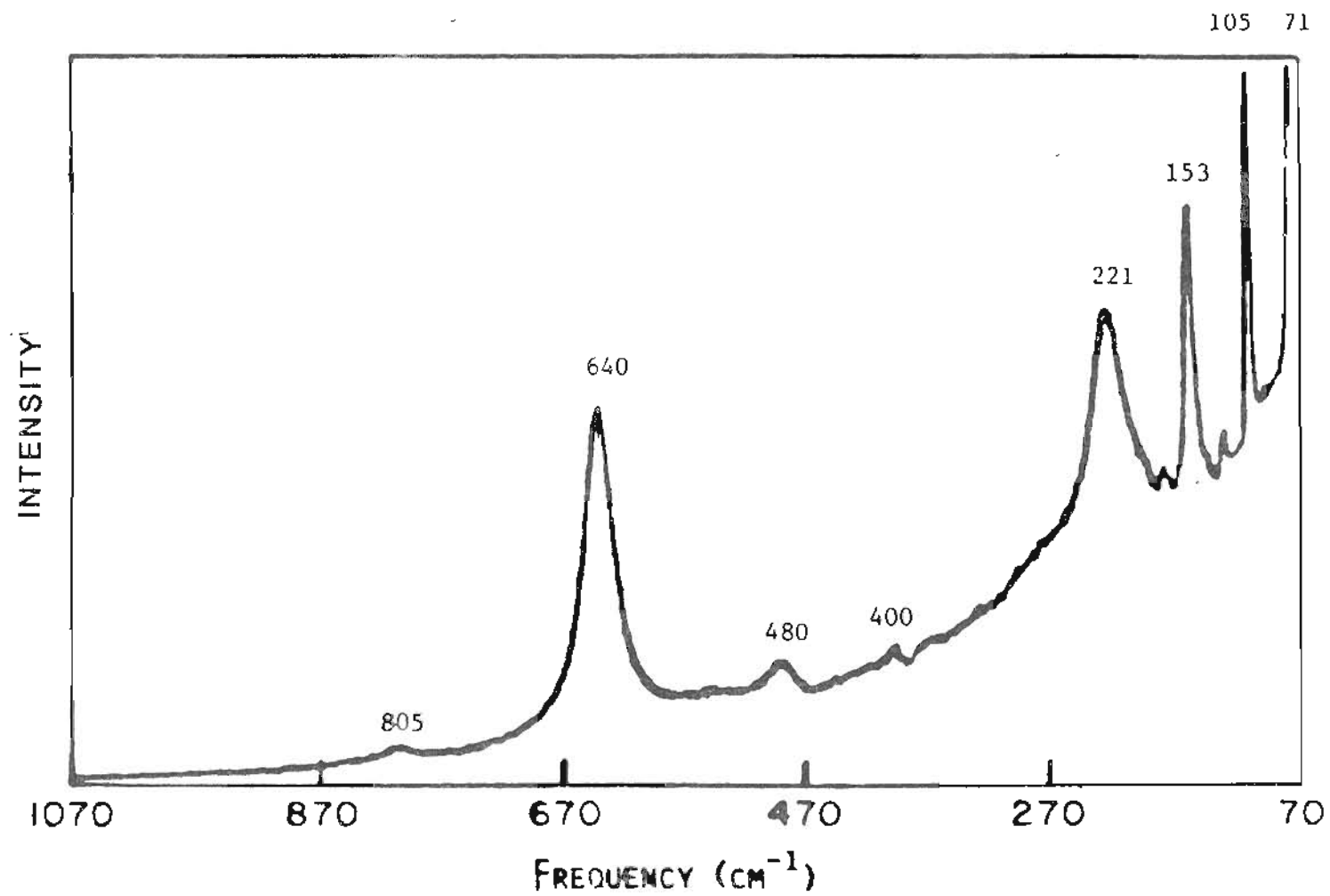
Figure 5.19 RAMAN SPECTRUM OF HEXAGONAL BaTiO₃

the presence of carbonate. This carbonate is not due to the unreacted carbonate from the barium carbonate , but it is the carbonate due to the surface adsorbed CO_2. This will be proved, while treating the spectra of doped samples (Eror et al.(159) have already proved this.). Similarly the band at 640 cm^{-1} is due to the presence of a small amount of hexagonal phase. When the material is sintered at high temperature, surface adsorbed species should be removed and material should achieve equilibrium at the sintering temperature. At 1275^0 C, from the phase diagram, the hexagonal phase is not stable and hence, if equilibrium is achieved the hexagonal phase should transform to the tetragonal phase. The Raman spectra of the sintered pellets demonstrate this. Peaks due to carbonate and hexagonal phase vanish in the spectra of the sintered material. Thus, the assignment of those two peaks is correct, and moreover, when barium titanate is made from the liquid mix technique, it does produce a small amount of hexagonal barium titanate, which has not been detectable by any other method. For example, no extra lines were observed in the X-ray diffraction pattern.

In the sintered samples, the peak at 309 cm^{-1} was stronger than the peak at 267 cm^{-1} whereas in the powder samples exactly the opposite phenomenon was observed. In the sintered sample after the peak at 160 cm^{-1} a trough is observed. It appears that the whole spectrum in the range, 50 - 250 cm^{-1}, is sitting over a broad peak from 0 - 200 cm^{-1}. The trough region can be obtained if one views a broad peak superimposed by two discrete energy levels, and by varying the peak width and intensity the trough size can be varied. Rousseau et al. (99) termed this as Auger like interference.

Figure 5.20 shows the Raman spectra of barium titanate from 85 to 503 K, the range which can be covered by the available instrumentation. The spectra have not changed much and the results agree well with the results of other
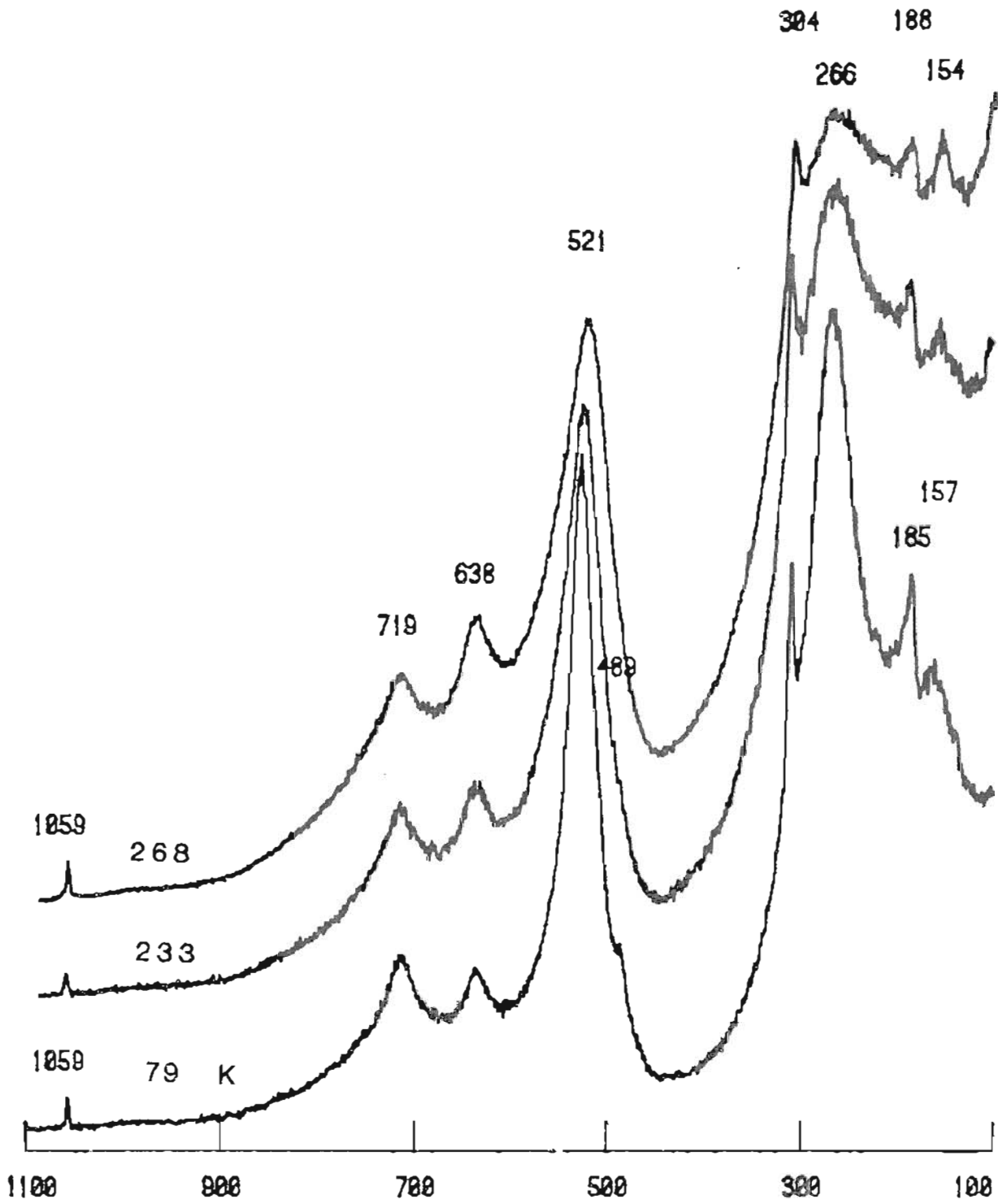
Figure 5.20   RAMAN SPECTRA OF BaTiO$_3$ AS A FUNCTION OF TEMPERATURE
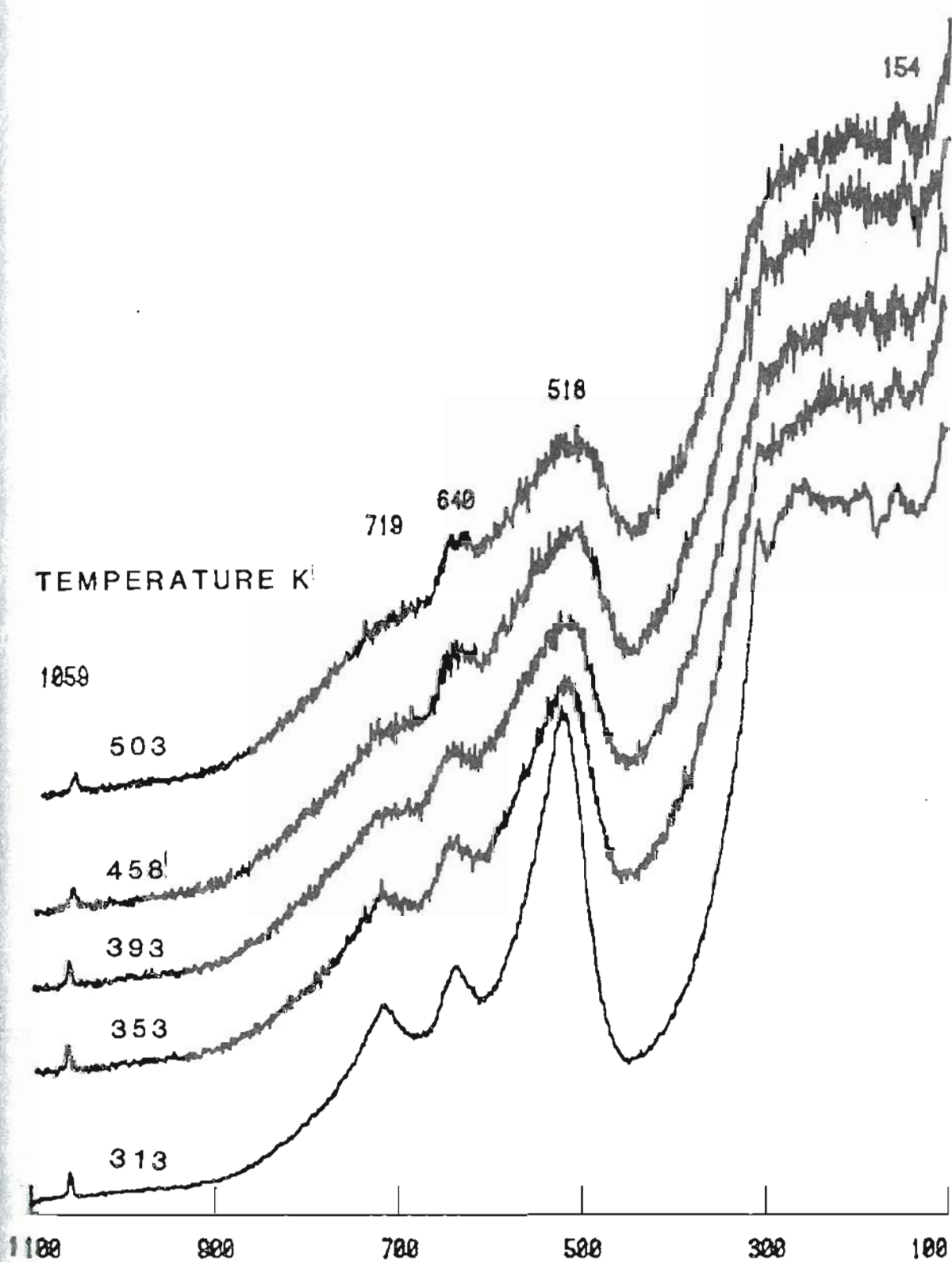
Figure 5.20   RAMAN SPECTRA OF $BaTiO_3$ AS A FUNCTION OF TEMPERATURE (Cont.)

workers (97, 145-148). Over the temperature range observed, barium titanate undergoes four different phase transformations, and as already shown in Table 5.2, by factor group analysis, the number of peaks in each phase should change. Above 400 K the cubic phase is stable. In the cubic phase, no vibrational mode is active in Raman scattering, and hence peaks should not be observed, though broad peaks were observed at 515, 720 and 280 cm^{-1}. The peaks at 520 and 720 cm^{-1} are still visible in the spectrum at 503 K. This led some workers to believe that the room temperature Raman spectrum is second order. It should be noted that although there are phase transitions no extra peaks were observed. As the temperature is lowered, the existing peaks become sharper. The most asymmetric peak at 520 cm^{-1} becomes symmetric and sharp as the temperature is lowered. Also, the intensity of the 264 cm^{-1} peak has increased considerably and it has also become symmetric. The spectra between 50 and 300 cm^{-1} have become more clear and the broad peak, over which these spectra are sitting, is lower in intensity and peak width. Also with decreasing temperature, the intensity of the peaks at 520, 720, 264 and 185 cm^{-1} has increased, whereas the intensity of the 309 cm^{-1} peak has decreased.

In Raman spectra peak contours are well defined. To resolve the asymmetry of the 520 cm^{-1} peak, curve fitting was carried out, for a room temperature Raman spectrum. As shown in Figure 5.21, first the background was subtracted from the spectrum then peaks were generated by giving peak position, width at half intensity and intensity. Slit opening was taken into account and various combinations of Gaussian and Lorenzian peak characteristics were tried. It is impossible to fit a single peak at 520 cm^{-1} and obtain the spectrum, but to get the spectrum an additional peak has to be considered. This additional peak position is at 575 cm^{-1}, with a width at half intensity of 100 cm^{-1}, a very broad

1100.00   900.00   700.00   500.00   300.00   100.00
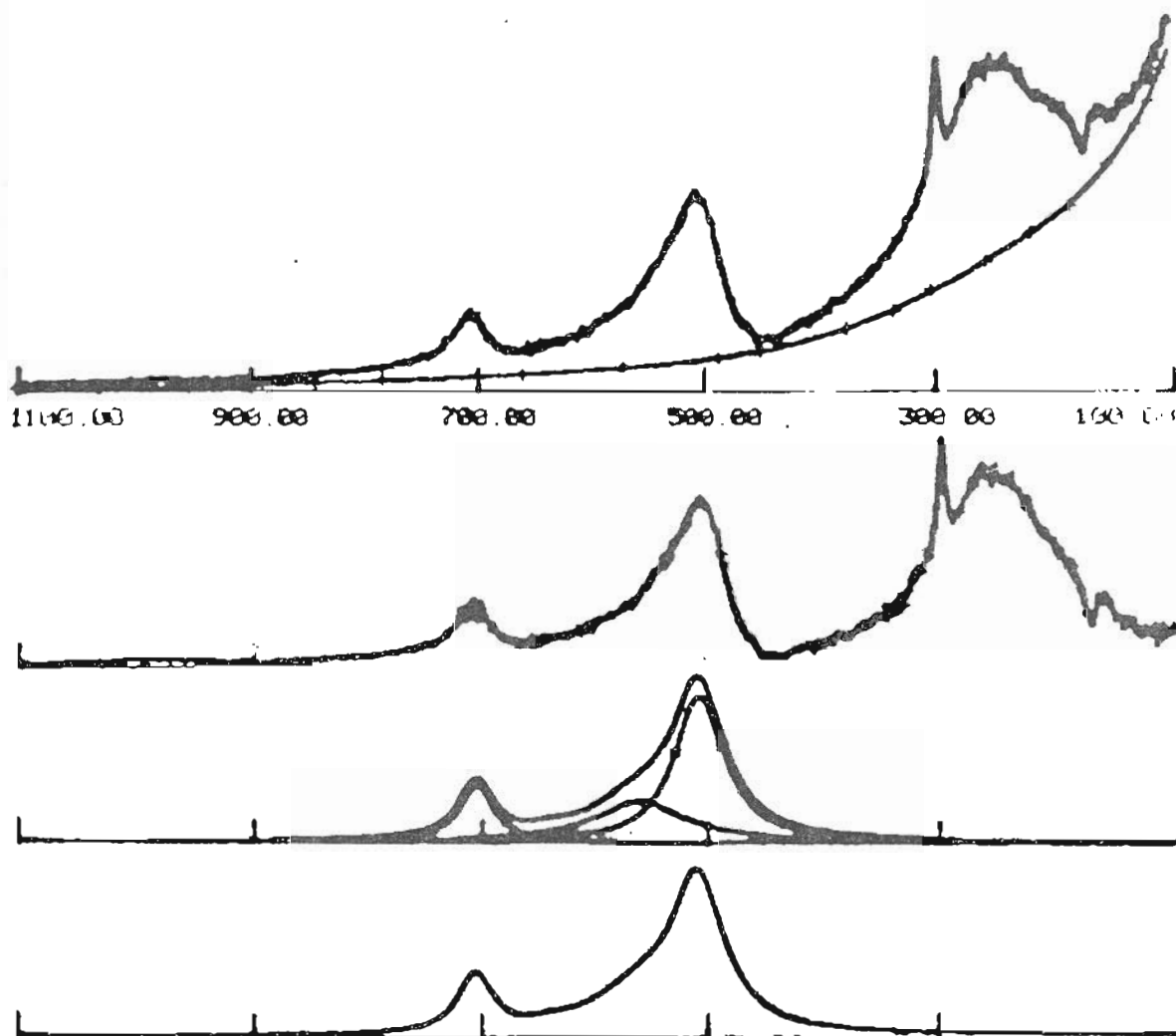
Figure 5.21   COMPUTER CURVE ANALYSIS OF THE RAMAN SPECTRUM OF $BaTiO_3$

peak with a low intensity. After taking this peak into account the exact contour of the 520 cm^{-1} peak was obtained. This proves that the 520 cm^{-1} peak at room temperature is in fact not a single peak but at least two peaks, of which one is very broad. At 85 K the peak at 520 cm^{-1} is very symmetric, and only one peak at 520 cm^{-1} has to be taken into the account for curve fitting, indicating that the intensity of peak at 575 cm^{-1} has gone to zero. As temperature is reduced, the peak at 520 cm^{-1} becomes symmetric, indicating that the contribution from the 575 cm^{-1} peak is decreasing as temperature is decreasing, whereas the intensity of 520 cm^{-1} peak is increasing.

In the first order Raman scattering process, only one phonon is taking part and hence it can originate only from the center of the Brillouin zone. This restriction comes from the momentum or wave vector and energy conservation considerations. In addition, the wave vector of the phonon is very small compared to the dimensions of the Brillouin zone. This gives discrete sharp lines in the first order spectrum, whereas in the second order spectrum two phonons are taking part in Raman scattering. Thus two phonons can originate anywhere in the Brillouin zone provided their wave vectors add up to zero. This gives rise to a very broad band in the second order spectrum which tends to be continuous.

The increase in intensities of the 520, 267 and 165 cm^{-1} bands with decreasing temperature suggests these bands are fundamental transitions. This fact coupled with the decreasing intensity of the 575 cm^{-1} band with decreasing temperature indicates that the room temperature Raman spectrum of barium titanate is neither pure first order nor pure second order but it is a combination of a first order spectrum superimposed on the second order spectrum as observed for $PbTiO_3$, $KNbO_3$ and $KTaO_3$ (148). As the temperature increases, first order contribution decreases, but it does not entirely vanish as predicted by the factor

group analysis. This may be due to the local symmetry. Also the phase transformation from the tetragonal to the cubic phase may be sluggish. At 500 K the first order contribution has almost vanished and the spectrum appears to be entirely second order.

Since all the samples investigated were multi-domain polycrystalline ceramics, no detailed study of the spectra for different directions of phonon propagation and polarization could be obtained. Hence the symmetry assignments, based on this study alone will be at most tentative. IR spectra were measured on five samples. For this purpose powder samples dispersed in pressed KBr pellet were used. The IR spectrum was measured at room temperature, which is shown in Figure 5.22. Taking the results of the IR spectra, temperature dependence of the Raman spectra, and help from the literature, band assignments are possible. Two absorption bands have been observed in the IR spectrum at room temperature. A very weak band centered at 1440 cm^{-1} with a half width of 45 cm^{-1}, a very broad asymmetric peak at 535 cm^{-1} which starts at 800 cm^{-1} and has a half width 185 cm^{-1}. Our results agree well with Last (109), who observed two peaks at the same position in the IR spectra between 300 and 800 cm^{-1}.

From factor group analysis there are seven modes $3A_1 + 4E$ active in the IR spectrum of barium titanate at room temperature. Of these $3A_1 + 3E$ modes come from $3F_{1u}$ active modes in the cubic phase and the remaining E mode comes from the silent F_{1u} mode. Last (109) observed the IR spectra at various temperatures, covering all phases. From the cubic to tetragonal to orthorhombic transitions, he did not observe any change in IR spectra. Thus, the IR spectrum is also not helpful in understanding the vibrational spectra of barium titanate. Thus, the vibrational spectra present many unusual features which makes the understanding of this material a very difficult and formidable problem.
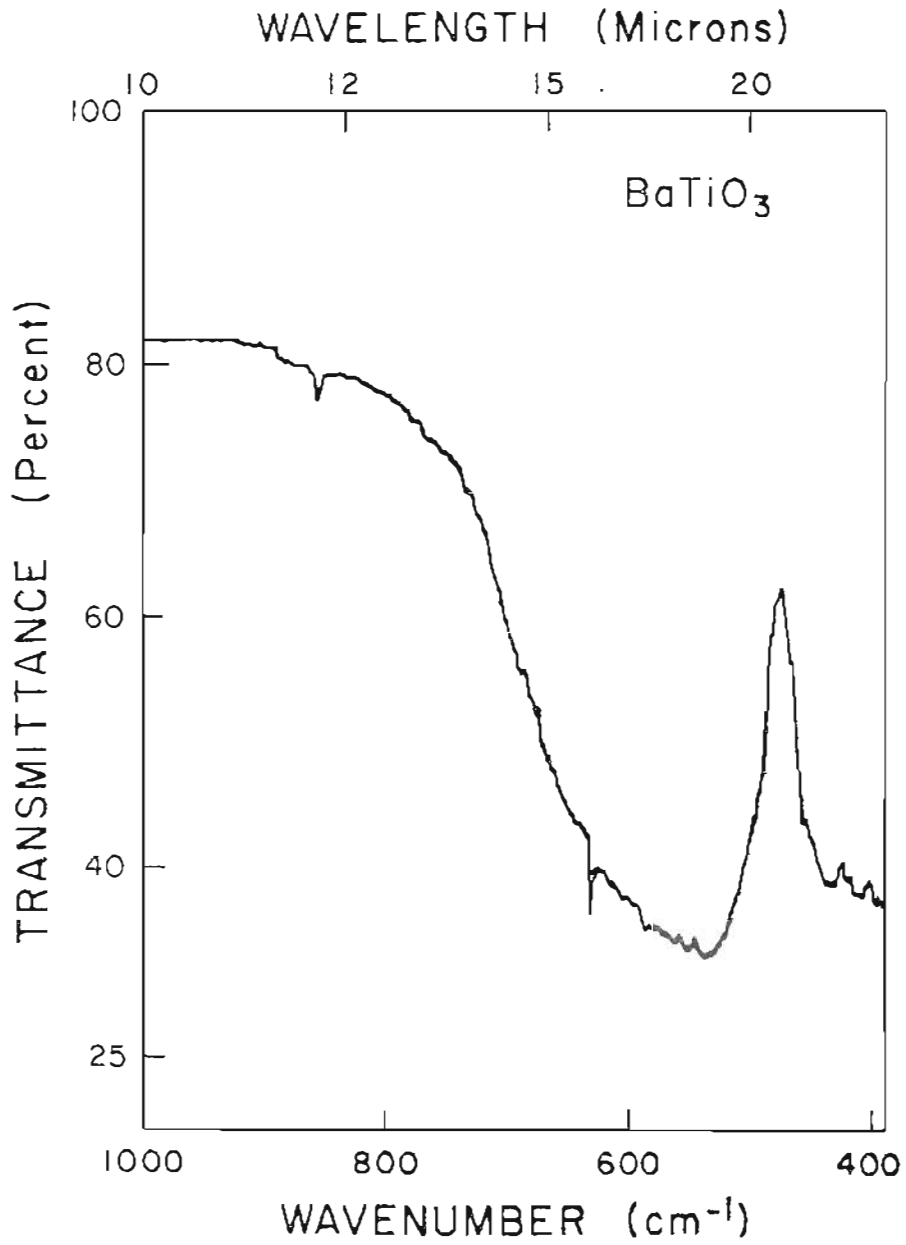
Figure 5.22   IR SPECTRUM OF BaTiO$_3$

It can be proven very easily by group theoretical techniques that, whether we consider the crystal as an assembly of individual atoms or as an ionic crystal, the symmetry as well as the total number of IR and Raman active modes is same. Only our interpretation regarding the origin of modes changes.

Attempt has been made by various workers (109, 149,150,107) to explain the IR and Raman spectra of perovskites based on molecular crystal assumption, considering an octahedral framework. Barium titanate can be viewed as consisting of Ba ions and TiO_6 octahedra, and a total of nine vibrations of the group can be classified by division into three vibrations of Ba - against the TiO_3 group, and six internal TiO_3 vibrations. The interaction between these two groups depends upon the masses and restoring forces of the vibrating atoms and can be expected to be small in the case of barium titanate. The Ba-(TiO_3) vibrations can be treated by considering the TiO_3 group as a point mass situated at the Ti position, which reduces the vibrational problem to that of a diatomic molecular crystal of equivalent structure (e.g. CsCl structure). In the cubic phase, this will lead to triply degenerate vibrations since three equivalent axes exist.

The TiO_3 group, is considered to be arranged as a central Ti atom octahedraly surrounded by six O half atoms, to give the group correct symmetry properties. This octahedron has the symmetry of point group O_h, which has six species of normal vibrations A_{1g}, E_g, F_{1u}, F_{1u}, F_{2u} and F_{2g}, of which $2F_{1u}$ are infrared active. As shown in Figure 5.23, if the vertical axis is chosen through the Ti - O chain, and two O half atoms laying along this chain are labeled as O_1 and the other four O half atoms are labeled as O_2, then the F_{1u} normal vibration can be viewed as shown in Figure 5.23. Figure 5.23 (a) shows the symmetric stretching vibration, in which the motion mainly consists of stretching Ti - O_1
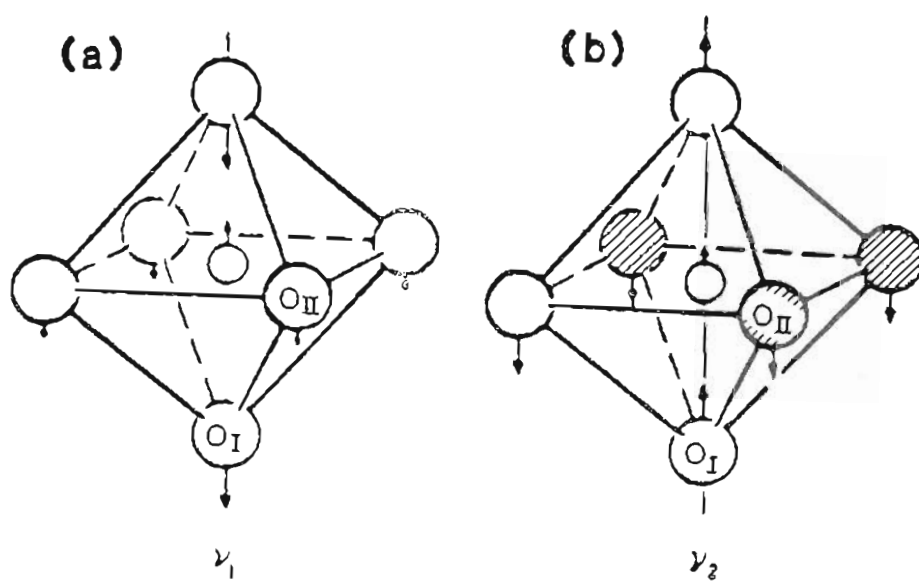
Figure 5.23   SCHEMATIC NORMAL VIBRATION OF A ZrO_6 OCTAHEDRON
ν_1 Higher frequency 'stretching vibration'
ν_2 Lower frequency 'bending vibration'

bonds. Figure 5.23 (b) shows the 'bending' vibration, in which the O_1 - Ti - O_2 bond angle changes. In both of the vibrations the relative magnitude and sign depends upon the force constants and relative masses of the atoms. In the case of a cubic lattice these vibrations will be triply degenerate.

When considering the energy required for various vibrations, internal (molecular) vibrations are always at higher energy than external or lattice vibrations. The lattice vibrations are ≤ 150 cm^{-1} in the Raman spectra. In the internal modes the stretching mode has a higher energy than bending, which in turn has a higher energy than the liberation mode. Based on all these considerations the 540 cm^{-1} band in the IR spectrum was assigned to symmetric stretching and the 380 cm^{-1} to the bending mode. In the Raman spectra the 520 and 480 cm^{-1} bands were assigned to the internal mode of TiO_3. In similar structures such as $PbTiO_3$, $KTaO_3$ and $KNbO_3$, Perry et.al. (148) invoked the same model to explain the spectra. Similarly Bartlett and Wall (150) assumed the NbO_3 octahedra in explaining the IR spectrum of in $SrNb_2O_6$ and $BaNb_2O_6$. Recently Suriyayothin (151) invoked a similar argument to explain the Raman spectra of. $CaZrO_3$ and $SrZrO_3$. Although the model is attractive and able to explain the IR spectra, it does not explain the Raman spectra of all these materials for the tetragonal phase. As in the tetragonal phase of $BaTiO_3$ and $PbTiO_3$ there is a band at 720 and 650 cm^{-1}, respectively, which has been assigned A_1 symmetry and as per our results has to be a fundamental transition. From the above model the highest internal mode has been assigned to 520 cm^{-1} in $BaTiO_3$. Hence the 720 cm^{-1} band becomes either a combination band or an overtone. From our temperature dependent Raman spectra results this is not true. Similarly in $PbTiO_3$, the peak at 650 cm^{-1} is a fundamental transition. In $CaZrO_3$ a band at 720 cm^{-1} has been observed. The TiO_3 structure remains in the O_h

symmetry in the cubic phase, with a Ti - O distance 2.004 A. but in the tetragonal phase the Ti - O_1 distance will be 1.87 and 2.17 A., for the top and bottom directions respectively. Thus there is a considerable deviation from symmetry and the F_{1u} mode in the cubic phase will be split into A_1 + E modes in the tetragonal phase. Of course the actual vibration splitting will depend upon the force constants between the atoms. In the IR spectra we do not observe this split, whereas in Raman we do observe a split. A small shoulder is observed on the 520 cm^{-1} band at 485 cm^{-1}, which increases in intensity as the temperature is decreased. Also considering vibrational problem of $BaTiO_3$ in terms of Ba-(TiO_3), i.e. TiO_3 octahedra suggest negligible force constant between Ba-O, which is not the case for $BaTiO_3$.

We propose a model considering $BaTiO_3$ as a diatomic molecule with NaCl structure consisting of two groups (TiO_2 is one group and BaO is the other group) and treat the whole vibrational spectra problem of $BaTiO_3$ in terms of internal modes of BaO and TiO_2, and external modes due to the interaction of these two groups. Both the groups belong to C_{4v} symmetry, as shown in Figure 5.24. In the TiO_2 group, Ti is situated at the center surrounded by 4 half O atoms, and Ti and O are not planar. Ti is slightly above the plane of O atoms, and thus it is the group C_{4v}. Otherwise it would have been the group T_d. The Ti - O distance will be 1.997 A. Similarly in the BaO group the Ba atom is situated at the center surrounded by 4 quarter O atoms. Ba is slightly below the plane of O atoms, and the Ba - O distance is 2.83 A. For both of these groups the vibrational symmetry will remain the same. Only the number of vibrations will change, which is governed by 3n-n, where n = number of atoms in the group, and 3 is the number of acoustic modes. For the C_{4v} group we get the vibrational modes of A_1, E, and B_1 symmetry, of which A_1 and E are IR active while all are
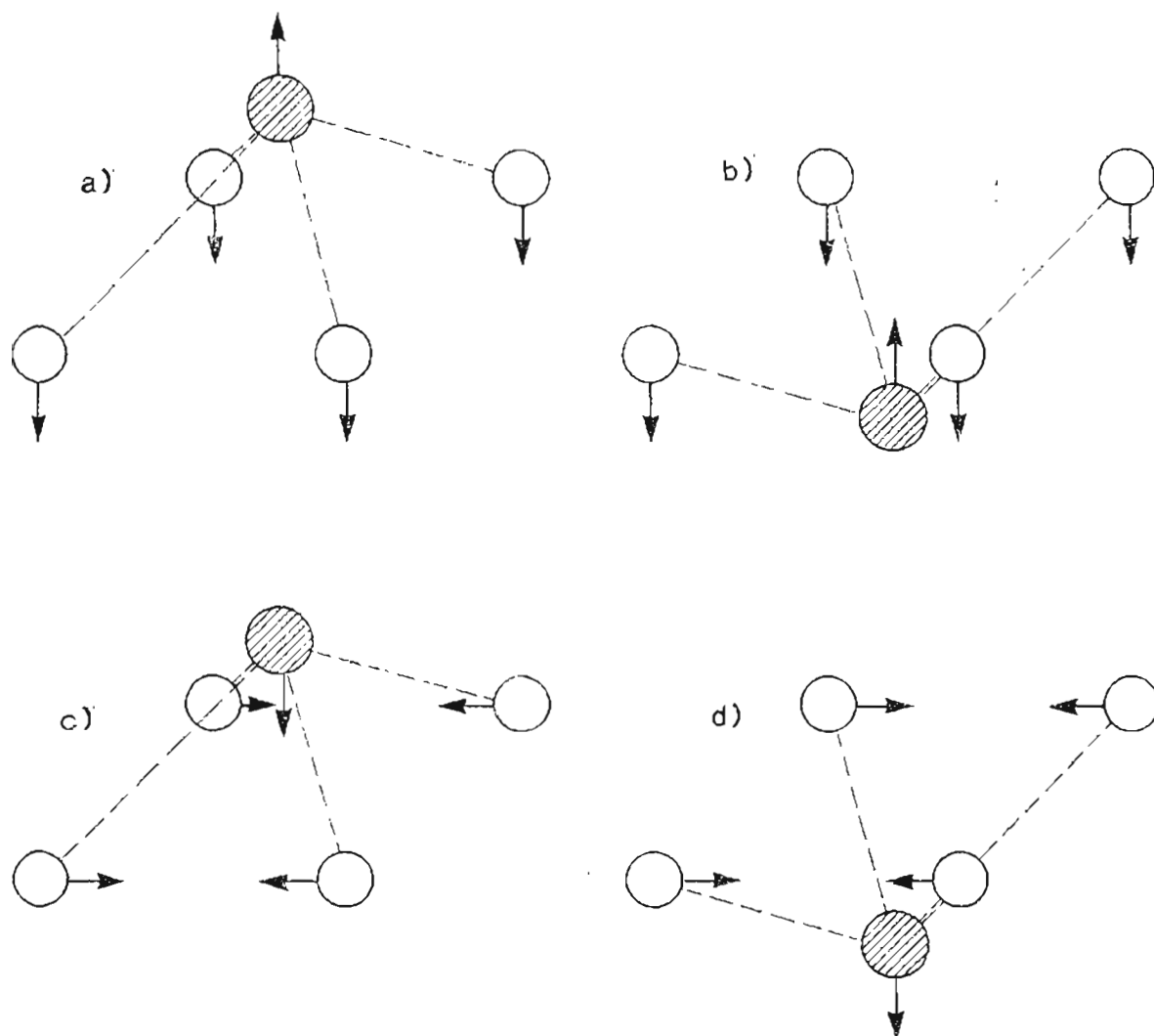
Figure 5.24   SCHEMATIC NORMAL VIBRATIONS OF C_{4v} GROUP
a) STRETCHING MODE OF TiO_2, b) STRETCHING MODE OF BaO
c) BENDING MODE OF TiO_2, d) BENDING MODE OF BaO

Raman active. For the A_1 vibration all Ti - O and Ba - O angles should change in the same way at the same time, which is clearly impossible. Hence we get the A_1 vibration as a stretching vibration as shown in figure 5.24 (a) and (c) and E as a bending vibration as shown in 5.24 (b) and (d). The objection to this model may come from the fact that the Ba - O distance is 2.83 A, whereas the highest distance in the Ti - O octahedra is 2.17 A, indicating a stronger bond for the case of Ti octahedra. Considering BaO which has the NaCl type structure with a lattice parameter 5.523 A, thus giving a Ba - O distance of 4.783 A. In case of anatase and rutile, the Ti - O distance is between 1.95 and 1.98 A. Considering TiO_2 and BaO distances in $BaTiO_3$, we note that the fact that the Ba - O distance is reduced and also Ba is a large atom (2.22 A) compared to Ti (1.47 A). This all gives credence to our model.

In the Raman spectrum of barium titanate , one can consider the peaks at 520 and 485 cm^{-1} to be an internal mode of TiO_2, with 520 cm^{-1} band assigned to A_1 symmetry and 488 cm^{-1} to E symmetry. These assignments have been verified by the IR and Raman spectra. This leaves the assignment of the 720 cm^{-1} mode to be A_1 symmetry from the BaO internal mode, and the 309 cm^{-1} peak to be E symmetry. The 235 cm^{-1} peak belonging to A_1 symmetry. These results agree with Scalabrin et.al. (145), DiDominico (100) and Burns and Scott (95).

In the case of barium titanate detailed knowledge of phonon dispersion and anharmonicity constants is still lacking. This is mainly because the mathematical problem involved is quite complex and due to the lack of ultra pure crystals, reliable experimental data are not available. Also the structure is not simple and undergoes five different phase transformations which makes it difficult to correlate experimental measurements with theory.

5.2.2 Effect of A/B Ratio

Raman spectra were measured on powders as well as on sintered pellets with the Ba/Ti ratio ranging from 1.01 to 0.985. As shown in Figure 5.21, first background was subtracted from the spectrum, then peak position, width at half intensity and intensity were measured. Using these data curve fitting was carried out. After curve fitting the areas under the 720 and 520 cm^{-1} peaks were measured, and the ratio of these areas was plotted against the Ba/Ti ratio. These results are shown in Figure 5.25. At Ba/Ti ratio ≈ 1, minimum in the plot is observed . On the Ba rich side the plot increases more steeply than on the Ti rich side. As the ratio reaches 1.0008 the plot evens out. For the ratio of 1.005 the value of the ratio of areas become almost equal to the value at the unity ratio. On the Ti reach side the plot evens out for the Ba/Ti ratio of 0.98. The result agrees well with Eror and Loehr (111). In the present study we have investigated a wide range of Ba/Ti ratio. Figure 5.26 shows the plot of the ratio of width at half intensity of the 520 and 720 cm^{-1} peaks, which is similar to figure 5.25. Thus small deviations from the stoichiometry can be studied. Comparing Figure 5.3, in which the lattice parameter with the Ba/Ti ratio was plotted, with Figure 5.25 one immediately sees the sensitivity of the Raman method. The change in the lattice parameter, for the range of the Ba/Ti ratio studied was very small. Also attaining accuracy was tedious, whereas for Raman scattering the change is quite large for the range observed, and moreover it is a non destructive in situ technique.

As excess titanium is introduced into the normal barium titanate lattice, equal numbers of barium and oxygen vacancies are introduced. As long as the material is single phase, the Raman spectrum should remain the same, but due to the slight shift from stoichiometry peak characteristics, i.e. intensity, width at
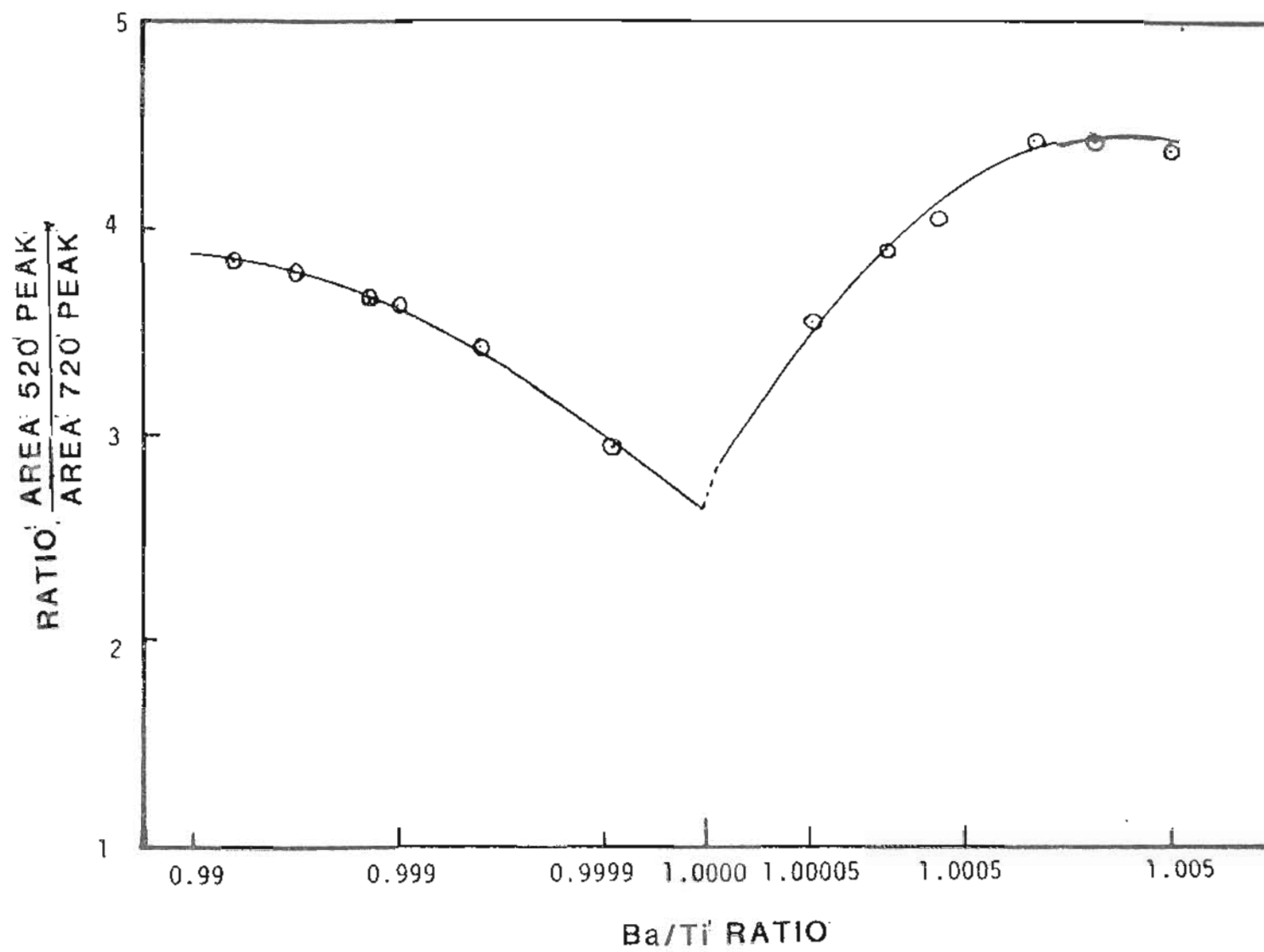
Figure 5.25   RELATION OF THE RATIO OF AREA OF 520 PEAK TO 720 PEAK
TO THE Ba/Ti RATIO
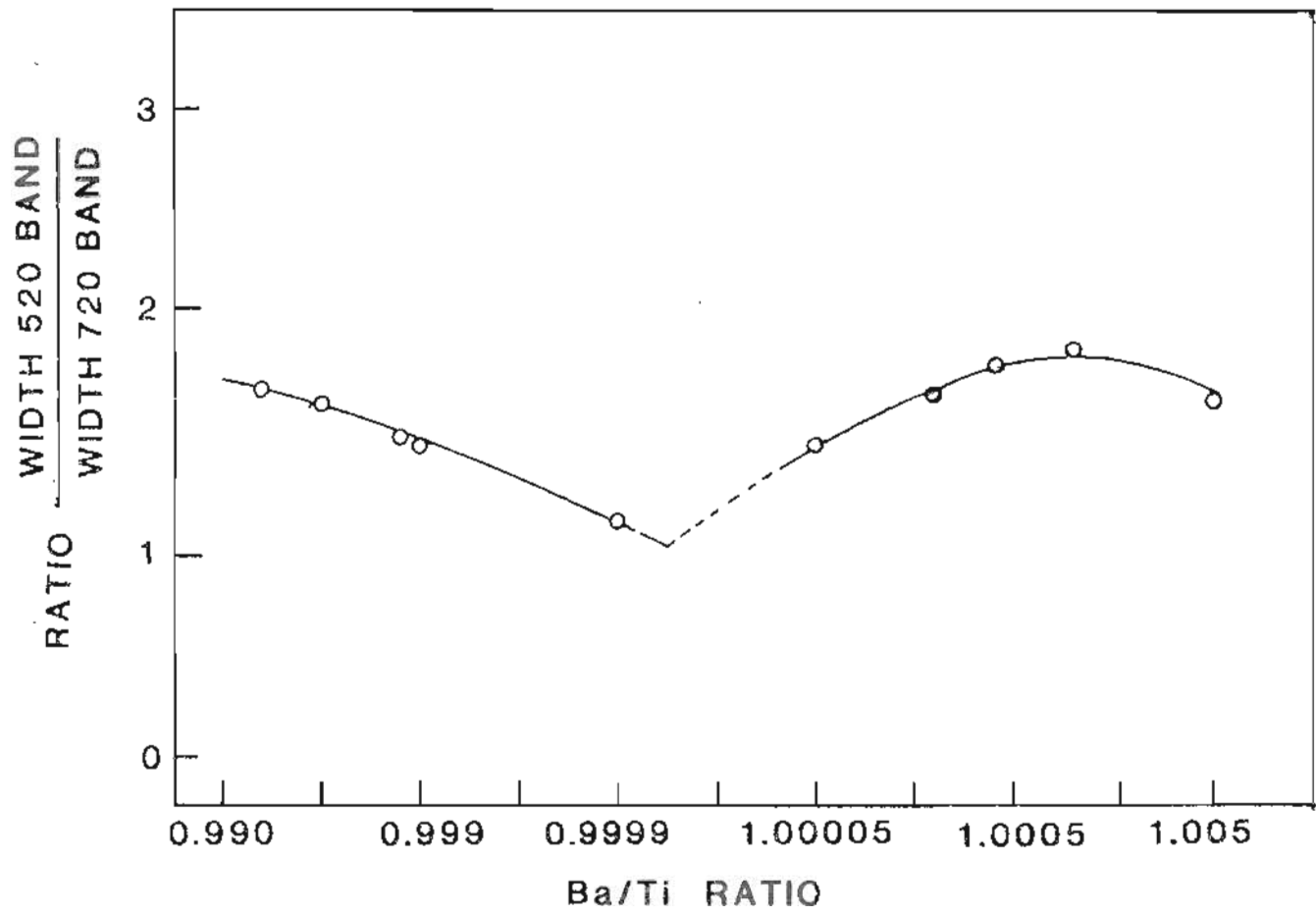
Figure 5.26   RELATION OF THE RATIO OF WIDTH OF 520 PEAK TO 720 WIDTH
TO THE Ba/Ti RATIO

half intensity will change. Thus, by measuring these peak characteristics, the small deviations from stoichiometry can be measured. In actual measurement external factors such as laser power, plot factor, slit opening etc. come into the picture. To avoid the effects due to the variation in these parameters the ratio of two peaks was taken. Thus results independent of external parameters were obtained. Eventually the change in composition, in the present case by the excess titanium, will lower to a phase boundary once, a two phase mixture will be obtained. In this mixture the major phase will have the phase boundary composition and composition of the minor phase will be governed by the phase diagram and equilibrium temperature. If the phase boundary is reached by non-stoichiometry then the areas ratio of the 520 cm^{-1} to 720 cm^{-1} peak should remain constant. The other phase which will be present in a very small quantity, will not necessarily give any spectrum. In the present case the plot evens out and then falls back to a lower value. This indicates barium titanate might be getting supersaturated by excess barium up to certain extent. Once the two phase region is reached the solubility of the end members again drops back, close to the stoichiometric composition. As we see from figure 5.25, the solubility limit of barium in barium titanate is reached at a Ba/Ti ratio of approximately 1.002. This result agrees well with the X-ray and microscopic observations. On the titanium rich side the solubility limit is reached for the Ba/Ti ratio of 0.995 and this result agrees well with the X-ray, microscopy and results of Sharma et.al.(141).

5.2.3 Effect of Reduction on Raman Spectra

Eight samples, after sintering at 1275^0 C for 6 hrs, were reduced in forming gas (H:N = 15:85) at 1000^0 C for 2 hrs. Raman spectra were recorded on these

reduced pellets. Figure 5.27 a) shows the spectrum from a reduced sample with a Ba/Ti ratio of 1.005. Spectra were recorded at three different laser lines. Table 5.4 shows the various compositions, which were reduced under identical conditions and the 820 cm^{-1} peak intensity variation with the various laser lines.

In the reduced spectra at all compositions, except the extremes i.e. 1.01 and 0.985, an extra peak at 820 cm^{-1} was observed. Depending upon the composition, the intensity of the 820 cm^{-1} peak varied and as the ratio increased from 1 to 1.005 the peak intensity increased. The peak seemed to be sensitive to the laser line used. This is evident from Figure 5.27 (b), (c) and (d) which shows the spectra at laser lines 514.5, 457.9 and 406.7 nm, respectively, for the sample with a Ba/Ti ratio of 1.002. The 820 cm^{-1} peak which is quite visible in the 514.5 nm line spectrum, has become a shoulder for the 457.9 nm line and has completely vanished in 406.7 nm line spectrum.

By reduction, oxygen vacancies are effectively created in the lattice. In some respects it is equivalent to doping with zero atomic weight dopants. When considering band origination in the Raman spectrum it is equivalent to doping and hence band origination will be discussed in detail in the next section.

The 820 cm^{-1} band can originate from two distinct possibilities. First it could be a second order combination or overtone band, and second it could be due to a localized mode, originating from V_O. Considering the selection rule for second order Raman scattering given by Loudon (89, 152) overtones and combination bands of all (A_1 and E) symmetries are allowed. Intensity of these second order peaks depend upon the volume of material and laser power. In the case of the 820 cm^{-1} band it could be perceived as a combination band due to 520 and 309 cm^{-1} fundamentals. This possibility of second order combination is ruled out due to the following reasons. In the case of the extreme composition studied i.e.
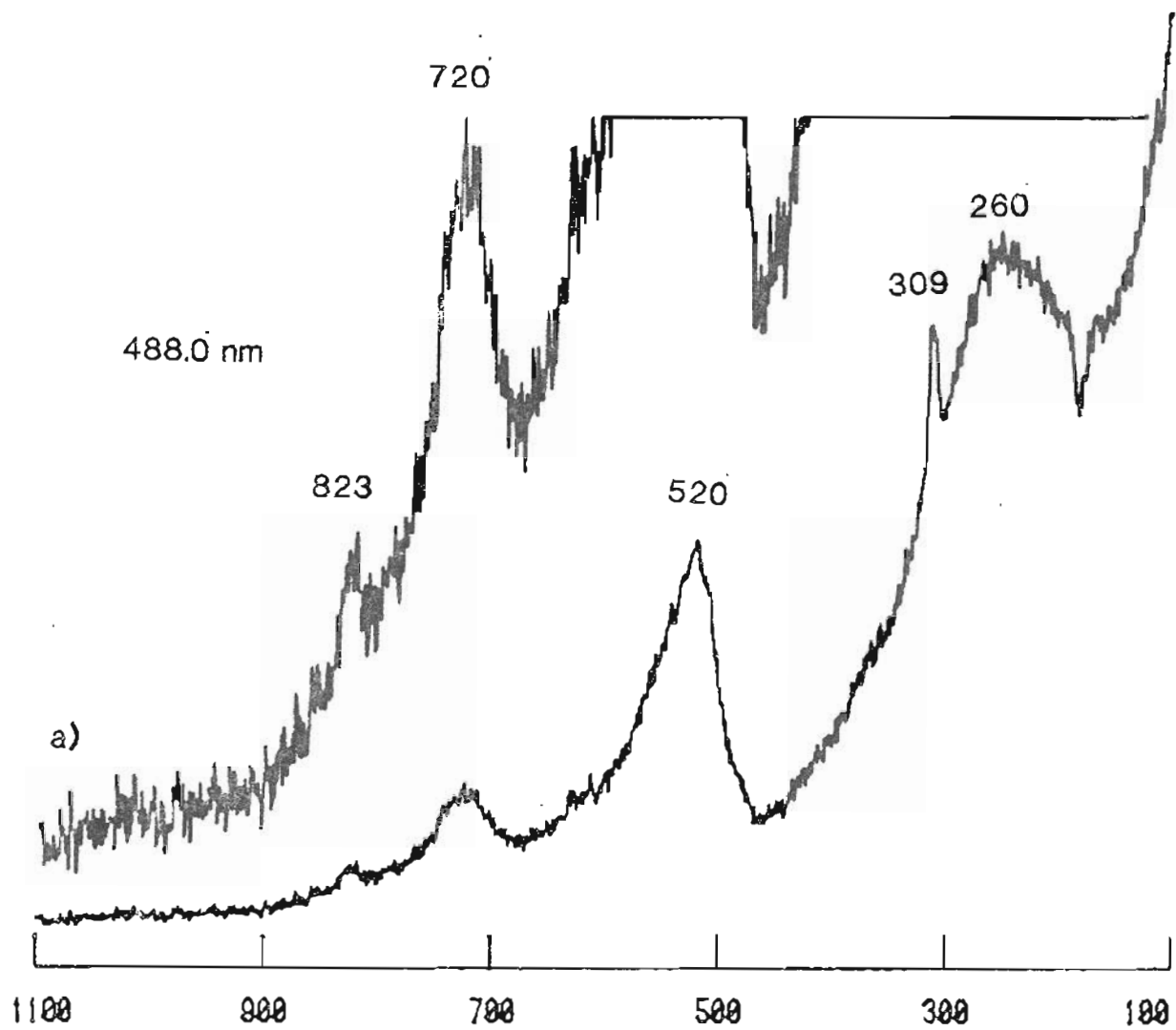
Figure 5.27 RAMAN SPECTRA OF REDUCED $BaTiO_3$ AS A FUNCTION OF
EXCITING WAVELENGTH (Red. 1000^0 C, 2 Hrs., Forming Gas)
a) 488.0 nm line
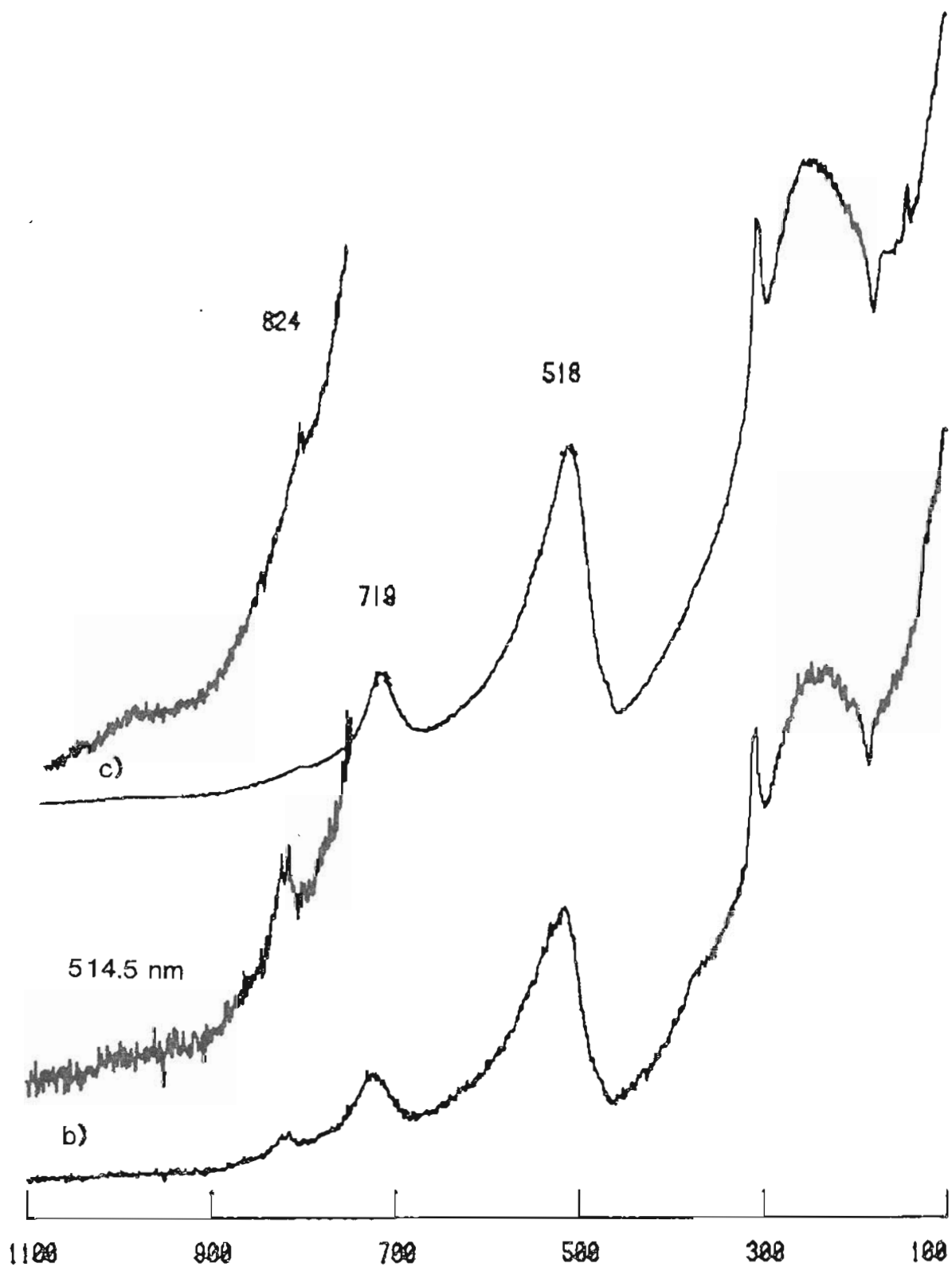
Figure 5.27   RAMAN SPECTRA OF REDUCED BaTiO$_3$ AS A FUNCTION OF
(Cont.)   EXCITING WAVELENGTH (Red. 1000^0 C, 2 Hrs., Forming Gas)
              b) 514.5 nm line, c) 457.8 nm line
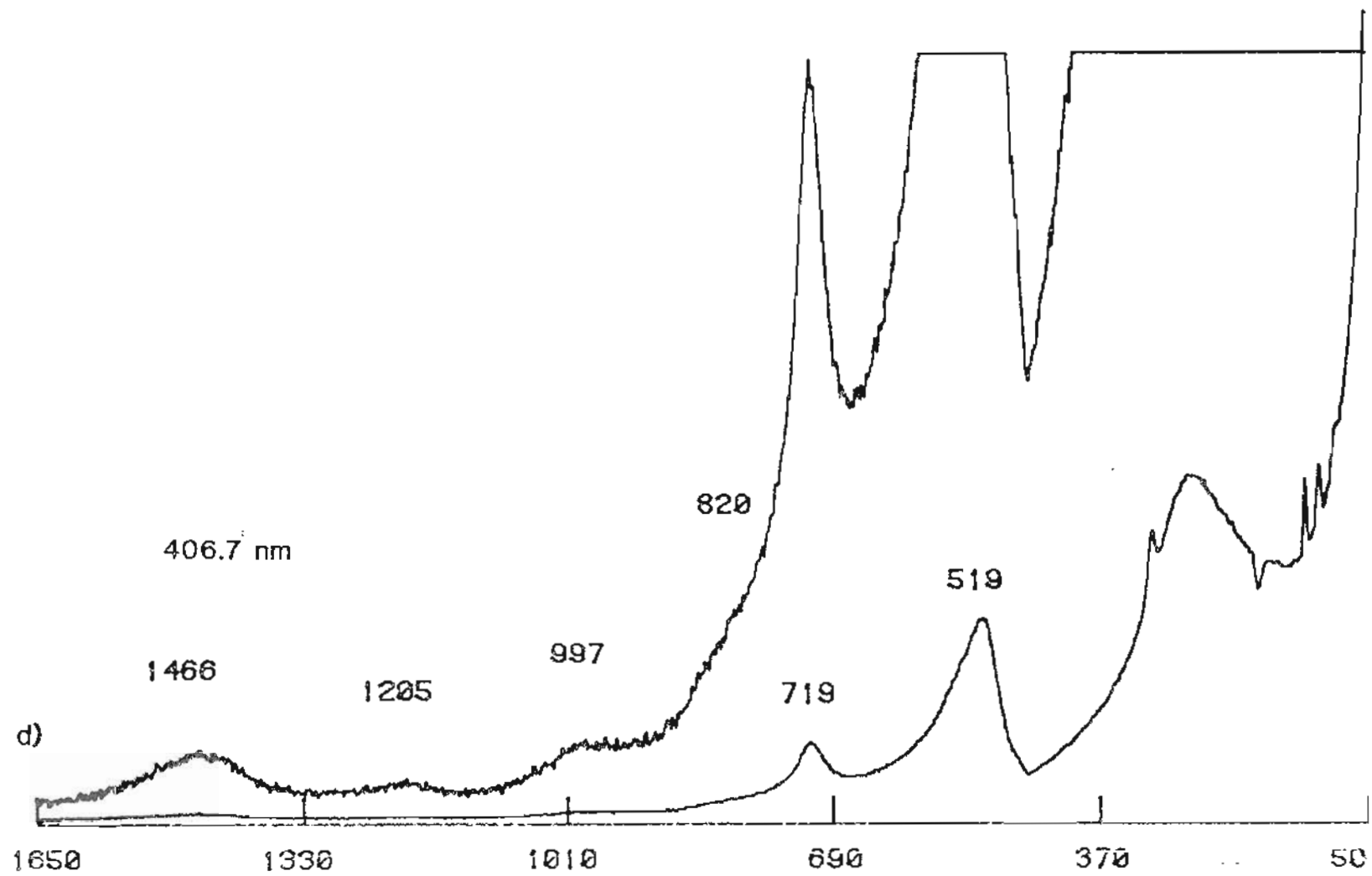
Figure 5.27 RAMAN SPECTRA OF REDUCED BaTiO$_3$ AS A FUNCTION OF
(Cont.)   EXCITING WAVELENGTH (Red. 1000^0 C, 2 Hrs., Forming Gas)
            d) 406.7 nm line

TABLE 5.4

Activity of 820 cm^{-1} Peak

A/B Ratio	514 nm	457.9 nm	406.7 nm
1.0002	shoulder	ab.	ab
1.005	well formed	well formed	suppresed
1.002	well formed	shoulder	suppresed
0.992	shoulder	suppressed	suppresed
0.998	shoulder	possibility	suppresed
1.01	absent	absent	absent
0.985	absent	absent	absent

with the ratio 1.01, two different sample thicknesses were used (1 and 2.2 mm) but the 820 cm^{-1} band still could not be observed. Also different laser power levels were used (30 ,100 and 190 mw) but still this band could not be observed. As shown in figure 5.27 (d) for the 407 nm line for a sample with the Ba/Ti ratio of 1.002, combination bands due to 520 and 720 cm^{-1} as well as overtones of 720 and 520 cm^{-1} peaks were observed. Even under these conditions, where individual bands are quite intense and produce second order combination and overtone bands, the 820 cm^{-1} band is not visible, even as a shoulder. Thus the possibility of a 820 cm^{-1} band as a combination band can be discounted and hence it is due to a local vibrational mode of V_O. The intensity of the 820 cm^{-1} peak will depend upon the concentration of oxygen vacancies. In the barium titanate system as the composition is shifted from stoichiometry vacancies on the titanium and the oxygen sites for barium excess, and on the barium and the oxygen sites for titanium excess are introduced. Thus for any nonstoichiometric composition within the single phase region there are always excess oxygen vacancies and by reducing, the number of oxygen vacancies is increased. This explains why as the composition is shifted away from the stoichiometry, the intensity of the 820 cm^{-1} peak increased, for the same amount of reduction. It also substantiates the previous conclusion, that the 820 cm^{-1} peak is due to a local mode and as a second phase is formed solubility of the end members decreases slightly.

5.2.4 Effect of Nickel Doping

For up to 1 at.% nickel doping the Raman spectra of as made powders and sintered pellets remains exactly the same as the spectra of tetragonal barium titanate. Also, as in the case of undoped powder, the Raman spectrum of nickel doped powders indicates the presence of small amount of hexagonal phase and

carbonate. In the powder samples as the nickel is increased from 1 to 10 at.% the Raman spectra are the same as the spectra of undoped powders except for a higher noise level. At 20 at.% nickel doping the spectrum is extremely noisy and seems to be a combination of tetragonal and hexagonal phases. The spectra for 10 and 20 at.% doped powders are shown in Figures 5.28 (a) and (b).

Changes which occur in the spectrum of the 1 at.% nickel doped sample, sintered at 1300^0 C have already been mentioned in the previous section. Also shown in Figures 5.13 (a), (b) and (c) are the spectra for 1, 3 and 5 at.% nickel doped samples (sintered pellets). The spectrum changes in going from 1 to 3 at.% nickel doping, in that a strong peak is observed at 575 cm^{-1} and the 520 cm^{-1} peak shifts to 529 cm^{-1}. Figures 5.29 (a), (b) and (c) shows the Raman spectra for the 10, 15 and 20 at.% nickel doped samples. In going from 5 to 10 at.% nickel the spectrum remains essentially the same except that the intensity of the 585 cm^{-1} peak has increased relative to the 520 cm^{-1} band and it does have a small peak at 632 cm^{-1} and a shoulder at 801 cm^{-1}. Thus the spectrum of the 10 at.% nickel doped sample seems to be a mixture of hexagonal and tetragonal phases with an extra peak at 585 cm^{-1}. The spectrum of the 15 at.% nickel doped sample looks different at first glance but after careful examination, it can be confirmed that it is similar to the spectrum of the 10 at.% nickel doped sample. In the spectrum of 15 at.% nickel doped sample, the widths of 529 and 585 cm^{-1} peaks have increased and hence only one peak is observed. The only difference between the 15 at.% and 10 at.% nickel doped sample spectra is an extra band at 1059 cm^{-1}. This band has already been assigned to the presence of carbonate. Thus we see presence of carbonate in the 15 at.% nickel doped samples. The spectrum of the 20 at.% nickel doped sample is the same as the spectrum of 15 at.% nickel doped sample.
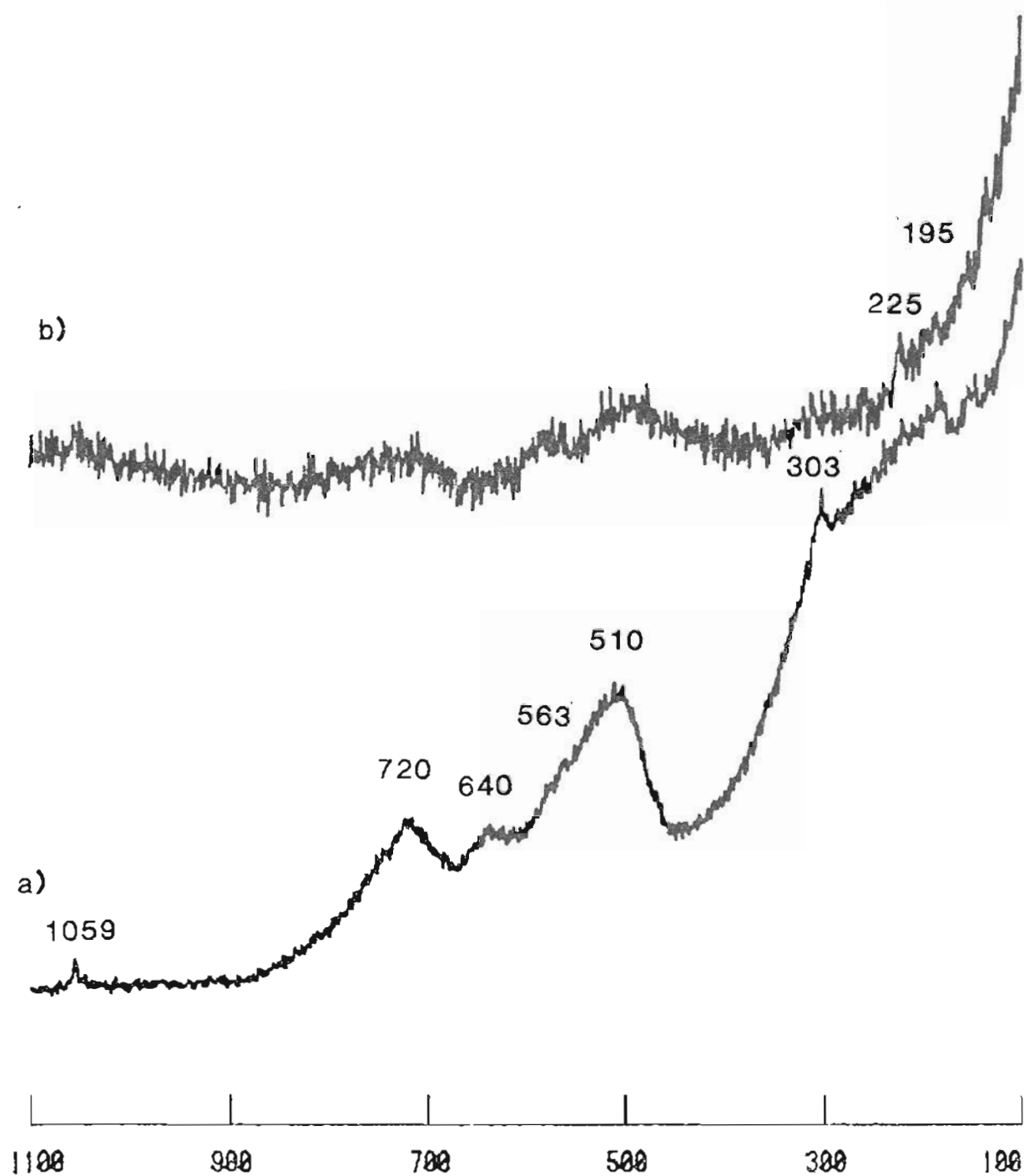
Figure 5.28   RAMAN SPECTRA OF BaNi$_x$Ti$_{1-x}$O$_3$ AS A FUNCTION OF NICKEL
CONCENTRATION (AS MADE POWDERS, 520 PEAK Max.)
a) 10 At.% Nickel, b) 20 At.% Nickel
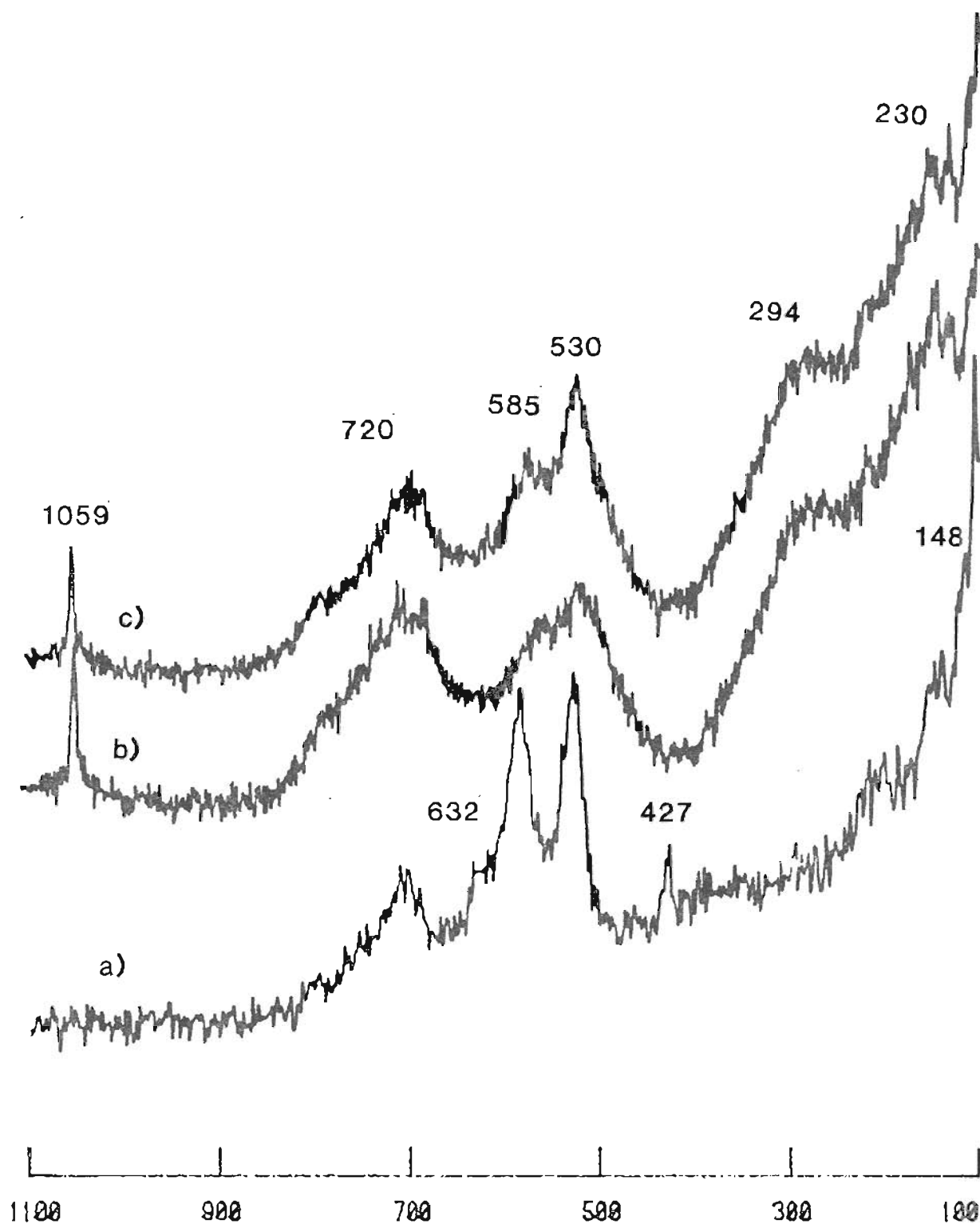
Figure 5.29   RAMAN SPECTRA OF $BaNi_xTi_{1-x}O_3$ AS A FUNCTION OF NICKEL
CONCENTRATION (PELLETS SIN. 1275^0 C, 6 Hrs., 520 PEAK max.)
a) 10 At.% Nickel, b) 15 At.% Nickel, c) 20 At.% Nickel

From X-ray measurements it was established that samples doped in excess of 5 at.% nickel have a hexagonal structure. Raman spectra showed it to be a mixture of hexagonal and tetragonal phases. To find out if two phases can be separated, as in the case of 1 at.% doped sample, after adjusting the sample and output for the 585 cm^{-1} peak, the sample was moved to find the area which will give maximum intensity for the 585 cm^{-1} peak, and the spectrum was then recorded. Such spectra for 15 and 20 at.% nickel doped samples is shown in Figures 5.30 (a) and (b), respectively. The only difference observed for the 15 at.% nickel doped sample is that the intensity of the 585 cm^{-1} peak has declined relative to the 529 cm^{-1} band, and the intensity of the carbonate (1059 cm^{-1}) peak has increased. Similar changes have been observed for the 20 at.% nickel doped sample. To verify the origin of the carbonate band a sample with 15 at.% nickel doping was heated to 1300^0 C, and the Raman spectrum was recorded immediately (see Figure 5.31). Due to this heating the carbonate was removed, as evident by the absence 1059 of cm^{-1} peak. Comparing this spectrum with the spectrum in Figure 5.29 (b) a sharp peak at 755 cm^{-1} is observed in the present case (Fig 5.31). This sharp peak does not seem to be an extra peak since a 790 cm^{-1} a shoulder is present in the previous case. The most dramatic change occurs in the 585 cm^{-1} peak. After heating, the intensity of this band has increased and has became nearly equal to that of the 529 cm^{-1} peak. Both peaks are clearly separated indicating that, the width of the 529 cm^{-1} peak has decreased. The rest of the features are the same in both spectra.

Although Raman spectroscopy does not just see the surface only, we do not know the depth from which it gathers information. This will of course depend upon the laser power, bulk material density, refractive index, colour and other optical properties of the material In order to obtain Raman spectra from the
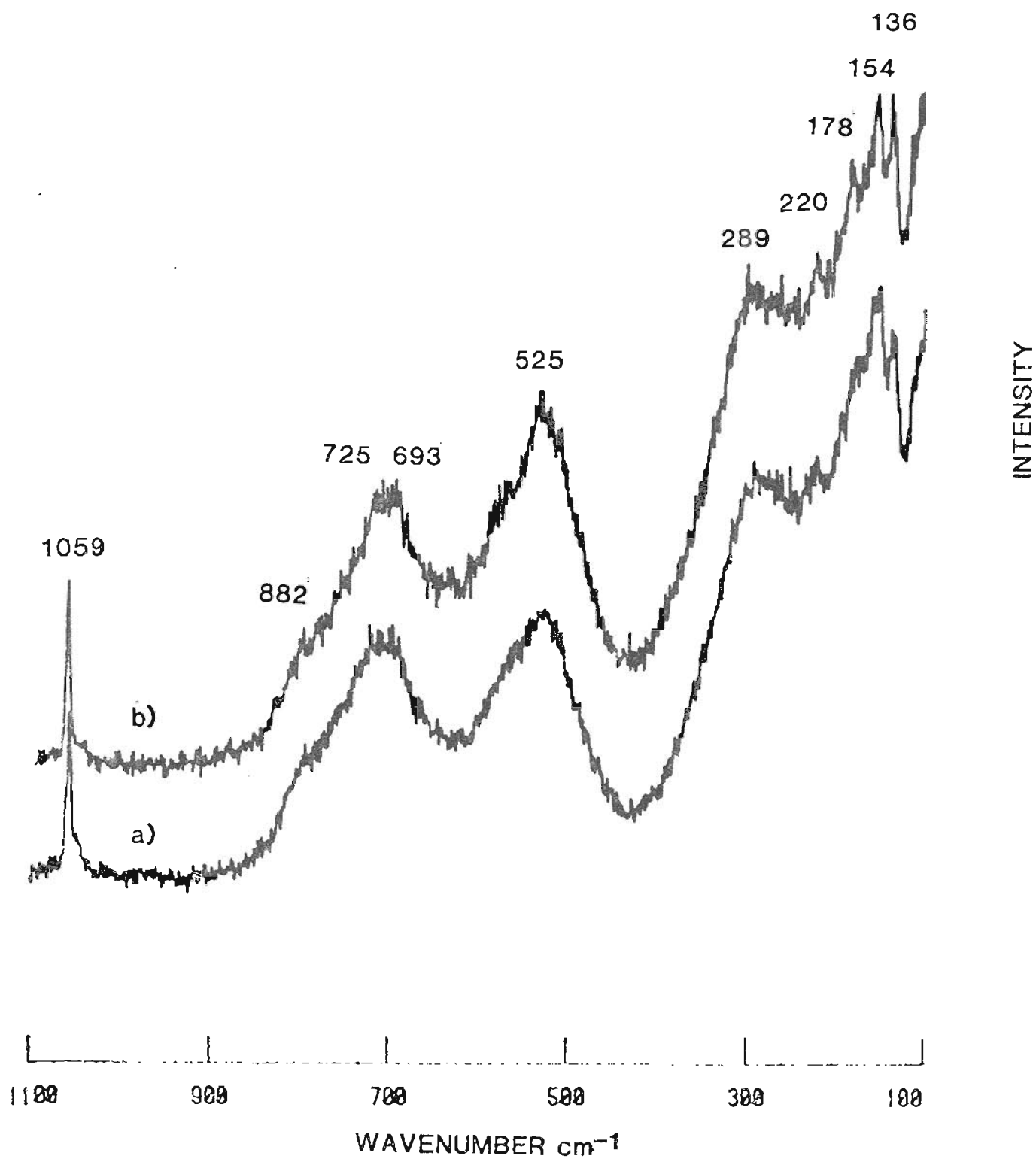
Figure 5.30   RAMAN SPECTRA OF $BaNi_xTi_{1-x}O_3$ AS A FUNCTION OF NICKEL
CONCENTRATION (PELLETS SIN. 1275^0 C, 6 Hrs., 588 PEAK max.)
a) 15 At.% Nickel, b) 20 At.% Nickel
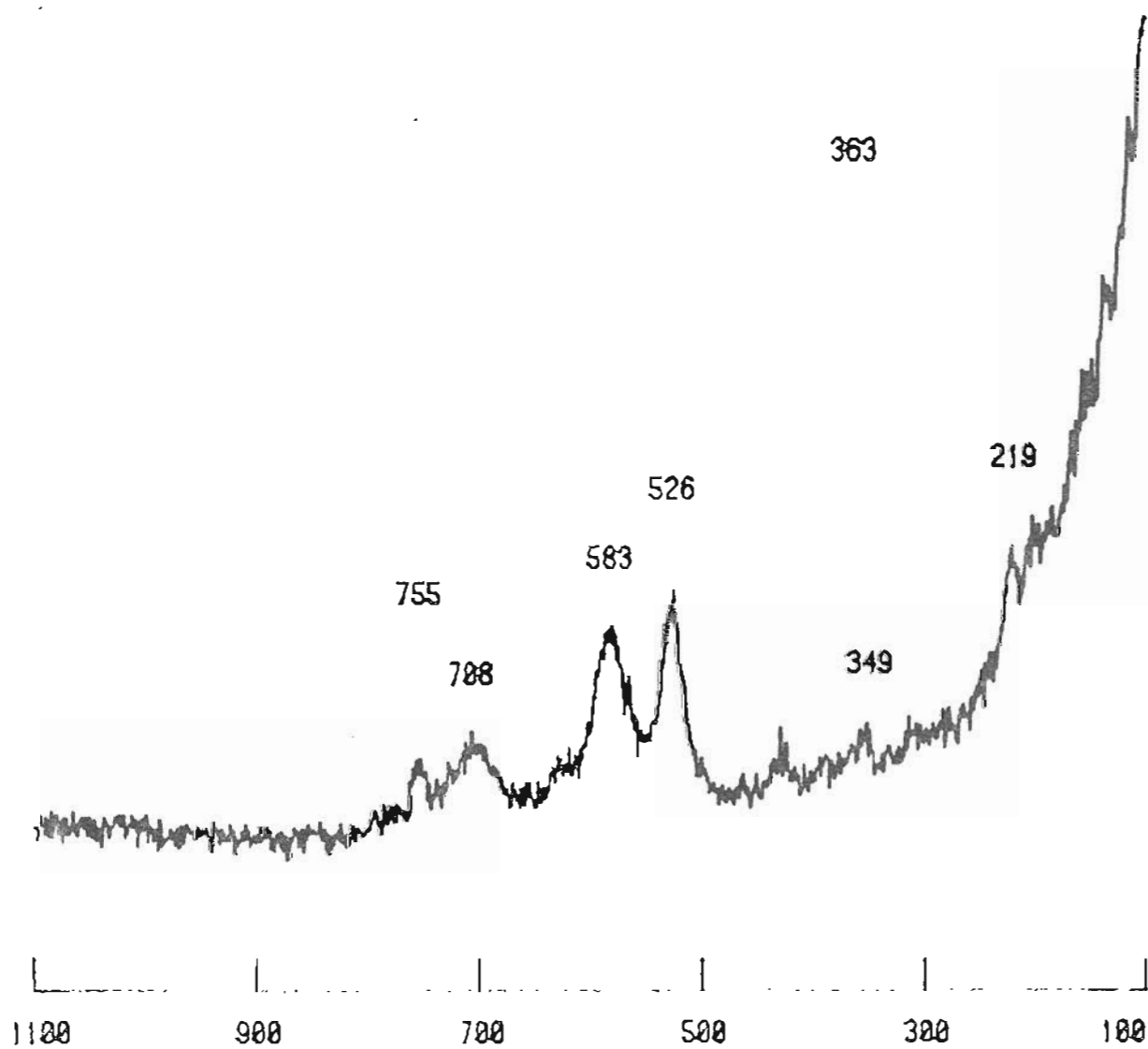
Figure 5.31   RAMAN SPECTRA OF $BaNi_{15}Ti_{85}O_3$
(PELLETS SIN. 1275^0 C, Sub. HEATED 1300^0 C, 1 Hrs.)

bulk of the sample, sintered pellets were ground and the spectra were recorded on these powder specimens. The spectra of 1, 3, 5, 10, 15 and 20 at.% nickel doped powders are shown in Figures 5.32 (a), (b), (c), (d), (e) and (f) respectively. Comparing these powder spectra with the respective pellet spectra, the following differences have been observed. A dramatic change is seen in the spectrum for the 3 at.% nickel doped sample. The spectrum is essentially the same as hexagonal barium titanate, except for small peaks at 705, 520 and 797 cm^{-1}, indicating this sample to be a mixture of hexagonal and tetragonal phase. The amount of tetragonal phase is probably 20%, thus substantiating the results of X-ray diffraction. From 5 to 20 at.% nickel doping there is not much difference between the powder and pellet spectra, except that the pellet spectra are less well defined. The only difference between the powder and pellet spectra of the 15 and 20 at.% nickel doped samples is that the intensity of the 1059 cm^{-1} peak has reduced substantially and, therefore, indicates that the bulk material does not have much carbonate and the carbonate peak is due to the surface adsorbed CO_2. X-ray studies show the 5 to 20 at.% nickel doped materials have hexagonal structure, and the lattice parameter decreases with increasing nickel content. The Raman spectra of 5 to 20 at.% nickel doped samples do not match with the hexagonal spectra of undoped barium titanate, whereas the sample with 3 at.% nickel doping does show a hexagonal spectrum which matches with that of the hexagonal spectrum of undoped barium titanate, except for the additional band at 585 cm^{-1}. One of the possibilities for these differences may be as follows. As nickel is increased up to 3 at.% tetragonal barium titanate is changed to the hexagonal structure, and at this point the material which is transformed to hexagonal structure does not have any (if it does then very little) nickel content. Essentially all the nickel is distributed in the tetragonal phase. Thus we will get

Raman spectra typical of undoped hexagonal structure and doped tetragonal structure. As the nickel is added (more than 3 at.%) all the additional nickel is taken up by the hexagonal phase. Thus though the structure is hexagonal for the X-ray, lattice dynamics have changed to give the different spectra.

By substituting nickel on the titanium site in the lattice, translational symmetry of the lattice is altered. The extent to which this happens depends upon the amount of nickel present. Since nickel is slightly smaller in size, and its weight is slightly more than the weight of titanium, probably force constants may not change much for small doping levels and the effects may not be apparent. Due to the change of translational symmetry, the phonon wave vector can take any value in the Brillouin zone, thus giving rise to some second order peaks, and some localized modes may result due to the impurity. In the case of up to 1 at.% nickel doping no extra peaks are observed nor any extensive peak shifts noted in the Raman spectra. At 1 at.% nickel doping two new bands have been observed, at 585 and 785 cm^{-1}. As the nickel concentration increased the structure became hexagonal and some bands have changed (due to the change in structure) but the 585 and 780 cm^{-1} bands remained unchanged (in terms of peak position). The intensity of the 585 cm^{-1} peak increased with increasing nickel concentration whereas the intensity of the 780 cm^{-1} peak remained constant. Also 780 cm^{-1} band is a very weak transition. Considering all these factors, we tentatively assigned the 585 cm^{-1} peak to the local mode of nickel in the barium titanate lattice and the 785 cm^{-1} band may be due to an electronic transition.

From 0.001 to 1 at.% nickel doping, where the structure is tetragonal, the area under 520 and 720 cm^{-1} was measured to check if the nickel concentration can be determined by the Raman technique. The ratio of the areas under the 520
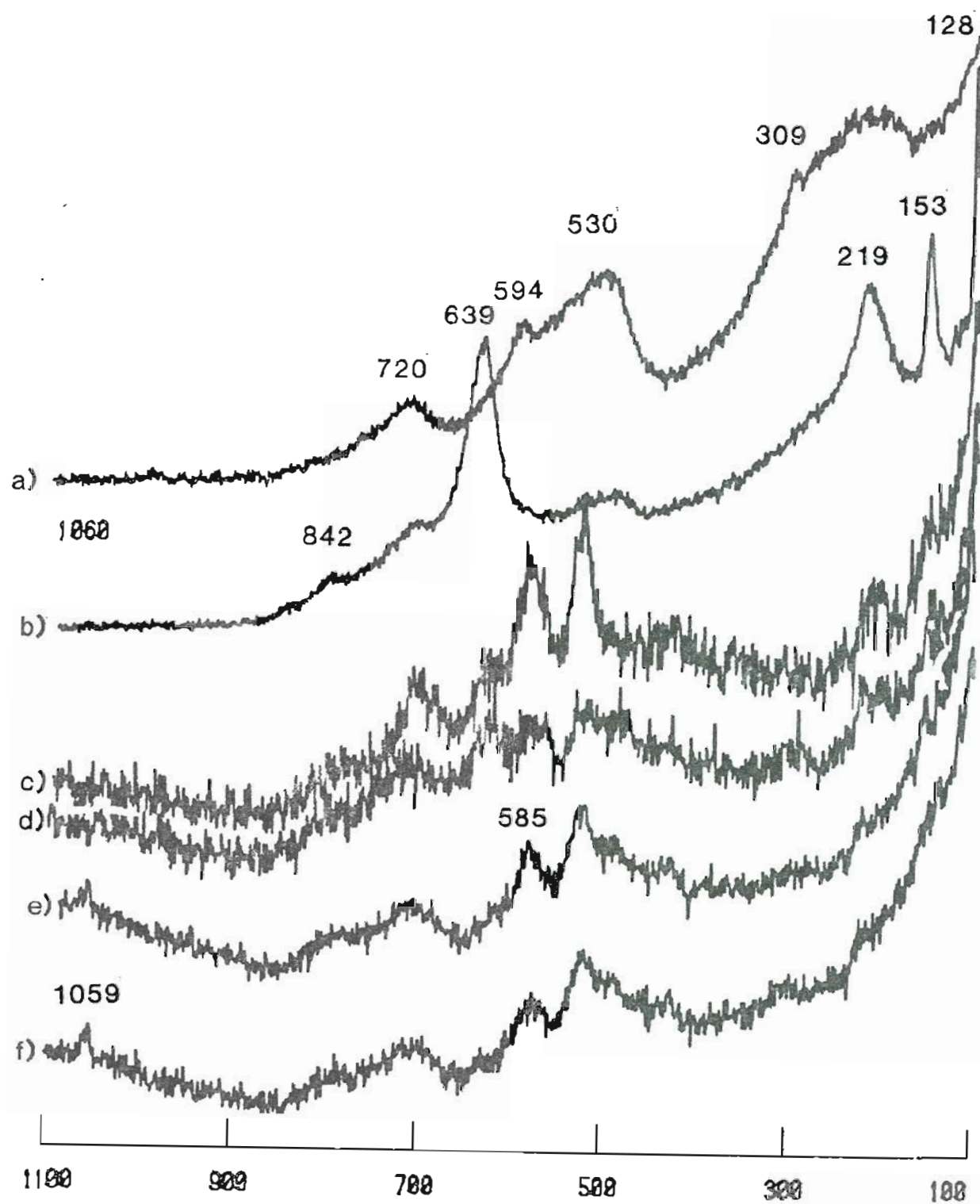
Figure 5.32   RAMAN SPECTRA OF BaNi$_x$Ti$_{1-x}$O$_3$ AS A FUNCTION OF NICKEL
CONCENTRATION (POWDER SAMPLES, SIN. 1275^0 C, 6 Hrs.)
a) 1 At.% Ni, b) 3 At.% Ni, c) 5 At.% Ni,
d) 10 At.% Ni, e) 15 At.% Ni, f) 20 At.% Ni

and 720 cm^{-1} peaks was plotted against the doping as shown in Figure 5.33. Also plotted are the widths at half intensity of the 520 to 720 cm^{-1} peak. A smooth variation was observed in all these quantities and the plots even out between 1 to 3 at.%nickel doping. Thus the amount of nickel dopant can be detected by this technique.

5.3 Electrical Conductivity at Moderate Temperatures

5.3.1 Conductivity Of Undoped $BaTiO_3$.

Indium based contacts have been reported as ohmic and low resistance when applied to oxide semiconductors and insulators (127-130), and they were applied as described in section 4.4, but it is necessary to check for ohmic behavior of these contacts, as conductivity was measured at moderately high temperature (550^0 C).

Figure 5.34 shows the measured conductivity versus field strength for a number of undoped and doped samples with various Ba/Ti ratios. As can be seen, ohmic behavior was obtained in all the cases for a 3 to 4 order of magnitude change in the applied field. All of the samples studied in this investigation were similarly tested, and all samples were found to be ohmic after application of contacts, in the field range of interest. The contacts were also tested for ohmic behavior at the highest temperature studied, and positive results were obtained. Initially it was planned to measure the electrical conductivity from room temperature to 550^0 C but soon it was found that the resistivity was very high from room temperature to 200^0 C, ranging from 2×10^{-13} to 2×10^{-12} Ω–cm. Considering the equipment capabilities it was thought that the resistivity measurement in the temperature range of room temp. to 200^0 C may not be reliable and hence 200^0 C was the minimum temperature studied. Higher limits on temperature
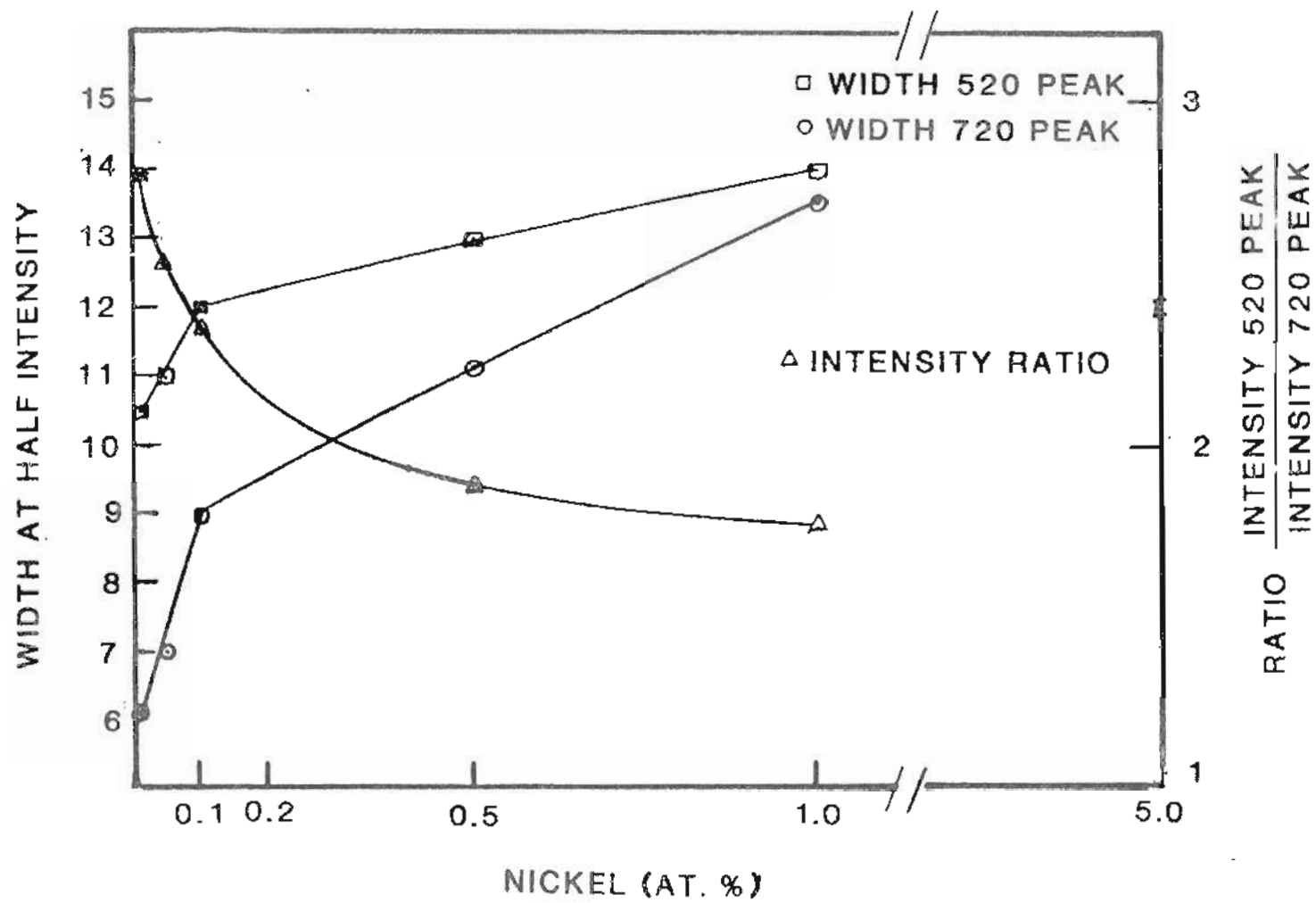
Figure 5.33 VARIATION OF WIDTH AND INTENSITY OF 520 AND 720 PEAK
WITH NICKEL DOPING
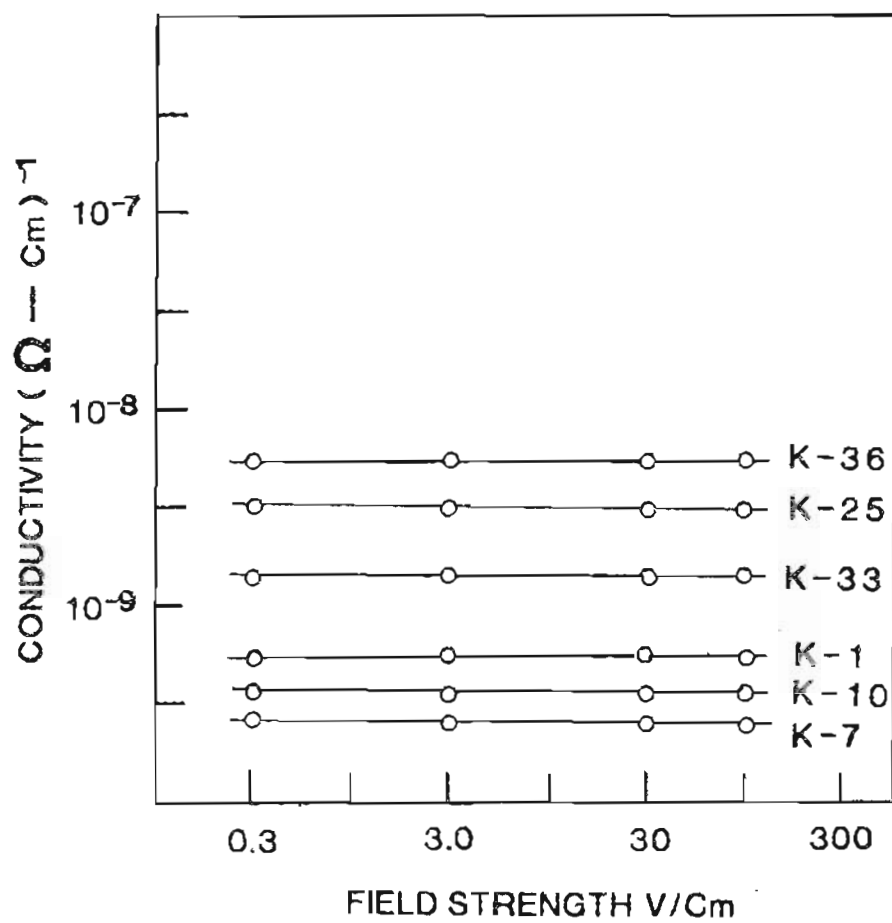
Figure 5.34 RELATION BETWEEN CONDUCTIVITY AND FIELD STRENGTH
FOR $BaTiO_3$ AND $BaNi_xTi_{1-x}O_3$

came from thermodynamic considerations. At around 500^0 C the ambient partial pressure of oxygen may start reacting with the sample and the composition may then change. Thus, 550^0 C was the highest temperature limit.

Figure 5.35 shows the log σ versus $1/T$ plots for undoped material with various Ba/Ti ratios. Although conductivity was measured for samples with 14 different ratios, in this plot only six different samples have been shown. This is to avoid confusion since the conductivities of all the samples were very close. For the Ba/Ti ratios between 0.995 and 1.005 a straight line behavior was observed, between 473 and 773 K, in the log σ versus $1/T$ plots. Activation energies were calculated from the slopes of these plots. The activation energy for the sample with the Ba/Ti ratio of unity was 1.36 eV and as the Ba/Ti ratio changed the activation energy increased. The highest activation energy was found to be 1.54 eV for the sample with a Ba/Ti ratio of 0.995. Table 5.6 shows the activation energy and the intrinsic thermal activation energy for the various samples. Here the quantity which is termed as intrinsic thermal activation energy will be the same as the band gap but not the band gap in the strictest sense. This is due to the fact that while calculating this quantity an assumption is made that, N_c does not vary with the temperature, whereas in reality N_c varies as $T^{2/3}$ which will introduce a small error in the given value. Also, the variation of band gap with the temperature was not considered. Otherwise it can be termed as equivalent to the band gap. In calculating the activation energy, equation 2.2 from section 2.4 was used and hence, the activation energy shown in Table 5.6 is the quantity A in that equation and the thermal activation energy is quantity 2A. As explained in that section, one can't deduce with certainty the intrinsic thermal ionization energy, from the slope of log σ versus $1/T$ plots, since the slope may give E or E/2. To be certain, one must see the conductivity temperature
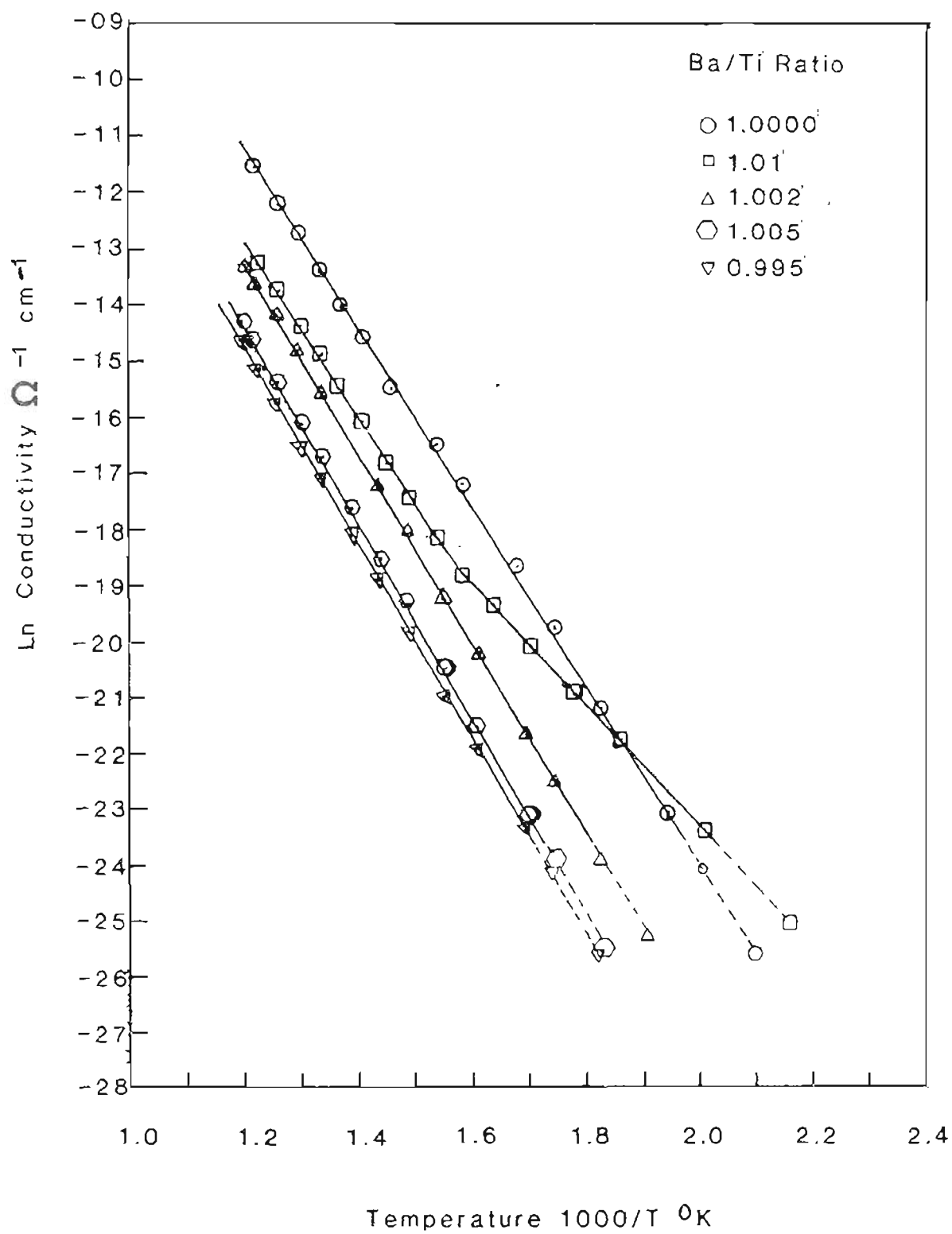
Figure 5.35 CONDUCTIVITY VERSUS TEMPERATURE OF $BaTiO_3$ WITH
THE VARIOUS Ba/Ti RATIO

TABLE 5.6

ACTIVATION ENERGY OF CONDUCTION FOR UNDOPED

$BaTiO_3$ WITH VARIOUS Ba/Ti RATIOS

Ratio	Activation Energy	Intrinsic Thermal Ionization Energy
	A	2A
	eV	eV
1.0000	1.371	2.74
1.005	1.495	2.99
1.01 (368)	0.951	-
1.01 (550)	1.362	2.72
0.995	1.535	3.07
1.0002	1.415	2.83
0.9995	1.398	2.80

relationship from a very low temperature (5 K) to 900 K, and then at a critical temperature the slope will change from E to E/2. Also, the intrinsic ionization energy calculated from the conductivity measurements will always be lower than the similar energy calculated by optical absorption measurements.

In this investigation, it was observed that as the Ba/Ti ratio was changed from unity the thermal ionization energy increased. The thermal ionization energy appears to be a function of the Ba/Ti ratio, and at unity ratio it is a minimum. Considering equation 2.2 from section 2.4 and substituting the values of various constants and assuming for unit volume a value of $N \approx 10^{22}$, then we get $\sigma_o \approx 30$ to 3000 cm^{-1}ohm^{-1} for intrinsic conduction. Taking the value of log σ = -15 at 641 K from Figure 5.35 for the sample with a Ba/Ti ratio of unity we get $\sigma_o \approx 52.54$ ohm^{-1}cm^{-1}, well within the range of intrinsic conductivity. Thus from the data it appears that the conductivity is electronic between 200 and 550^0 C for undoped samples. Glower and Heckman (59) found a single crystal to be an electronic conductor between 100 and 600^0 C, and polycrystalline undoped samples were 100% ionic conductors at 200^0 C but electronic at 500^0 C. If conductivity changes from ionic to electronic, then one should observe a change in the slope of log σ versus 1/T plots, at the point where conductivity becomes predominantly electronic from ionic. This change in slope has not been observed in the present study, thus indicating the conductivity to be predominantly electronic in nature. For the time being, if it is assumed that the conductivity observed is intrinsic, then the energy which is termed as the thermal ionization energy will be near the value of the band gap energy. Branwood and Tredgold (47) found barium titanate to be an intrinsic electronic conductor with an activation energy of 1.22 eV, and the band gap to be 2.44eV. Our results agree with this but the band gap was found to be 2.72 eV. This difference may be due to

difference in the samples; ours are high purity polycrystalline ceramics whereas they used flux grown single crystals. The band gap found by optical methods was 3 eV by Horie (56) and 3.3 eV by DiDomenico (57). The difference between the measurements of the band gap is expected as mentioned earlier.

For the sample with a Ba/Ti ratio of 1.01 two slopes were observed. From 200 to 368^0 C the activation energy was found to be 0.95 eV, and from 368 to 550^0 C the activation energy was found to be 1.33 eV, equivalent to a band gap of 2.66 eV, a value very close to that of the sample with a Ba/Ti ratio of unity. In this sample there was a second phase present as shown in section 5.1.2 but the amount of second phase is very small and probably did not affect the conductivity values.

From Figure 5.35 it is quite evident that, the absolute value of conductivity is highest for the sample with a Ba/Ti ratio of unity. Slight departures from stoichiometry are accommodated by compensating vacancies on oxygen and barium or titanium sites. These vacancies will provide acceptor and donor levels, thus increasing the conductivity of a nonstoichiometric sample. Our data indicates exactly the opposite, which can be explained as follows. When excess barium or titanium is introduced in the barium titanate lattice, and as long as this excess Ba or Ti is compensated by the required amount of oxygen, no localized states are introduced. This excess Ba or Ti and O will produce lattice strain , which may modify the band gap energy. The excess vacancies created on the Ba or Ti and oxygen sites will compensate each other, and overall effect is no net donor and acceptor levels. Apart from these facts, there is always a preponderance of acceptor impurities in this material as suggested by Chan et.al. (18) and an equilibrium number of oxygen vacancies. As samples have been made from the same raw materials, and under exactly the same conditions, all the effects

due to extraneous factors should be the same. As previously noted we are in the intrinsic range and the band gap is varying with the Ba/Ti ratio. Thus at a given temperature the number of carriers is proportional to the band gap.

As is known, the concentration of intrinsic carriers is related to the band gap as shown in equation 5.1 and the electrical conductivity, σ, is related to the carriers as shown in equation 5.2

$$n_i = \left[N_v N_c \right]^{1/2} \exp\left(\frac{-E_i}{2kT} \right) \qquad (5.1)$$

$$\sigma = n_o e \mu_n + p_o e \mu_p \qquad (5.2)$$

where

n_i = no. of charge carriers

N_c, N_v = effective density of states in conduction and

valency band

E_i = band gap

k = Boltzman's constant

T = temperature in kelvin

n_o, p_o = no. of electrons

and holes in respective bands

μ_n = electron mobility

μ_p = hole mobility

e = charge of electron

$$N_c = 2 \left(\frac{m_c k_0 T}{2\pi h^2} \right)^{3/2} \qquad (5.3)$$

substituting values of various constants in eq. 5.3 we get

$$N_c = 4.83 \times 10^{15} \left(\frac{m_c}{m_o} \right)^{3/2} T^{3/2}$$

where

$$m_c = \text{effective mass of electron}$$

Now substituting the values of band gap energy for the two extreme cases from our data at 250 and 500^0 C. [K1, Ba/Ti ratio $= 1.000$, $E_i = 2.72$ eV and K7, Ba/Ti ratio $= 0.995$, $E_i = 3.08$ eV] in equation 5.1 we get

At 250^0 C

$$n_i = (N_c N_v)^{1/2} \times 4.0284 \times 10^{-13} \qquad \text{cm}^{-3} \text{ for K1}$$

$$n_i = (N_c N_v)^{1/2} \times 9.218 \times 10^{-15} \qquad \text{cm}^{-3} \text{ for K7}$$

and at 500^0 C

$$n_i = (N_c N_v)^{1/2} \times 1.358 \times 10^{-9} \qquad \text{cm}^{-3} \text{ for K1}$$

$$n_i = (N_c N_v)^{1/2} \times 9.1028 \times 10^{-11} \qquad \text{cm}^{-3} \text{ for K7}$$

Taking the value of m_c to be 6.5 from the work of Berglund and Bear(54) and assuming $m_c = m_v$ and substituting these values of m_c, m_v in equation 5.3 and similar expression for N_v the values of n_i are as follows.

At 250^0 C

$$n_i = 3.857 \times 10^8 \qquad \text{For K1}$$

$$n_i = 8.826 \times 10^6 \qquad \text{For K7}$$

and at 500^0 C

$$n_i = 2.3358 \times 10^{12} \qquad \text{For K1}$$

$$n_i = 1.565 \times 10^{11} \qquad \text{For K7}$$

Taking the values of conductivity from Figure 5.35 for the K1 and K7 samples at 250^0 C, $\sigma = 1.53 \times 10^{-10}$ and $1.7 \times 10^{-12} \text{ohm}^{-1}\text{cm}^{-1}$, respectively. Thus, there are two orders of magnitude difference in the conductivity values and slightly less in the n_i values. At 500^0 C the conductivities for the K1 and K7 samples are 2.8×10^{-6} and $6.8 \times 10^{-8} \text{ohm}^{-1}\text{cm}^{-1}$, respectively, and exactly the

same order of magnitude difference is observed in their n_i values. This conclusively proves, as suggested by our data, that due to the change in the Ba/Ti ratio from unity, the band gap increased and result is a decreased conductivity.

Also, n_i can be calculated from equation 5.2. Under intrinsic conduction $n_0 = p_0 = n_i$, and taking the value of $\mu_n = 0.1$ cm^{-1}V^{-1}sec^{-1} from references (51-53), and the value of $\mu_p = 10^{-4}$cm^{-1}V^{-1}sec^{-1} and substituting values of conductivity from Figure 5.35 for the K1 and K7 samples at 250 and 500^0 C. We get

At 250^0 C

$n_i = 1.014 \times 10^{10}$ cm^3 for K1

$n_i = 9.692 \times 10^7$ cm^3 for K7

and at 500^0 C

$n_i = 1.846 \times 10^{14}$ cm^3 for K1

$n_i = 4.256 \times 10^{12}$ cm^3 for K7

These calculated values of n_i depend upon the mobility values and are at least 50 times higher than those found from equation 5.1. It should also be noted that the values at lower temperature (250^0 C) are much closer to the values from equation 5.1 than the values at higher temperatures. This is expected due to the following reasons. While calculating N_c and N_v, it was assumed that they are equal. which may not be the case. Sueter (17) gave the ratio of $\left(\dfrac{N_v}{N_c}\right) = 10^4$ and $(N_c N_v)^{1/2} = 5 \times 10^{20}$ at 300 K. If this value of $(N_c N_v)$ is used when calculating n_i (using equation 5.1), then the value of n_i will be close to the value calculated from equation 5.2. The value of m_c used is the room temperature value. In barium titanate the structure changes from tetragonal to cubic as the temperature is changed from room temperature to 200^0 C. This change in the structure changes the band shapes as mentioned in sec. 2.4, which in turn may change the

values of m_c and m_v. The value of the band gap used is the value at 300^0 C. As the temperature increases the band gap decreases. Fridkin (154) gave the relationship of change in the band gap with temperature in the paraelectric phase, as $\left(\dfrac{dE_g}{d_T}\right) = -4\times10^{-4}$ eV deg^{-1}. With the band gap energy of 2.96 eV at 150^0 C, this relation gives a band gap of 2.90 eV at 300^0 C. This change in the band gap will change the n_i value by at least a factor of two. As mentioned in the literature review section, various values of μ_n and μ_p have been quoted, and these values differ by at least an order of magnitude. Considering these various factors we have obtained a good comparison in the value of n_i calculated from equation 5.1 and 5.2, and thus proved our contention that the conductivity in the temperature range investigated is an intrinsic conductivity.

5.3.2 Effect of Nickel Doping

Figure 5.36 shows the log σ versus $1/T$ plots for the doped samples with a Ba/Ti ratio of unity. Nickel was varied from 0.005 to 1 at.%. Behavior is also shown for the 3 at.% doped sample. Similar plots for nickel doping but with the A/B ratio of 0.995 and 1.005 are shown in Figures 5.38 and 5.37, respectively.

In the log σ versus $1/T$ plots a kink is observed, and for any A/B ratio two regions are observed. For sample with an A/B ratio of unity, the activation energy was found to be 0.98 $\pm$ 0.03 eV, for any doping level, from 200 to 325^0 C, and 1.55 $\pm$ 0.05 eV from 325 to 550^0 C depending upon the doping. Basically as doping increased the activation energy decreased, except for the highest doping (1 at.%), for which the activation energy increased. Details are shown in Table 5.7. Similar information for the doped samples with A/B ratios of 1.005 and 0.995 have been tabulated in Table 5.8 and 5.9, respectively. For the samples
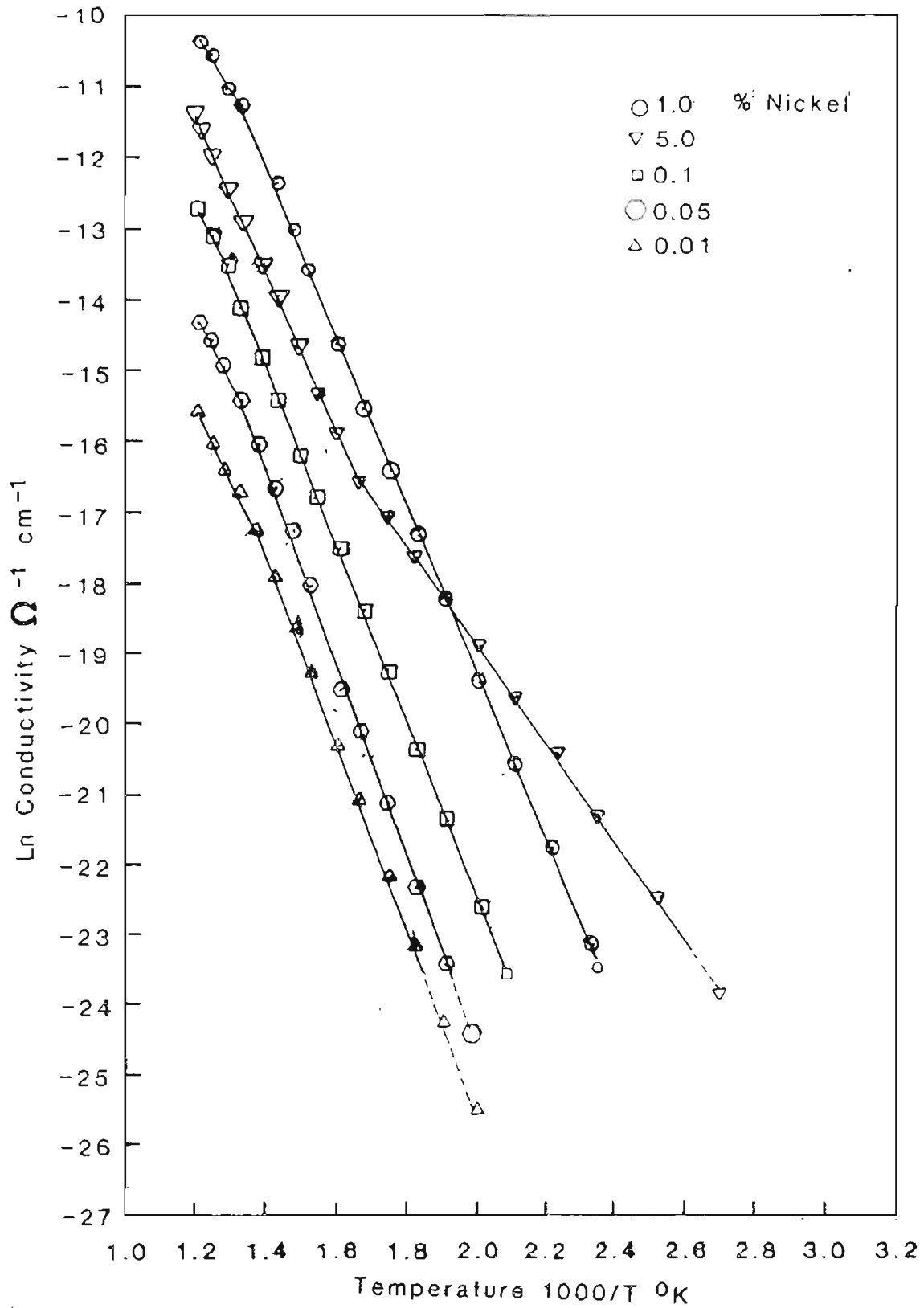
Figure 5.37 CONDUCTIVITY VERSUS TEMPERATURE OF $BaNi_xTi_{1-x}O_3$
WITH THE A/B RATIO OF 1.005
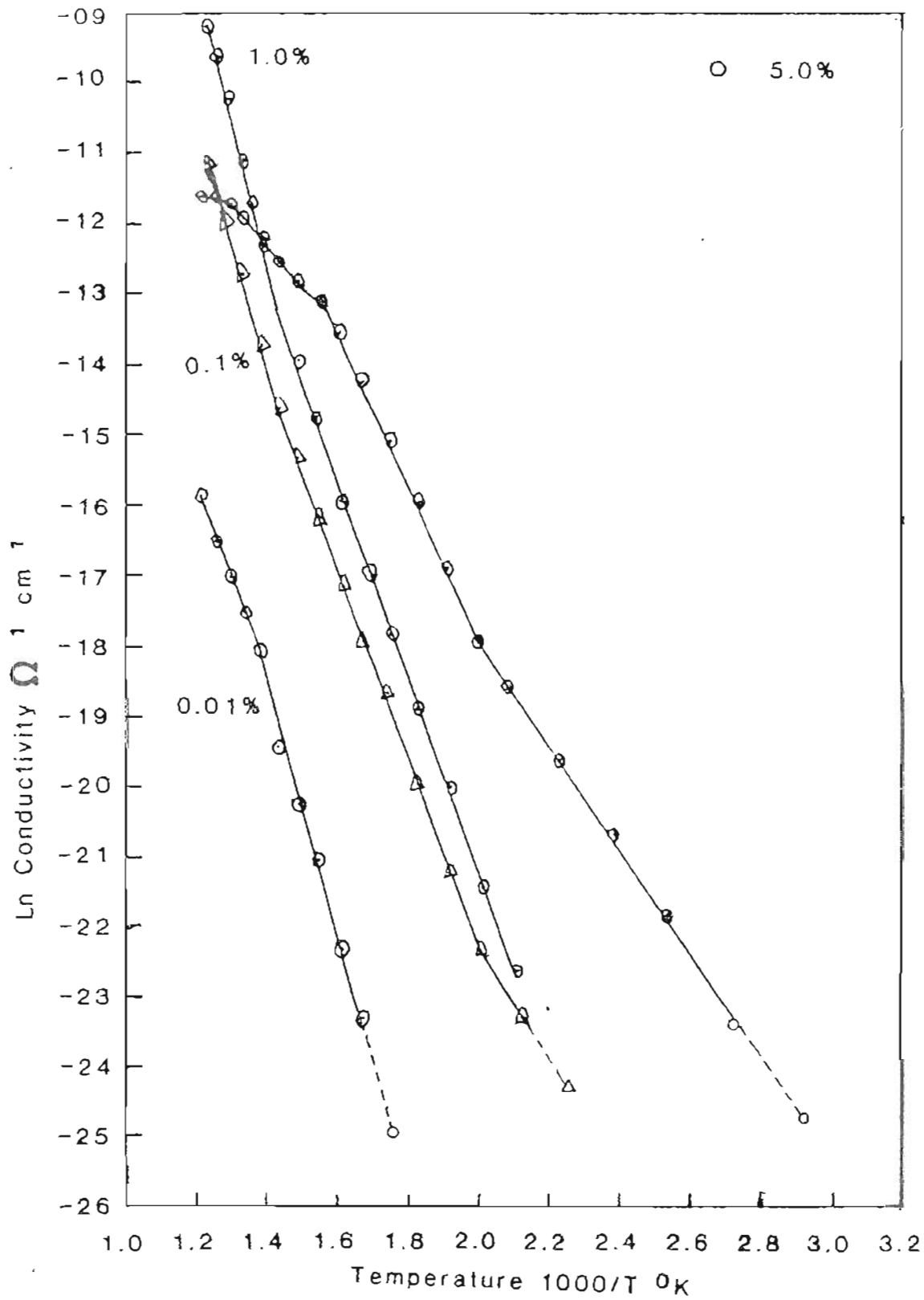
Figure 5.38   CONDUCTIVITY VERSUS TEMPERATURE OF $BaNi_xTi_{1-x}O_3$
WITH THE A/B RATIO OF 0.995

TABLE 5.7

EFFECT OF NICKEL DOPING ON THE ACTIVATION ENERGY

OF $BaTiO_3$ WITH A/B RATIO OF 1.000.

Ni Doping At.% Nickel	Temperature Range ^0C	Activation Energy eV	Temperature Range ^0C	Activation Energy eV
0.8	325-550	1.435	185-325	0.9725
0.1	325-550	1.27	225-325	0.968
0.01	325-550	1.33	200-325	1.07
0.005	325-550	1.55	175-325	0.977

TABLE 5.8

EFFECT OF NICKEL DOPING ON THE ACTIVATION ENERGY

OF $BaTiO_3$ WITH A/B RATIO OF 0.995.

Ni Doping At.% Nickel	Temperature Range ^0C	Activation Energy eV	Temperature Range ^0C	Activation Energy eV
0.01	375-550	1.51	200-375	0.975
0.1	375-550	1.55	200-375	1.11
1.0	375-550	1.65	200-375	1.14

TABLE 5.9

EFFECT OF NICKEL DOPING ON THE ACTIVATION ENERGY

OF $BaTiO_3$ WITH A/B RATIO OF 1.005.

Ni Doping At.% Nickel	Temperature Range ^0C	Activation Energy eV	Temperature Range ^0C	Activation Energy eV
0.01	425-550	1.25	200-425	1.08
0.05	425-550	1.20	200-425	1.11
0.1	425-550	1.28	200-425	1.03
1.0	425-550	1.30	200-425	0.98

with an A/B ratio of 1.005 a transition temperature is found at 425^0 C. The activation energy before the transition is $1.03 \pm .05$ eV and between 1.20 and 1.30 eV after the transition. For doped samples with an A/B ratio of 0.995 the transition temperature was 375^0 C, and the activation energy before the transition was $1.06 \pm .05$ eV, and 1.51 - 1.65 eV after the transition.

In the case of doped samples two slopes were observed in the log σ versus 1/T plots, whereas for undoped samples one slope was observed. Thus, the effect of doping is evident for small doping (0.005 at.%). The activation energy decreased in the temperature range of 200 to 325^0 C for the doped samples compared to the undoped samples. The activation energy remains constant up to 325^0 C, and thus this can be considered as a thermal ionization energy of nickel in barium titanate. Once all the nickel is ionized, intrinsic conduction is observed.

To determine the sign of the predominant electronic carriers a thermoelectric probe, as suggested by Dunlap (153) was tried without success. From the high temperature data, which will be presented in the next section, it appears samples are 'p' type at room temperature, however.

Considering the log σ versus 1/T plots for various doping levels and A/B ratios, the significant fact is that the activation energy before the transition temperature remains constant, and can be averaged to be 1.00 ± 0.08 eV. This constant activation energy coupled with the fact that it is not observed in undoped samples, suggest that this is due to the doping, and hence this is the ionization energy (acceptor ionization energy in the band gap) of nickel in barium titanate. It was shown in the previous section that nickel enters on the titanium site in the lattice and it can take any valency from +3 to +1. Under these conditions it will act as an acceptor, as verified by the high temperature

conductivity data.

After the transition temp., the activation energy again approaches the value close to the value of activation energy in undoped materials. Thus, before the transition temp., we are in the acceptor dominated region and after the transition, we enter the intrinsic region, thus getting the same activation energy as the band gap. This coupled with the fact that, we could not conclusively prove the sign of majority carriers by a thermal probe proves that at high temperature (after transition) we are getting intrinsic conduction and observed energy is the band gap energy.

Figure 5.39 shows the variation of conductivity with doping at 300, 400 and 525^0 C for an A/B ratio of unity. Similar behavior has been observed for two other ratios (0.995 and 1.005). Figure 5.39 indicates that the undoped sample has higher conductivity than the lightly doped (50 ppm) sample. At 500 ppm nickel doping the conductivity was equal to that of undoped sample. It was expected that the conductivity would increase with nickel doping but in the present case it was found to decrease initially. This was not totally unexpected considering the difference in the mobility values of electrons and holes. As a numerical evaluation consider the situation at 325^0 C, where the approximate value of n_i from equation 5.1 will be 1.05×10^{10} cm^{-3} and under the conditions from eq. 5.2 the conductivity σ will be 1.5×10^{-10}cm^{-1}ohm^{-1}. If the doped sample with 10^{12}cm^{-3} ionized acceptors is considered then, under these conditions $n_0 = 10^8$ and $p_0 = 10^{12}$ cm^{-3} and $\sigma = 1.00 \times 10^{-11}$ohm^{-1}cm^{-1}. Thus, by acceptor doping the conductivity actually decreases.

Also from the data it is clear that all the acceptors are not ionized. For the 50 ppm nickel doped sample we have an 7.8×10^{18}cm^{-3} acceptor concentration. If
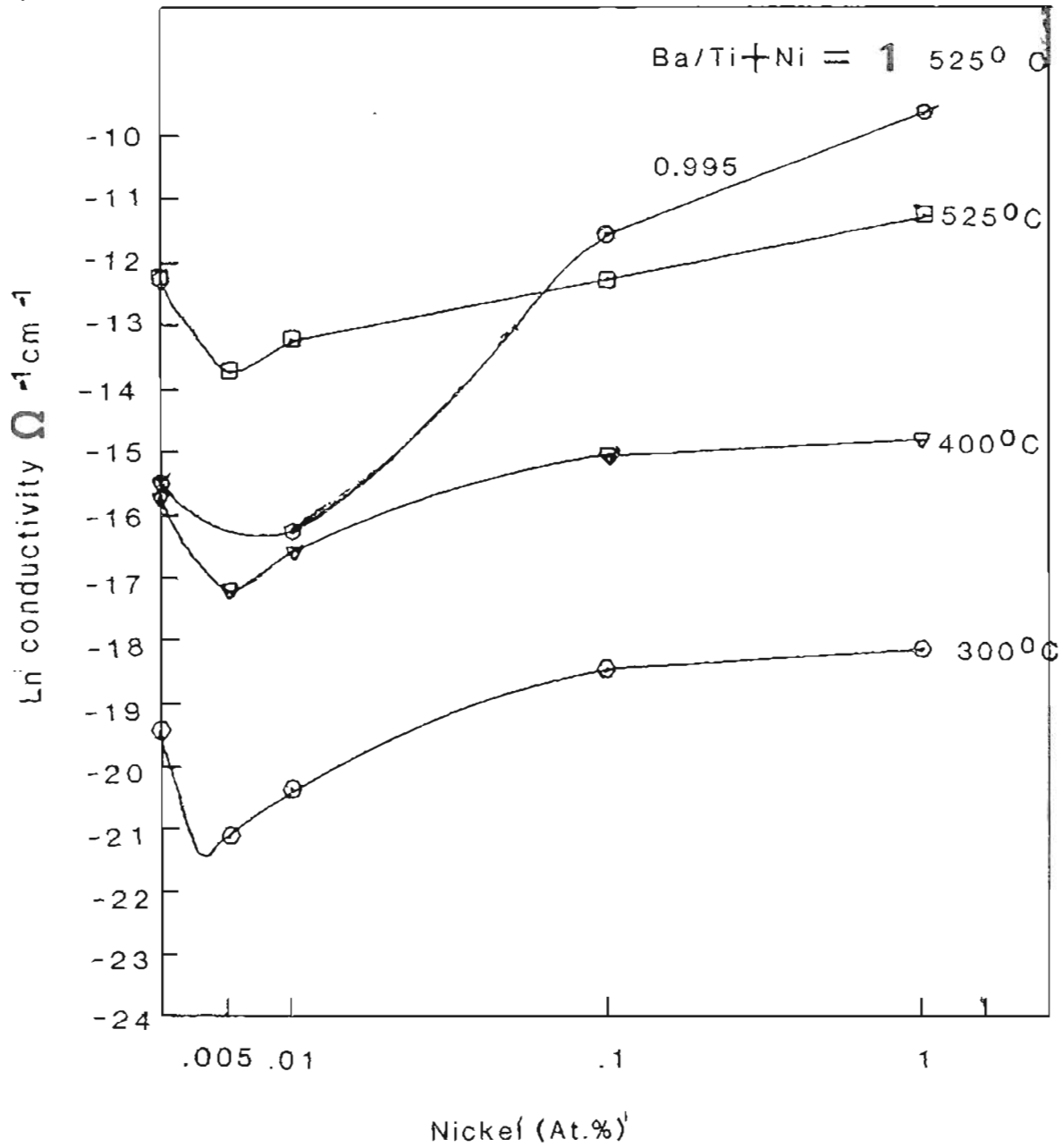
Figure 5.39 EFFECT OF NICKEL DOPING ON THE ELECTRICAL CONDUCTIVITY
OF $BaTiO_3$

all of these would have been ionized, we should have observed an increase in the conductivity, which has not been observed. The ratio of ionized acceptors to the total acceptors is a function of band gap, the ionization energy of the acceptors, and variation of Fermi energy. The variation of Fermi energy could have been calculated provided m_c and m_v are known precisely together with their variation with the temperature. Since these parameters are not known precisely, it is meaningless to calculate the ratio of ionized acceptors.

5.4 ELECTRICAL CONDUCTIVITY AT HIGH TEMPERATURES.

5.4.1 Electrical Conductivity of Undoped Stoichiometric Sample.

Figure 5.40 shows the electrical conductivity of polycrystalline barium titanate, in the temperature range of 900 to 1100^0 C and in equilibrium with oxygen partial pressures between 10^0 to 10^{-21} atm, for a sample with Ba/Ti ratio of unity. In the temperature range studied the sample is p-type at ambient oxygen pressure. For the entire temperature range observed, the conductivity changes from p-type to n-type as the partial pressure of oxygen is decreased. The data were found to be proportional to the -1/5.5 power of oxygen partial pressure, at 1100^0 C, and -1/5 power at 900^0,for the oxygen pressure range of 10^{-12} to 10^{-20} atm., and proportional to the 1/4.2 power of oxygen partial pressure for the pressure range of 10^0 to 10^{-4} atm..

The n-Type Region

In this region the log σ versus log P_{O2} data were linear for at least eight decades of oxygen partial pressure for a given temperature. In addition to the general shape of the curves, the numerical values of the measured conductivity shows a good agreement with the values derived from the literature (15-22). We
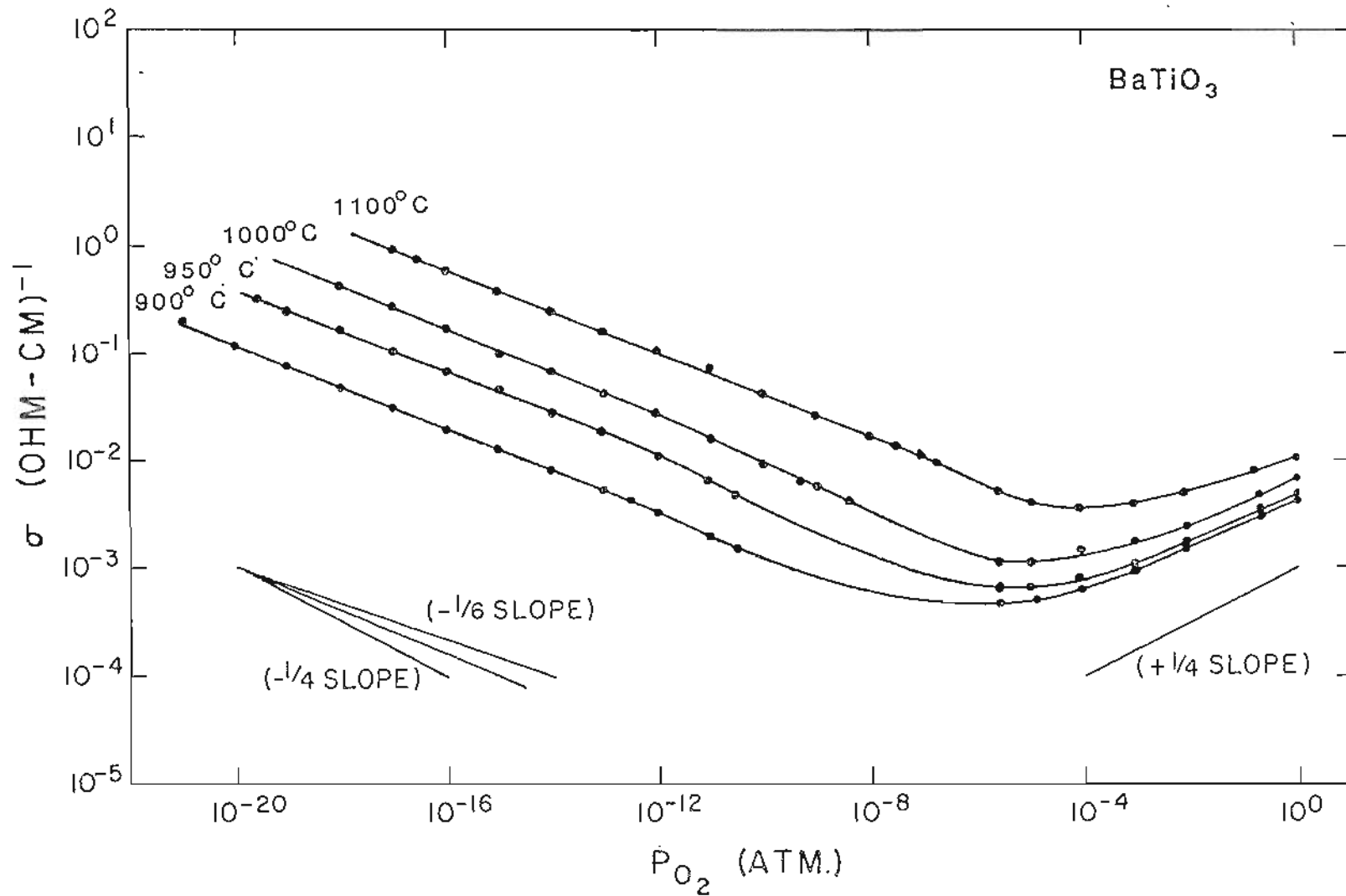
Figure 5.40   THE ELECTRICAL CONDUCTIVITY OF $BaTiO_3$ AS A FUNCTION OF OXYGEN PARTIAL PRESSURE AT VARIOUS TEMPERATURES

have found a slope of approximately -1/5.25 for the log σ versus log P_{O2} in this region, which is similar to that found for barium titanate (15,17-19,22, 23, 29) calcium titanate (35,134), and strontium titanate (37,38, 134).

Although the value of conductivity and general shape of the log σ versus log P_{O2} data were found to be almost the same by various investigators in barium titanate, strontium titanate and calcium titanate, the value of the slope, 1/m, in low partial pressures of oxygen and high temperature was found vary between -1/4 and -1/6. Based on this, two explanations have generally been proposed. It has been proposed that oxygen vacancies are the dominating defect in this region and they may be either singly or doubly ionized. Singly ionized oxygen vacancy should give an ESR signal, since it has a single unpaired electron. Also, Ti^{+3}, with single unpaired electron should give an ESR signal. Our efforts, to observe such a signal from the samples with various Ba/Ti ratios in the oxidized and the reduced state, at room temperature and 77 K, did not yield any signal. This indicates that if any Ti^{+3} is present it is in very small quantity or is not present at all. It also indicates that the oxygen vacancies in the reduced samples are either doubly ionized or not ionized at all at room temperature. Yamada and Miller (155) determined the carrier concentration by Hall effect in a strontium titanate single crystal, quenched from equilibrium with various partial pressures of oxygen and found a relationship similar to ours between electron concentration and the partial pressure of oxygen. The same authors also found that the oxygen vacancies are doubly ionized at room temperature and above.

If we assume that the mobilities of electrons and holes in the measured temperature and P_{O2} ranges are constant, then the conductivity will be directly proportional to [n] or [p] and the log σ versus log P_{O2} curve will be parallel to the dominant defect versus P_{O2} curve as shown in Figure 2.4 with the same slope. If

either $\mu_n \gg \mu_p$ or vice versa then the conductivity may not be parallel to the dominant electronic defect.

In the low P_{O2} range the variation of electrical conductivity with P_{O2} can be explained in terms of the doubly ionized oxygen vacancy model. The reaction involves the removal of oxygen from the normal lattice, thus creating oxygen vacancies which are doubly ionized providing two electrons for conduction. The reaction is

$$O_O = 1/2 O_2 + V_O^{\cdot\cdot} + 2e \tag{5.4}$$

The equilibrium constant for reaction 5.4 is

$$K_{5.4} = [V_O^{\cdot\cdot}] \, n^2 + P_{O2}^{1/2} = \exp\left(\frac{-\Delta G_{5.4}}{RT}\right) \tag{5.5}$$

Where $n = e$ and $\Delta G_{5.4}$ is the Gibbs standard free energy for reaction 5.4. Since two electrons result from each oxygen vacancy, we get the following relationship

$$[n] \approx 2[V_O^{\cdot\cdot}] \tag{5.6}$$

Substituting eq. 5.6 in to 5.5 and the free energy in terms of enthalpy ΔH and entropy ΔS we get

$$K_{5.4} \approx \frac{1}{2} [n] \, n^2 \, P_{O2}^{1/2} = \exp\left[\frac{\Delta S_{5.4}}{R}\right] \exp\left[\frac{-\Delta H_{5.4}}{RT}\right] \tag{5.7}$$

and

$$[n] \approx 2^{1/3} \, P_{O2}^{-1/6} \exp\left[\frac{\Delta S_{5.4}}{3R}\right] \exp\left[\frac{-\Delta H_{5.4}}{3RT}\right] \tag{5.8}$$

Thus, at a constant temperature and when the dominating defects are $[n]$ and $|V_O^{\cdot\cdot}|$, from Eq.5.8 we get, $\log \sigma$ versus $\log P_{O2}$ to be a straight line with $-1/6$ slope. The data in Figure 5.40 and Table 5.10 indicate that the slopes are slightly less than $-1/6$.

TABLE 5.10

P_{O2} DEPENDENCE OF CONDUCTIVITY IN THE REGION

10^{-12} TO 10^{-21} atm. FOR $BaTiO_3$.

Temperature ^0C	m for $\sigma_n \alpha P_{O2}^{-1/m}$
900	5.2
950	5.22
1000	5.36
1100	5.48

Log σ versus log P_{O2} will have the slope of -1/4 if either the oxygen vacancies are singly ionized or if the acceptors are the dominating defect. The case of ionized acceptors as a dominating defects will be treated in detail in the next section.

A transition region between -1/4 and -1/6 slopes will have a in between slope as proposed by Kevane (158). This region can be explained qualitatively as follows. Assume a situation in which given material has a preponderance of acceptor impurities. Chan and Smyth (18) reported the net acceptor impurities of about 130 ppm (atomic) for undoped barium titanate. Our material has been prepared by the same technique, and thus it will have a comparable quantity of acceptor impurities. At any given temperature the ratio of ionized acceptor impurities to total impurities will depend upon, the band gap of the material, the ionization energy of those acceptors in the band gap, and the Fermi energy. Thus it is not difficult to conceive a situation in which total acceptor impurities are greater than the ionized acceptors at a given temperature. i.e. $[\, A_{total} \,] \,>\, [\, A' \,]$. At this temperature reducing the partial pressure of oxygen will create oxygen vacancies which are doubly ionized as given by Eq.5.4. The effect of adding these ionized oxygen vacancies, which act as a donor, is to shift the Fermi energy towards the conduction band in the band gap. This in turn will increase the number of ionized acceptors. Thus the number of electrons available for conduction, will less than given by Eq. 5.6. Since part of them will be required to compensate for the ionized acceptors. Thus we will not realize the slope of -1/6 in log σ versus log P_{O2} plots as given by Eq. 5.8 but the slope will be in between -1/6 and -1/4.

Considering again Eq. 5.8 if we plot the log σ versus 1/T at a constant P_{O2}, then the slope of those plots should give the value of enthalpy for the oxygen

extraction reaction. Of-course this procedure assumes that the mobility of electrons and N_c is constant during the temperature range of interest. Such plots of $\log \sigma$ versus $1/T$ at constant P_{O2} are shown in Figure 5.41 and the values of activation energy calculated from the slopes are listed in Table 5.11. An average value of 7.00 ± 0.05 eV |162.00 kcal/mole| is estimated for ΔH_f. Eror and Smyth (19) reported it to be 5.79 eV, and Chan et.al.(20) reported it to be 5.90 eV . Walter and Grace (37) reported the value of 6.3 eV for strontium titanate. While calculating the enthalpy from eq. 5.8 we have taken $n \propto \dfrac{\Delta H_f}{3KT}$, whereas if all the electrons are not available for the conduction as explained earlier then the factor of 3 in the denominator will be less thus reducing the value of enthalpy.

The p-Type Region [$P_{O2} \geq 10^{-4}$]

In this region the conductivity increased with increasing partial pressures of oxygen which is indicative of p-type conductivity. In this region, the range of linearity is small, which increases with decreasing temperature since the p- to n-transition moves to lower P_{O2}. Table 5.12 shows the slopes of $\log \sigma$ versus $\log P_{O2}$ plots, for the various temperatures. The slopes are very close to 1/4.

Since the range of linearity in this region is small, especially at the high temperatures where the range is only two decades, measurements of slope become tenuous. Values of 1/4 for the slope have been reported by various workers (15,17,19,20), and all of them have invoked the presence of excess acceptor impurities and their related [V_O] in explaining the behavior in this region.

Presence of acceptor impurities is an accepted fact. Part of these acceptor impurities will be ionized as [A'], which will be compensated by ionized oxygen
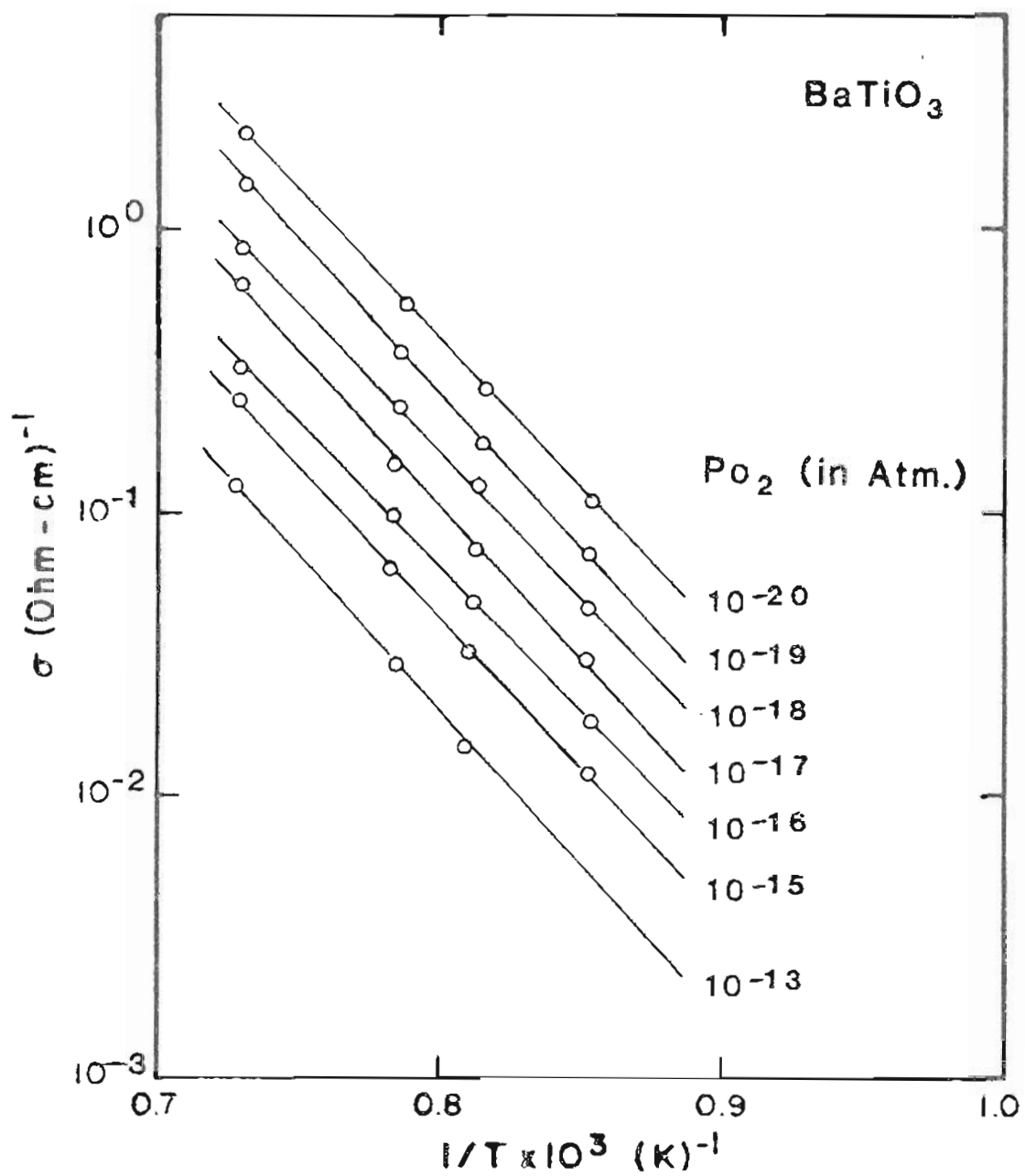
Figure 5.41   TEMPERATURE DEPENDENCE OF CONDUCTIVITY OF BaTiO₃
IN THE N-TYPE REGION

Table 5.11

ACTIVATION ENTHALPY FOR CONDUCTION IN THE REGION

10^{-21} TO 10^{-13} Atm. FOR $BaTiO_3$.

P_{O2}	Activation Enthalpy	
atm.	kcal/mole	eV
10^{-21}	163.78	7.07
10^{-18}	168.64	7.21
10^{-17}	162.39	7.04
10^{-16}	162.90	7.06
10^{-15}	162.20	7.03
10^{-14}	160.40	6.96
10^{-13}	158.16	6.86

TABLE 5.12

P_{O2} DEPENDENCE OF CONDUCTIVITY IN THE

p-TYPE REGION FOR $BaTiO_3$.

Temperature ^0C	m for $\sigma_n \alpha P_{O2}^{1/m}$
900	4.08
950	4.10
1000	4.11
1100	4.11

vacancies $[V_O^{\cdot\cdot}]$ near the stoichiometric region. Thus the condition for charge neutrality in this region will be

$$2\ [V_O^{\cdot\cdot}] = [A'] \tag{5.9}$$

and the oxygen incorporation reaction could be written as

$$[V_O^{\cdot\cdot}] + \frac{1}{2}O_2 = O_O + [2h^{\cdot}] \tag{5.10}$$
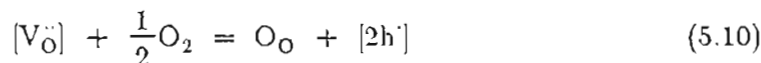
and the equilibrium constant for reaction 5.10 will be

$$K_{5.10} \approx \frac{[p]^2}{[V_O^{\cdot\cdot}]}\ P_{O2}^{-1/2} = \exp\left[\frac{-\Delta G_{5.10}}{RT}\right] \tag{5.11}$$

substituting eq. 5.9 in 5.11 and rearranging terms we get

$$[p] \approx P_{O2}^{1/4}\left[\frac{A'}{2}\right]^{1/2}\exp\left[\frac{\Delta S_{5.10}}{2R}\right]\exp\left[\frac{-\Delta H_{5.10}}{2RT}\right] \tag{5.12}$$

Equation 5.12 will be valid as long as an insignificant quantity of impurity related oxygen vacancies are filled.

For the p-type conductivity the log σ versus log P_{O2} should be a straight line with slope 1/4, which has been observed in the present case if we assume the hole mobility and N_V do not vary with the temperature and P_{O2}. Also at constant P_{O2} the slope of log σ versus 1/T should give the activation enthalpy for the oxygen incorporation reaction. These values are approximately 1.28 eV and are given in Table 5.13. This value has been calculated taking in to account the factor of 2 in the denominator in equation 5.12. Eror and Smyth (19) reported this value to be 0.82 eV and Chan and Smyth (20) found it to be 0.89 eV.

From this model it is expected that the P_{O2} dependence in the low P_{O2} region just below the p-n transition is given by a combination of equation 5.9 and 5.5, which is

$$n \approx \left[\frac{2K_{5.4}}{A'}\right]^{1/2}\ P_{O2}^{-1/4} \tag{5.13}$$

Table 5.13

ACTIVATION ENTHALPY FOR CONDUCTION IN THE

p-TYPE REGION FOR $BaTiO_3$.

P_{O2}	Activation Enthalpy	
atm.	kcal/mole	eV
10^0	29.31	1.28
$10^{-0.699}$	29.52	1.28
$10^{-2.065}$	29.7	1.29
$10^{-3.02}$	29.88	1.30

Thus, immediately following the p-n transition, on the low P_{O2} end one should observe a slope of -1/4. We have not observed such a transition in the undoped samples, but on careful inspection of Figure 5.40, we do see a slope of -1/4 in this range. This region was not investigated due to the limitation of our experimental set up in obtaining P_{O2} value near the p-n transition region.

The Transition Region

Becker and Frederikse (156) showed that the band gap energy, extrapolated to zero temperature, can be determined for a insulator or semiconductor, which shows a p to n transition, from the Arrhenius plots of log conductivity minima versus temperature. The band gap was calculated by taking the minimum values of log conductivity and plotting it against $1/T$, and measuring the slope of such plots. For undoped barium titanate with the Ba/Ti ratio of unity, the value of band gap works out to be 2.75 eV, which is very close to the value obtained (2.72 eV) from the low temperature measurements.

Since our values of conductivity match very closely with those of Eror and Smyth (19), which was on the study of a single crystal, it can be safely concluded that the grain boundaries do not have a pronounced effect on the electrical conductivity.

5.4.2 Effect of Nonideal Cation Ratio

Until now all the studies (15, 17, 18) of nonideal cation - cation ratio in undoped barium titanate were on the titanium rich side. This is mainly because the solubility of BaO in $BaTiO_3$ was considered to be negligible and crystals were inherently titanium rich. Sueter (17) investigated the effect of 1.5 at.% excess BaO on the electrical conductivity and found it to be the same as excess

titanium.

Figure 5.42 shows the plots of log σ versus log P_{O2}, between 825 and 1100^0 C and P_{O2} between 10^0 to 10^{-20} atm. for polycrystalline $BaTiO_3$ with the Ba/Ti ratio of 1.01. As in the case of Ba/Ti $= 1$ the conductivity changes from p-type to n-type as the partial pressure of oxygen is reduced. Figure 5.43 shows the log σ versus log P_{O2} at 1100^0 C for a sample with Ba/Ti ratios of 1.0 and 1.01.

The log σ versus log P_{O2} data are linear in the n-type region for seven decades of P_{O2}, and the slope varies from -1/4.5 to -1/4.85 as shown in Table 5.14. The region of linearity in the p-type region increases with decreasing temperature. The oxygen pressure range is the same for both samples (Ba/Ti $= 1.000$ and 1.01). The p to n transition has moved very little toward lower P_{O2} as evident from Figure 5.43. The slopes measured are shown in Table 5.15 for the p-type region, which has a average value of 1/3.85.

As indicated in section 5.1 this composition does have a small amount of second phase, since the solubility of BaO in $BaTiO_3$ is negligibley small. Presence of a small amount of a second phase will affect the conductivity, and the extent to which this happens will depend upon morphology and properties of the second phase. The effect on conductivity arises from two sources. First, due to the second phase whole sample forms a series parallel network of resistors. Second source is the constant composition of the matrix phase. As evident from the moderate temperature conductivity measurements, this second phase does have an effect. From 300^0 C onward up to 550^0 C the conductivity value is the same as that of the undoped sample with Ba/Ti $= 1$, as are the activation energies for conduction. These measurements also showed that the addition of excess Ba or Ti is not tantamount to the addition of excess acceptors as was believed to
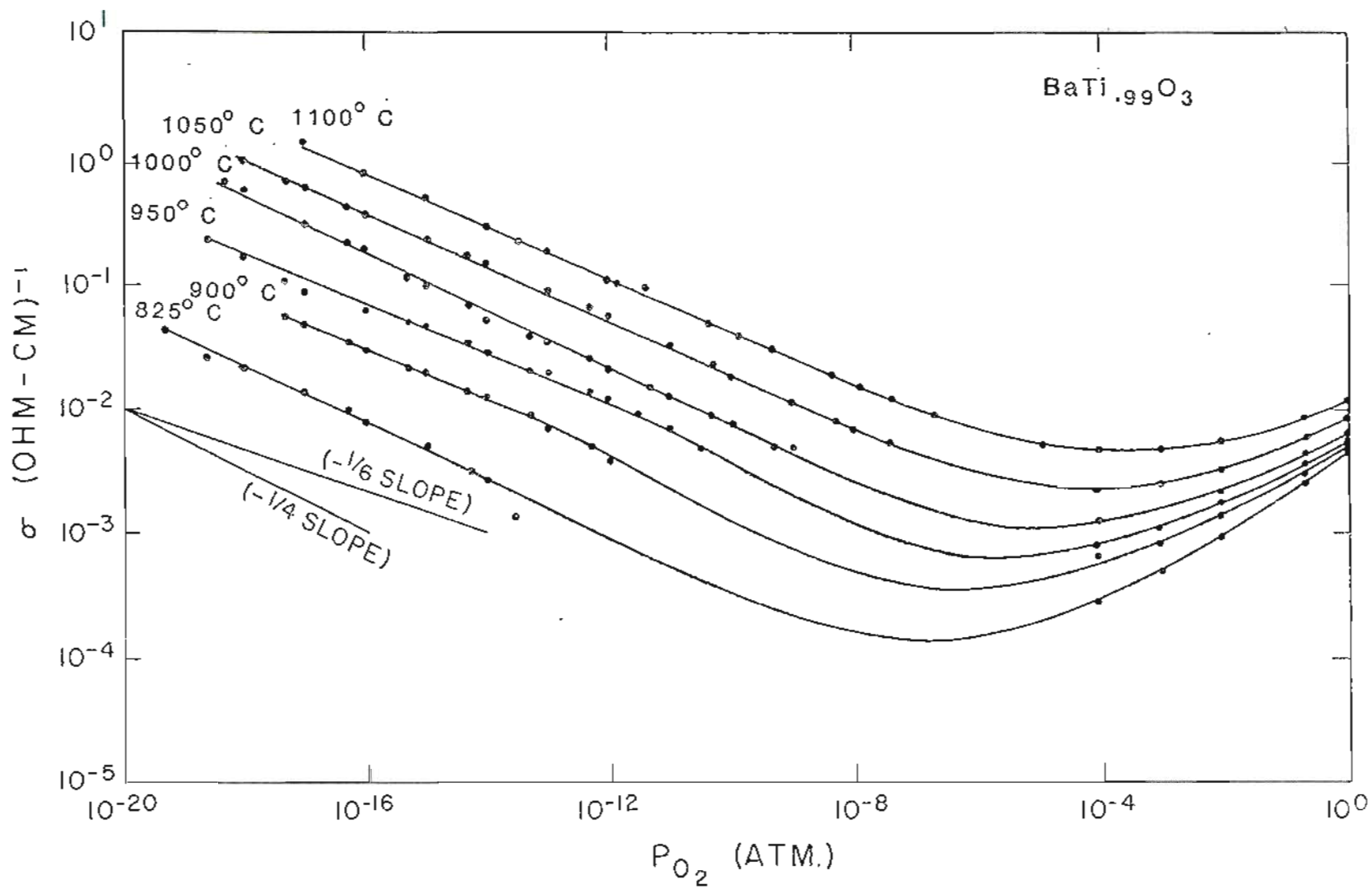
Figure 5.42 THE ELECTRICAL CONDUCTIVITY OF BaTi$_{.99}$O$_3$ AS A FUNCTION OF OXYGEN PARTIAL PRESSURE AT VARIOUS TEMPERATURES
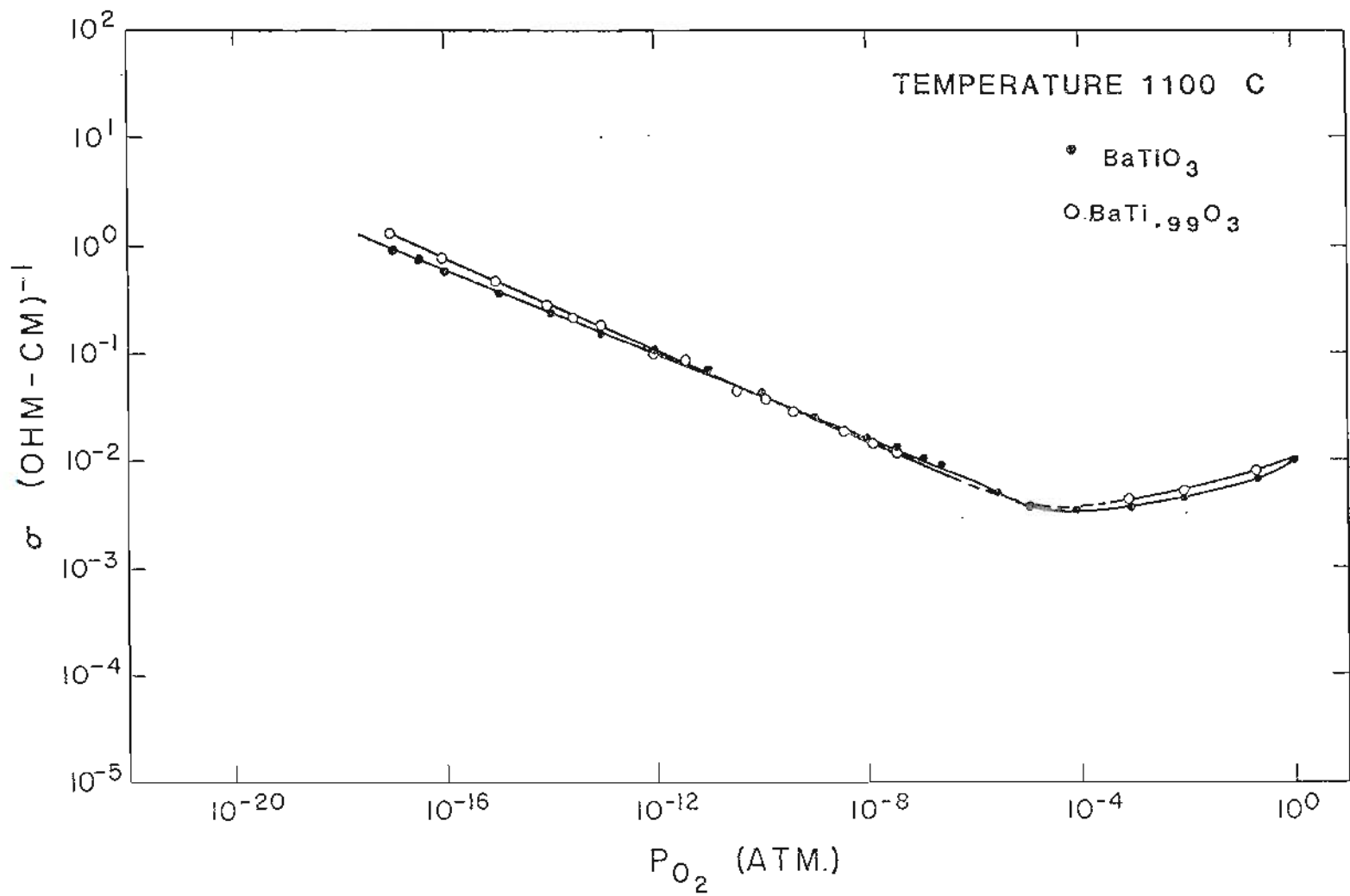
Figure 5.43 ELECTRICAL CONDUCTIVITY OF OF BaTiO₃ AND BaTi.₉₉O₃
AT 1100⁰ C

TABLE 5.14

P_{O2} DEPENDENCE OF CONDUCTIVITY IN THE REGION 10^{-12}

TO 10^{-21} atm. FOR $BaTiO_3$ WITH Ba/Ti RATIO OF 1.01

Temperature ^0C	m for $\sigma_n \alpha P_{O2}^{-1/m}$
825	4.50
900	4.90
950	4.90
1000	4.80
1050	4.85
1100	4.85

TABLE 5.15

P_{O2} DEPENDENCE OF CONDUCTIVITY IN THE

p-TYPE REGION FOR $BaTiO_3$ WITH Ba/Ti RATIO OF 1.01

Temperature ^{0}C	m for $\sigma_n \alpha P_{O2}^{1/m}$
825	3.7
900	3.75
950	3.80
1000	3.85
1050	3.87
1100	3.91

be happening. Excess Ba or Ti may be accommodated by vacancies on the other cation and oxygen sublattice or the formation of neutral vacancy pair $(V_O^{..}, V_{Ba}'')$. At all times an extrinsic impurity , which is normally an acceptor will dominate. If this is so, the samples which were prepared under identical conditions with various Ba/Ti ratios, should give the same behavior in variation of conductivity with P_{O2}. Inspection of Figure 5.43 shows that is indeed the case. There are small differences in the slopes, which may be due to the small amount of second phase.

Activation enthalpies as derived in the previous section have been calculated and the values are reported in Table 5.16 for the n-type region and in Table 5.17 for the p-type region. In the n-type region the activation enthalpy is found to be 6.44 eV (149.12 kcal/mole), and 1.04 eV (24 kcal/mole) in the p-type region. These values are close to the values of sample with Ba/Ti = 1. The band gap calculated from the minima of conductivity is 2.74 eV.

5.4.3 Effect of Acceptor Doping

The electrical conductivity of polycrystalline nickel doped samples $BaNi_xTi_{1-x}O_3$ (with x = 0.005, 0.01, 0.1 and 1 at.%) with P_{O2}, at various temperatures is shown in Figures 5.44 to 5.47. Figures 5.48 and 5.49 show the conductivity with respect to the partial pressures of oxygen for undoped and four nickel doped samples at 950 and 1100^0 C, respectively.

From Figure 5.44 which is for the 0.005 at.% nickel doped sample, 3 different regions are observed. For oxygen partial pressures $< 10^{-13}$ atm. a slope of -1/5.25 is found, for oxygen partial pressures between 10^{-12} and 10^{-9} atm. a slope of -1/4.3 is found and for oxygen partial pressures $> 10^{-5}$ atm. a slope of 1/4.2 is observed. For all other nickel doped samples except for 1 at.% doped

Table 5.16

ACTIVATION ENTHALPY FOR CONDUCTION IN THE REGION 10^{-18}

TO 10^{-12} Atm. FOR $BaTiO_3$ WITH Ba/Ti RATIO OF 1.01

P_{O2}	Activation Enthalpy	
atm.	kcal/mole	eV
10^{-18}	148.91	6.43
10^{-17}	148.97	6.43
10^{-16}	149.13	6.44
10^{-15}	149.10	6.43
10^{-14}	149.10	6.43
10^{-13}	149.23	6.44
10^{-12}	149.40	6.45

Table 5.17

ACTIVATION ENTHALPY FOR CONDUCTION IN THE

p-TYPE REGION FOR $BaTiO_3$ WITH Ba/Ti RATIO OF 1.01.

| P_{O2}	Activation Enthalpy	
atm.	kcal/mole	eV
10^0	23.92	1.03
$10^{-0.599}$	24.05	1.04
$10^{-2.065}$	24.1	1.04
$10^{-3.02}$	23.93	1.03
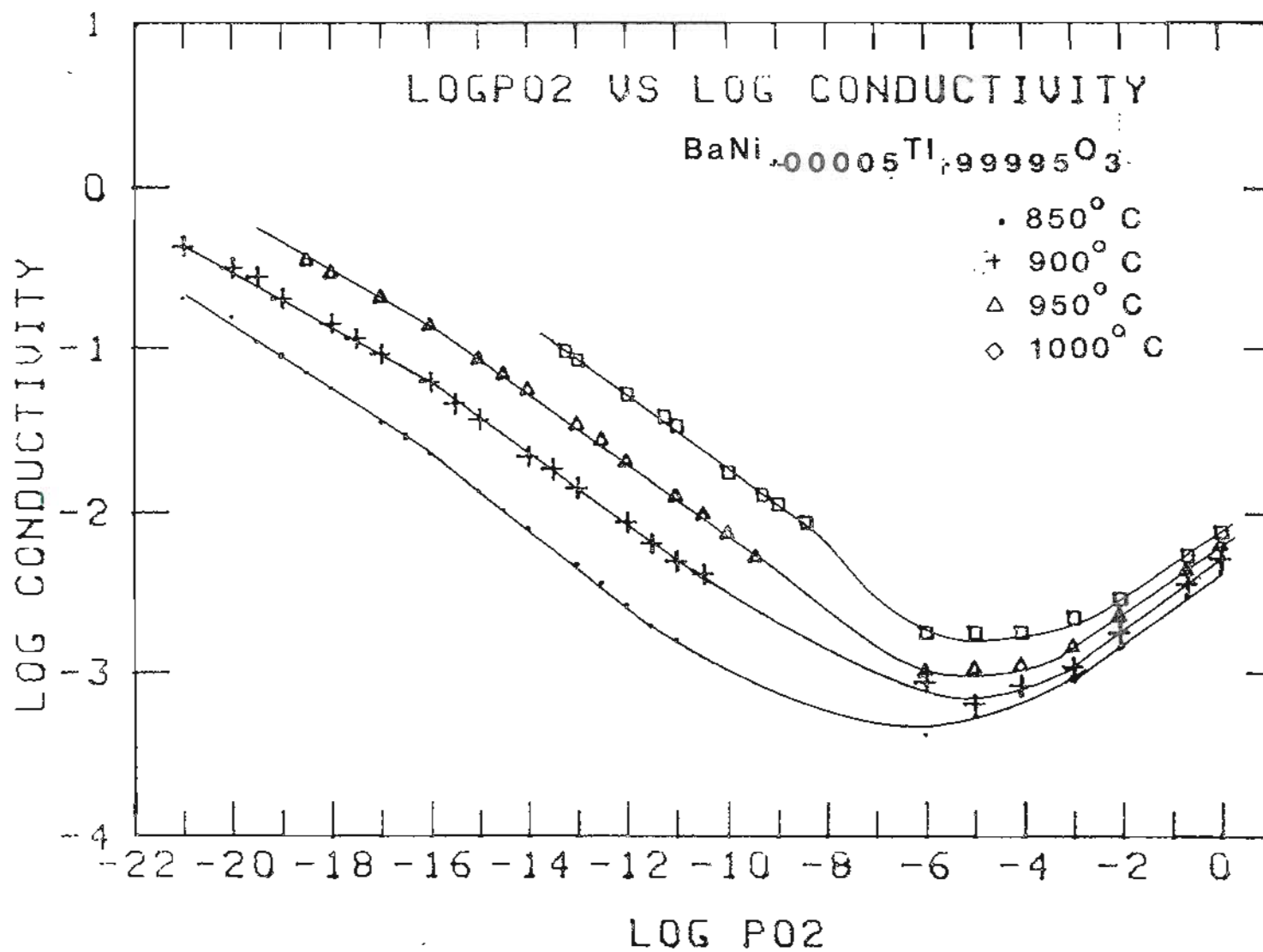
Figure 5.44 THE ELECTRICAL CONDUCTIVITY OF BaNi$_{.00005}$Ti$_{.99995}$O$_3$ AS A FUNCTION
OF OXYGEN PARTIAL PRESSURE AT VARIOUS TEMPERATURES
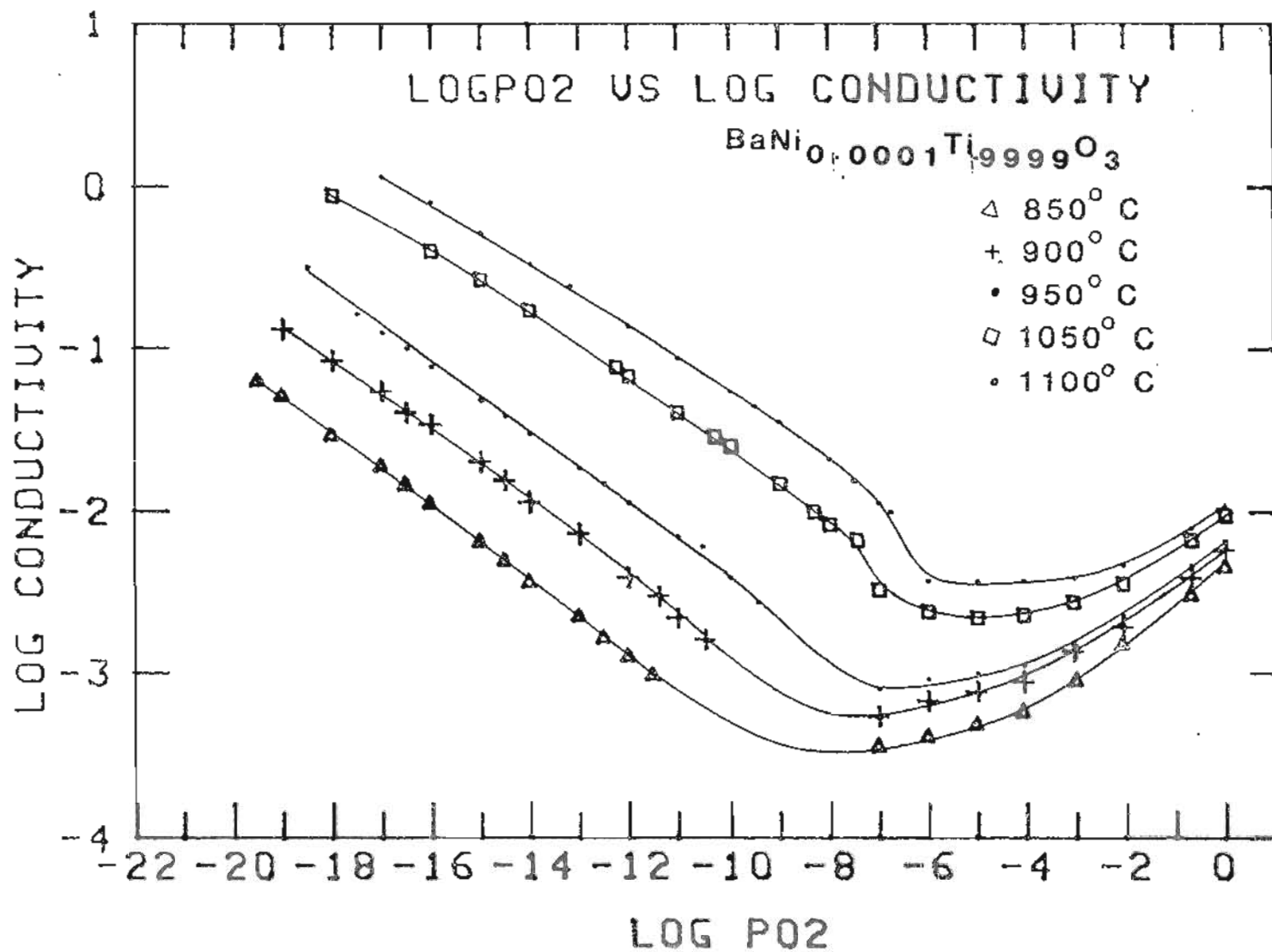
Figure 5.45 THE ELECTRICAL CONDUCTIVITY OF $BaNi_{.0001}Ti_{.9999}O_3$ AS A FUNCTION
OF OXYGEN PARTIAL PRESSURE AT VARIOUS TEMPERATURES
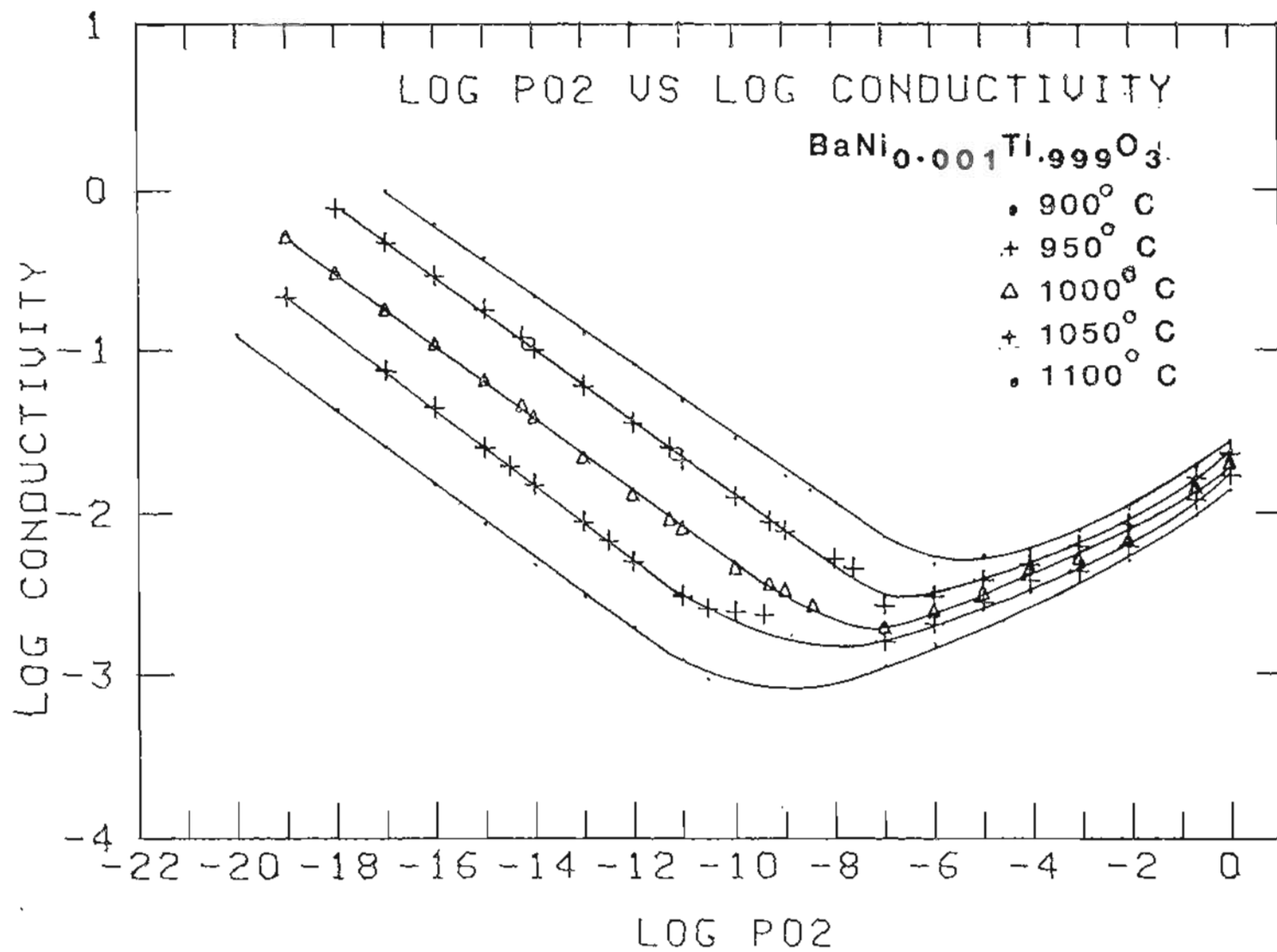
Figure 5.46   THE ELECTRICAL CONDUCTIVITY OF $BaNi_{.001}Ti_{.999}O_3$ AS A FUNCTION
OF OXYGEN PARTIAL PRESSURE AT VARIOUS TEMPERATURES
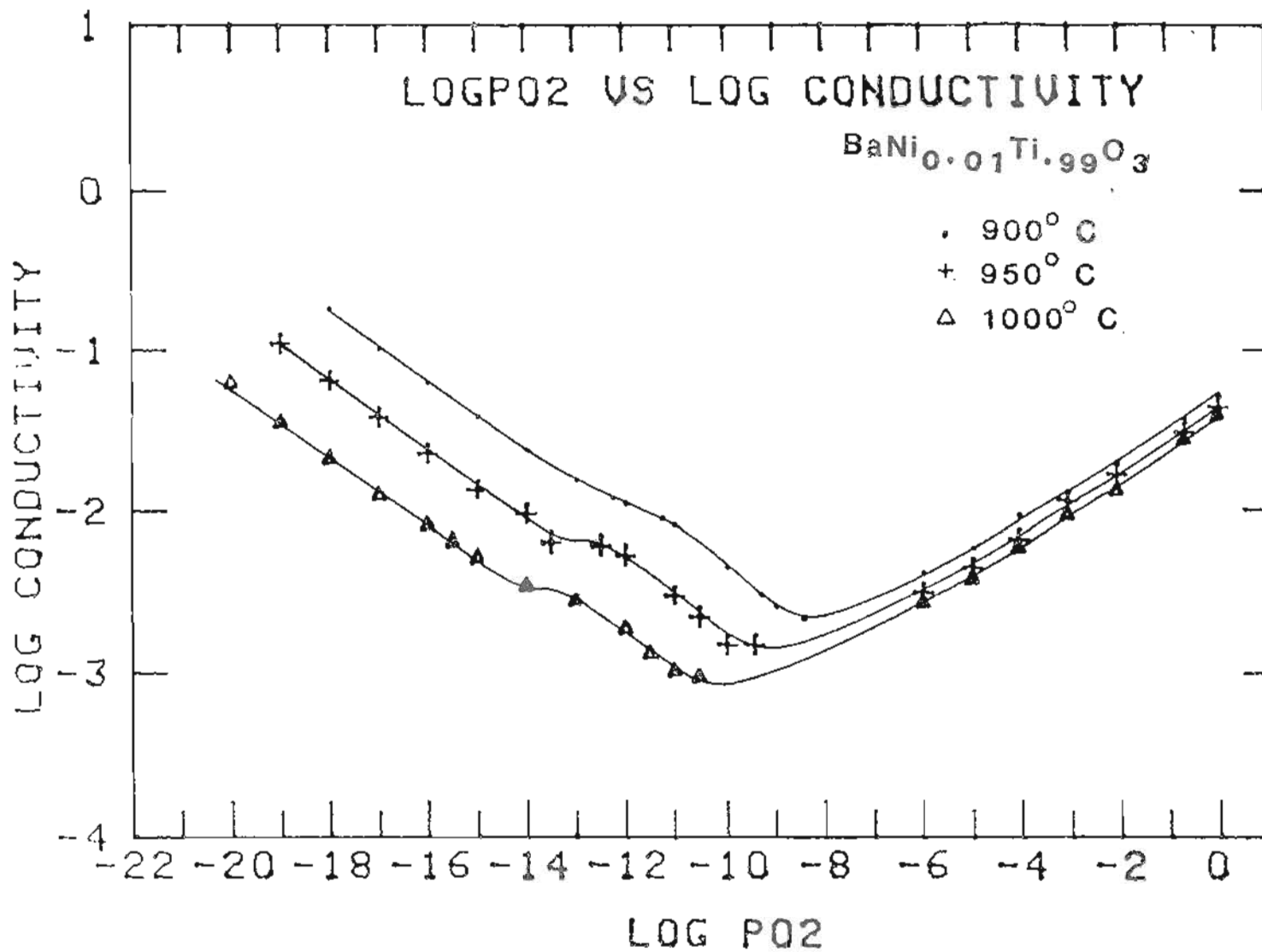
Figure 5.47 THE ELECTRICAL CONDUCTIVITY OF $BaNi_{.01}Ti_{.99}O_3$ AS A FUNCTION OF OXYGEN PARTIAL PRESSURE AT VARIOUS TEMPERATURES
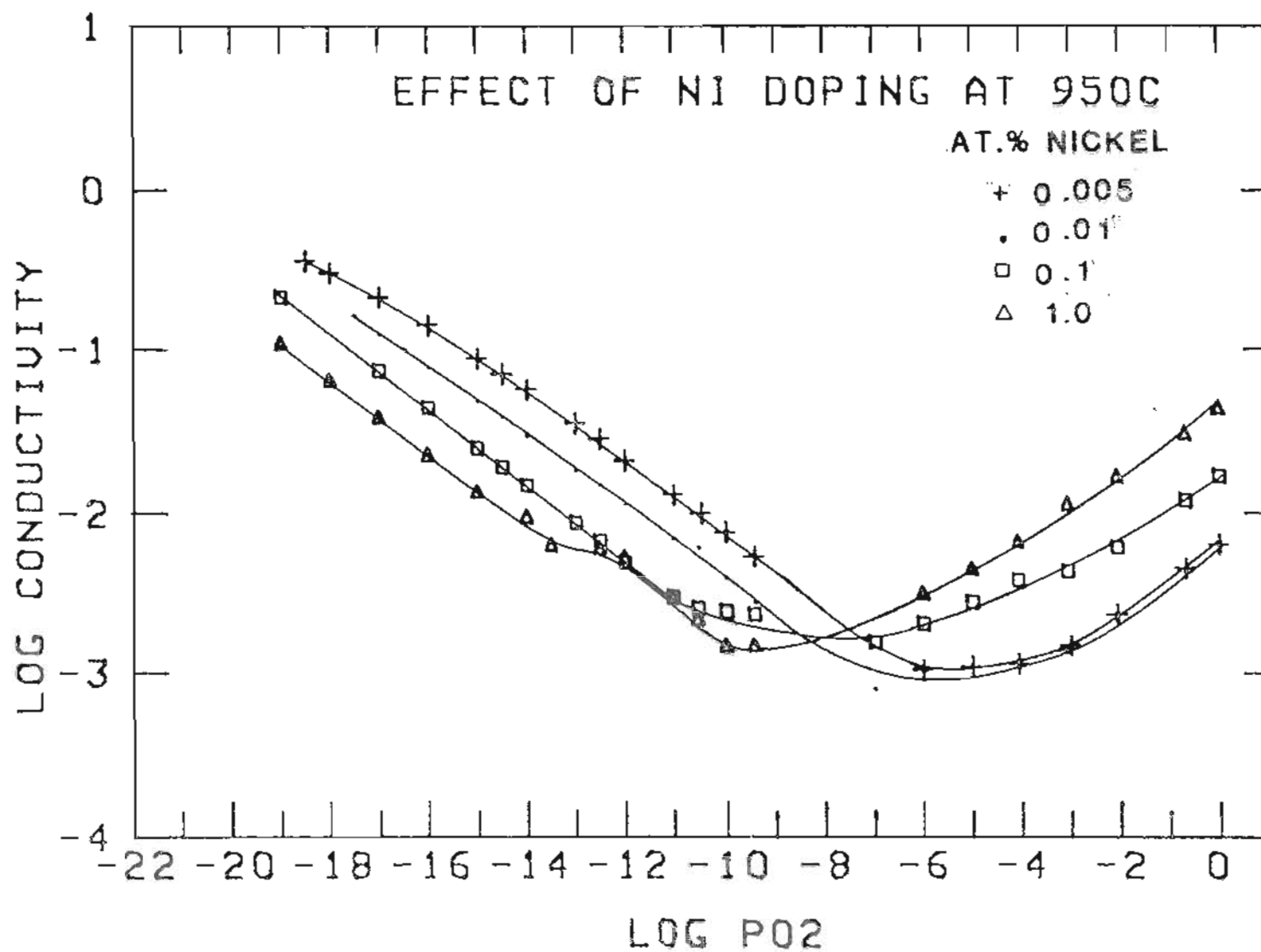
Figure 5.48   ELECTRICAL CONDUCTIVITY OF $BaNi_{.00005}Ti_{.99995}O_3$, $BaNi_{.0001}Ti_{.9999}O_3$, $BaNi_{.001}Ti_{.999}O_3$ AND $BaNi_{.01}Ti_{.99}O_3$ AT 950^0 C
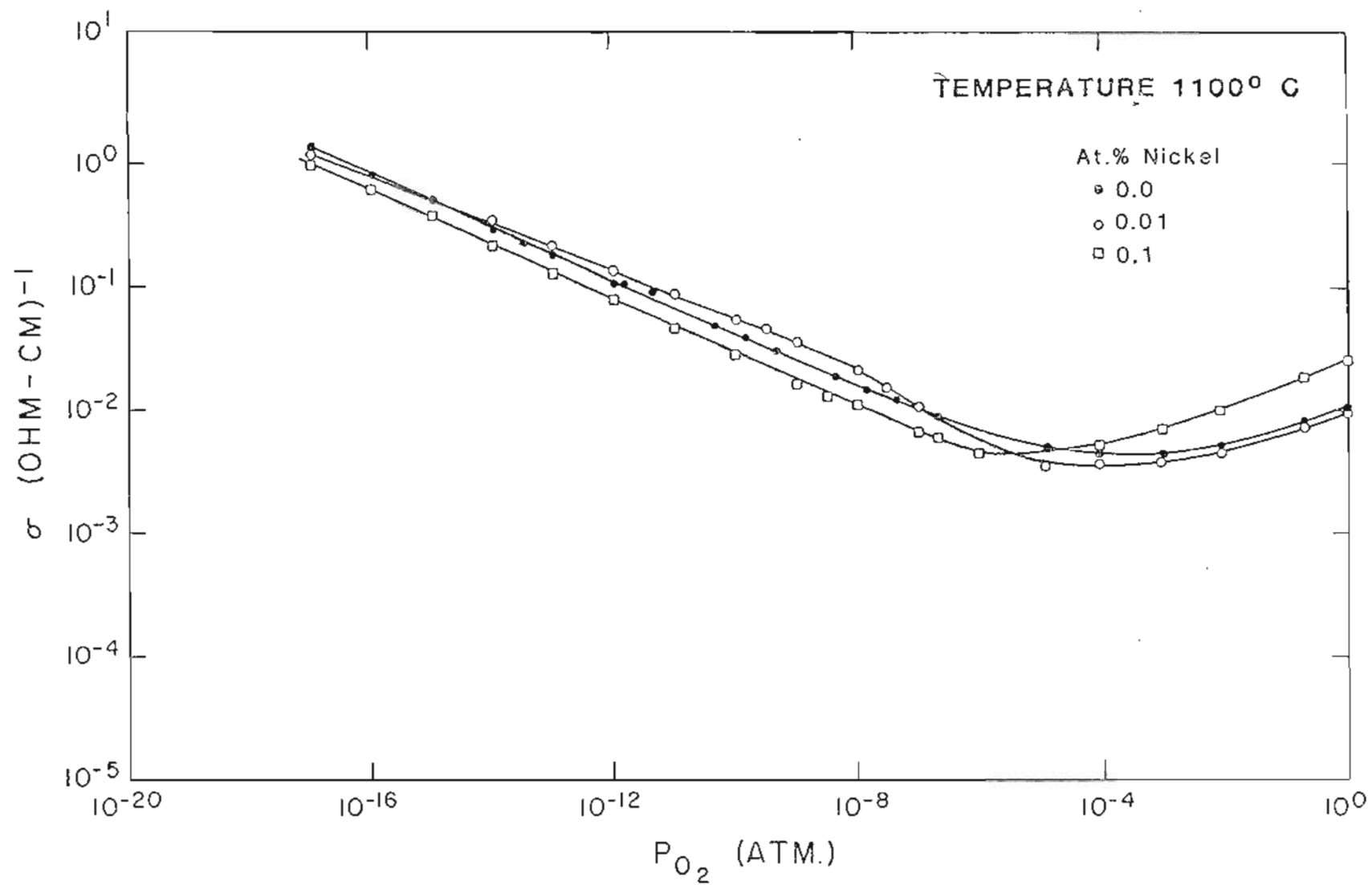
Figure 5.49   ELECTRICAL CONDUCTIVITY OF $BaTiO_3$, $BaNi_{.0001}Ti_{.9999}O_3$
AND $BaNi_{.001}Ti_{.999}O_3$ AT 1100^0 C

sample, only two regions were observed. For oxygen partial pressures $< 10^{-9}$ atm. log conductivity is proportional to the -1/4 power of oxygen partial pressure, and it is proportional to the 1/4 power of oxygen partial pressure, for oxygen partial pressures $> 10^{-5}$ atm..

It has already been shown in Sec. 5.2 that, nickel substitutes for titanium in the lattice. From Figures 5.48 and 5.49 it is clear that as the concentration of nickel increases the p-type conductivity increases, at a given partial pressure of oxygen and temperature. Also the value of σ minimum changes very little but shifts to lower partial pressures of oxygen, and the n-type conductivity values decrease. Minimum in the conductivity is shifted by an order of magnitude, for 0.005 at.% doping at 950^0 C, at lower oxygen partial pressure in comparison to the undoped sample and it is more than three order of magnitude for 1 at.% nickel doping (Fig. 5.48 and 5.49). The conductivity minima shifts to higher oxygen partial pressure as the temperature is increased for any given nickel concentration.

The slopes of log σ versus log P_{O2} in the n-type region are given in Table 5.18. The values of m in the σ_n α $P_{O2}^{-1/m}$ are in the range of 4 to 4.8. As explained in the case of undoped samples, the charge neutrality condition for these samples will be

$$[A^{'}] \; = \; 2 \; [V_{O}^{\cdot\cdot}] \tag{5.14}$$

For sample with the lowest doping, i.e. 0.005 at.% , after exhausting all ionized acceptors, we see the change in the neutrality condition and the neutrality condition is the same as Eq. 5.6. Changes in the slope are also observed for this sample, the slope changes from -1/4.5 to -1/5.25. Also in this sample as the temperature is increased the partial pressure of oxygen at which the slope changes

Table 5.18

P_{O_2} DEPENDENCE OF CONDUCTIVITY IN $BaNi_xTi_{1-x}O_3$

IN THE n-TYPE REGION

Temp. ^{0}C	x in atom %	m for $\sigma_p \alpha P_{O2}^{-1/m}$			
		0.005	0.01	0.1	1.0
850		5.15, 4.44	4.29	-	-
900		5.23, 4.42	4.32	4.29	4.92, 4.1
950		5.26, 4.52	4.76	4.34	4.5, 3.92
1000		4.49, -	-	4.38	4.20, 4.20
1050		-	4.81	4.45	-, -
1100		-	5.09	4.5	

from -1/4.5 to -1/5.25 decreased, which is expected if the behavior is controlled by the ionized acceptors.

Nickel can exist in two valency states, Ni^{+3} and Ni^{+2}. We could not detect an ESR signal to decide the valence state of nickel. Ihrig (157) observed the valence state of various 3d doping elements in a $BaTiO_3$ matrix by a magnetic method, and proposed nickel to be present as Ni^{+2} in the oxidized condition. His assignment was tentative. Subsequently Hagemann and Ihrig (76) measured the valence state of various 3d elements in the oxidized and reduced state by magnetic and thermogravimetric methods. In the case of nickel they could not obtain information about the valence by the magnetic susceptibility method but by the thermogravimetric method, they decided nickel exists as Ni^{+2} in the $BaTiO_3$ lattice under both oxidized and reduced conditions. Considering the accuracy of the thermogravimetric method and the very small changes in weight which have been observed, the results should be taken very cautiously. Our results of moderate temperature electrical conductivity suggest, nickel substituting for titanium as Ni^{+3}. Also, the electrical conductivity data, at high temperature for 1 at.% doping support this view. It can be easily observed from Figure 5.47 that for the n-type region there is an initial -1/4 slope until the partial pressure of oxygen is approximately 10^{-12} atm.. Upon further reduction the conductivity remains nearly constant, and for $P_{O2} < 10^{-13}$ atm. the log σ versus log P_{O2} data have a slope of -1/4. This behavior can be explained on the basis of nickel reducing its + valence, thus supplying additional holes at that reduction, which in turn causes the n-type conductivity either to remain constant, or to increase very little. There are two possibilities, either nickel changing from Ni^{+3} to Ni^{+2} or changing from Ni^{+2} to Ni^{+1}. Out of these two possibilities the first one is energetically more favorable and our moderate temperature (where composition

remains unchanged) conductivity data supports that conclusion. These results also proves that nickel substitutes on the titanium site in the barium titanate lattice. Since if nickel would have substituted on the barium site·then, the changes in the conductivity data as observed here would not have been observed.

The different valence states of nickel will not change the slopes but will change the conductivity value. Thus for nickel as Ni^{+3} the neutrality condition will be as shown in Eq. 5.14. Taking this charge neutrality condition along with the mass action expression for the oxygen extraction reaction, Eq. 5.4, we get

$$n \ \alpha \ P_{O2}^{-1/4} \tag{5.15}$$

Thus, in the n-type region, conductivity should vary as -1/4 power of oxygen partial pressure. The observed data are very close to this value especially at high temperature and high doping. The activation enthalpy for the conduction can be obtained from the temperature dependence of conductivity at constant oxygen partial pressure. The calculated average values of the activation enthalpy for conductance are 4.24 eV (97.8 kcal/mole), 4.61 eV (106.25 kcal/mole), 5.16 eV (119 kcal/mole) and 5.2 eV (119.8 kcal/mole) for the 0.005, 0.01, 0.1 and 1 at.% nickel doped samples, respectively. Table 5.19 shows the actual values at the various partial pressures of oxygen.

In the p-type region, the observed slopes of log σ versus log P_{O2} plots are in the range of 1/4 to 1/4.8 for all doping levels. For the sample with 0.01 at.% nickel doping, the slopes are on the higher side and range from 1/4.95 to 1/5.2. The actual values are shown in Table 5.20. The activation energy for conduction in this region is shown in Table 5.21. The average values of activation energies are 1.2 eV (27.59 kcal/mole), 1.27 eV (29.37 kcal/mole), 0.997 eV (22.99 kcal/mole) and 1.00 eV (23.06 kcal/mole) for 0.005, 0.01, 0.1 and 1 at.% nickel doped samples, respectively.

Table 5.19

ACTIVATION ENTHALPY FOR CONDUCTION IN $BaNi_xTi_{1-x}O_3$

IN THE n-TYPE REGION

PO_2	x in atom %	Activation enthalpy kcal/mole			
		0.005	0.01	0.1	1.0
10^{-11}		111.68	-	-	118.07
10^{-12}		111.54	114.03	120.49	
10^{-13}		-	110.83	120.31	
10^{-14}		-	107.54	120.05	110.19
10^{-15}		102.88	106.05	119.36	118.08
10^{-16}		99.73	104.85	119.25	117.71
10^{-17}		96.75	105.07	118.24	118.82
10^{-18}		97.85	106.08	118.75	119.05
10^{-19}		96.50	108.10	119.03	120.04
10^{-20}		96.40	109.1	119.56	120.83

Table 5.20

P_{O2} DEPENDENCE OF CONDUCTIVITY IN $BaNi_xTi_{1-x}O_3$

IN THE p-TYPE REGION.

Temp. ^{0}C	x in atom %	0.005	0.01	0.1	1.0

Temp. ^{0}C	x in atom %	0.005	0.01	0.1	1.0
850		4.15	4.95		
900		4.21	4.98	4.3	4.5
950		4.23	5.03	4.31	4.7
1000		4.27	5.10	4.35	4.80
1050		-	5.17	4.36	
1100		-	5.22	4.36	

m for $\sigma_p \alpha P_{O2}^{1/m}$

Table 5.21

ACTIVATION ENTHALPY FOR CONDUCTION IN $BaNi_xTi_{1-x}O_3$

IN THE p-TYPE REGION

PO$_2$	x in atom %	Activation enthalpy kcal/mole			
		0.005	0.01	0.1	1.0
10^0		21.60	24.43	22.74	22.89
10^{-1}		25.43	25.85	22.31	22.73
10^{-2}		26.38	26.61	22.85	23.05
10^{-3}		32.09	35.09	23.38	22.70
10^{-4}		32.45	34.89	23.13	23.13
10^{-5}				23.53	23.52
10^{-6}					23.41

As discussed earlier nickel will exist as Ni^{+3}, under high partial pressures of oxygen. Thus the neutrality condition would be the same as Eq. 5.14

$$[A'] \approx 2 [V_{\ddot{O}}] = Const.$$

where $[A']$ represents Ni^{+3} on Ti^{+4} site, i.e. single level acceptor Ni_{Ti}'. Added oxygen will fill the oxygen vacancies related to the acceptor impurities realizing two holes. As explained in the previous section , Chapter 2 and Figure 2.4, the electron concentration in this region varies as -1/4 power, and the holes as 1/4 power, of oxygen partial pressure. Initially, electrons are in a majority, but as shown in Figure 2.4 at some point [p] becomes greater than [n] and then the p-type varies as the 1/4 power of oxygen partial pressure. Our data are in good agreement with the theoretically predicted model.

5.5 DC Degradation

For all samples, doped and undoped, current - d.c. field measurements were made at three different temperatures and various field strengths from 0.083 to 17 kV/cm. Current was measured with respect to time, at field strengths of 0.083 to 17 kV/cm, until a steady state or minimum current was achieved. In some cases it took 50 hrs to achieve the steady state current. In the plots of log current versus log field or log current versus $\sqrt{field}$ the steady state or minimum value of current was used, as proposed by Payne (5).

For most of the degradation studies so far, in the plots of log current versus log field, the value of current used was the value of current at some fixed time interval, after applying the field. Our data clearly shows that if current at some arbitrary time is used (which may not be the true equilibrium current, since some samples took 50 hrs to reach the steady state current), then the data will be meaningless.

Generally two types of behavior were observed in the current versus time data. Figures 5.50 and 5.51 show the two types of isothermal current versus time characteristics at various field levels, for an undoped sample with an A/B ratio of unity and doped sample with A/B ratio of unity, respectively, at 150^0 C. All the samples have characteristics similar to these two samples. In one case the current starts falling and remains steady for 10 to 30 hrs, whereas in the second case after a steady current, the current starts increasing with time, and the higher the electrical stress the greater the rate of rise of current. Higher temperatures also result in greater rates of increase of current for a given field. As mentioned previously the value of the steady state current or minimum current is used while plotting log current versus log field strength. Undoped samples with Ba/Ti ratios of 1.005 and 0.995 have characteristics similar to the first case (Fig 5.50) and steady state current was achieved in relatively short time (30 to 60 minutes.) at all temperatures and field levels up to 2kV/cm. At field strengths of more than 16 kV/cm the current started increasing after remaining steady for a few hours for all temperatures, for both doped and undoped samples. Generally it was observed that, as the Ba/Ti ratio increased from 0.990 to 1.01, which were the limits of nonstoichiometry observed in this study, the time to reach steady state current increased. For samples with a Ba/Ti ratio of unity this time was 45 - 60 minutes, depending upon the temperature. Similar behavior was observed for the nickel doped samples.

On the log current versus log field plots, ohmic behavior would have a slope of one and for space-charge limited behavior the current is proportional to the square of the field and would have a slope of two. These lines are drawn on the plots for a reference. On the plots of log current versus $\sqrt{\text{field}}$, schottky emission would be indicated by a straight line whereas a curved line would indicate any
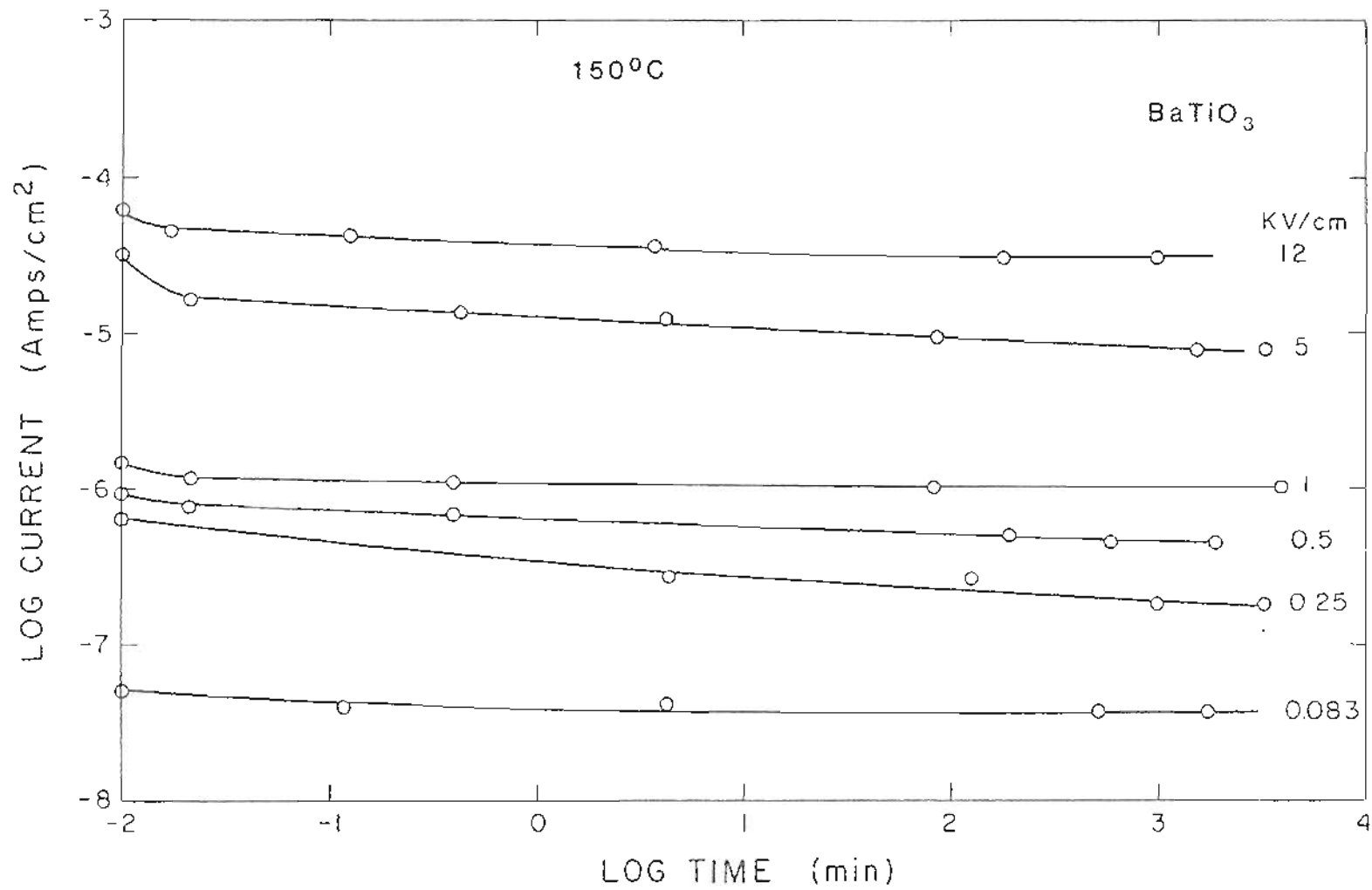
Figure 5.50   CURRENT VS. TIME BEHAVIOR FOR UNDOPED BaTiO₃ AT 150⁰ C
AND AT VARIOUS FIELD LEVELS
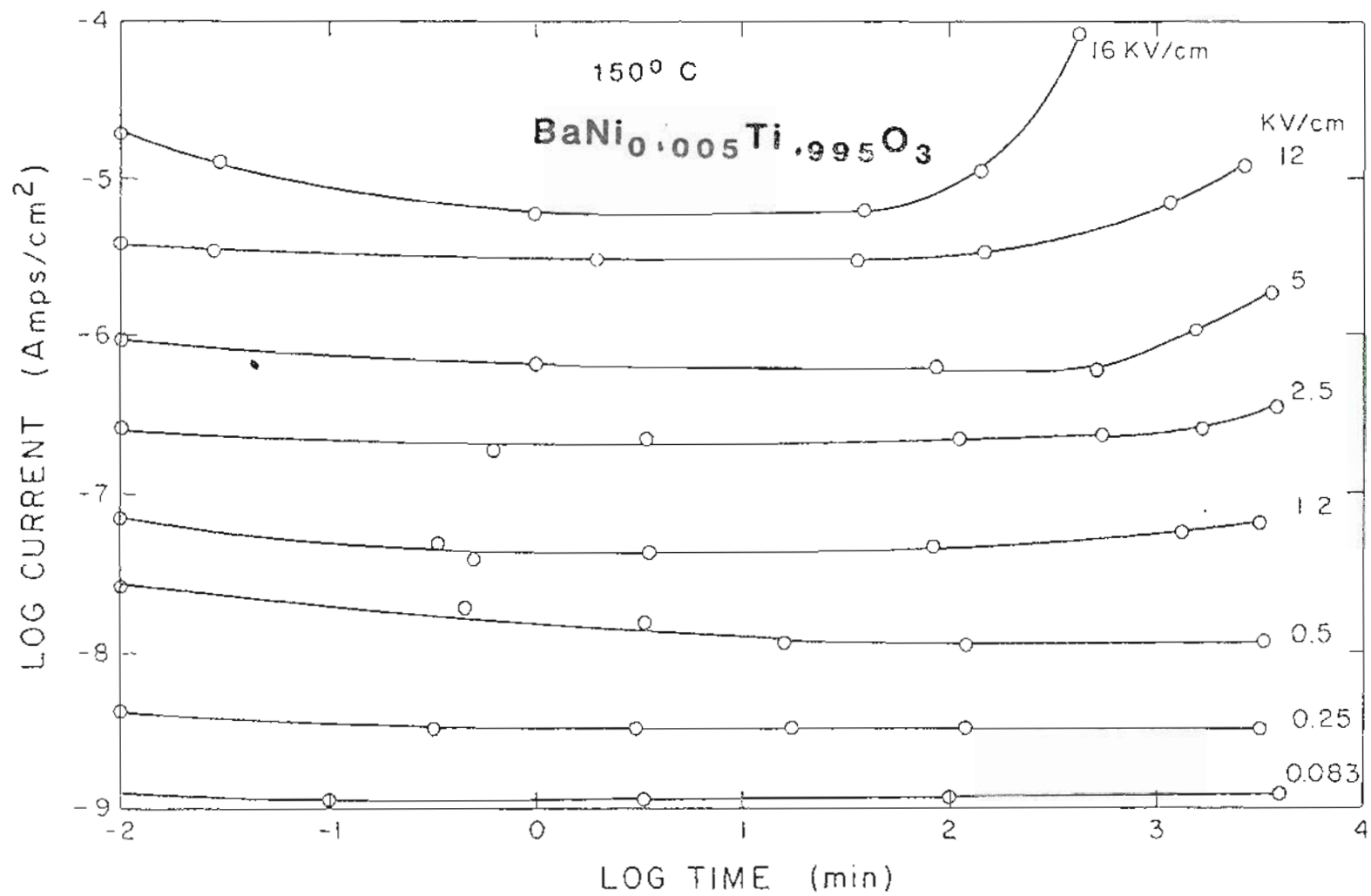
Figure 5.51   CURRENT VS. TIME BEHAVIOR FOR $BaNi_{.005}Ti_{.995}O_3$ AT 150^0 C
AND AT VARIOUS FIELD LEVELS

other behavior.

Figure 5.52 shows the log current versus log field plots for five different samples at 150^0 C. Three undoped samples with Ba/Ti ratios of 0.995, 1 and 1.005 are shown and two nickel doped samples with 0.5 at.% nickel and A/B ratios of 1.000 and 1.005 are also shown. For the two undoped specimens with Ba/Ti ratios of 1.000 and 0.995, and for both the nickel doped samples, two regions are observed. In the low field region for fields up to 4.7 kV/cm a straight line behavior with a slope between 1.15 and 1.25 was observed, whereas in the high field region, for fields from 4.7 to 17 kV/cm, all samples have a straight line behavior but with different slopes. Both of the undoped samples have a slope of 2.4 and both of the nickel doped samples have much higher slopes. The undoped sample with a Ba/Ti ratio of 1.005 shows the same slope of 1.2 for the entire range of field observed. These results indicate that for a low field and 150^0 C all samples can be considered as behaving ohmically or nearly ohmic, but as the field is increased above 4.7 kV/cm the samples are no longer ohmic and the nickel doped samples certainly do not show any space-charge limited behavior, and the space-charge limited behavior of the undoped samples is also doubtful.

Figure 5.53 shows the log current versus log field behavior at 250^0 C for the same five samples shown in Figure 5.52. For all samples the behavior has changed considerably. Straight line behavior was observed for a very short range of field up to 0.9 kV/cm. Up to this field the behavior was nearly ohmic. For any field higher than 0.9 kV/cm, behavior was nonlinear. For undoped samples with Ba/Ti ratios of 0.995 and 1.000, the curve is concave downward, whereas for both the nickel doped samples it was concave upwards.

Figures 5.54 and 5.55 show the plot of log current versus $\sqrt{\text{field}}$ at 150 and 250^0 C, respectively for the same five samples shown in the previous case.

Figure 5.52   ISOTHERMAL CURRENT VERSUS FIELD BEHAVIOR FOR UNDOPED WITH VARIOUS RATIO AND NICKEL DOPED BaTiO$_3$ AT 150^0 C
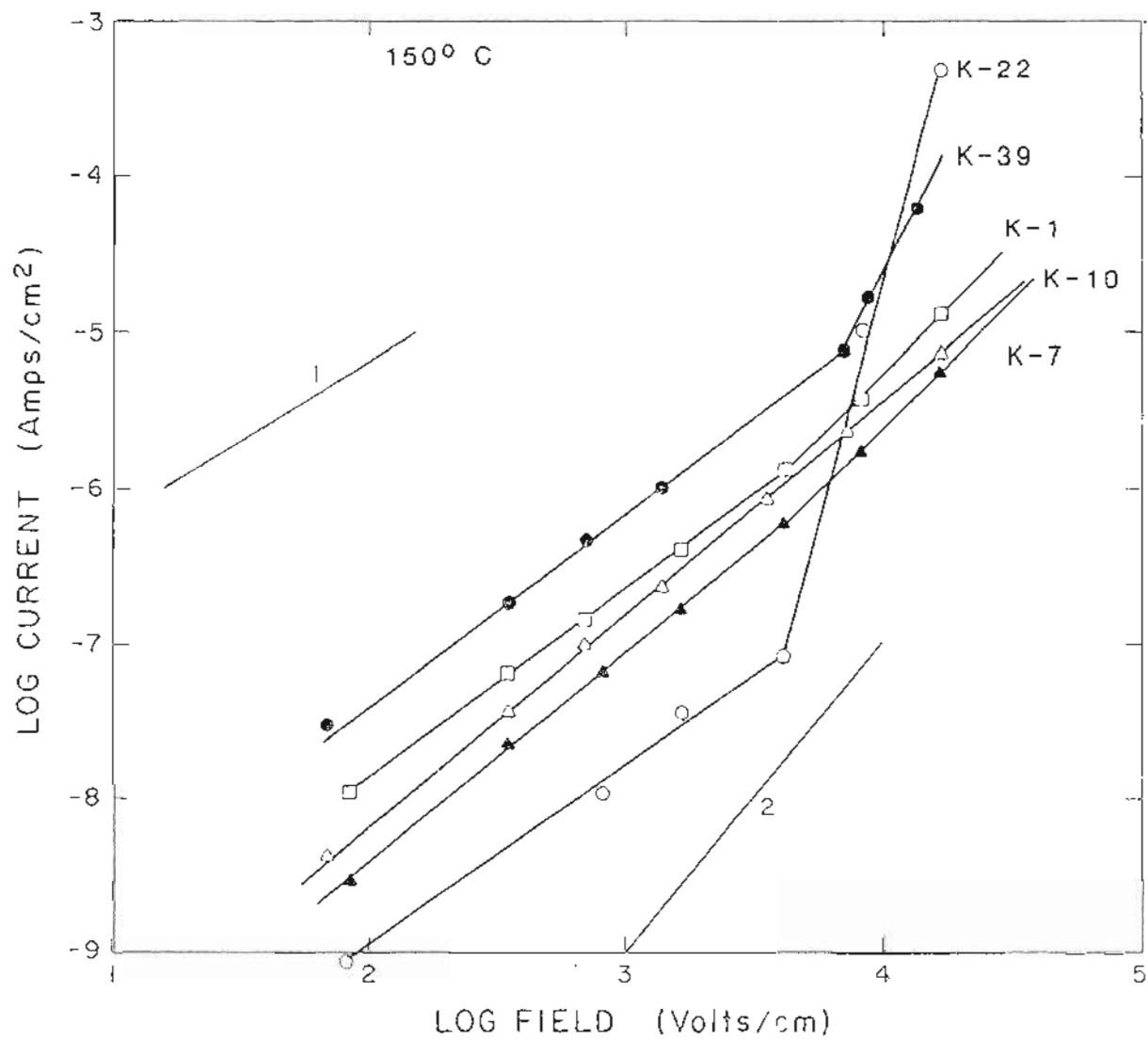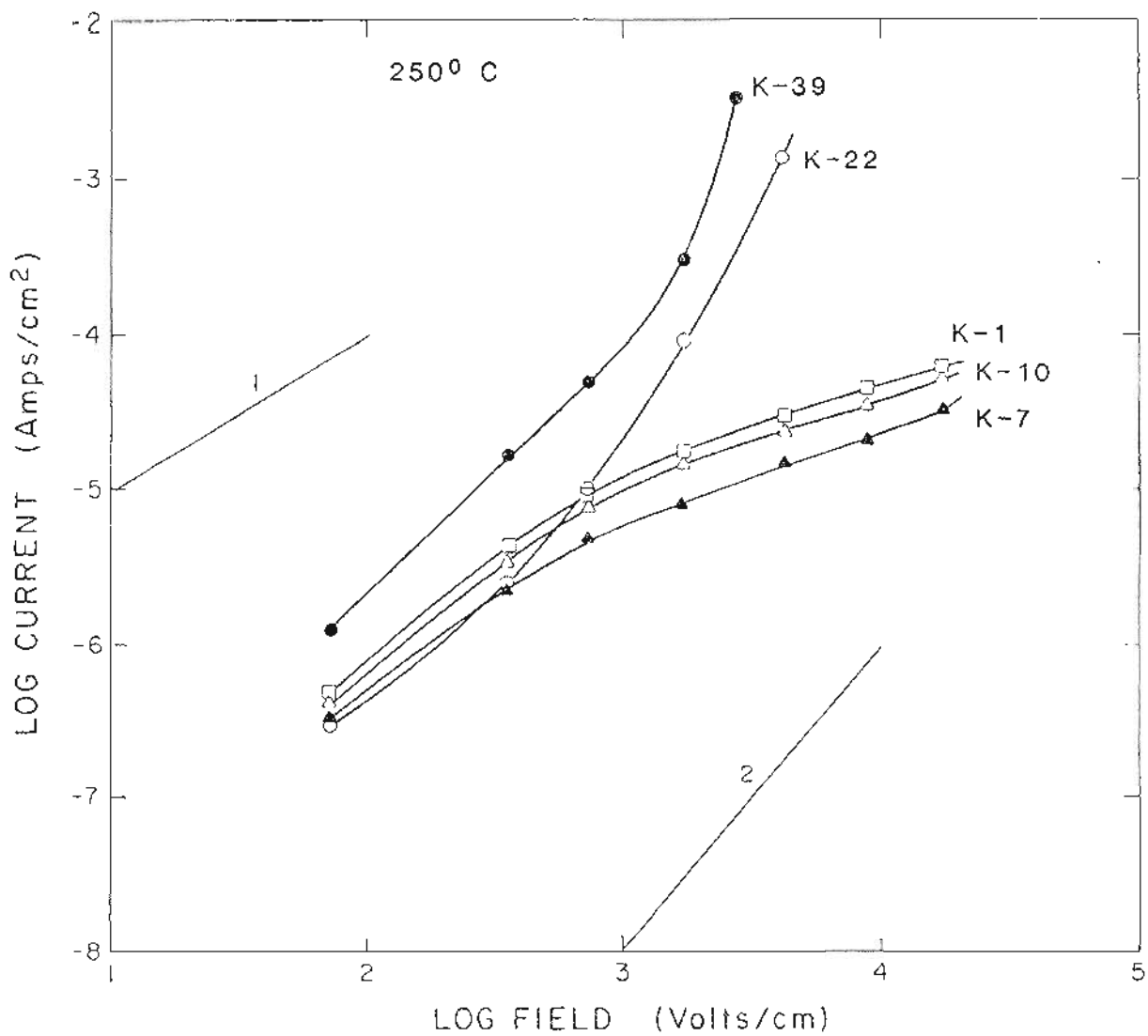
Figure 5.53   ISOTHERMAL CURRENT VERSUS FIELD BEHAVIOR FOR UNDOPED WITH
VARIOUS RATIO AND NICKEL DOPED BaTiO$_3$ AT 250^0 C
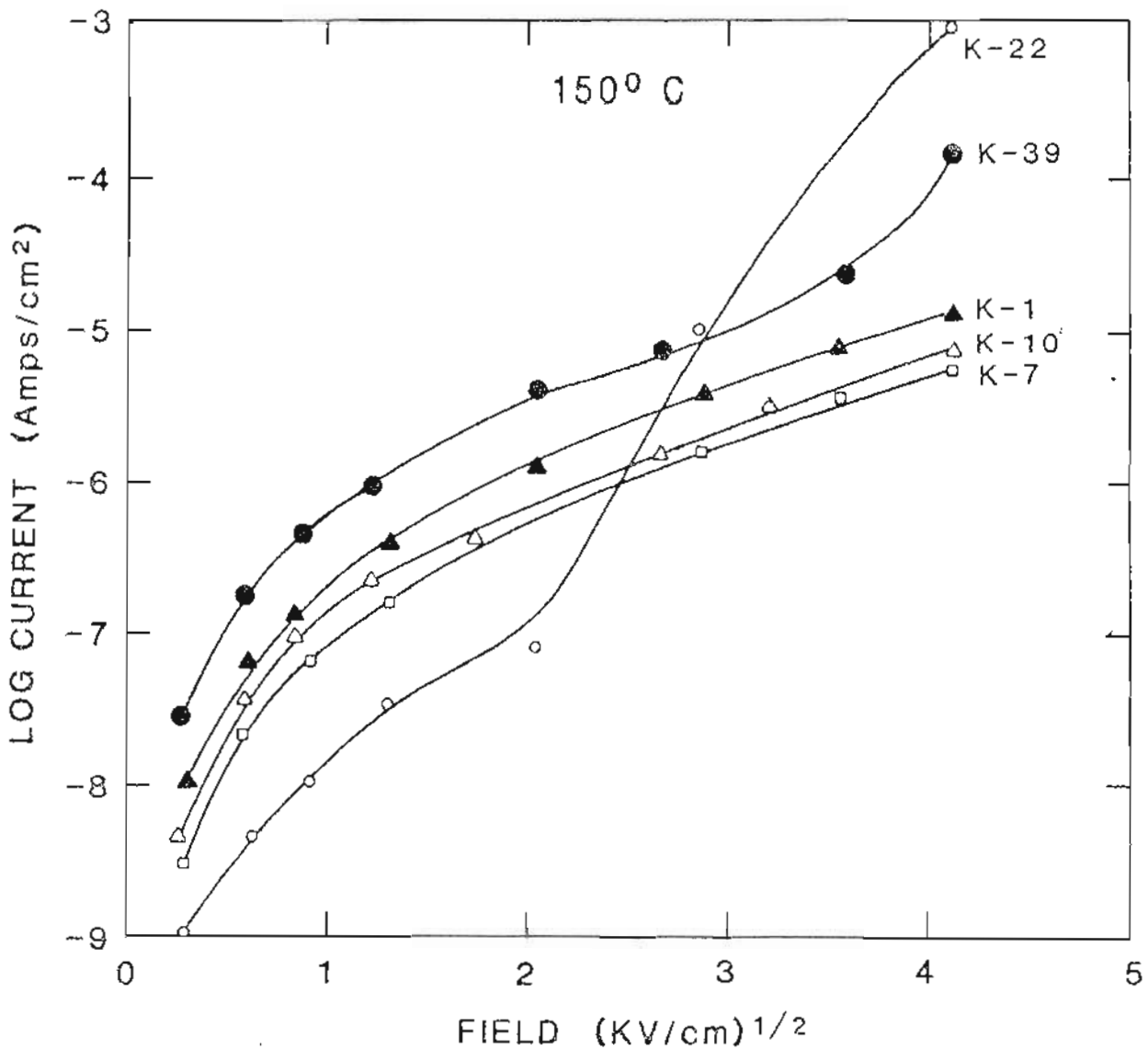
Figure 5.54   CURRENT VERSUS $\sqrt{\text{FIELD}}$ BEHAVIOR FOR UNDOPED WITH VARIOUS
RATIO AND NICKEL DOPED BaTiO$_3$ AT 150^0 C
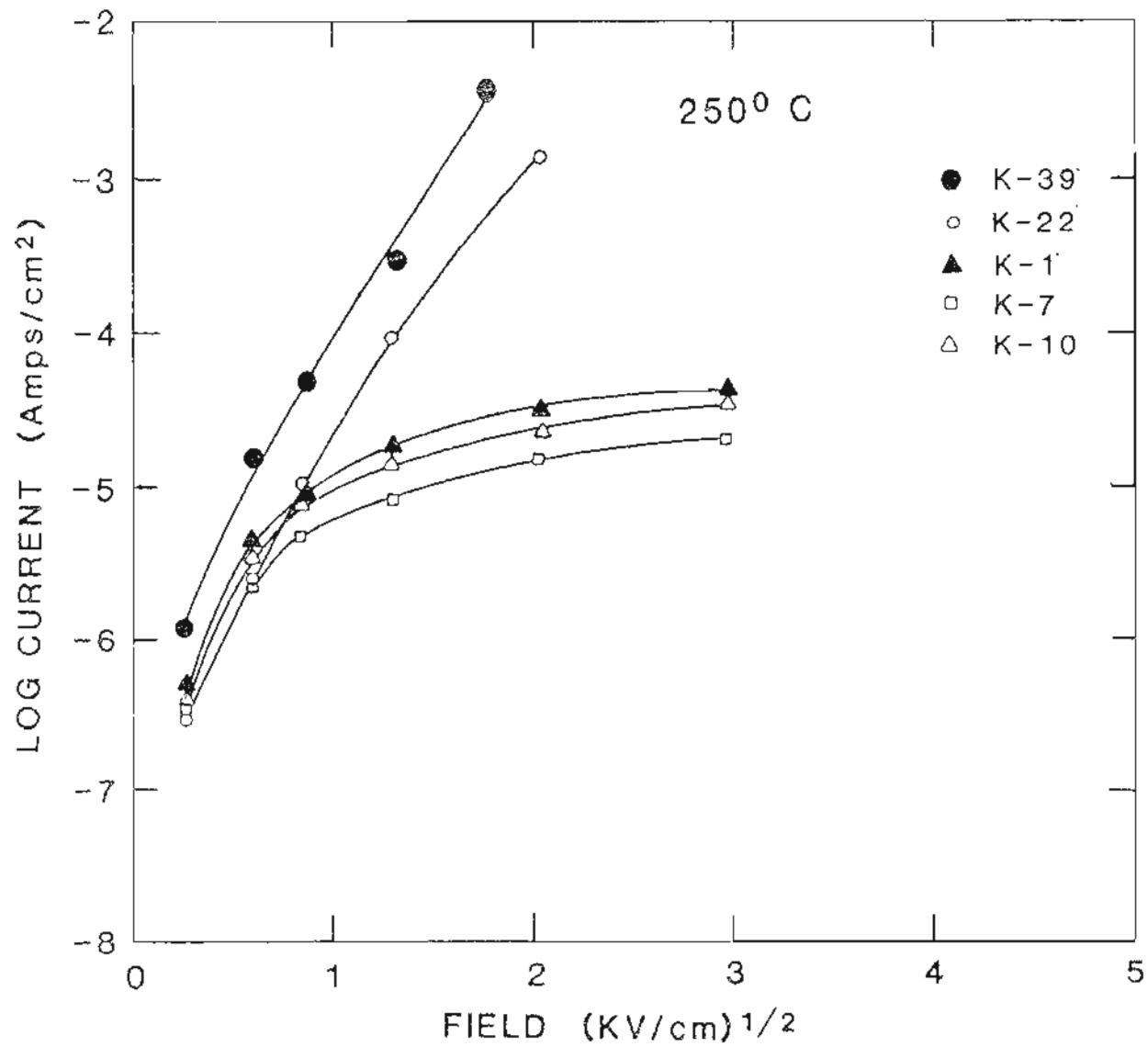
Figure 5.55 CURRENT VERSUS $\sqrt{\text{FIELD}}$ BEHAVIOR FOR UNDOPED WITH VARIOUS RATIO AND NICKEL DOPED $BaTiO_3$ AT 250^0 C

At 150^0 C for undoped samples no straight line behavior was observed in the log current versus $\sqrt{field}$ data. This precludes any possibility of Schottky emission. For the case of the 0.5 at.% nickel doped sample with an A/B ratio of 1.000, two regions were observed in the low field region, straight line behavior for fields up to 4.1 kV/cm and a concave line for higher fields.

At 250^0 C all undoped samples show nonlinear behavior in the log current versus $\sqrt{field}$ plots. At high fields (from 4.6 to 17 kV/cm) the data may be interpreted as a straight line but overall it is curved. For the nickel doped samples the data are nonlinear. Thus at 250^0 C no Schottky emission was observed.

The data shown here (Fig. 5.50 - 5.55) are for the two extreme behaviors observed. Data for other undoped samples and nickel doped samples with three different A/B ratios, falls between these two extremes. From all the data, the conclusions which can be easily reached are that no Schottky emission was observed, in any sample, at any temperature between 150 and 250^0 C. Generally all the samples behave ohmically in the low field region. In the high field region deviation from ohmic behavior was observed. This deviation from ohmic behavior was reflected in the current versus time plots, by an increase in the current after achieving a steady state value. It was observed that the shorter the time of steady state current the greater the deviation from ohmic behavior.

All the samples were tested at 150 to 250^0 C and up to 17 kV/cm field strength for a minimum of 24 hrs. The only exceptions were for samples, which showed a large increase in current with time and reached the limits of the experimental setup.

From the previous degradation studies (4,5,85) it was expected for 250^0 C and a 10 kV/cm field strength that the samples would degrade rapidly and

colour centers might develop, which could be further analyzed. In this investigation no degradation was observed at 250^0 C for up to 15 kV/cm stress level for 24 hrs in any undoped samples. Current versus time behavior for stress levels higher than 16 kV/cm could not be observed due to the unavailability of stable power supply. Since in all the undoped samples steady current was achieved after 24 hrs. no definite conclusions could be drawn about the effect of A/B ratio on the resistance to degradation.

For nickel doped samples up to 0.05 at.% doping and for all three A/B ratios, the samples behaved similarly to the undoped samples. Steady current was observed up to 15 kV/cm at 250^0 C, for 24 hrs. For higher nickel doping the time for which the current remained steady decreased and current started increasing as a function of nickel concentration Table 5.22 shows the steady state current and highest current reached and time at which highest current was measured for various nickel doped samples. From Table 5.22 it is clear that as the nickel concentration increased the resistance to degradation decreased. For nickel doping of 0.1 at% the current increased by a factor of two in 24 hours, whereas for 1 at.% nickel doping the current increased ten times in half the time. These results also show that the A/B ratio does have an effect. As the A/B ratio increased from 0.995 to 1.005 the resistance to degradation increased but this increase is marginal at best. The activation energy for the conduction was not calculated, since the measurements were made at three temperatures only.

During this investigation after applying the electrical stress of 17 kV/cm for 24 hrs at 250^0 C, colour regions were not developed in any sample in contrast to what was observed by others (3,4). Keck and Anderson (84) also did not observe any colour regions. Considering the various studies, it is quite evident that colour regions developed either in commercial samples or in impure materials.

Table 5.22

DEGRADATION BEHAVIOR AT 250^0 C.

Composition		Applied Field	Steady Current	Final current	Time
Doping	Ratio				
at.%		kV/cm	amps/cm^2	amps/cm^2	Hrs.
0.1	0.995	16.66	3.27×10^{-6}	7.35×10^{-6}	24
0.3	0.995	16.66	1.01×10^{-5}	8.00×10^{-5}	24
0.5	0.995	16.66	3.01×10^{-4}	1.04×10^{-3}	18
1.0	0.995	16.66	2.97×10^{-4}	3.05×10^{-3}	12
0.1	1.000	16.66	4.57×10^{-6}	8.05×10^{-6}	24
0.3	1.000	16.66	1.02×10^{-5}	7.99×10^{-5}	24
0.5	1.000	16.66	3.16×10^{-4}	1.05×10^{-3}	18
1.0	1.000	16.66	2.05×10^{-4}	1.11×10^{-3}	12
0.1	1.005	16.66	2.95×10^{-6}	6.85×10^{-6}	24
0.3	1.005	16.66	9.97×10^{-6}	6.58×10^{-5}	24
0.5	1.005	16.66	2.62×10^{-4}	9.69×10^{-4}	18
1.0	1.005	16.66	1.12×10^{-4}	1.20×10^{-3}	12

The impurity was either intentional or accidental. Thus it can be safely concluded that oxygen vacancies alone are not responsible for the development of colour regions as concluded by Lehovec and Shirn (4), but it may be either a combination of impurities and oxygen vacancies or impurities alone. Nonstoichiometry is accommodated by vacancies on both cation and oxygen sites. Thus a shift toward either the Ba or Ti rich side, will cause excess oxygen vacancies. Assuming that on the Ti rich side a neutral complex formation of ($V_{Ba}^{''}, V_{O}^{\cdot\cdot}$) is taking place as proposed by Eror and Smyth (19), at any given temperature a certain number of oxygen vacancies are going to remain free, whose concentration will be dictated by the stability of the complex. Under those conditions the oxygen vacancy migration will also be a relatively low energy process. This is because free vacancies are available for conduction. Thus, any composition away from stoichiometry should have a low resistance to degradation. This is not the case and not a single study so far suggests this. In fact in the present study the variation in the resistance to degradation with respect to A/B ratios in undoped samples is marginal at best. Also, our low temperature conductivity study did not indicate appreciable ionic conductivity or ionized oxygen vacancies at 250^{0} C. Efforts were made to observe an ESR signal from undoped samples which were exposed to 17 kV/cm at 250^{0} C for 60 hrs, but no signal could be detected that could be assigned to the presence of Ti^{+3} or oxygen vacancies.

The effect of acceptors on degradation is not well understood. Our moderate temperature conductivity data suggest that the conductivity is p-type and the added nickel is partially compensated by additional oxygen vacancies. Thus the effect of acceptors is to add oxygen vacancies which might cause a decrease in resistance to degradation, if migration of oxygen vacancies is a dominant mechanism. Although samples with nickel addition of more than 0.3 at.%,

showed a slight decrease in the resistance to degradation, this can not be definitely attributed to the migration of oxygen vacancies. This is so because if we assume that the migration of oxygen vacancies towards the cathode is responsible for the degradation, then this migration should concurrently reduce either Ti^{+4} to Ti^{+3} or Ni^{+3} to Ni^{+2}. In either case the concentration of electrons is increasing but since electrons are not the majority carriers, an increase in their concentration should not increase the conductivity until the electron concentration becomes equal to that of the hole concentration. Also, the addition of nickel up to .1 at.% does not reduce the resistance to degradation. In fact, resistance to degradation is slightly improved or remains the same.

Harwood (159) observed the improved resistance to degradation by addition of Mn in Titanium Dioxide. He attributed this to the preferential reduction of Mn from valency +4 to +3 over Ti and suggested that Mn does not provide 3d band electrons for the conduction.

In this investigation, we could not degrade the sample totally under the given experimental conditions. Also, the effect of acceptor impurities seems to be beneficial until 0.3 at.% doping. The difference between resistance to degradation of the 0.5 at% nickel doped sample and the 1.0 at% nickel doped sample is very small. Most of the samples behaved ohmically for fields up to 4 KV/cm and for higher fields, the behavior was close to space-charge limited. There is some uncertainity here since the slope of the of the log current vs. log field plots were not exactly equal to 2 but close to 2.2. Our data do not support the hypothesis that degradation is caused by the migration of oxygen vacancies towards the cathode. If migration of oxygen vacancies is responsible for the degradation, then certainly other impurities are also playing a role. To arrive at any definite conclusion, further work is necessary. The potential drop at various points between the

electrodes should be measured while measuring current vs. time, at various potentials. The area near the anode and cathode should also be analyzed for composition and the valence state of various ions.

6. CONCLUSIONS

As mentioned in Chapter 3, we set various tasks. The first and prime task was to develop an experimental technique to evaluate the concentration of oxygen vacancies. During the course of this investigation we did find an extra peak in the Raman spectrum of reduced barium titanate. This peak has been assigned to the presence of oxygen vacancies and termed as an electronic transition. Although we have shown that the 823 cm^{-1} band is due to the presence of oxygen vacancies, whether it is an electronic transition or not can be verified by optical absorption spectra. Never-the-less a technique has been developed to directly measure the oxygen vacancies concentration.

Equipped with this tool to measure the concentration of oxygen vacancies, the next logical step was to apply this tool to the degraded samples. In this investigation we did not observe any colour region development near the anode and the cathode as mentioned by the previous researchers. Also, our samples were found to have a better resistance to degradation. Since colour centers were not developed and samples were not degraded to a great extent, we were unable to analyze the regions near the anode and the cathode for oxygen vacancies.

Considering these facts and the fact that the samples used in most of the previous studies were either commercial dielectrics or more impurity laden than ours, one can safely conclude that oxygen vacancies alone, are not responsible for the degradation. From this investigation it was not possible to conclude the exact role played by the impurities in degradation. This study also showed that for up to 0.3 at.% nickel doping there was a beneficial or neutral effect on the resistance to degradation. It was observed that for nickel dopant concentrations greater than 0.3 at.% higher nickel concentrations were associated with lower resistance to degradation. We did not observe any correlation between poor

resistance to degradation and Schottky or space-charge limited currents.

Other significant conclusions from this study are as follows.

Nickel substitutes on titanium sites in the barium titanate lattice with a +3 valence.

Solubility of nickel in barium titanate is a function of temperature, and at 1275^0 C the solubility is 1.5 at.% nickel. The second phase that formed when the nickel concentration was in excess of 1.5 at.% has a hexagonal structure.

The room temperature Raman spectrum of barium titanate is a combination of first order and second order scattering processes

Barium titanate is an intrinsic conductor between 200 and 550^0 C with a band gap of 2.80 ± 0.03 eV.

The ionization energy of nickel in the band gap is 0.97 ± 0.03 eV.

For reduction in a partial pressure of oxygen less than 10^{-12} atm. and nickel doping greater than 1 at.%, the valency of nickel changes from +3 to +2.

7. RECOMMENDATIONS FOR FUTURE WORK

A major degradation study should be undertaken in which the potential drop, at various points in between the anode and cathode should be measured at various temperatures and applied field strengths. This should be done with high purity, commercial, acceptor and donor doped samples, and with various dopants. This will help in understanding the degradation process. Also these samples should be degraded and then analyzed by the micro Raman technique as mentioned bellow to study the migration of oxygen vacancies and to determine if there is any change in the Ba/Ti ratio near the anode and the cathode.

The Raman technique should be further developed for measuring the oxygen vacancy concentration using variation in the intensity of the 820 cm^{-1} peak with various reductions and Ba/Ti ratio changes. This technique then can further be used, with micro Raman to study degraded samples to verify the migration of oxygen vacancies. Optical absorption spectrum of high purity barium titanate should be measured and results compared with the Raman spectrum of reduced $BaTiO_3$ to determine whether the 823 cm^{-1} band is an electronic transition or not. The Raman spectrum of reduced barium titanate should be measured at low temperatures (sub zero).

Accommodation of an extra BaO layer in the barium titanate structure is suggested to be a mechanism for excess Ba accommodation, from the X-ray work. This suggestion can be further verified by lattice imaging using high resolution electron microscopy.

In this study the high temperature electrical conductivity of nickel doped samples was measured for A/B = 1. This study should be further extended to include similarly doped samples but with different A/B ratios. This will help in

substantiating the defect structure proposed herein and understanding, the effect of Ba/Ti ratio on electrical conductivity and defect structure.

Nickel doping reduces the band gap of barium titanate and thus it may be a prospective candidate material for the semiconductor electrode in the photoelectrolysis of water. Further studies in this direction can be undertaken.

REFERENCES

1) M. C. McQuarrie, Am. Ceram. Soc. Bull. 34, 169, (1955).

2) R. M. Gruver and W. R. Bussem, Technical Report, AFML - Tr 66-164, May (1966).

3) Y. Goto and S.Kachi, J. Phys. Chem. Sol. 32, 889, (1971).

4) K. Lehovec and G. A. Shirn, J. Appl. Phys. 33, 2036, (1962).

5) D. A. Payne Proceeding of Sixth Annual Reliability Physics Symposium, IEEE, California, p 257, (NY 1968).

6) J. B. Macchesney, P. K. Gallagher and F. V. Dimarcello, J. Amer. Ceram. Soc. 46, 197, (1963).

7) K. Okazaki and I. Igaraski, Ferroelectrics, 27, 263, (1979).

8) W. A. Schulze, L. E. Cross and W. R. Bussem, J. Amer. Ceram. Soc., 63, 83, (1980).

9) W. J. Minford, IEEE Trans. Components, Hybrids, Manf. Technol., 5, 297, (1982).

10) M. Pechini, U. S. Patent, 3,330,697, July 11, (1967).

11) F. A. Kroger and H. J. Vink, Solid State Physics, 3, 307, (1956).

12) H. Schmalzried and C. Wagner, Z. Phys. Chem. (N. F.) 31, 198, (1962).

13) H. Veith, Z. Angew. Phys. 20, 16, (1965).

14) F. Kosek and H. Arend, Phys. Stat. Solidi, 24, K69, (1967).

15) S. A. Long and R. N. Blumenthal, J Amer. Ceram. Soc., 54, 515, (1971).

16) S. A. Long and R. N. Blumenthal, J Amer. Ceram. Soc., 54, 577, (1971).

17) A. M. J. H. Sueter, Phillips Res. Rep. Suppl., No 3, (1974).

18) N. H. Chan and D. M. Smyth, J Electrochem. Soc. 123, 1585, (1976).

19) N. G. Eror and D. M. Smyth, J Solid State Chem., 24, 235, (1978).

20) N. H. Chan, R. K. Sharma and D. M. Smyth, J. Amer. Ceram. Soc., 64, 556, (1981).

21) N. H. Chan, R. K. Sharma and D. M. Smyth, J. Amer. Ceram. Soc., 65, 167, (1982).

22) J. Daniels and K. H. Hardtl, Phillips Res. Rept., 31, (part 1), 489, (1976).

23) J. Daniels and K. H. Hardtl, Phillips Res. Rept., 31, (part 2), 505, (1976).

24) G. Goodman, J. Amer. Ceram. Soc., 46, 48, (1963).

25) W. Heywang, Sol. St. Elec., 3, 51, (1961).

26) O. Saburi, J. Amer. Ceram. Soc., 44, 54, (1961).

27) T. Ashida and H. Toyoda, Jap. J. Appl. Phys., 5, 269, (1966).

28) G. H. Jonker, Mat. Res. Bull., 2, 401, (1967).

29) Z. Piotrowski, A. Podgorecka, M. Rekas and Wierzbicka, Acad. Pol. Sci. Ser. Sc. Chim., 29, 393, (1981).

30) N. G. Eror and D. M. Smyth, in Eyring LeRoy and O'Keefe (Eds.), 'The Chemistry of Extended Defects in Non-metallic Solids', P. 62-83, North Holland Publishing Co. Amsterdam (1970).

31) D. Hennings, Phillips Res. Rept. 31, (part 3), 516, (1976).

32) J. Novak and H. Arend, J. Amer. Ceram. Soc., 47, 530, (1964).

33) H. J. Hagemann and D. Hennings, J. Amer. Ceram. Soc., 64, 590, (1981).

34) H. Arend and L. Kilborg, J. Amer. Ceram. Soc., 52, 63, (1969).

35) W. L. George and R. E. Grace, J. Phys. Chem. Solids, 30, 881, (1969).

36) W. L. George and R. E. Grace, J. Phys. Chem. Solids, 30, 889, (1969).

37) L. C. Walters and R. E. Grace, J. Phys. Chem. Solids, 28, 239, (1967).

38) L. C. Walters and R. E. Grace, J. Phys. Chem. Solids, 28, 245, (1967).

39) U. Balachandran and N. G. Eror, J. Solid State Chem., 39, 351, (1981).

40) U. Balachandran and N. G. Eror, J. Solid State Chem., 42, 227, (1982).

41) N. H. Chan, R. K. Sharma and D. M. Smyth, J. Electrochem. Soc., 128, 1762, (1981).

42) U. Balachandran and N. G. Eror, Mat. Sci. and Engg., 54, 221, (1982).

43) U. Balachandran and N. G. Eror, J. Solid State Chem., 41, 185, (1982).

44) A. H. Wilson, Proc. Roy. Soc. A, 133, 458, (1931) and 134, 277, (1932).

45) N. F. Mott and R. W. Gurney, Electronic Process in Ionic Crystals, Oxford University Press (1940).

46) J. G. Simmons, Phys. Rev., B, 15, 964, (1977).

47) A. Branwood and R. H. Tredgold, Proc. Phys. Soc. 76, 93, (1960).

48) B. N. Matsonashvili, Soviet Physics, (Solid State) 8, 2586, (1967).

49) V. Logo and F. Ricciardiello, Science of Ceramics, 11, 539, (1981).

50) E. K. Weise and I.A. Lesk. J. Chem. Phys., 41, 872, (1964).

51) H. Ikushima and S. Hayakawa, Jap. J. Appl. Phys., 6, 454, (1967).

52) F. M. Rayn and E. C. Subbarao, Appl. Phys. Lett., 1, 69, (1962).

53) S. Ikegami and I. Ueda, J. Phys. Soc. Japan., 19, 159, (1964).

54) C. N. Berglund and W. S. Bear, Phys. Rev., 157, 358, (1967).

55) G. A. Cox and R. H. Tredgold, Phys. Lett., 11, 22, (1964).

56) T. Horie, K. Kawabe and S. Sawada, J. Phys. Soc. Japan., 9, 823, (1954).

57) M. DiDomenico and S. H. Wemple, Phys. Rev., 166, 565, (1968).

58) C. N. Berglund and H. J. Braun, Phys. Rev., 164, 790, (1967).

59) D. D. Glower and R. C. Heckman, J. Chem. Phys., 41, 872, (1964).

60) J. Maier, G. Schwitzgebel and H. J. Hagemann, J. Solid State Chem., 58, 1, (1985).

61) A. H. Kahn and A. J. Leyendecker, Phys. Rev., 135, A 1321-5, (1964).

62) F. M. Michel-Calendini and G. Mesnard, Phys. Stat. sol. (b), 44, K117 (1971).

63) F. M. Michel-Calendini and G. Mesnard, J. Phys. C, 6, 1709, (1973).

64) P. Gerthsen, R. Groth, K. H. Hardtl, D. Heese and H. G. Reik, Sol. St. Comm., 3, 165, (1965).

65) H. G. Riek and D. Heese, Phys. Stat. Sol. 24, 281, (1967).

66) H. Ikushima and S. Hayakawa, J. Phys. Soc. Japan, 19, 1986, (1964).

67) H. Ikushima and S. Hayakawa, J. Phys. Soc. Japan, 20, 1517, (1965).

68) H. Ikushima and S. Hayakawa, J. Phys. Soc. Japan, 21, 1866, (1966).

69) H. Ikushima and S. Hayakawa, J. Phys. Soc. Japan, 23, 540, (1967).

70) S. B. Desu and E. C. Subbarao, Advances in Ceramics Vol. 1, L. M. Levinson Ed., P 189, Amer. Ceram. Soc. Publication, (1981).

71) B. W. Faghnan, Phys. Rev. B, 4, 3623, (1971).

72) P. Koidl, K. W. Blazey, W. Berlinger and K. A. Muller, Phys. Rev. B, 14, 2703, (1976).

73) R. A. Serway, W. Berlinger, K. A. Muller and R. W. Collins, Phys. Rev. B,

16, 4761, (1977).

74) E. S. Kirkpatrik, K. A. Muller and R. S. Rubins, Phys. Rev., 135, A86, (1964).

75) M. Nakahara and T. Murakami, J. Appl. Phys., 45, 3795, (1974).

76) H. J. Hagemann and H. Ihrig, Phys. Rev. B20, 3871, (1979).

77) B. W. Faghnan and Z. J. Kiss, IEEE J. of Quantum Electronics, QE5, 17, (1960).

78) L. Azzaroff and J. Brophy, Electronic Process in Materials, 305-326, MaGraw - Hill Book Co. N.Y. (1963).

79) A. Chynoweth, Progress in Semiconductors Vol. 4, 97-123, John Wiley and Sons Inc. N.Y. (1960).

80) A. Rose, Phys. Rev. 97, 1538, (1955).

81) A. Branwood, O. H. Huges, J. D. Hurd and R. H. Tredgold, Proc. Phys. Soc., 79, 1161, (1962).

82) G. T. Mullick and P. R. Emtage, J. Appl. Phys., 39, 3088, (1968).

83) L. Benguigui, Proc. Int. Meeting of Ferroelectricity, Prague 1966, Vol. 2, P - 326, (1966).

84) J. D. Keck, Ph.D., Thesis Submitted to University of Missouri, Rolla, (1976).

85) J. Rodel and G. Tomandl, J. Mat. Sci., 19, 3515, (1984).

86) F. Jona and G. Shirane, Ferroelectric Crystals, Pergamon Press, Oxford, England (1962).

87) W. Cochran, Adv. Phys., 9, 387, (1960).

88) R. A. Cowley, Phys. Rev. 134, A981, (1964).

89) R. Loudon, Adv. Phys., 13, 423, (1964).

90) S. P. S. Porto, G. B. Wright (Ed.) Light Scattering Spectra of Solids, P - 1, Springer - Verlag N.Y. (1969).

91) J. M. Worlock and S. P. S. Porto, Phys. Rev. Lett., 15, 697, (1965).

92) G. Benedeck and G. F. Nardelli, Phys. Rev. B, 154, 872, (1967).

93) R. E. Dietz, G. I. Parisot and A. E. Meixner, Phys. Rev. B, 4, 2302, (1971).

94) P. S. Pershan and W. B. Lancina, G. B. Wright (Ed.), Light Scattering Spectra of Solids, P - 439, Springer - Verlag, N.Y. (1969).

95) G. Burns and B. A. Scott, Solid State Comm., 9, 813, (1971).

96) G. Burns and B. A. Scott, Phys. Rev. Lett., 25, 1191, (1970).

97) C. H. Perry and D. B. Hall, Phys. Rev. Lett., 15, 700, (1965).

98) V. Dvorak, Phys. Rev., 159, 652, (1967).

99) D. L. Rousseau and S. P. S. Porto, Phys. Rev. Lett., 20, 1354, (1968).

100) M. DiDomenico, S. H. Wemple, S. P. S. Porto and R. P. Bauman, Phys. Rev., 174, 522, (1968).

101) M. P. Fontana and M. Lambert, Solid State Comm., 10, 1, (1972).

102) G. A. Barbosa, A. Chaves and S. P. S. Porto, Solid State Comm., 11, 1053, (1972).

103) A. Scalabrin, S. P. S. Porto, H. Vergas, C. A. S. Lima and L. C. Miranda, Solid State Comm., 24, 291, (1977).

104) M. S. Jang, S. Kojima, T. Nakamura and M. Iakashige, Ferroelectrics, 37, 717, (1981).

105) B. Jannot, L. Gninihvi and G. Godefroy, Ferroelectrics, 37, 669, (1981).

106) H. Vogt, J. A. Sanjurjo and G. Rossbroich, Phys. Rev. B, 26, 5904, (1982).

107) Ya. S. Bobovich and E. V. Bursian, Opt.i Spectroscopia, 11, 131, (1961).
[Transl. Opt. Spectry., 11, 69, (1961).]

108) S. Ikegami, J. Phys. Soc. Japan, 19, 46, (1964).

109) J. T. Last, Phys. Rev., 105, 1740, (1957).

110) J. M. Ballantye, Phys. Rev., 136, A429, (1964).

111) N. G. Eror and T. M. Loehr, J. Solid State Comm., 12, 319, (1975).

112) J. S. Smith, T. R. Dolloff and K. S. Mazdiyasni, J. Amer. Ceram. Soc., 53, 91, (1970).

113) M. Pechini, U. S. Patent, 3,231,328, Jan 25, (1966).

114) Marcilly, P. Courty and B. Delmon, J. Amer. Ceram. Soc., 53, 56, (1970).

115) T. M. Loehr, W. E. Keyes and P. A. Pincus, Anal. Biochemistry, 96, 456, (1979).

116) B. M. Sjoberg, T. M. Loehr and J. S. Loehr, Biochemistry, 21, 96, (1982).

117) L. J. Van der Pauw, Phil. Tech. Rev., 20, 220, (1958).

118) L. J. Van der Pauw, Phil. Res. Rept., 13, 1, (1958).

119) S. Amer, Sol. St. Elec., 6, 141, (1963).

120) W. L. V. Price, Sol. St. Elec., 16, 753, (1973).

121) R. Whwang, B. J. Smith and C. R. Crowell, Sol. St. Elec., 17, 1217, (1974).

122) D. M. Boerger, J. J. Kramer and L. D. Partian, J. Appl. Phys., 52, 269, (1981).

123) C. Y. Chang, Y. K. Fang and S. M. Sze, Sol. St. Elec., 14, 541, (1971).

124) V. L. Rideout, Sol. St. Elec., 18, 541, (1975).

125) R. S. Popovic, Sol. St. Elec., 21, 1133, (1978).

126) S. S. Flaschen and L. G. Vanvitert, J. Appl. Phys., 27, 190, (1956).

127) H. M. Landis, J. Appl. Phys., 36, 2000, (1965).

128) J. E. Carnes and A. M. Goodman, J. Appl. Phys., 38, 3091, (1967).

129) J. W. Fleming Jr. and H. M. O'Bryan Jr., Am. Ceram. Soc. Bull., 55, 715, (1976).

130) J. Narayanan and V. N. Shukla, J. Appl. Phys., 51, 3444, (1980).

131) J. B. Price and J. B. Wagner, Z. Phys. Chem., 49, 257, (1966).

132) S. P. Mitoff, J. Chem. Phys., 35, 882, (1961).

133) N. G. Eror, Ph.D. Thesis, Northwestern University, Evanston IL (1965).

134) U. Balachandran, Ph.D. Thesis, Oregon Graduate Center, Bvtn OR (1980).

135) D. E. Rase and R. Roy, J. Amer. Ceram. Soc., 38, 102, (1955).

136) F. Kulcsar, J. Amer. Ceram. Soc., 39, 13, (1956).

137) G. H. Jonker and W. Kwestroo, J. Amer. Ceram. Soc., 41, 390, (1958).

138) H. C. Grahm, N. M. Tallan and K. S. Mazdiyasni, J. Amer. Ceram. Soc., 54, 548, (1971).

139) T. Negas, R. S. Roth, H. S. Parker and D. Minor, J. Solid St. Chem., 9, 297, (1974).

140) H. M. O'Bryan Jr. and J. Thompson Jr., J. Amer. Ceram. Soc., 57, 522, (1974).

141) R. K. Sharma, N. -H. Chan and D. M. Smyth, J. Amer. Ceram. Soc., 64, 448, (1981).

142) R. S. Roth, Private Communication.

143) S. Bhagvantam and T. Venkatarayudu, Proc. Indian Acad. Sci., 9A, 224, (1939).

144) W. G. Fately, F. R. Dollish, N. T. McDevitt and F. F. Bentley, Infrared and Raman Selection Rules for Molecular and Lattice Vibrations., Interscience. N.Y. (1972).

145) A. Scalabrin, A. S. Chaves, D. S. Shim and S. P. S. Porto, Phys. Stat. Sol. (b), 79, 731, (1977).

146) J. L. Werble, E. Gallego-Liasma, S. P. S. Porto, J. Raman Spectr., 7, 7, (1978).

147) A. S. Chaves, R. S. Katiyar and S. P. S. Porto, Phys. Rev., B10, 3522, (1974).

148) C. H. Perry and N. G. Tornberg, Light Scattering Spectra of Solids, (Ed. G. B. Wright), P 467, Springer Verlag N.Y. (1969).

149) G. Burns, J. D. Axe and D. F. O'Kane, Solid State Comm., 7, 933, (1969).

150) K. G. Bartlett and L. S. Wall, J. Appl. Phys., 44, 5192, (1973).

151) N. Suriyayothin, Ph.D Thesis, Oregon Graduate Center, Bvtn, OR (1984).

152) R. Loudon, Phys. Rev., 137, A1784, (1965).

153) W. C. Dunlap Jr., An Introduction to Semiconductors, John Wiley and Sons, Inc. N.Y. (1953).

154) V. M. Fridkin, Ferroelectric Semiconductors, Plenum Publishing Corp., N.Y. (1980).

155) H. Yamada and G. R. Miller, J. Solid State Chem., 6, 169, (1973).

156) J. H. Backer and H. P. R. Frederikse, J. Appl. Phys., 33 (suppl.), 447, (1962).

157) H. Ihrig, J. Phys. C (Sol. St. Phys.), 11, 819, (1978).

158) C. J. Kevane, Phys. Rev., 133A, 1431, (1964).

159) N. G. Eror, T. M. Loehr and B. C. Cornilsen, Ferroelectrics, 28, 321, (1980).

- BIOGRAPHICAL NOTE -

Sudhir R. Kulkarni was born on November 11, 1951 in Bombay, India. He graduated from school in 1967 from Narayangaon, India. He attended the M. S. University of Baroda, Baroda and received B. E. in metallurgical engineering in June 1974. In July 1976 he received M. Tech. from Indian Institute of Technology Kanpore, India.

In the period from Sept. 76 to Oct. 80 he worked with Hindustan Brown Boveri Ltd. Baroda, at their R and D center. He enrolled at the Oregon Graduate Center Beaverton, Oregon in Nov. 80 and completed the requirements for his Ph.D in Materials Science in May 1986.